

https://dspace.org/

Thermo-mechanical processing and testing of titanium alloys for potential dental applications

Nape, Kgetjepe Tlhologelo

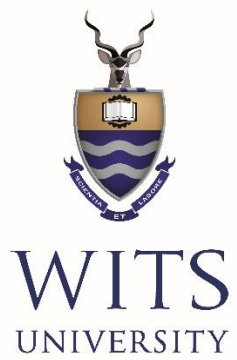
2022-12

University of the Witwatersrand, Johannesburg

https://hdl.handle.net/10539/41701

Nape, Kgetjepe Tlhologelo. (2022). Thermo-mechanical processing and testing of titanium alloys for potential dental applications. [Master's dissertation, University of the Witwatersrand, Johannesburg]. https://hdl.handle.net/10539/41701

Downloaded from a DSpace repository. https://dspace.org/



MSc Research Dissertation

Thermo-mechanical processing and testing of titanium alloys for potential dental applications

Student name/number: Kgetjepe Tlhologelo Nape (573762)

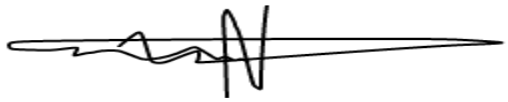
Month, year: December 2022

Submitted to

School of Chemical and Metallurgical Engineering, Faculty of Engineering and the Built Environment, University of the Witwatersrand, Johannesburg, South Africa.

Declaration

I, Kgetjepe Tlhologelo Nape, hereby declare that this dissertation, unless otherwise acknowledged, is my own original work. The dissertation is submitted for the award of Masters of Science in Engineering in the School of Chemical and Metallurgical Engineering, University of the Witwatersrand, Johannesburg, South Africa. This work has not been previously submitted at this, or any other institution of learning for any degree or examination.



…….

Kgetjepe Tlhologelo Nape

Student No: 573762

20 December 2022

Abstract

New titanium alloy compositions were identified for potential dental implants on the basis of having two-phase microstructures for good mechanical properties and by avoiding problematic elements to increase biocompatibility. The Thermo-Calc program with the TTTI3 (TT Ti-alloy) database was used to calculate new Ti compositions, without toxic Al and V as alloying elements. The aim was to mimic the α+β phase proportions in Ti-6Al-4V and Ti-10.1Ta-1.7Nb-1.6Zr (TTNZ) (an analogue for Ti-6Al-4V). Copper (Cu = 1, 3, 5 and 10 wt%) was varied to give the Ti_2Cu phase, which gives good hardness and antibacterial properties. A cost analysis was done and the less expensive Ti-6Nb-4Zr-*x*Cu and Ti-8Nb-4Zr-*x*Cu (*x* = 0 and 5 wt%) compositions were selected for experimental work. The samples were made by arc-melting and prepared for microstructural studies to understand the influence of alloying elements, and to compare with the commercial Ti-6Al-4V and reported Ti-10.1Ta-1.7Nb-1.6Zr (TTNZ) alloys. Hot deformation of the as-received Ti-6Al-4V and TTNZ alloys was investigated, using a Gleeble 3500® Thermo-mechanical Simulation Facility, at 850°C and 950°C and strain rates of 0.1 s^{-1} and 10 s^{-1}.

The as-cast Ti-6Nb-4Zr-*x*Cu and Ti-8Nb-4Zr-*x*Cu (*x* = 0 and 5 wt%) alloys comprised αTi and βTi, with Ti_2Cu once Cu was added, although EDX indicated some inhomogeneity. The XRD analyses identified αTi and small amounts of βTi with solid solution (shifted peaks), with some Ti_2Cu. The Ti-8Nb-4Zr alloy (285 ± 7 HV) had similar hardness to Ti-6Nb-4Zr (280 ± 13 HV), and was considered the better alloy. Adding 5 wt% Cu increased the hardness due to Ti_2Cu.

With the Gleeble, deformation at 950°C and 10 s^{-1} led to a finer Ti-6Al-4V microstructure, whereas finer Ti-10.1Ta-1.7Nb-1.6Zr (TTNZ) microstructures occurred at 850°C and 10 s^{-1}. The XRD of all deformed Ti-6Al-4V and Ti-10.1Ta-1.7Nb-1.6Zr samples indicated αTi and βTi, with shifted βTi peaks. The Ti-6Al-4V (324 ± 9 HV) deformed at 850°C and 0.1 s^{-1} had higher hardness than both deformed TTNZ samples. Higher flow stress were obtained at higher strain rate (10 s^{-1}) and lower temperature (850°C). The Ti-6Al-4V alloy had higher flow stress than the TTNZ alloy. Therefore, the TTNZ alloy was considered better, due to its lower flow stress, which indicated better formability. The new alloys had similar hardnesses to Ti-6Al-4V, and were higher than for TTNZ, suggesting that they might have similar properties to Ti-6Al-4V.

Dedication

This dissertation is dedicated to my mother Lephepane Ivy Nape, my grandmother Matawane Elizabeth Nape, my aunt Tlakale Maria Nkopodi and her late husband Mogase Silas Nkopodi, my uncle Makotanyane Tebogo Samuel Morewane, and also my family (The Nape's), cousins and friends for their support and encouragement.

Acknowledgements

I would like to give my sincere gratitude to the following people and organisations for their help and support to complete this project:

- Prof. L.A. Cornish and Prof. L.H. Chown for their supervision, support, motivation and guidance.
- The DSI-NRF and Centre of Excellence in Strong Materials (CoE-SM) for their financial support.
- The School of Chemical and Metallurgical Engineering at the University of the Witwatersrand, for providing facilities and equipment.
- Mintek, for providing facilities and equipment to make the samples, with the assistance of Mr Edson Muhuma to cast the alloys.
- Petra Dinham for assisting with the SEM analysis.
- Dr Michael Oluwatosin Bodunrin and Japheth Obiko for assisting with Gleeble 3500® Thermo-mechanical Simulation Facility.
- Kiyaasha Dyal Ukabhai and Nthape Percival Mphasha for sharing their experience, knowledge and guidance as postgrads.

Table of Contents

List of Figures ix
List of Tables xviii
List of Abbreviations xxi
Chapter 1: Introduction 1
1.1 Background 1
1.2. Problem statement and research motivation 3
1.3. Research questions 3
1.4. Hypothesis 3
1.5 Aim and Objectives 4
1.5.1. Aims 4
1.5.2. Objectives 4
1.6. Structure of the dissertation 4
Chapter 2: Literature Review 5
2.1. Titanium and its general properties 5
2.2. Processing and manufacturing of titanium alloys 7
2.3. Phases in titanium alloys 8
2.4 Different titanium alloys 10
2.4.1. Alpha (α) and near-α alloys 13
2.4.2. The α+β alloys 14
2.4.3. Beta (β) and metastable-β alloys 15
2.5. Microstructures of Ti alloys 15
2.6. Important mechanical properties for biomedical alloys 19
2.7. Titanium alloys in biomedical applications 23
2.8. Biomedical implant infections 26
2.9. Copper additions to titanium alloys 28
2.10. Thermo-mechanical simulation using the Gleeble 3500® Thermomechanical Simulation Facility 38
2.11. Summary of the literature review and rationale of the research project 44
Chapter 3: Experimental Procedure 46
3.1. Thermo-Calc calculations 46
3.2. Cost analysis 47

3.3. Materials and Methods 48
3.3.1. Production and Preparation of samples 48
3.3.2. Microstructural Studies 50
3.3.3. X-ray diffraction analysis 51
3.3.4. Hardness testing 51
3.3.5. Hot compression testing 52
Chapter 4: Thermo-Calc Results 54
4.1. Ti-6Al-4V-*x*Cu compositions 54
4.2. Ti-10.1Ta-1.7Nb-1.6Zr-*x*Cu compositions 56
4.3. Ti-6Nb-4Zr-*x*Cu compositions 59
4.4. Ti-8Nb-4Zr-*x*Cu compositions 61
4.5. Ti-6Nb-2Zr-1.7Ta-*x*Cu compositions 63
4.6. Ti-6Zr-4Ta-4Nb-*x*Cu compositions 65
4.7. Ti-4Ta-1.8Zr-1.5Mo-*x*Cu compositions 67
4.8. Ti-6Ta-2Zr-1.5Mo-*x*Cu compositions 69
4.9. Ti-8Ta-1.5Mo-1.5Zr-*x*Cu compositions 71
4.10. Ti-8Zr-4Ta-2Mo-*x*Cu compositions 73
4.11. Ti-3.5Ta-3Nb-3Zr-*x*Cu compositions 75
4.12. Ti-4.5Nb-4Ta-1.5Zr-*x*Cu compositions 77
4.13. Ti-6Zr-4Nb-*x*Cu compositions 79
4.14. Ti-6Zr-2Mo-*x*Cu compositions 81
4.15. Ti-10Ta-8Zr-*x*Cu compositions 83
4.16. Discussion of Thermo-Calc results 85
4.17. Cost analysis 87
Chapter 5: Experimental Results 89
5.1. Optical and SEM microstructural analysis 89
5.1.1. As-received Ti-6Al-4V alloy 89
5.1.2. As-received Ti-10.1Ta-1.7Nb-1.6Zr (TTNZ) alloy 90
5.1.3. As-cast Ti-6Nb-4Zr-*x*Cu alloy 91
5.1.4. As-cast Ti-8Nb-4Zr-*x*Cu alloy 93
5.2. Vickers micro-hardness testing 95
5.3. Hot compression testing 96

5.3.1. Microstructures of the deformed Ti-6Al-4V alloy 96
5.3.2. Microstructures of the deformed Ti-10.1Ta-1.7Nb-1.6Zr alloy 100
5.3.3. Deformation behaviour of the as-received Ti-6Al-4V and Ti-10.1Ta-1.7Nb-1.6Zr alloys 104
Chapter 6: Discussion 107
6.1. XRD analyses and phase identification 107
6.2. Microstructures 107
6.3. Vickers micro-hardness 108
6.4. Hot deformation behaviour of the as-received Ti-6Al-4V and Ti-10.1Ta-1.7Nb-1.6Zr alloys 109
Chapter 7: Conclusions 111
Chapter 8: Recommendations 112
References 113
Appendix A: Cost calculations 126
Appendix B: Published and submitted work from this research 127

List of Figures

Figure 2.1: Crystal structure of hcp α and bcc β phase of titanium (Leyens & Peters, 2003). 6

Figure 2.2: Schematic Ti phase diagrams showing the effects of selected alloying elements (Leyens & Peters, 2003). ……..……..……..……..……..... 8

Figure 2.3: Ti-Al phase diagram (Massalski, 1990). ……..……..……..... 10

Figure 2.4: Schematic Ti phase diagrams: (a) to classify Ti alloys (Leyens & Peters, 2003), and (b) schematic binary isomorphous phase diagram showing martensite start temperature (M_S) and other phases (Kolli & Devaraj, 2018). ……..……..... 11

Figure 2.5: Schematic diagram showing thermomechanical treatment of titanium alloys (Leyens & Peters, 2003). ……..... 16

Figure 2.6: Optical micrographs showing different Ti-6Al-4V microstructures: (a) lamellar, (b) equiaxed and (c) bimodal (Rack & Qazi, 2006), and after slow cooling (50ºC/h) and water quenching from (d) 1050ºC, (e) 800ºC and (f) 650ºC. Light areas are α phase, dark areas are β phase (Leyens & Peters, 2003). ……..…..……..... 18

Figure 2.7: Schematic diagram showing bone integration (Hanawa, 2012). ..……... 21

Figure 2.8: Phase proportion diagrams for Ti-10.1Ta-1.7Nb-1.6Zr and Ti-6Al-4V (wt%) (Stenlund et al., 2015). ….... 26

Figure 2.9: Cluster of bacteria associated with peri-implantitis. ……..... 27

Figure 2.10: Assessed phase diagram of the Cu-Ti binary system, showing congruent formation of Ti_2Cu without Ti_3Cu (Ansara et al., 2021). ……..... 29

Figure 2.11: Numbers of bacterial colonies after co-culturing with Ti-6Al-4V-xCu alloys (Ren et al., 2014). …….……..... 30

Figure 2.12: Antibacterial rate of Ti-Cu alloys against E. coli and S. aureus at different Cu content (Liu et al., 2014a). ……..……... 31

Figure 2.13: Schematic illustration of the antibacterial mechanism of Ti-Cu alloys (Ma et al., 2015). 32

Figure 2.14: Microstructures of Ti-10Cu (wt%): (A) after rapid quenching from 798°C and (B) after ageing at 400°C (Fowler et al., 2019b). 33

Figure 2.15: Microstructures of: (A) Ti-10.1Ta-1.7Nb-1.6Zr-3Cu and (B) Ti-10.1Ta-1.7Nb-1.6Zr-5Cu (wt%) showing Ti_2Cu (Fowler et al., 2019d). 34

Figure 2.16: Mechanical properties of cast Ti-xCu (x = 2, 5 and 10 wt%) alloys (Takahashi et al., 2002). 35

Figure 2.17: Tensile strength, yield strength, and elongation of Ti alloys (Kikuchi et al., 2003). 36

Figure 2.18: Corrosion studies of Ti-6Al-4V-xCu: (a) Potential polarization and (b) Electrochemical corrosion currents and pitting potentials (Ren et al., 2014). 37

Figure 2.19: Morphologies of MG63 cells cultured on Ti-10Cu and CP-Ti surfaces, showing similar cell growth: (a) Ti-10Cu for 1 day, (b) Ti-10Cu for 3 days, (c) CP-Ti for 1 day and (d) CP-Ti for 3 days (Liu et al., 2014b). 38

Figure 2.20: Tensile stress-strain curves of Ti-6Al-4V at $5x10^{-2}$-$5x10^{-4}$ s^{-1} and 750-950°C from a Gleeble 3800® (Vanderhasten, 2008). 41

Figure 2.21: Tensile stress-strain curves of Ti-6Al-4V at 600-950°C and 10^{-1}-10^{-3} s^{-1} strain rate from a Gleeble 3800® (Dos Santos, 2017). 41

Figure 2.22: Starting microstructure of Ti-6Al-4V (dark phase is α and light is β) (Dos Santos, 2017). 42

Figure 2.23: Microstructures of deformed Ti-6Al-4V at 700°C and 850°C for 10^{-3} s^{-1} strain rate (dark phase is α and light is β) (Dos Santos, 2017). 42

Figure 2.24: Microstructures of deformed Ti-6Al-4V at 950°C for 10^{-3} s^{-1} strain rate (Dos Santos, 2017). 43

Figure 2.25: Compressive engineering stress-strain curves of as-cast Ti-6Al-*x*V-*y*Fe at a strain of (a) 0.6 and (b) 1.2, from a Gleeble 3500® (Bodunrin et al., 2017). ……..... 44

Figure 3.1: Flow diagram showing the experimental procedure for the project. ….……..……46

Figure 3.2: Hot compression testing: (a) test sample and (b) testing in the Gleeble 3500® (Bodunrin, 2018). ……..……..... 53

Figure 4.1: Phase proportion diagram for Ti-6Al-4V (*wt%*). ……..... 55

Figure 4.2: Phase proportion diagram for Ti-6Al-4V-1Cu (*wt%*). ……..... 55

Figure 4.3: Phase proportion diagram for Ti-6Al-4V-3Cu (*wt%*). ……..... 55

Figure 4.4: Phase proportion diagram for Ti-6Al-4V-5Cu (*wt%*). ……..... 55

Figure 4.5: Phase proportion diagram for Ti-6Al-4V-10Cu (*wt*%). ……..... 55

Figure 4.6: Phase proportion diagram for Ti-10.1Ta-1.7Nb-1.6Zr. ……..... 58

Figure 4.7: Phase proportion diagram for Ti-10.1Ta-1.7Nb-1.6Zr-1Cu. ...……..... 58

Figure 4.8: Phase proportion diagram for Ti-10.1Ta-1.7Nb-1.6Zr-3Cu. ..……..... 58

Figure 4.9: Phase proportion diagram for Ti-10.1Ta-1.7Nb-1.6Zr-5Cu. ..……..... 58

Figure 4.10: Phase proportion diagram for Ti-10.1Ta-1.7Nb-1.6Zr-10Cu. ..…….…..... 58

Figure 4.11: Phase proportion diagram for Ti-6Nb-4Zr. ……..... 60

Figure 4.12: Phase proportion diagram for Ti-6Nb-4Zr-1Cu. ……..……..... 60

Figure 4.13: Phase proportion diagram for Ti-6Nb-4Zr-3Cu. ……..……..... 60

Figure 4.14: Phase proportion diagram for Ti-6Nb-4Zr-5Cu. ……..……..... 60

Figure 4.15: Phase proportion diagram for Ti-6Nb-4Zr-10Cu. ……...……..... 60

Figure 4.16: Phase proportion diagram for Ti-8Nb-4Zr. ……...……..... 62

Figure 4.17: Phase proportion diagram for Ti-8Nb-4Zr-1Cu. ……..……..... 62

Figure 4.18: Phase proportion diagram for Ti-8Nb-4Zr-3Cu. 62

Figure 4.19: Phase proportion diagram for Ti-8Nb-4Zr-5Cu. 62

Figure 4.20: Phase proportion diagram for Ti-8Nb-4Zr-10Cu. 62

Figure 4.21: Phase proportion diagram for Ti-6Nb-2Zr-1.7Ta. 64

Figure 4.22: Phase proportion diagram for Ti-6Nb-2Zr-1.7Ta-1Cu. 64

Figure 4.23: Phase proportion diagram for Ti-6Nb-2Zr-1.7Ta-3Cu. 64

Figure 4.24: Phase proportion diagram for Ti-6Nb-2Zr-1.7Ta-5Cu. 64

Figure 4.25: Phase proportion diagram for Ti-6Nb-2Zr-1.7Ta-10Cu. 64

Figure 4.26: Phase proportion diagram for Ti-6Zr-4Ta-4Nb. 66

Figure 4.27: Phase proportion diagram for Ti-6Zr-4Ta-4Nb-1Cu. 66

Figure 4.28: Phase proportion diagram for Ti-6Zr-4Ta-4Nb-3Cu. 66

Figure 4.29: Phase proportion diagram for Ti-6Zr-4Ta-4Nb-5Cu. 66

Figure 4.30: Phase proportion diagram for Ti-6Zr-4Ta-4Nb-10Cu. 66

Figure 4.31: Phase proportion diagram for Ti-4Ta-1.8Zr-1.5Mo. 68

Figure 4.32: Phase proportion diagram for Ti-4Ta-1.8Zr-1.5Mo-1Cu. 68

Figure 4.33: Phase proportion diagram for Ti-4Ta-1.8Zr-1.5Mo-3Cu. 68

Figure 4.34: Phase proportion diagram for Ti-4Ta-1.8Zr-1.5Mo-5Cu. 68

Figure 4.35: Phase proportion diagram for Ti-4Ta-1.8Zr-1.5Mo-10Cu. 68

Figure 4.36: Phase proportion diagram for Ti-6Ta-2Zr-1.5Mo. 70

Figure 4.37: Phase proportion diagram for Ti-6Ta-2Zr-1.5Mo-1Cu. 70

Figure 4.38: Phase proportion diagram for Ti-6Ta-2Zr-1.5Mo-3Cu. 70

Figure 4.39: Phase proportion diagram for Ti-6Ta-2Zr-1.5Mo-5Cu. ……..……..... 70

Figure 4.40: Phase proportion diagram for Ti-6Ta-2Zr-1.5Mo-10Cu. ……..……..……..... 70

Figure 4.41: Phase proportion diagram for Ti-8Ta-1.5Mo-1.5Zr. ……..…….……..... 72

Figure 4.42: Phase proportion diagram for Ti-8Ta-1.5Mo-1.5Zr-1Cu. ……...…….……..... 72

Figure 4.43: Phase proportion diagram for Ti-8Ta-1.5Mo-1.5Zr-3Cu. ……...…….……..... 72

Figure 4.44: Phase proportion diagram for Ti-8Ta-1.5Mo-1.5Zr-5Cu. ……...……..... 72

Figure 4.45: Phase proportion diagram for Ti-8Ta-1.5Mo-1.5Zr-10Cu. ……...……...……..... 72

Figure 4.46: Phase proportion diagram for Ti-8Zr-4Ta-2Mo. ……..…….……..... 74

Figure 4.47: Phase proportion diagram for Ti-8Zr-4Ta-2Mo-1Cu. …….…….……..... 74

Figure 4.48: Phase proportion diagram for Ti-8Zr-4Ta-2Mo-3Cu. …….…..…….……..... 74

Figure 4.49: Phase proportion diagram for Ti-8Zr-4Ta-2Mo-5Cu. ….…..…….……..... 74

Figure 4.50: Phase proportion diagram for Ti-8Zr-4Ta-2Mo-10Cu. ……...…….……..... 74

Figure 4.51: Phase proportion diagram for Ti-3.5Ta-3Nb-3Zr. ...…….…….……..... 76

Figure 4.52: Phase proportion diagram for Ti-3.5Ta-3Nb-3Zr-1Cu. ...…….…….……..... 76

Figure 4.53: Phase proportion diagram for Ti-3.5Ta-3Nb-3Zr-3Cu. ...…….…….……..... 76

Figure 4.54: Phase proportion diagram for Ti-3.5Ta-3Nb-3Zr-5Cu. ...…….…….……..... 76

Figure 4.55: Phase proportion diagram for Ti-3.5Ta-3Nb-3Zr-10Cu. ...……...…….……..... 76

Figure 4.56: Phase proportion diagram for Ti-4.5Nb-4Ta-1.5Zr. …….…….……..... 78

Figure 4.57: Phase proportion diagram for Ti-4.5Nb-4Ta-1.5Zr-1Cu. …….…….……..... 78

Figure 4.58: Phase proportion diagram for Ti-4.5Nb-4Ta-1.5Zr-3Cu. …….…….……..... 78

Figure 4.59: Phase proportion diagram for Ti-4.5Nb-4Ta-1.5Zr-5Cu. …….…….……..... 78

Figure 4.60: Phase proportion diagram for Ti-4.5Nb-4Ta-1.5Zr-10Cu. ……..... 78

Figure 4.61: Phase proportion diagram for Ti-6Zr-4Nb. ……..……..... 80

Figure 4.62: Phase proportion diagram for Ti-6Zr-4Nb-1Cu. ……..……..... 80

Figure 4.63: Phase proportion diagram for Ti-6Zr-4Nb-3Cu. ……..……..... 80

Figure 4.64: Phase proportion diagram for Ti-6Zr-4Nb-5Cu. ……..……..... 80

Figure 4.65: Phase proportion diagram for Ti-6Zr-4Nb-10Cu. ……..……..... 80

Figure 4.66: Phase proportion diagram for Ti-6Zr-2Mo. …..……..... 82

Figure 4.67: Phase proportion diagram for Ti-6Zr-2Mo-1Cu. …..……..... 82

Figure 4.68: Phase proportion diagram for Ti-6Zr-2Mo-3Cu. …..……..... 82

Figure 4.69: Phase proportion diagram for Ti-6Zr-2Mo-5Cu. …..……..... 82

Figure 4.70: Phase proportion diagram for Ti-6Zr-2Mo-10Cu. …..…..……..... 82

Figure 4.71: Phase proportion diagram for Ti-10Ta-8Zr. ……...…..……..... 84

Figure 4.72: Phase proportion diagram for Ti-10Ta-8Zr-1Cu. ……...…..……..... 84

Figure 4.73: Phase proportion diagram for Ti-10Ta-8Zr-3Cu. ……....…..……..... 84

Figure 4.74: Phase proportion diagram for Ti-10Ta-8Zr-5Cu. ……...…..……..... 84

Figure 4.75: Phase proportion diagram for Ti-10Ta-8Zr-10Cu. ……...…..……..... 84

Figure 4.76: Ti_2Cu formation temperatures of the different titanium compositions.…….……87

Figure 4.77: Effect of beta-stabilisers on: (a) beta phase proportions at 400°C and (b) Ti_2Cu formation temperatures ……..…87

Figure 5.1: As-received Ti-6Al-4V (wt%): (a) Optical micrograph and (b) SEM-BSE image. (wt%). ...……..…….. 89

Figure 5.2: XRD analysis of the wrought Ti-6Al-4V (wt%) alloy (Bodunrin, 2018), showing αTi and βTi peaks shifted due to alloying. ……...……..... 90

Figure 5.3: As-received Ti-10.1Ta-1.7Nb-1.6Zr (wt%): (a) Optical micrograph and (b) SEM-BSE image. ……...……...……..... 90

Figure 5.4: XRD analysis of the as-received Ti-10.1Ta-1.7Nb-1.6Zr (wt%) (TTNZ) alloy, showing mainly shifted αTi peaks due to the alloying. ……..... 91

Figure 5.5: As-cast Ti-6Nb-4Zr (wt%): (a) Optical micrograph and (b) SEM-BSE image. ……...……..... 92

Figure 5.6: As-cast Ti-6Nb-4Zr-5Cu (wt%): (a) Optical micrograph and (b) SEM-BSE image. ……...……..……...…..……..... 92

Figure 5.7: XRD analysis of the as-cast Ti-6Nb-4Zr (wt%) alloy, showing mainly shifted αTi peaks due to alloying. ……...……..... 93

Figure 5.8: XRD analysis of the as-cast Ti-6Nb-4Zr-5Cu (wt%) alloy, showing mainly shifted αTi peaks, with some Ti_2Cu. ……...…...……..... 93

Figure 5.9: As-cast Ti-8Nb-4Zr (wt%): (a) Optical micrograph and (b) SEM-BSE image. ..……...……..……..... 94

Figure 5.10: As-cast Ti-8Nb-4Zr-5Cu (wt%): (α) Optical micrograph and (b) SEM-BSE image. ……..... 94

Figure 5.11: XRD analysis of the as-cast Ti-8Nb-4Zr (wt%) alloy, showing peaks for αTi, and small peaks for βTi shifted by alloying. ……...……...…...…...……..... 95

Figure 5.12: XRD analysis of the as-cast Ti-8Nb-4Zr-5Cu (wt%) alloy, showing αTi, and small βTi peaks shifted by alloying and Ti_2Cu. ……..…….....……..... 95

Figure 5.13: Mean Vickers hardness of the investigated alloys. ……..…..... 96

Figure 5.14: Optical micrographs of as-received Ti-6Al-4V (wt%) deformed at 0.1 s^{-1} strain rate: (a) 850°C and (b) 950°C. …..……....……...…..…..... 97

Figure 5.15: SEM-BSE images of as-received Ti-6Al-4V (wt%) deformed at 0.1 s^{-1} strain rate: (a) 850°C and (b) 950°C. ……..……..…..... 97

Figure 5.16: XRD analysis of the as-received Ti-6Al-4V deformed at 850°C and 0.1 s^{-1} strain rate, showing αTi and βTi peaks shifted by alloying. ……....……...…...……..... 98

Figure 5.17: XRD analysis of the as-received Ti-6Al-4V deformed at 950°C and 0.1 s^{-1} strain rate, showing αTi and βTi peaks shifted by alloying. ...……....…...……..... 98

Figure 5.18: Optical micrographs of as-received Ti-6Al-4V deformed at 10 s^{-1}strain rate: (a) 850°C and (b) 950°C. ……...……...……...…..…..... 99

Figure 5.19: SEM-BSE images of as-received Ti-6Al-4V deformed at 10 s^{-1}strain rate: (a) 850°C and (b) 950°C. ……...…….……...…..... 99

Figure 5.20: XRD analysis of the as-received Ti-6Al-4V deformed at 850°C and 10 s^{-1} strain rate, showing αTi and βTi peaks shifted by alloying. …….……..…….…..... 100

Figure 5.21: XRD analysis of the as-received Ti-6Al-4V deformed at 950°C and 10 s^{-1} strain rate, showing αTi and βTi peaks shifted by alloying. ……....……...…...……..... 100

Figure 5.22: Optical micrographs of as-received Ti-10.1Ta-1.7Nb-1.6Zr deformed at 0.1 s^{-1} strain rate: (a) 850°C and (b) 950°C. ……....……..……...…..….. 101

Figure 5.23: SEM-BSE images of as-received Ti-10.1Ta-1.7Nb-1.6Zr deformed at 0.1 s^{-1}strain rate: (a) 850°C and (b) 950°C. ……...…….……..... 101

Figure 5.24: XRD analysis of the as-received Ti-10.1Ta-1.7Nb-1.6Zr deformed at 850°C and 0.1 s^{-1} strain rate, showing mainly αTi with βTi peaks, shifted by alloying. …….…..... 102

Figure 5.25: XRD analysis of the as-received Ti-10.1Ta-1.7Nb-1.6Zr deformed at 950°C and 0.1 s^{-1} strain rate, showing mainly αTi with βTi peaks, shifted by alloying. ……..……... 102

Figure 5.26: Optical micrographs of as-received Ti-10.1Ta-1.7Nb-1.6Zr deformed at 10 s^{-1}strain rate: (a) 850°C and (b) 950°C. ..……....……..……...…….... 103

Figure 5.27: SEM-BSE images of as-received Ti-10.1Ta-1.7Nb-1.6Zr deformed at 10 s^{-1}strain rate: (a) 850°C and (b) 950°C. ……...…….……...….. 103

Figure 5.28: XRD analysis of the as-received Ti-10.1Ta-1.7Nb-1.6Zr deformed at 850°C and 10 s^{-1} strain rate, showing mainly αTi with βTi peaks, shifted by alloying. ……...…..... 104

Figure 5.29: XRD analysis of the as-received Ti-10.1Ta-1.7Nb-1.6Zr deformed at 950°C and 10 s^{-1} strain rate, showing mainly αTi with βTi peaks, shifted by alloying. …...……..…..... 104

Figure 5.30: Stress-strain curves of the as-received Ti-6Al-4V and Ti-10.1Ta-1.7Nb-1.6Zr (wt%) alloys deformed at 850°C and 950°C, and (a) 0.1 s^{-1} and (b) 10 s^{-1} strain rates. …….……..... 105

Figure 5.31: Mean Vickers hardness of the as-received and deformed alloys. ……..... 106

List of Tables

Table 2.1: General properties of titanium (Liu et al., 2004). 6

Table 2.2: Alloying elements which are α-stabilisers and β-stabilisers in Ti alloys (Leyens & Peters, 2003). 9

Table 2.3: Mechanical properties of different types of titanium alloys (Leyens & Peters, 2003). ……..... 12

Table 2.4: Different commercially pure Ti grades with oxygen, iron contents and yield strengths (Long & Rack, 1998; Leyens & Peters, 2003). 13

Table 2.5: Important mechanical properties of different microstructures (Leyens & Peters, 2003). ……... 19

Table 2.6: Mechanical properties of different Ti alloys for biomedical applications (Niinomi, 1998). 20

Table 3.1: The α-β stabilisers and alloying elements for titanium (Leyens & Peters, 2003). 47

Table 3.2: Compositions calculated with Thermo-Calc. ……..……..... 47

Table 3.3: Costs for the powders for Ti and alloying elements (https://www.sigmaaldrich.com) (8/10/2019). …….. 47

Table 3.4: Compositions of the samples studied. ……..….…..... 49

Table 3.5: Metallographic preparation of the Ti alloys studied. 50

Table 3.6: Hot compression testing parameters. …..... 53

Table 4.1: Phases in the TTTI3 database. ……..…….…….... 54

Table 4.2: Phase information for the Ti-6Al-4V-*x*Cu compositions. ……..... 56

Table 4.3: Phase information for Ti-10.1Ta-1.7Nb-1.6Zr-*x*Cu compositions. ……..... 57

Table 4.4: Phase information for Ti-6Nb-4Zr-*x*Cu compositions. 59

Table 4.5: Phase information for Ti-8Nb-4Zr-*x*Cu compositions. ……..... 61

Table 4.6: Phase information for the Ti-6Nb-2Zr-1.7Ta-*x*Cu compositions. ……..... 63

Table 4.7: Phase information for Ti-6Zr-4Ta-4Nb-*x*Cu compositions. ……..……..... 65

Table 4.8: Phase information for Ti-4Ta-1.8Zr-1.5Mo-*x*Cu compositions. …..……..... 67

Table 4.9: Phase information for Ti-6Ta-2Zr-1.5Mo-*x*Cu compositions. 69

Table 4.10: Phase information for Ti-8Ta-1.5Mo-1.5Zr-*x*Cu compositions. 71

Table 4.11: Phase information for Ti-8Zr-4Ta-2Mo-*x*Cu compositions. ……..... 73

Table 4.12: Phase information for Ti-3.5Ta-3Nb-3Zr-*x*Cu compositions. ……..... 75

Table 4.13: Phase information for the Ti-4.5Nb-4Ta-1.5Zr-*x*Cu compositions. …..... 77

Table 4.14: Phase information for Ti-6Zr-4Nb-*x*Cu compositions. ……..... 79

Table 4.15: Phase information for Ti-6Zr-2Mo-*x*Cu compositions. ……..... 81

Table 4.16: Phase information for Ti-10Ta-8Zr-*x*Cu compositions. 83

Table 4.17: Liquidus (T_L) and solidus (T_S), and Ti_2Cu formation temperatures of the different titanium compositions. ……..……..... 86

Table 4.18: Costs for the different Ti compositions. ……..……..……..... 88

Table 5.1: EDX analyses of the as-received Ti-6Al-4V (*wt%*) alloy. ……..……..... 89

Table 5.2: EDX analyses of the as-received Ti-10.1Ta-1.7Nb-1.6Zr (*wt%*) (TTNZ) alloy. …..... 91

Table 5.3: EDX analyses of the as-cast Ti-6Nb-4Zr-xCu (*wt%*) alloys. ……..…..…….. 92

Table 5.4: EDX analyses of the as-cast Ti-8Nb-4Zr-xCu (*wt%*) alloys. 94

Table 5.5: EDX analyses of the as-received Ti-6Al-4V (*wt%*) alloy deformed 850°C and 950°C for 0.1 s^{-1} strain rate. ……..……..…..…….…… 97

Table 5.6: EDX analyses of the as-received Ti-6Al-4V (*wt%*) alloy deformed 850°C and 950°C for 10 s^{-1} strain rate. ……..…..……..... 99

Table 5.7: EDX analyses of the as-received Ti-10.1Ta-1.7Nb-1.6Zr (*wt%*) alloy deformed 850°C and 950°C for 0.1 s^{-1} strain rate. ……..... 101

Table 5.8: EDX analyses of the as-received Ti-10.1Ta-1.7Nb-1.6Zr (wt%) alloy deformed 850°C and 950°C for 10 s^{-1} strain rate. ……... 103

Table 6.1: Solidification sequences of the different titanium alloy compositions. ……..…… 107

List of Abbreviations

(α+β)	The two-phase alpha plus beta phase field
α+β	The alpha plus beta titanium alloy type
bcc	Body-centred cubic
BSE	Back-scattered electron
CP-Ti	Commercially pure titanium
EIS	Electrochemical impedance spectroscopy
EDX	Electron dispersive X-ray spectroscopy
FEG-SEM	Field-Emission Gun Scanning Electron Microscope
hcp	Hexagonal closed packed
SEM	Scanning electron microscopy or Scanning electron microscope
SEI	Secondary electron image
TTNZ	Ti-10.1Ta-1.7Nb-1.6Zr
XRD	X-ray diffraction

Chapter 1: Introduction

This chapter provides a brief overview of the dissertation. The background, problem statement and research motivation, research questions and objectives and the structure of the dissertation are provided.

1.1 Background

Titanium is a light-weight material with a high strength to weight ratio, good fatigue resistance and excellent corrosion resistance, and is widely used in aerospace, power generation and biomedical applications (Bothe et al., 1940; Leventhal & Bone, 1951). Materials are being implanted in the human body to restore lost functions caused by disease, trauma and infection (Brånemark et al., 1977). This is done through surgical techniques and enables patients to live longer, and aid in maintaining or regaining mobility for a more fulfilling life (Brånemark et al., 1969). Titanium and its alloys are the biomaterials most commonly used in dentistry and load bearing orthopaedics to replace hard tissue and to mend broken bones (Bothe et al., 1940; Brånemark et al., 1977). The alloys are used as artificial knees, hip-joints and as supports for artificial teeth (Brånemark et al., 1969). Commercially pure titanium (CP-Ti) and the Ti-6Al-4V (wt%) alloy have been used in these applications due to their ability to bond with bone, which is termed “osseointegration” (Brånemark et al., 1969).

More than 100 titanium alloys have been developed and categorised as alpha (α), alpha+beta (α+β) or beta (β) alloys (Leyens & Peters, 2003; Long et al., 2014). The Ti-6Al-4V alloy is a two-phase (α+β) alloy with the desired mechanical properties for biomedical applications, and is the most investigated compared to other Ti alloys (Long & Rack, 1998; Leyens & Peters, 2003; Long et al., 2014). The existence of the α/β transformation in Ti alloys means that different microstructures and properties can be achieved, for example by thermo-mechanical processing (Leyens & Peters, 2003). The properties of Ti-6Al-4V include: high yield and tensile strength, good ductility, and excellent fatigue and corrosion resistance (Welsch et al., 1993; Niinomi, 1998; Roos-Jansaker et al., 2003). However, CP-titanium and Ti-6Al-4V have a fundamental disadvantage as implant materials: commercially pure titanium does not have sufficient strength for load bearing implant applications, whereas Ti-6Al-4V has raised considerable concerns as the alloying elements,

aluminium and vanadium, are considered to be toxic to the human body (Eisenbarth et al., 2004; Akahori et al., 2005). Therefore, the biocompatibility of Ti-6Al-4V could be a concern.

Zirconium, tantalum, niobium and molybdenum have been proposed as the potential non-toxic alloying elements to replace Al and V (Eisenbarth et al., 2004). Therefore, these elements can be considered to be biocompatible (Kuroda et al., 1998; Eisenbarth et al., 2004), because they can minimize adverse tissue reactions originating from the release of metal ions from the implant (Meng et al., 2014).

The osseointegration and biocompatibility concepts have led to studies to develop new Ti alloys for biomedical applications. The common goal is to have a low Young's modulus closer to that of bone, to avoid bone resorption (Long & Rack, 1998; Niinomi, 1998), and add copper for good antibacterial properties against inflammation and a progressive bone loss due to peri-implantitis (Hultin et al., 2002; Ren et al., 2014). Stenlund et al. (2015) developed the Ti-10.1Ta-1.7Nb-1.6Zr alloy to improve the mechanical strength and osseointegration performance compared with Ti-6Al-4V.

In this study, an attempt has been made to determine new titanium alloys for biomedical applications. The aim was to mimic the α+β phase proportions in Ti-6Al-4V by replacing toxic Al and V with biocompatible elements. The commercial Ti-6Al-4V and reported Ti-10.1Ta-1.7Nb-1.6Zr alloys were used as the basis for the investigations, and were compared in deformation studies, without copper. Work has been occurring already for adding copper to the latter alloy (Fowler et al., 2019) so this was not repeated. Instead, new alloys with different copper compositions (Cu = 0, 1, 3, 5 and 10 wt%) were varied to give the Ti_2Cu phase, which gives good hardness (Takahashi et al., 2002; Aoki et al., 2004) and antibacterial properties (Ren et al., 2014; Fowler et al., 2019a). The microstructures, hardness and thermo-mechanical properties, with and without copper additions, were studied.

The compositions and phase proportions were calculated using the Thermo-Calc program, with the TTTI3 (TT Ti-alloy) database, to give good phase distribution at 400°C (the lowest temperature where the data are taken to be reliable). The Ti-6Nb-4Zr-*x*Cu and Ti-8Nb-4Zr-*x*Cu (x = 0 and 5 wt%) samples were made by arc-melting and prepared for microstructure studies to understand the influence of alloying elements, and to compare with the Ti-6Al-4V and Ti-10.1Ta-1.7Nb-1.6Zr

alloys. The thermo-mechanical investigations, using the Gleeble 3500® Thermomechanical Simulation Facility, were done to study the hot deformation behaviour of Ti-6Al-4V and Ti-10.1Ta-1.7Nb-1.6Zr, whereas hardness testing was done to investigate the effect of Ti_2Cu precipitates due to copper additions.

1.2. Problem statement and research motivation

Recent research on titanium alloys with copper additions showed very promising biocompatibility, corrosion, mechanical and antibacterial properties (Ren et al., 2014; Zhang et al., 2016a; Fowler et al., 2019a). However, due to the novelty of Ti-Cu alloys in biomedical applications, much is unknown regarding their microstructures and thermo-mechanical properties. Therefore, the Ti-6Al-4V, Ti-10.1Ta-1.7Nb-1.6Zr and the new identified Ti alloys were investigated for improved microstructures and mechanical properties. The biocompatibility, corrosion and antibacterial properties of Ti-Cu alloys were studied by Ren et al. (2014), Zhang et al. (2016a) and Fowler et al. (2019a).

1.3. Research questions

- How does adding Cu, to Ti-6Al-4V, Ti-10.1Ta-1.7Nb-1.6Zr, and the compositions identified, affect the phase proportions and formation temperatures?
- How does Cu influence the microstructures and mechanical properties of some Ti alloys?
- How does thermo-mechanical treatment affect the microstructures and mechanical properties?
- How do thermo-mechanical properties and microstructure of Ti-10.1Ta-1.7Nb-1.6Zr (a Ti-6Al-4V analogue) differ from Ti-6Al-4V?
- What are the potential alloying compositions for the replacement of toxic Al and V?

1.4. Hypothesis

It is expected that adding enough copper will give the Ti_2Cu phase, and good hardness (Takahashi et al., 2002; Aoki et al., 2004) as well as good antibacterial properties (Ren et al., 2014; Fowler et al., 2019a), but the latter was not studied in this work. It was also expected that replacement of Al and V with Zr, Nb, Ta and Mo will give similar $\alpha+\beta$ proportions as Ti-6Al-4V, and similar microstructures.

1.5 Aim and Objectives

1.5.1. Aims

- To use Ti-6Al-4V and Ti-10.1Ta-1.7Nb-1.6Zr as a basis to develop new α+β titanium alloys with better mechanical properties for biomedical applications.
- To replace the Al and V in Ti-6Al-4V with non-toxic alloying elements.
- To achieve similar α+β phase proportions as the α+β Ti-6Al-4V alloy, and also have the Ti_2Cu phase after adding Cu to the Ti alloys.
- To investigate the microstructures and hardness of selected new Ti alloys.
- To investigate the microstructures, hardness and thermo-mechanical properties of Ti-6Al-4V and Ti-10.1Ta-1.7Nb-1.6Zr alloys.

1.5.2. Objectives

- To use Thermo-Calc to vary and determine copper compositions suitable for alloying the Ti-6Al-4V and Ti-10.1Ta-1.7Nb-1.6Zr, and identify some new Ti alloy compositions.
- To perform Thermo-Calc calculations on Ti alloys with replacements for Al and V, with non-toxic elements for α and β stabilising, and see the overall effect.
- To perform SEM and XRD analysis, and microhardness testing of the Ti alloys.
- To investigate the thermo-mechanical properties of selected Ti alloys using the Gleeble 3500® Thermomechanical Simulation Facility.

1.6. Structure of the dissertation

This dissertation has seven chapters, divided into: Introduction, Literature Review, Experimental Procedure, Thermo-Calc Results, Experimental Results, Discussion, and Conclusions and Recommendations. Chapter 1 details the background, problem statement and research motivation, research questions and aims/objectives of the research. Chapter 2 is the literature survey based on the previous studies and findings. The experimental methods with step-by-step procedures are summarised in Chapter 3, and Chapter 4 gives the Thermo-Calc results. The experimental results are presented in Chapter 5. The detailed discussion of the results is given in Chapter 6, and the research conclusions and recommendations for future work are presented in Chapter 7.

Chapter 2: Literature Review

This chapter is based on the history and previous studies on titanium and its alloys. The general properties are summarized, and the processing and manufacturing of Ti alloys are explained. Different Ti alloys with different phases, microstructures, biocompatibility and mechanical properties are also detailed. A general overview of the effect of copper additions and the thermo-mechanical treatment of Ti alloys is also given.

2.1. Titanium and its general properties

Titanium was first discovered in England in 1790 by Sir Willian Gregor, a British mineralogist and chemist, and named in 1795 by the German chemist Martin Heinrich Klaproth (Leyens & Peters, 2003; Liu et al., 2004). It is one of the transition elements in Group IV and Period 4 of the Periodic Table, and has an atomic number of 22 and an atomic weight of 47.90. Titanium is a nonferrous light metal with a melting point of 1668ºC and a density of 4.54 g/cm^3, and exists in more than one crystallographic form i.e. is allotropic (Long & Rack, 1998; Leyens & Peters, 2003). At room temperature, Ti has a hexagonal close-packed (hcp) structure, alpha (α) phase, αTi. Above 882ºC, it transforms into a body-centred cubic (bcc) structure, beta (β) phase, βTi, and the basal planes of $\{0001\}_\alpha$ change to $\{110\}_\beta$ planes (Figure 2.1) (Donachie, 2000; Leyens & Peters, 2003). The αTi phase is anisotropic and denser (Long & Rack, 1998; Leyens & Peters, 2003).

The hcp structure has only three slip systems, while bcc has a maximum of 48 slip systems (Long & Rack, 1998; Chandrasekaran & Zhang, 2005), although not all are active at a single temperature. This affects the response to plastic deformation and leads to large differences in the workability of the phases (Chandrasekaran & Zhang, 2005). Thus, the bcc phase is more likely to undergo plastic deformation (Leyens & Peters, 2003). Figure 2.1 shows the unit cells of the hcp αTi and the bcc βTi with their most densely packed planes and directions highlighted, and Table 2.1 gives their properties.

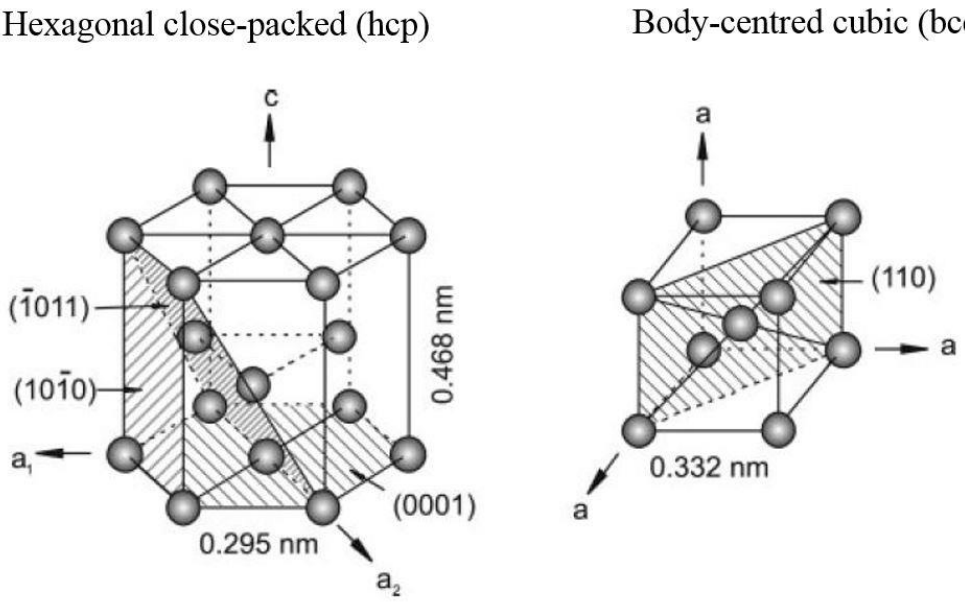


Figure 2.1: *Crystal structure of hcp α and bcc β phase of titanium (Leyens & Peters, 2003).*

Table 2.1: *General properties of titanium (Liu et al., 2004).*

Property	Value
Atomic number	22
Atomic weight (g/mol)	47.90
Crystal structure	
Alpha, hexagonal, closely packed	
c (Å)	4.6832 ± 0.0004
a (Å)	2.9504 ± 0.0004
Beta, cubic, body centered	
a (Å)	3.28 ± 0.003
Density (g cm^{-3})	4.54
Coefficient of thermal expansion, α, at 20 °C (K^{-1})	8.4×10^{-6}
Thermal conductivity (W/(m K))	19.2
Melting temperature (°C)	1668
Boiling temperature (estimated) (°C)	3260
Transformation temperature (°C)	882.5
Electrical resistivity	
High purity (μΩ cm)	42
Commercial purity (μΩ cm)	55
Modulus of elasticity, α, (GPa)	105
Yield strength, α, (MPa)	692
Ultimate strength, α, (MPa)	785

2.2. Processing and manufacturing of titanium alloys

Titanium passes through four stages of processing from ore to finish product (Lütjering & Williams, 2003). The stages include: 1) reduction of titanium ore to a porous titanium sponge; 2) melting of the sponge (or a master alloy) to form an ingot; 3) primary fabrication of the ingots into mill products; 4) secondary fabrication of mill products into finished titanium shapes (ASM, 1994; Lütjering & Williams, 2003). Titanium sponge must meet strict specifications to assure a control of compositions in the ingots (Lütjering & Williams, 2003). The most important factor is to keep the content of hard, brittle and refractory Ti oxides, Ti nitrides or complex Ti oxynitride particles at negligible levels (ASM, 1994; Lütjering & Williams, 2003). If retained, they will act as crack initiation sites in the final product (Lütjering & Williams, 2003). Residual elements commonly found in Ti sponge are oxygen, carbon, nitrogen, silicon and iron. High quantities of these elements have been shown to increase the strength, but reduce the ductility of the final product, and therefore must be kept at acceptable low levels (Leyens & Peters, 2003; Lütjering & Williams, 2003).

Modern melting techniques are employed to remove volatile substances from the sponge to produce ingots of high quality (Lütjering & Williams, 2003). Vacuum arc melting is used for production of Ti alloy ingots of 75 mm to 1.5 m diameter, for industry applications (Leyens & Peters, 2003; Lütjering & Williams, 2003). The process uses pure argon gas to create an oxygen-free environment in the furnace for melting and re-melting to give homogenization and refining of ingots casted in water-cooled copper crucibles (Leyens & Peters, 2003; Lütjering & Williams, 2003). The advantages are the elimination of hydrogen, nitrogen and oxygen which may cause brittleness and cracking (Lütjering, 1998; Leyens & Peters, 2003). The rate of melting and solidification depends on the operating conditions (Damkroger & Edwards, 1990; Lütjering, 1998). Increased solidification rates lead to an increased risk of micro-segregation, which is compositional variations in the ingot (Lütjering, 1998; Leyens & Peters, 2003). However, the inhomogeneity can be alleviated by thermomechanical processing (Lütjering, 1998). The cooling rates influence the grain structure produced during solidification (Lütjering & Williams, 2003). In general, higher cooling rates result in finer grains and homogeneous microstructures (Lütjering, 1998; Lütjering & Williams, 2003).

The primary fabrication is done to break down the coarse and inhomogeneous ingot structure, by preheating and forging in the β phase field, at 100°C-150°C above the β-transus temperature (ASM,

1994; Lütjering & Williams, 2003). The forging process is divided into cogging and upsetting, which differ by how the forging die is hot worked (Lütjering & Williams, 2003). Round ingots are pressed between flat dies along the ingot length during cogging, whereas the ingots are pressed along the ingot axis in upsetting (ASM, 1994; Lütjering & Williams, 2003). The forging temperature is controlled and dropped below β-transus temperature, to allow enough hot work in the ingot for subsequent heat treatments (Lütjering, 1998; Leyens & Peters, 2003).

2.3. Phases in titanium alloys

Titanium alloys are classified according to the morphology, size and the amounts of the α and β phases at room temperature (Leyens & Peters, 2003). The classification also depends on how any α/β stabilisers affect the β transformation temperature (T_β). The β-transus temperature, 882ºC for pure Ti, separates the β phase field from the α+β field (Leyens & Peters, 2003; Guillemot et al., 2004). Beta (β) exists as a stable phase above the β-transus (Leyens & Peters, 2003). Alpha stabilisers increase the β transformation temperature, whereas β stabilisers decrease it (Leyens & Peters, 2003; Akahori et al., 2005). Solid solution strengthening elements do not affect the β-transus temperature, and are considered neutral (Long & Rack, 1998; Leyens & Peters, 2003). These influences are shown in Figure 2.2 (Leyens & Peters, 2003).

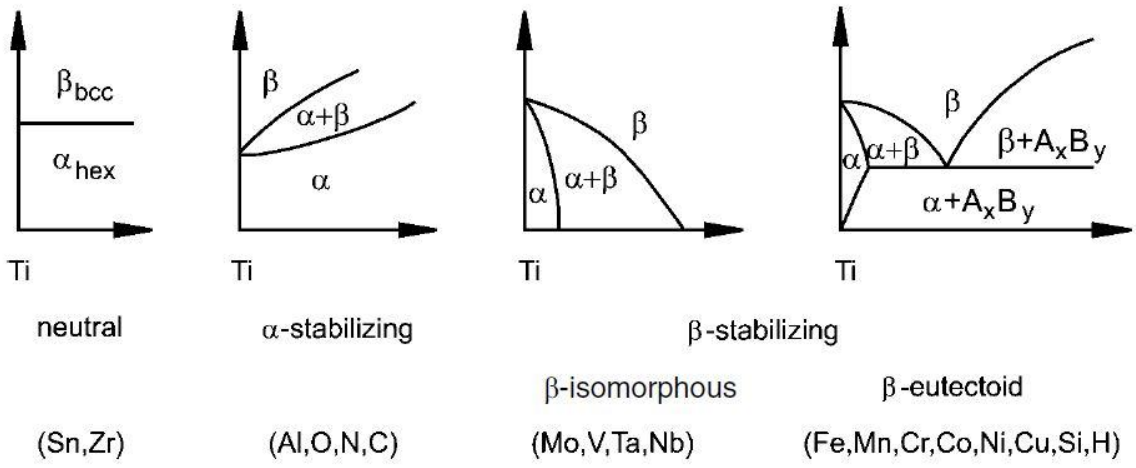


Figure 2.2: *Schematic Ti phase diagrams showing the effects of selected alloying elements (Leyens & Peters, 2003).*

Table 2.2 gives the α and β stabilisers, and neutral elements for the alloying of titanium. There are two types of β stabilisers, eutectoid and isomorphous (Leyens & Peters, 2003), Table 2.2. The β-eutectoid stabilisers have eutectoid behaviour and are compound formers, whereas β-isomorphous stabilisers are soluble in β (and do not form brittle intermetallic compounds) (Leyens & Peters, 2003; Chandrasekaran & Zhang, 2005). The modulus of the β phase decreases with decreasing content of the β-stabilising elements (Laheurte et al., 2010; Jung et al., 2013).

Table 2.2: *Alloying elements which are α-stabilisers and β-stabilisers in Ti alloys (Leyens & Peters, 2003).*

α-stabilizing	**Neutral**	**β-stabilizing**	
		β-isomorphous	**β-eutectoid**
Al	Sn	Mo	Fe
O	Zr	V	Mn
N		Ta	Co
C		Nb	Ni
Ga			Cu
			Si
			H
			W
			Cr

Figure 2.3 is one of the several versions of the Ti-Al systems (Massalski, 1990). Apart from the (αTi) and (βTi) phases, there are intermetallic phases such as α_2-Ti_3Al, γ-TiAl, $TiAl_2$ and $TiAl_3$ (Massalski, 1990; Leyens & Peters, 2003). Alloys with the α_2-Ti_3Al and γ-TiAl phases are used in the aerospace industry due to their low density, high-specific strength and stiffness, high-temperature creep and oxidation resistance (Lütjering, 1998; Leyens & Peters, 2003). Titanium aluminides such as $TiAl_2$ and $TiAl_3$ have poorer ductility and fracture toughness at room temperature, and therefore their applications are limited (Leyens & Peters, 2003). However, their ductility can be improved by refining the microstructures of the alloys (Lütjering, 1998; Leyens & Peters, 2003). Figure 2.3 also shows that the brittle $\alpha TiAl_3$ phase is formed above 60 wt% Al. To avoid the formation of Ti_3Al precipitates in the αTi phase, the Al content in most Ti alloys is limited to 6 wt% (Lütjering, 1998; Leyens & Peters, 2003). Ageing at 500°C will precipitate Ti_3Al, whereas heat treatment at 600°C or above is used to relieve stress (Massalski, 1990; Lütjering,

1998). Titanium aluminides based on Ti_3Al usually contain 20 - 45 wt% of β stabilisers (Lütjering, 1998).

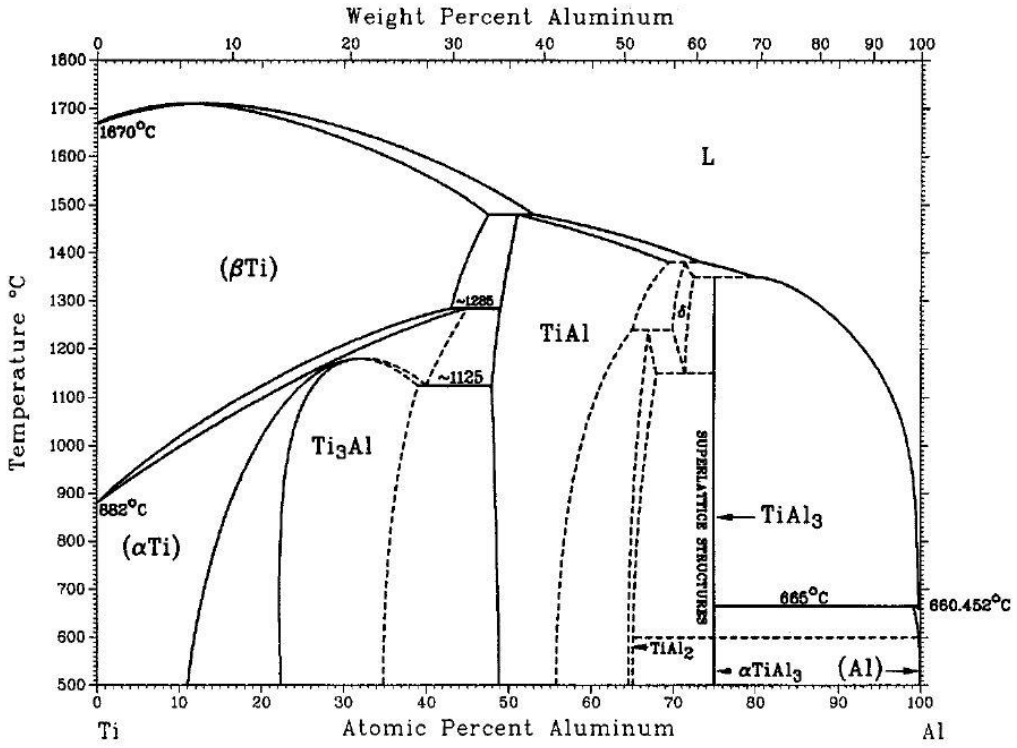


Figure 2.3: *Ti-Al phase diagram (Massalski, 1990).*

2.4 Different titanium alloys

Titanium alloys can be categorised as α, near-α, α+β, β and metastable β alloys (Polmear, 1981; Collings, 1984; Leyens & Peters, 2003). Figure 2.4a shows a three-dimensional phase diagram to classify the Ti alloys. The α alloys are commercially pure titanium (CP-Ti) and alloys with α-stabilising and/or neutral elements (Long & Rack, 1998; Leyens & Peters, 2003). A near-α alloy has small amounts of β stabilising elements (Bania, 1993; Schutz, 1993; Leyens & Peters, 2003). The α+β alloys have a β volume fraction of 5% to 40% at room temperature (Long & Rack, 1998; Peters & Lütjering, 2001).

Metastable β alloys are β alloys with sufficient β stabilising elements so that β no longer transforms to martensite on quenching (Leyens & Peters, 2003; Zhou et al., 2004), shown in Figure 2.4b. The

martensite can be divided into hexagonal α′ martensite and orthorhombic α″ martensite, the latter being observed on quenching below 900°C (Collings, 1984; Leyens & Peters, 2003). The α″ martensite is softer than α′ martensite (Collings, 1984). Higher solution treatment temperatures, and lower amounts of β stabilising elements, lead to the formation of hexagonal α′ on quenching from above 900°C (Leyens & Peters, 2003). The hcp-α′ has an acicular, or sometimes fine lamellar, microstructure, and is similar to the α phase (Leyens & Peters, 2003; Zhou et al., 2004). In general, the α″ martensite and α′ martensite formation and size depend on the composition of β, and the quenching rate from the β field (Zhou et al., 2004). The martensite start temperature (M_s) and finish temperature (M_f) are composition dependent, and decrease with increasing solute concentration (Collings, 1984; Zhou et al., 2004). When the M_f is below room temperature, the β phase partly transforms, whereas when the M_s is below room temperature, the martensite transformation is completely suppressed and the β phase is entirely retained (Collings, 1984). A stress-induced martensitic transformation from the β phase to α″ martensite will result in a very low yield stress (Hao et al., 2006; Zhang et al., 2012), although still with a higher strength than αTi (Leyens & Peters, 2003). The α″ martensite has lower strength and hardness, but better ductility than the β phase (Hao et al., 2002).

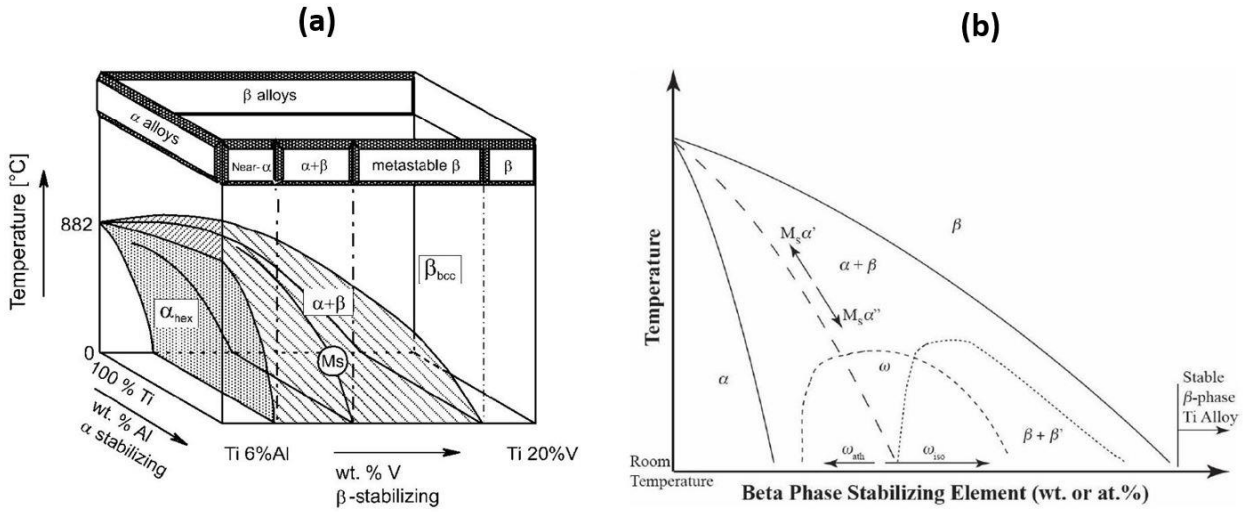


Figure 2.4: *Schematic Ti phase diagrams: (a) to classify Ti alloys (Leyens & Peters, 2003), and (b) schematic binary isomorphous phase diagram showing martensite start temperature (M_S) and other phases (Kolli & Devaraj, 2018).*

The Young's modulus depends on the composition of the alloying elements and the type of phases present in the Ti alloys, and it is not sensitive to the grain size (Collings, 1984; Hao et al., 2002; Matlakhova et al., 2005). For example, the metastable ω-phase (hcp) may form during slow quenching from the β phase or during isothermal aging at 200-350°C intermediate temperatures (Hao et al., 2002; Leyens & Peters, 2003; Kolli & Devaraj, 2018) (Figure 2.4b). The formation of this phase can be prevented by the presence of oxygen (Leyens & Peters, 2003). The ω-phase has the highest Young's modulus, followed by the α′-phase and α″-phase, whereas the β-phase has the lowest in most Ti alloys (Collings, 1984; Zhou et al., 2004; Matlakhova et al., 2005). Table 2.3 compares the mechanical properties of different Ti alloys (Leyens & Peters, 2003).

High cycle fatigue resistance depends on the resistance to crack nucleation, whereas low cycle fatigue resistance depends on resistance to crack propagation (Collings, 1984; Lütjering, 1998). The macrocrack propagation resistance and fracture toughness are improved by a large α size (Lütjering, 1998), whereas small α grains give improved yield strength, ductility, microcrack propagation resistance and fracture toughness (Lütjering, 1998). The microcrack propagation rate increases with increasing number of slip planes, and decreases with increasing cooling rate (Lütjering & Williams, 2003). The size of α depends on the cooling rate from the β phase field and the prior β grain size (Collings, 1984; Lütjering, 1998). Increased cooling rate leads to a reduced α size and an improved low cycle fatigue resistance (Lütjering & Williams, 2003). Increasing the α size (decreasing cooling rate) of the a+β alloys will decrease the propagation rate of the macrocracks, thus improving the fracture toughness (Lütjering, 1998; Lütjering & Williams, 2003).

Table 2.3: *Mechanical properties of different types of titanium alloys (Leyens & Peters, 2003).*

Properties	**α alloys**	**α+β alloys**	**β alloys**
Yield Strength	Low	High	High
Ductility	Medium	High	Low (for high strength β alloys)
Density	Low	Medium	High
Fracture toughness	Microstructure dependent	Microstructure dependent	Microstructure dependent
Creep strength	High (hcp lattice)	Medium to high	Low (bcc lattice)
Corrosion resistance	High	High	High
Young’s modulus	High	Medium to low	Low

The mechanical properties of titanium are enhanced by its allotropic behaviour, and are microstructure and heat treatment dependent. Their microstructures are influenced by the chemical composition and thermo-mechanical processing (Lütjering & Williams, 2003).

2.4.1. Alpha (α) and near-α alloys

Alpha and near-α alloys have superior corrosion resistance, but lower yield strength than α+β and β alloys (Long & Rack, 1998; Leyens & Peters, 2003). The α alloys are single-phase alloys and are generally not heat treatable and weldable, and have good notch toughness and good creep resistance at 300ºC (Smith, 1981; Leyens & Peters, 2003). The near-α alloys are primarily α alloys with small amounts of retained β phase in the final microstructure (Leyens & Peters, 2003). They are a good compromise between the higher strength of α+β alloys and the creep resistance of α alloys, with small additions (1 to 2 wt%) of β stabilisers to improve the strength and workability (Long & Rack, 1998; Leyens & Peters, 2003). Both α and near-α alloys are mostly used in aero-engines for high temperature application (Leyens & Peters, 2003).

Commercially pure titanium belongs to the α-Ti alloys, and the grades differ in oxygen and iron content (Long & Rack, 1998; Leyens & Peters, 2003). Table 2.4 gives different Ti grades and their yield strengths. The grades are used for biomedical applications such as dental screws (Long & Rack, 1998; Leyens & Peters, 2003).

Table 2.4: *Different commercially pure Ti grades with oxygen, iron contents and yield strengths (Long & Rack, 1998; Leyens & Peters, 2003).*

Type	**Oxygen content (wt%)**	**Iron content (wt%)**	**Yield strength (MPa)**
Grade 1	0.18	0.20	240
Grade 2	0.25	0.30	345-400
Grade 3	0.35	0.30	450-500
Grade 4	0.40	0.50	550-740

Increased oxygen increases the yield strength (Table 2.4), but with a simultaneous reduction in ductility (Leyens & Peters, 2003). The fatigue strength also increases significantly as the oxygen content increases (Leyens & Peters, 2003). The oxygen content must be kept as low as possible to

optimize fracture toughness, and be sufficient to meet tensile strength requirements (Long & Rack, 1998; Leyens & Peters, 2003).

Types of α alloys include CP-Ti (Grades 1-4) and Ti-5Al-2.5Sn, and near-α alloys include: Ti-8Al-1Mo-1V and Ti-6Al-2Sn-4Zr-2Mo.

2.4.2. The α+β alloys

The α+β alloys are two-phase alloys at room temperature (Smith, 1981; Long & Rack, 1998), and are the most commonly used titanium alloys for biomedical applications (Schutz, 1993; Leyens & Peters, 2003). These alloys have high Young's modulus, high strength and good formability, but do not have as good creep resistance at elevated temperatures as the α and near-α alloys (Smith, 1981). Their mechanical properties depend on the alloy composition, α/β phase proportions, heat treatment and thermo-mechanical processing conditions (Schutz, 1993; Bania, 1994; Leyens & Peters, 2003). The α+β alloys usually contain 4 - 6 wt% of β stabilisers, which allow substantial amounts of β phase to be retained on quenching from above T_β (Smith, 1981; Leyens & Peters, 2003). They are heat treatable to give a moderate increase in strength, depending on the β content (Long & Rack, 1998; Leyens & Peters, 2003; Nag et al., 2005). The volume fraction of β in the α+β alloys is around 40 vol.% (Peters & Lütjering, 2001), but may vary between 10-50 vol.% depending on the heat treatment (Lütjering, 1998).

The amounts of α and β phase can be tailored according to the desired properties of the alloy: high tensile strength versus fracture toughness, good creep resistance versus low cycle fatigue, and high tensile strength versus high cycle fatigue (Leyens & Peters, 2003). Heat treating and processing to adjust the microstructure, and precipitation of the β phase, can enhance the desired properties (Leyens & Peters, 2003). For example, the high elastic modulus of α+β alloys is due to the high-volume fraction of the α phase (Long & Rack, 1998; Nag et al., 2005). Heat treatment (ageing) at 882°C gives small amounts of α-precipitates in the β matrix, and this is a reliable method for improving the tensile and yield strength of the α+β alloys (Long & Rack, 1998; Lütjering & Williams, 2003; Jablokov et al., 2005).

Types of α+β alloys include Ti-6Al-4V, Ti-10.1Ta-1.7Nb-1.6Zr, Ti-6Al-7Nb, Ti-5Al-2.5Fe and Ti-6Al-6V-2Sn.

2.4.3. Beta (β) and metastable-β alloys

Beta alloys, with up to 30 wt% β-stabilisers, retain 100% β phase on quenching to room temperature (Bania, 1994; Jha & Ravichandran, 2000). They have good combinations of low Young's modulus, excellent corrosion resistance, good ductility, high yield strength and biochemical compatibility (Bania, 1993; Schutz, 1993; Long & Rack, 1998). The β alloys are heat treatable and have good formability (Schutz, 1993; Bania, 1994). However, they have low high-cycle fatigue performance than α+β alloys at equivalent yield strength (Kokuoz et al., 2005). In general, β alloys can be processed to higher strength levels and exhibit better notch properties and fracture toughness than α+β alloys (Wang, 1996; Niinomi, 1998). One of the ways to improve the processing of Ti alloys is to use β stabilisers to facilitate forging at lower temperatures (Chandrasekaran & Zhang, 2005). The β alloys are mostly preferred for biomedical applications due to their low Young's modulus that is closer to that of bone (Schutz, 1993; Bania, 1994; Jha & Ravichandran, 2000).

Metastable-β alloys contain 10 - 15 wt% of β-stabilisers, and small amounts of α-stabilisers as strengthening elements (Lütjering, 1998). They can be aged to form very fine Widmanstätten α phase in the β-matrix (Lütjering, 1998; Leyens & Peters, 2003). The metastable-β alloys have high yield strength, toughness and are forgeable (Leyens & Peters, 2003). They are most commonly used in aircraft applications (Lütjering, 1998; Leyens & Peters, 2003).

Types of β alloys include Ti-13Nb-13Zr, Ti-15Mo, Ti-29Nb-13Ta-4.6Zr, Ti-15Mo-2.8Nb-0.2Si and Ti-15Mo-5Zr-3Al.

2.5. Microstructures of Ti alloys

The microstructure can be tailored by heat treatment or thermo-mechanical treatment (Schutz, 1993; Bania, 1994). Thermo-mechanical treatment is a complex sequence of solution heat treatment, deformation, re-crystallisation, ageing and annealing for stress relief (Schutz, 1993; Olsson, 2008), shown in Figure 2.5. This is usually done to optimise the mechanical properties of titanium alloys, i.e. ductility, strength, fatigue resistance or fracture toughness (Boyer & Hall, 1993; Leyens & Peters, 2003), and is very important because alloying elements alone have small influence on the mechanical properties (Niinomi, 1998).

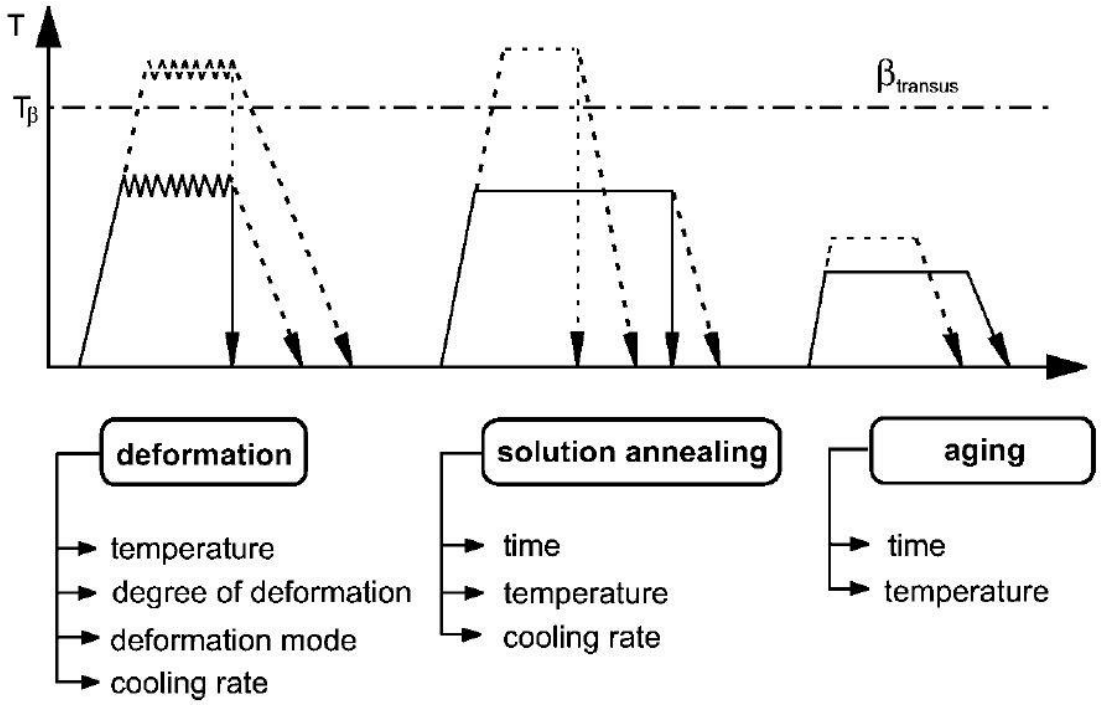


Figure 2.5*: Schematic diagram showing thermomechanical treatment of titanium alloys* (*Leyens & Peters, 2003).*

Due to temperature variations during forging, the microstructure can be non-uniform with globular (primary) α and transformed β (Widmanstätten) phases when heat treated in the α+β phase field (Damkroger & Edwards, 1990; Pederson, 2002). A heat treatment at 50-75°C above the β-transus is usually applied after forging to minimize the microstructural variations (Lütjering, 1998). The stored work after forging promotes recrystallisation, and the heating time is kept at minimum to prevent excessive grain growth (Pederson, 2002). However, normal heat treated grain sizes are about 500 µm (Lütjering, 1998; Pederson, 2002). During cooling, the α phase forms in the prior β grain boundaries, whereas basketweave α forms within the β grains via Widmanstätten transformation (Damkroger & Edwards, 1990; Lütjering, 1998). High cooling rates are preferred to reduce the grain boundary thickness of α phase, due to its deleterious effect on subsequent hot working (Damkroger & Edwards, 1990). This also promotes a finer basketweave α structure within the prior β grains (Damkroger & Edwards, 1990; Pederson, 2002). Different factors such as heat treatment, alloying compositions and microstructures contribute to the mechanical and physical properties of titanium and its alloys (Damkroger & Edwards, 1990; Lütjering, 1998).

In general, fine microstructures are beneficial for high strength, ductility, retarding crack nucleation and growth, and are also needed for plastic deformation (Lütjering, 1998; Rack & Qazi, 2006). Coarser microstructures are resistant to creep and fatigue crack growth (Pederson, 2002; Rack & Qazi, 2006).

The types of microstructures that are of interest are lamellar and equiaxed microstructures or bimodal, which is a combination of the two (Leyens & Peters, 2003; Rack & Qazi, 2006). The coarser α lamellar microstructure is formed by slow cooling from the β phase field (Leyens & Peters, 2003; Ding & Guo, 2004). Below the β-transus temperature (T_β), alpha (α) nucleates at grain boundaries and grows as lamellae into the prior β grains (Leyens & Peters, 2003). Slowly cooled (50ºC/h) Ti alloys show β as a small seam around the coarse α lamellae (Leyens & Peters, 2003; Rack & Qazi, 2006) (Figure 2.6a). Air cooling results in a needle-like hcp α-phase (acicular α) (Rack & Qazi, 2006).

Subsequent solution heat treatment in the α+β field and slow cooling lead to a recrystallised and fine equiaxed microstructure (Leyens & Peters, 2003; Rack & Qazi, 2006). The alloy first has to be highly deformed in the α+β field to introduce enough cold work into the material (Damkroger & Edwards, 1990; Leyens & Peters, 2003). Extended annealing coarsens the equiaxed microstructure, shown in Figure 2.6b (Rack & Qazi, 2006). Solution heat treatment just below the β-transus temperature and quenching from 750ºC result in a bimodal microstructure consisting of primary α grains in a transformed β-matrix (Figure 2.6c) (Leyens & Peters, 2003; Rack & Qazi, 2006). Figure 2.6d shows a fine needle-like microstructure due to the martensitic transformation of β, after rapid quenching (at 1050ºC) (Leyens & Peters, 2003). With fast cooling rates from 800ºC, above the martensitic start temperature (M_s) and through the two-phase field, β transforms into martensite (Figure 2.6e) (Lütjering, 1998; Leyens & Peters, 2003). At lower temperatures (650ºC) and below M_s, the β volume fraction further decreases and no longer transforms to martensite (Figure 2.6f) (Damkroger & Edwards, 1990; Leyens & Peters, 2003).

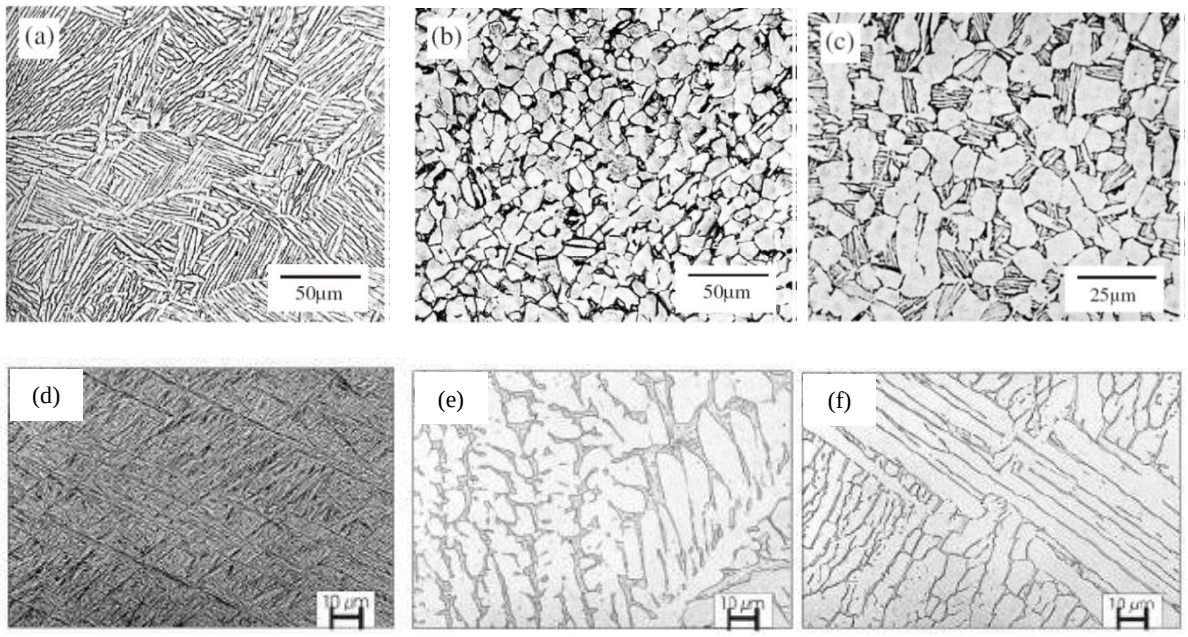


Figure 2.6: *Optical micrographs showing different Ti-6Al-4V microstructures: (a) lamellar, (b) equiaxed and (c) bimodal (Rack & Qazi, 2006), and after slow cooling (50ºC/h) and water quenching from (d) 1050ºC, (e) 800ºC and (f) 650ºC. Light areas are α phase, dark areas are β phase (Leyens & Peters, 2003).*

A coarse lamellar structure (Figure 2.6a) has high fatigue crack propagation resistance and high fracture toughness (Lütjering, 1998; Filip et al., 2003), but with reduced strength and ductility compared to the equiaxed microstructure (Figure 2.6b) (Rack & Qazi, 2006). Fatigue crack initiation for titanium alloys decreases with coarsening of the microstructure (Filip et al., 2003; Leyens & Peters, 2003). A fine equiaxed microstructure is preferred for α+β titanium alloys, due to high fatigue strength and ductility (Manivasagam, 2003; Rack & Qazi, 2006). The bimodal structure (Figure 2.6c) has improved yield stress, tensile stress, ductility and fatigue strength (Lütjering, 1998; Rack & Qazi, 2006). Table 2.5 gives the general mechanical properties of lamellar and equiaxed microstructures, and how coarsening of the microstructure influences the important mechanical properties (Leyens & Peters, 2003).

Table 2.5: *Important mechanical properties of different microstructures (Leyens & Peters, 2003).*

Property	**Lamellar**	**Equiaxed**	**Fine**	**Coarse**
Young's modulus	Un-affecting	Good/Bad (texture)	Un-affecting	Un-affecting
Strength	Bad	Good	Good	Bad
Ductility	Bad	Good	Good	Bad
Fracture toughness	Good	Bad	Bad	Good
Fatigue crack initiation	Bad	Good	Good	Bad
Fatigue crack propagation	Good	Bad	Bad	Good
Creep strength	Good	Bad	Bad	Good

2.6. Important mechanical properties for biomedical alloys

Titanium alloys have become the material of choice for biomedical applications due to their most desirable properties: high mechanical strength, excellent corrosion resistance, and good biocompatibility, especially their ability to bond with bone (i.e. osseointegration) (Steinemann, 1998; Leyens & Peters, 2003). The demands on the mechanical performance of the implants have increased as people tend to live longer, remain active, while gaining weight (Toss, 2009). The mechanical properties of titanium alloys are mainly determined by the composition, heat treatments and the resulting microstructure (Bothe et al., 1940; Leyens & Peters, 2003).

The alpha (α) phase has a higher Young's modulus than the β phase, so the α+β Ti-6Al-4V alloy has higher Young's modulus than β alloys due to the higher proportion of α phase (Leyens & Peters, 2003; Banerjee et al., 2005). Young's modulus is a measure of the stiffness of a material (Long & Rack, 1998). Titanium and its alloys, e.g. α+β Ti-6Al-4V and Ti-6Al-4V ELI (extra low interstitial), have higher Young's moduli than human bone (Table 2.6) (Long & Rack, 1998; Niinomi, 1998; Leyens & Peters, 2003). Human bone has a Young's modulus of about 10-40 GPa, and the lowest for titanium alloys is around 50 GPa (Long & Rack, 1998; Leyens & Peters, 2003).

The Young's modulus of a multiphase alloy is mainly determined by the modulus of its individual phases and by their volume fractions (Lee & Welsch, 1990; Fan, 1993; Hao et al., 2002). For a two-phase alloy, the Young's modulus can be predicted as:

$$E = V_1 E_1 + (1-V_1) E_2 \quad \text{..... Equation 2.1}$$

where: E is the Young's modulus of the two-phase alloy, and E_1 and E_2 are Young's moduli of phases 1 and 2, respectively. The V_1 is the volume fraction of the phase 1 (Hao et al., 2002; Zhou et al., 2004). Table 2.6 gives the mechanical properties of different Ti alloys (Niinomi, 1998).

Table 2.6: *Mechanical properties of different Ti alloys for biomedical applications (Niinomi, 1998).*

Alloy	Tensile strength (UTS) (Mpa)	Yield strength (σ_y)	Elongation (%)	RA (%)	Modulus (GPa)	Type of alloy
1. Pure Ti grade 1	240	170	24	30	102.7	α
2. Pure Ti grade2	345	275	20	30	102.7	α
3. Pure Ti grade 3	450	380	18	30	103.4	α
4. Pure Ti grade 4	550	485	15	25	104.1	α
5. Ti–6Al–4V ELI (mill Annealed)	860–965	795–875	10–15	25–47	101–110	$\alpha+\beta$
6. Ti–6Al–4V (annealed)	895–930	825–869	6–10	20–25	110–114	$\alpha+\beta$
7. Ti–6Al–7Nb	900–1050	880–950	8.1–15	25–45	114	$\alpha+\beta$
8. Ti–5Al–2.5Fe	1020	895	15	35	112	$\alpha+\beta$
9. Ti–5Al–1.5B	925–1080	820–930	15–17.0	36–45	110	$\alpha+\beta$
10. Ti–15Sn–4Nb–2Ta–0.2Pd						
(Annealed)	860	790	21	64	89	
(Aged)	1109	1020	10	39	103	
11. Ti–15Zr–4Nb–4Ta–0.2Pd						$\alpha+\beta$
(Annealed)	715	693	28	67	94	
(Aged)	919	806	18	72	99	
12. Ti–13Nb–13Zr (aged)	973–1037	836–908	10–16	27–53	79–84	β
13. TMZF (Ti–12Mo–6Zr–2Fe) (annealed)	1060–1100	100–1060	18–22	64–73	74–85	β
14. Ti–15Mo (annealed)	874	544	21	82	78	β
15. Tiadyne 1610 (aged)	851	736	10		81	β
16. Ti–15Mo–5Zr–3Al						β
(ST)	852	838	25	48	80	
(aged)	1060–1100	1000–1060	18–22	64–73		
17. 21RX (annealed) (Ti–15Mo–2.8Nb–0.2Si)	979–999	945–987	16–18	60	83	β
18. Ti–35.3Nb–5.1Ta–7.1Zr	596.7	547.1	19.0	68.0	55.0	β
19. Ti–29Nb–13Ta–4.6Zr (aged)	911	864	13.2		80	β

The Young's modulus of biomaterials should match that of bone to avoid stress shielding that could lead to bone resorption (Long & Rack, 1998; Albrektsson et al., 2015), implant loosening and failure of the implant (Ho et al., 1999). Bone resorption, due to lower applied stress (because the bone is supporting less load than normal), is the breaking down of the bone into its minerals, and it is caused by a large difference in Young's modulus between bone and implant material (Long & Rack, 1998; Sumner et al., 1998). When a load is applied, the implant absorbs the load

and hinders bone regeneration while enhancing bone resorption (Sumner et al., 1998). This leads to an inability of the implant to bond with bone (Long & Rack, 1998; Niinomi, 1998).

When a fractured bone is integrated with an implant material (Figure 2.7) such as bone plate, screws and bone nail, the implant endures load-bearing and shields the bone from the necessary stressing required to maintain its strength (Hanawa, 2012). Therefore, stress shielding would be induced (Huiskes et al., 1992; Hanawa, 2012), leading to inability of the bone to support the weight, due to the mismatch in Young's modulus.

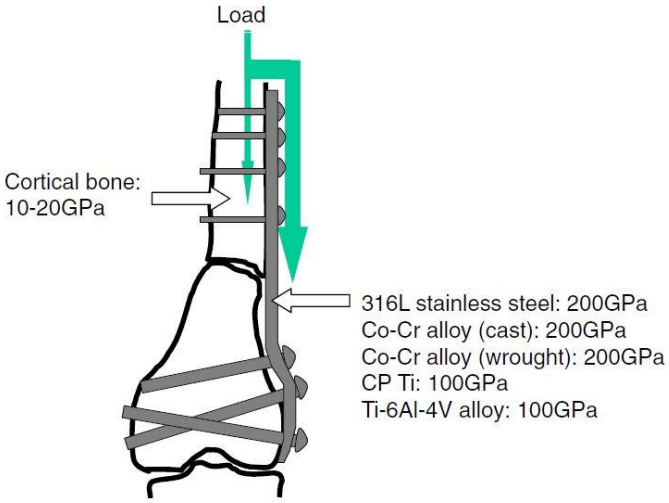


Figure 2.7: *Schematic diagram showing bone integration (Hanawa, 2012).*

In the orthopedic industry, the need to lower Young's modulus to match that of bone has led to the development of three β alloys, Ti-13Nb-13Zr (wt%) and Ti-12Mo-6Zr-2Fe (wt%) (Mishra et al., 1993; Wang et al., 1993), and Ti-15wt% Mo (Kuroda et al., 1998). The Ti-35Nb-7Zr-5Ta (wt%) (Ahmed et al., 1996) and Ti-29Nb-13Ta-4.6Zr (wt%) (Kuroda et al., 1998) alloys, also β type alloys, were developed to have excellent mechanical performance and Young's modulus lower than Ti-6Al-4V (Akahori et al., 2004; Banerjee et al., 2005; Nutt et al., 2005). Niinomi et al. (2016) found a Young's modulus of 60 GPa for the Ti-29Nb-13Ta-4.6Zr (wt%) alloy. There have also been attempts to understand the influence of alloying additions on the modulus and yield strength

of Ti alloys (Kuroda et al., 1998; Song et al., 1999). Kuroda et al. (1998) designed Ti alloys with lower Young's moduli for potential implant materials, and the Ti-Nb-Ta-Zr system was considered a suitable candidate. The development of the aforementioned β type titanium alloys may have also resolved the issue of biocompatibility by alloying with non-toxic and non-allergic elements like Nb, Ta, Mo and Zr (Mishra et al., 1993; Kuroda et al., 1998).

In addition to low Young's modulus, most β alloys have a lower yield strength than the α+β Ti-6Al-4V due to the stress-induced martensitic transformation (Leyens & Peters, 2003; Gepreel & Niinomi, 2013). Precipitation hardening is usually done by annealing to increase the yield strength of β alloys (Niinomi, 1998), without sacrificing the low Young's modulus (Meng et al., 2014). It is important to enhance the mechanical properties of Ti alloys to achieve a good combination of high strength and low Young's modulus (Zhou et al., 2004; Meng et al., 2014). The tensile strength can also be increased by grain refinement without varying Young's modulus (Zhou et al., 2004). The β Ti-36Nb-5Zr (wt%) alloy annealed at 425°C for 25 minutes by Meng et al. (2014), showed a yield strength of 720 MPa and an ultimate tensile strength of 860 MPa, and a low Young's modulus of 48 GPa (no errors were supplied). This excellent combination of low Young's modulus and high strength indicated a great potential for biomedical applications (Zhou et al., 2004; Meng et al., 2014).

A useful relationship between strength and Young's modulus for implant applications is referred as the "elastic admissible strain" of an alloy (Song et al., 1999a). The elastic admissible strain is the yield stress-to-modulus ratio, and is an important parameter considered in orthopaedic applications (Song et al., 1999a, 1999b). A higher elastic admissible strain is more suitable for implant applications (Song et al., 1999a, 1999b).

The beta titanium alloys Ti-3Al-15V-3Cr-3Sn, Ti-4.5Al-3V-2Mo-2Fe and Ti-3Al-8V-6Cr-4Mo-4Zr (wt%) were studied for high strength, fracture toughness and ductility for biomedical applications (Wood, 2015). The alloys were annealed at 700-825°C for 25-60 minutes, and aged at 450-600°C for 24 hours. Annealing increased the alloys' fracture toughness and ductility while ageing increased the strength (Wood, 2015).

Implant materials sometimes fail due to cyclic loading, fatigue and corrosion (Ahmed et al., 1996; Akahori et al., 2004). Therefore, tensile, corrosion and fatigue performances are also important

properties for Ti alloys in biomedical applications (Leyens & Peters, 2003; Akahori et al., 2004). These mechanical properties are affected by the microstructures obtained from heat treatments or thermo-mechanical treatments, hence Akahori et al. (2004) studied the tensile, corrosion, and plain and fretting fatigue properties of β Ti-29Nb-13Ta-4.6Zr (wt%). The cold-rolled Ti-29Nb-13Ta-4.6Zr, aged at 450°C, showed high fatigue strength in both low and high cycle fatigue life regions (Akahori et al., 2004). The fatigue strength was 770 MPa, nearly the same as that of hot-rolled Ti-6Al-4V ELI aged at 450°C. The forged Ti-29Nb-13Ta-4.6Zr had a fretting fatigue limit of 180 MPa after solution treatment, and 285 MPa (no errors were reported) when aged at 450°C. Passive current densities of forged and solution-treated Ti-29Nb-13Ta-4.6Zr, were smaller than those of forged Ti-15Mo-5Zr-3Al after annealing and hot-rolled Ti-6Al-4V ELI after ageing (Akahori et al., 2004).

Fatigue strength was also affected by surface processing and finishing, and surface treatments (Niinomi, 2003b; Niinomi & Nakai, 2011). The alloy underwent solution treatment at 790°C for 1 hour, and was aged at 400°C for 72 hours (Niinomi 2003b). The yield strength of Ti-29Nb-13Ta-4.6Zr (wt%) increased from 420 MPa to 1100 MPa, and the fatigue strength increased from 325 MPa to 775 MPa (errors were not reported) (Niinomi, 2003b). However, this was at the expense of an increase in the Young's modulus from 65 GPa to 85 GPa after the treatments, and no errors were reported (Niinomi, 2003b; Niinomi & Nakai, 2011).

Beta-titanium alloys generally have good corrosion resistance, depending on the alloy composition and the environment (Schutz, 1993). Niobium and zirconium contribute to the formation of a highly protective passive film on titanium alloys and are not released into the environment, and are thus biocompatible (Kovacs & Davidson, 1993).

2.7. Titanium alloys in biomedical applications

Most commercial Ti alloys are used as landing gear and engine components in aerospace applications, where the Ti-6Al-4V alloy covers about 70% of the market (Donachie, 2000; Akahori et al., 2005). The remaining 30% is mainly the commercially pure (CP) titanium (Leyens & Peters, 2003; Rack & Qazi, 2006).

The Ti-6Al-4V is a two-phase alloy at room temperature and the most common of the α+β titanium alloys (Smith, 1981; Long & Rack, 1998). The Al in α+β Ti-6Al-4V stabilises the α phase, and V

stabilises β (Long & Rack, 1998; Leyens & Peters, 2003). The Ti-6Al-4V ELI (extra low interstitial) alloy is a purer version of Ti-6Al-4V, with lower oxygen, iron and carbon contents (Smith, 1981; Leyens & Peters, 2003). Both Ti-6Al-4V and Ti-6Al-4V ELI have an excellent combination of yield strength and fracture toughness with excellent corrosion resistance (Leyens & Peters, 2003). The Ti-6Al-4V ELI has better toughness and is used for biomaterials, bone fixation plates and the stems of artificial hip joints, due to small amounts of interstitial impurities which decrease the fatigue strength (Leyens & Peters, 2003; Hanawa, 2012). The mechanical properties of Ti-6Al-4V are due to the composition which determines the microstructure, which is a good balance between hcp (α phase) and bcc (β phase) (Leyens & Peters, 2003; Akahori et al., 2005). The Ti-6Al-4V alloy has a 0.2% offset yield strength of 895MPa, and tensile strength of about 1000 MPa with adequate ductility (Long & Rack, 1998; Leyens & Peters, 2003; Hanawa, 2012). The alloy also has high resistance to wear, hence is employed in jewellery and motor industries (Hanawa, 2012).

Commercially pure titanium and Ti-6Al-4V alloy started to replace both stainless steels and cobalt-based alloys in many medical applications, especially in orthopaedic and dental areas, as early as in the 1940s (Bothe et al., 1940; Leventhal & Bone, 1951). Commercially pure titanium is widely used for load-bearing bone implants, although it does not have the sufficient strength (Leyens & Peters, 2003; Akahori et al., 2005). The Ti-6Al-4V alloy has higher yield strength than CP-Ti and often used for load-bearing bone implants (Johansson et al., 1989; Albrektsson, 2008). However, the Ti-6Al-4V alloy as an implant has raised considerable concerns due to its alloying elements, aluminium and vanadium, which are considered to be toxic to the human body (Leyens & Peters, 2003; Akahori et al., 2005). Additionally, Ti-6Al-4V has also shown signs of not going through osseointegration to the same extent as CP-Ti (Han et al., 1998; Steinemann, 1998). This is due to the body's response to toxic Al and V, and the difference in Young's modulus between bone (10-40 GPa) and the implant material (100-110 GPa for Ti-6Al-4V) (Long & Rack, 1998; Steinemann, 1998; Niinomi, 2003a).

Implant materials are expected to be non-toxic and should not cause any inflammatory or allergic reactions in the human body (Long & Rack, 1998; Niinomi, 2003a). The success of the biomaterials mainly depends on the reaction of the human body to the implant, and this determines the biocompatibility of a material (Leyens & Peters, 2003). When implants are exposed to human

tissues and fluids, they react with the host and these reactions dictate the acceptability of the materials by the body (Niinomi, 2003a).

There have been attempts to develop new biomedical alloys by replacing Al and V which are toxic (Long & Rack, 1998; Niinomi, 2003a), or trying to create the metastable β alloys with low Young's modulus (Akahori et al., 2005). The attempts aimed to achieve microstructures and mechanical properties similar to or better than those of the α+β Ti-6Al-4V alloy. Aluminium has been associated with Alzheimer's disease and phosphorous deficiency (Gurappa, 2002) in blood and bone, whereas vanadium has shown cytotoxic and carcinogenic properties (Gurappa, 2002; Nag et al., 2007). Zirconium, tantalum, tin, iron, niobium and molybdenum are considered to be biocompatible, and proposed as the potential non-toxic alloying elements to replace Al and V (Long & Rack, 1998; Leyens & Peters, 2003).

Okazaki et al. (2004) evaluated the Ti-6Al-4V and Ti-15Zr-4Nb-4Ta (wt%) alloys in rat tibia tissues (*in vivo*) for 48 weeks. The Ti-15Zr-4Nb-4Ta implant had lower Ti in the tibia tissues than the Ti-6Al-4V. The Zr, Nb and Ta amounts in the tibia tissues were also very low (Okazaki et al., 2004). Okazaki & Gotoh (2005) investigated the metal release of Grade 2 CP-Ti, Ti-6Al-4V, Ti-6Al-7Nb and Ti-15Zr-4Nb-4Ta (wt%) alloys, *in vitro*, at 37°C for 7 days. The metal release from the Ti-15Zr-4Nb-4Ta alloy was less than that of Ti-6Al-4V and Ti-6Al-7Nb (Okazaki & Gotoh, 2005). Therefore, the Ti-15Zr-4Nb-4Ta alloy was considered good for long-term implants (Okazaki et al., 2004; Okazaki & Gotoh, 2005).

Stenlund et al. (2015) developed the Ti-10.1Ta-1.7Nb-1.6Zr (wt%) alloy, where Ta and Nb were chosen for β stabilising and Zr as a solution-hardening element. They determined the compositions using the Thermo-Calc software, and combining data from Ansara et al. (1998) (COST507 database) with the Zr-Nb data by Guillermet (1991). The goal was to mimic the microstructure and the α+β phase proportions of Ti-6Al-4V (Figure 2.8), using only non-toxic elements to improve the mechanical strength. Figure 2.8 shows the phase proportion diagrams for Ti-10.1Ta-1.7Nb-1.6Zr (Stenlund et al., 2015) and Ti-6Al-4V.

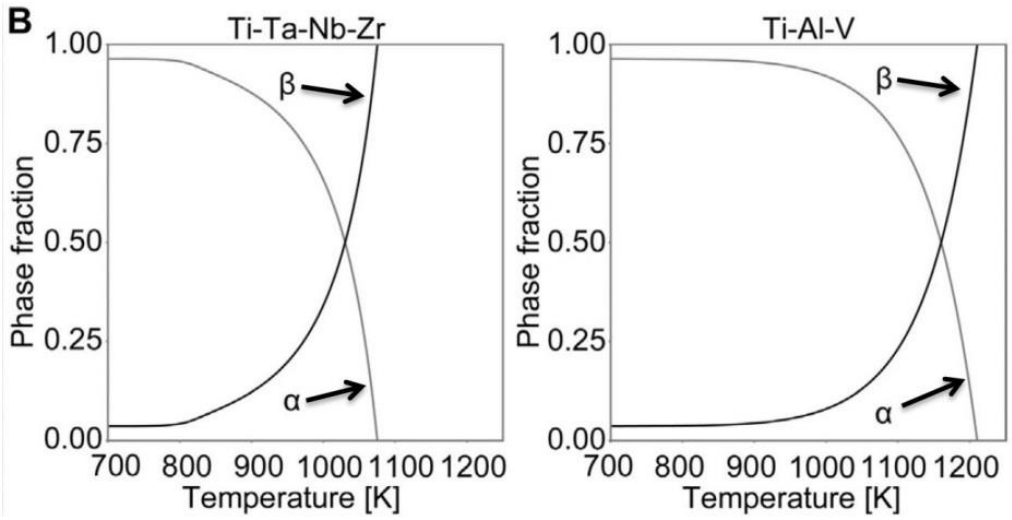


Figure 2.8: *Phase proportion diagrams for Ti-10.1Ta-1.7Nb-1.6Zr and Ti-6Al-4V (wt%) (Stenlund et al., 2015).*

The Ti-10.1Ta-1.7Nb-1.6Zr alloy was also evaluated for osseointegration (Stenlund et al., 2015), and showed increasing implant stability from 7 to 28 days, and with no sign of cytotoxicity or adverse tissue reactions. Compared to pure Grade 4 Ti, the alloy demonstrated equal cytocompatibility, induced less inflammatory response and became equally well osseointegrated (Stenlund et al., 2015).

2.8. Biomedical implant infections

Dental implants are currently being used in dentistry, and an estimated 7% patients suffer complete failure within 10 years (Leyens & Peters, 2003). Most of these failures are related to peri-implantitis, a disease that leads to inflammation and a progressive bone loss around the implant (Hultin et al., 2002; Ren et al., 2014), as shown in Figure 2.9.

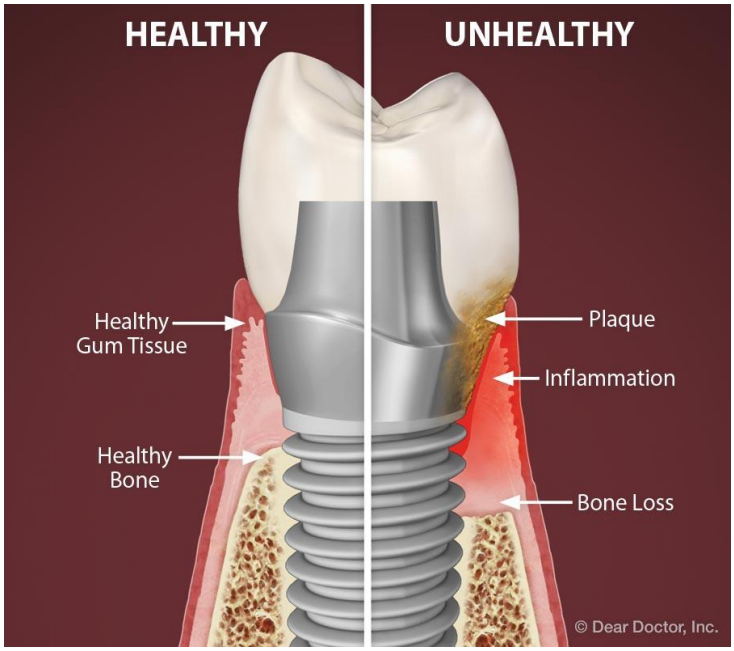


Figure 2.9: *Cluster of bacteria associated with peri-implantitis (Rayant, 2016).*

The bacteria causing peri-implantitis include: *Peptostreptococcus micros, Porphyromonas ginigivalis* and *Treponema denticola* (Fransson et al., 2005; Mazel et al., 2019). Fransson et al. (2005) reported 28% of patients with peri-implantitis, and Atieh et al. (2013) with 19%, whereas Derks & Tomasi (2015) reported 22%. The devastating outcome is not the associated cost, but the irreversible loss of bone (Fransson et al., 2009). Peri-implantitis is an ongoing problem in the dental industry (Ren et al., 2014; Yoda et al., 2014) and strategies are needed to minimise this problem (Fowler et al., 2019a; Mazel et al., 2019).

The antibiotic treatment of peri-implantitis has been a clinical practice, but the prescription of more potent antibiotics is not feasible (Hawkey, 2008; Alani et al., 2014). Khan et al. (2017) used organic compounds (oils) for bacterial colonisation to treat dental caries against *Streptococcus mutans*, and showed good antibacterial ability. Bacterial colonisation depends on the formation of biofilms (Arciola et al., 2012), which have the ability to survive antibiotic treatments due to less growth and poor penetration of antibiotics (Stewart, 2002; Vasudevan et al., 2019). The *Staphylococcus epidermidis* and *Staphylococcus aureus* are biofilm forming bacteria common in implant infections, and are suitable for testing the antibacterial ability of biomaterials (Zhang et al., 2003; Fowler et al., 2019a). Gill et al. (2005) reported the virulence and gene mutations by

Staphylococcus epidermidis and the antibiotic resistance of *Staphylococcus aureus*. Prevention of peri-implantitis is therefore important in developing antibacterial biomaterials (Ren et al., 2014; Yoda et al., 2014).

There have been studies to reduce the bacterial effect on implants, which include: surface treatments (Yoda et al., 2014; Cao et al., 2018), use of photochemical reactions (Unosson et al., 2016), surface coating with silver (Velasco et al., 2016), and alloying titanium with silver (Song et al., 2012) and copper (Ren et al., 2014; Zhang et al., 2016a; Fowler et al., 2019b). Silver appeared to be effective only at 37-60°C (Russel & Hugo, 1994; Yanovska et al, 2014), whereas Cu (*in vitro*) showed good antibacterial ability at ambient conditions (Michels et al., 2009). For this reason, Cu is being investigated for its antibacterial ability in thin films (Stranak et al., 2011; Jäger et al., 2019), ionic form (Mathews et al., 2013; Fowler et al., 2019c), and in titanium alloys (Liu & Zhang, 2015; Fowler et al., 2019a; Ke et al., 2019).

2.9. Copper additions to titanium alloys

Different titanium alloys, including the Ti-Cu alloy, have been studied. Copper is a β-stabiliser, and depending on the composition range, the melting point of the Ti-Cu alloy decreases with increased Cu content (Murray, 1983). The Ti-Cu alloy is classified as a titanium alloy with a eutectoid transformation and has a eutectoid point of (αTi) and Ti-Cu intermetallic compounds (Murray, 1983). Ansara et al. (2021) evaluated the Cu-Ti binary system showing congruent formation of Ti_2Cu phase, Figure 2.10.

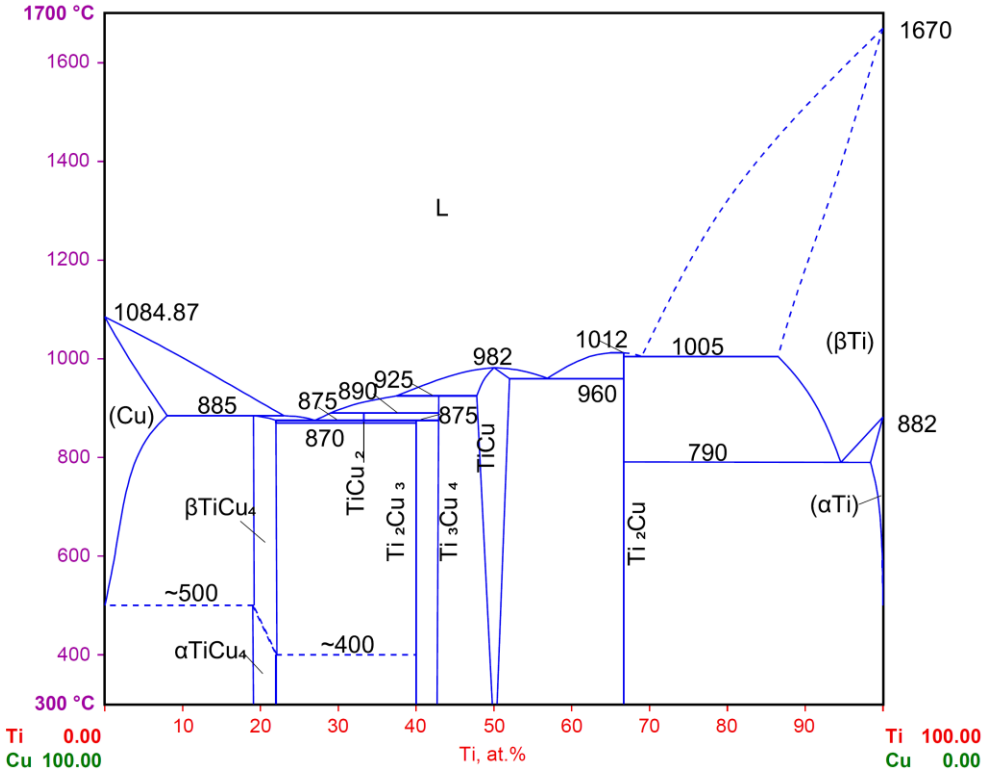


Figure 2.10: *Assessed phase diagram of the Cu-Ti binary system, showing congruent formation of Ti_2Cu without Ti_3Cu (Ansara et al., 2021).*

Recent studies have indicated titanium-copper alloys as promising antibacterial materials (Hanssen & Rand, 1998; Moreira et al., 2015), and copper has proven to be a good antibacterial agent for biomedical applications (Ren et al., 2014; Zhang et al., 2016a). However, an excess of copper can be harmful to the human body (Bull et al., 1993). Copper can reduce bacterial populations by ion release into solutions (Mathews et al., 2013; Fowler et al., 2019c), as well as by direct contact with the bacteria (Jin et al., 2015; Fowler et al., 2019a).

Ren et al. (2014) studied the antibacterial properties of as-cast Ti-6Al-4V-*x*Cu (*x* = 1, 3 and 5 wt%) alloys, at 37°C for 24 hours. The results showed improved antibacterial abilities against both *Escherichia coli* and *Staphylococcus aureus* bacteria for increased Cu contents. The number of bacterial colonies reduced to nearly zero for the Ti-6Al-4V-5Cu alloy (Figure 2.11) (Ren et al., 2014).

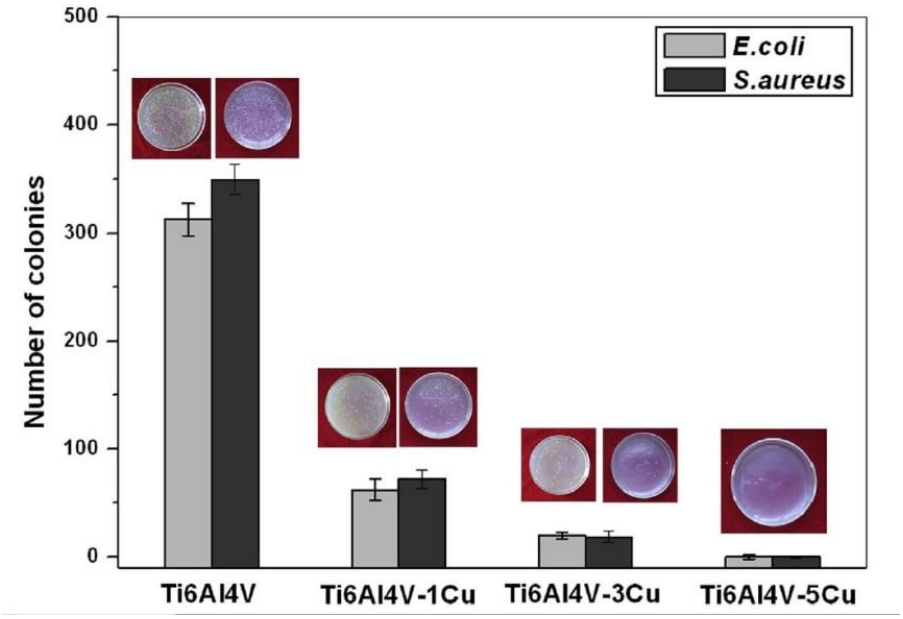


Figure 2.11: *Numbers of bacterial colonies after co-culturing with Ti-6Al-4V-xCu alloys (Ren et al., 2014).*

Ma et al. (2015) also studied the as-cast Ti-6Al-4V-5Cu alloy at 37°C for 24 hours, and showed excellent antibacterial properties. Jung et al. (2014) electrochemically deposited small amounts of Cu onto Ti discs and both *Escherichia coli* and *Staphylococcus aureus* bacteria had a decrease in growth. The Ti-*x*Cu (*x* = 2, 3 and 4 wt%) by Zhang et al. (2016a) and Ti-*x*Cu (*x* = 5 and 10 wt%) by Zhang et al. (2016b) showed an increased antibacterial ability with increased Cu content and fine Ti_2Cu phases. This supported the results by Shirai et al. (2009) and Liu et al. (2014a) who reported increased antibacterial rates for the Ti-*x*Cu (*x* = 2, 5, 10 and 25 wt%) alloys. The alloys with 5 wt% Cu and more showed a strong and stable antibacterial rate (Figure 2.12) (Liu et al., 2014a).

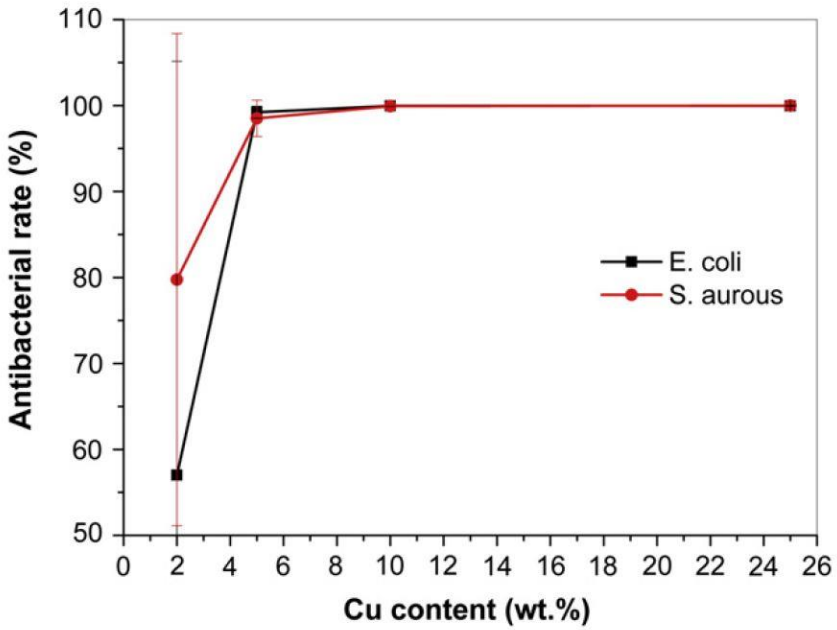


Figure 2.12: *Antibacterial rate of Ti-Cu alloys against E. coli and S. aureus at different Cu content (Liu et al., 2014a).*

Fowler et al. (2019a) investigated the effect of Cu ions on *Staphylococcus epidermidis* bacteria and cells. There was no significant difference in bactericidal effect for the Ti-*x*Cu (x = 0, 1, 2.5, 3 and 10 wt%) alloys after 2 hours. However, the Ti-10Cu alloy had higher reduction of bacterial population in a direct contact test after 6 hours (Fowler et al., 2019a). Based on the antibacterial and Cu ions release analyses, the antibacterial mechanism of Ti-Cu alloys is schematically shown in Figure 2.13 (Ma et al., 2015).

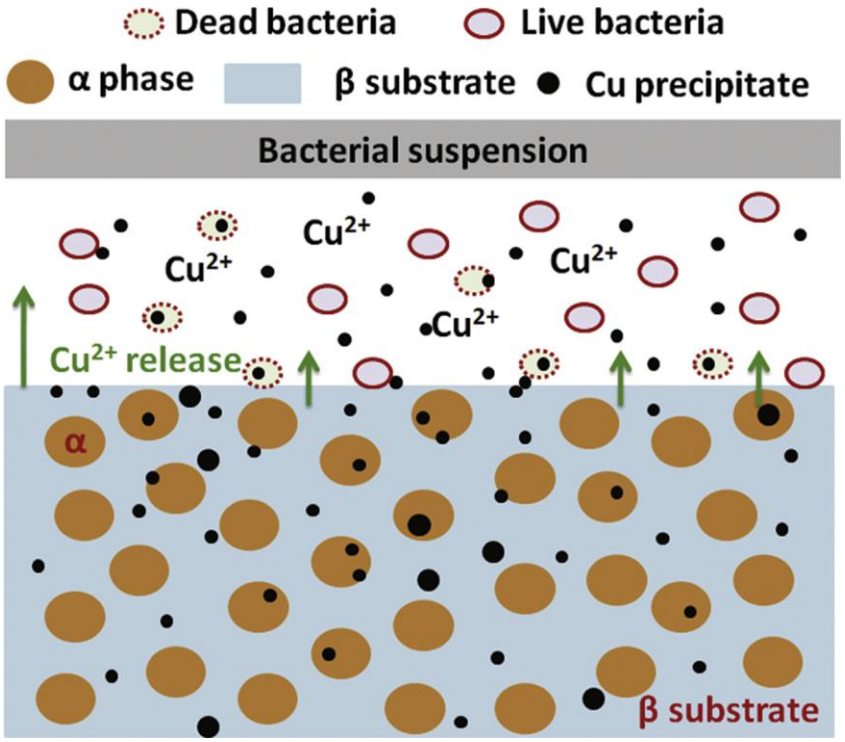


Figure 2.13: *Schematic illustration of the antibacterial mechanism of Ti-Cu alloys (Ma et al., 2015).*

When enough Cu is added to Ti-Cu alloys, it will be present in both βTi and αTi phases (Figure 2.13). Exposing the Ti-Cu alloy in a bacterial suspension, trace amounts of Cu ions will release from the alloy with increasing immersion time and kill the bacteria (Ma et al., 2015). Thus, at least some Cu ions need to go into solution.

The antibacterial effect is only one aspect of successfully functioning antibacterial biomaterials (Leyens & Peters, 2003). The mechanical, cytotoxicity and corrosive properties are also important and should be considered (Leyens & Peters, 2003). Excessive Cu additions lead to formation of Ti_2Cu (Kumar et al., 1996) and Ti_3Cu (Canale & Servant, 2002) intermetallic compounds, which can cause brittleness (Appel & Oehring, 2003; Zhang et al., 2016a). It is recommended to add enough Cu to give Ti_2Cu and good antibacterial resistance without degrading the mechanical properties (Zhang et al., 2016b). Although Ti-10Cu (wt%) gave the best antibacterial ability, the 3 wt% Cu was proposed for similar mechanical and corrosive performance as CP-Ti (Fowler et al., 2019a). This agreed with the results by Zhang et al. (2016a). Fowler et al. (2019b) studied the effect of Cu on the as-cast Ti-*x*Cu (x = 0, 1, 3, 5 and 10 wt%) alloys, and after ageing at 400°C.

The aged Ti-3Cu and Ti-5Cu alloys had higher hardness, but less Ti_2Cu phases than the aged Ti-10Cu alloy (Figure 2.14) (Fowler et al., 2019b). However, the unaged Ti-10Cu alloy showed good antibacterial effect and superior hardness. Small amounts of Ti_3Cu were found in the unaged Ti-5Cu alloy but not shown by Figure 2.14 (Fowler et al., 2019b). Therefore, a careful balance of desired properties should be the objective prior to ageing (Fowler et al., 2019b).

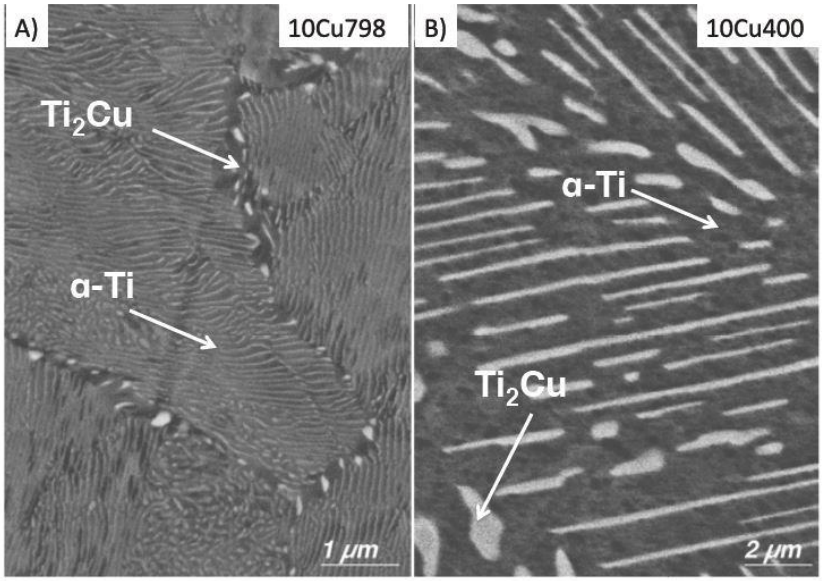


Figure 2.14: *Microstructures of Ti-10Cu (wt%): (A) after rapid quenching from 798°C and (B) after ageing at 400°C (Fowler et al., 2019b).*

Copper (Cu = 0, 1, 3, 5 and 10 wt%) was added to the Ti-10.1Ta-1.7Nb-1.6Zr (wt%) alloy, to study the microstructures (Fowler et al., 2019d). The Ti_2Cu phase was present above 3wt% Cu (Figure 2.15). The hardness increased with increased Cu, and remained the same for concentrations above 3 wt% Cu (Fowler et al., 2019d).

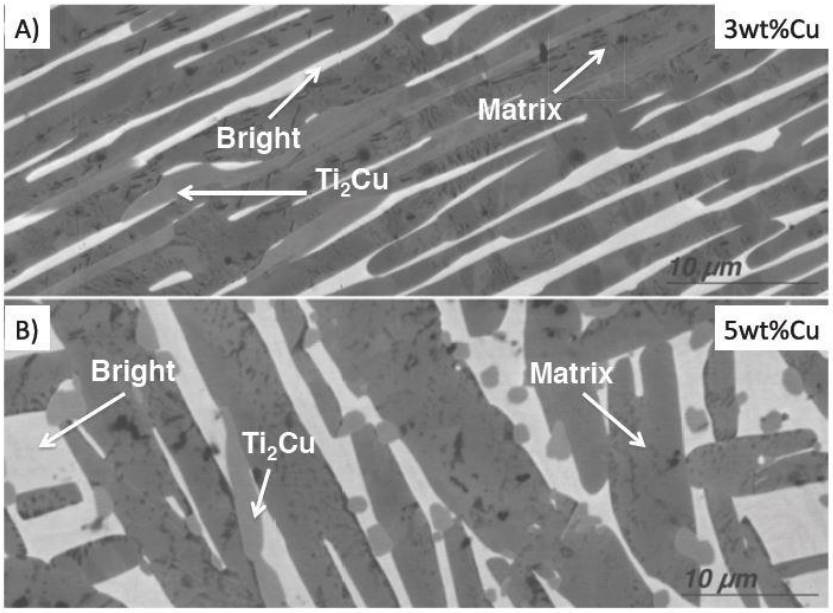


Figure 2.15**:** *Microstructures of: (A) Ti-10.1Ta-1.7Nb-1.6Zr-3Cu and (B) Ti-10.1Ta-1.7Nb-1.6Zr-5Cu (wt%) showing Ti_2Cu (Fowler et al., 2019d).*

Aoki et al. (2004) examined the mechanical properties of cast Ti-6Al-4V-*x*Cu (*x* = 1, 4 and 10 wt%) alloys. The Ti-6Al-4V-1Cu alloy had higher tensile strength (1016 MPa) than the Ti-6Al-4V-10Cu (387 MPa) (Aoki et al., 2004) (no errors were given). The elongation decreased with increased Cu content, hence the Ti-6Al-4V-10Cu had the highest bulk hardness but was brittle (Aoki et al., 2004). Takahashi et al. (2002) studied the mechanical properties of Ti-*x*Cu (*x* = 2, 5 and 10 wt%), and the tensile strength, yield strength, and hardness increased with increased Cu (Figure 2.16). The mechanical properties were better than those of CP-Ti, but with reduced ductility due to the Ti_2Cu precipitates (Takahashi et al., 2002). The Ti-5Cu and Ti-10Cu alloys had the same tensile strength, around 700 MPa (Figure 2.16) (Takahashi et al., 2002).

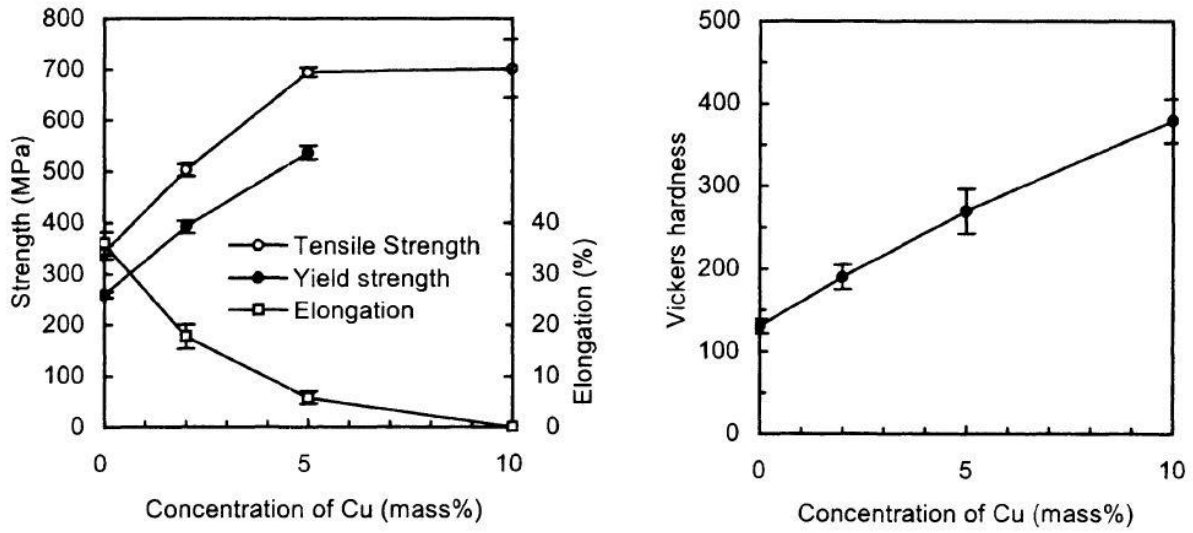


Figure 2.16: *Mechanical properties of cast Ti-xCu (x = 2, 5 and 10 wt%) alloys (Takahashi et al., 2002).*

The results by Zhang et al. (2016b) of as-cast Ti-*x*Cu (*x* = 5 and 10 wt%) alloys also showed that high proportions of Ti_2Cu precipitates gave higher strength and hardness, but reduced ductility. Kikuchi et al. (2003) studied the cast Ti-*x*Cu (*x* = 0.5, 1, 2, 5 and 10 wt%) alloys, and Figure 2.17 shows that alloys with less Cu had lower strength, but higher ductility. The alloy with 10 wt% Cu had reduced ductility, whereas a balance between strength and ductility was observed for the alloy with 5 wt% Cu (Figure 2.17) (Kikuchi et al., 2003).

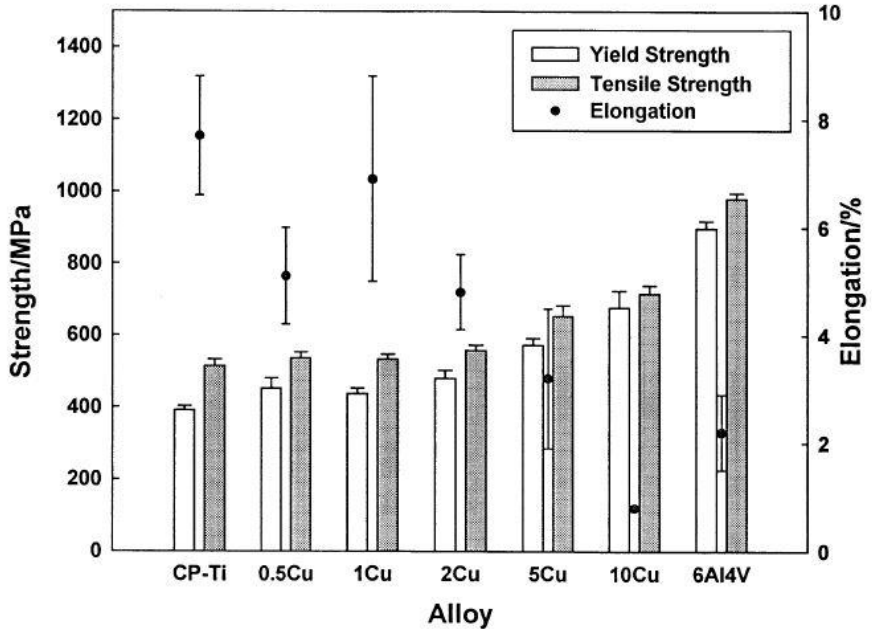


Figure 2.17: *Tensile strength, yield strength, and elongation of Ti alloys (Kikuchi et al., 2003).*

Corrosion resistance has also been the focus of recent studies on Ti implant materials. Lin et al. (1990) and Takada et al. (2001) showed no significant difference in corrosion resistance between CP-Ti and Ti-Cu alloys with copper concentrations up to 30 wt%. The corrosion studies by Ren et al. (2014) on Ti-6Al-4V-*x*Cu (*x* = 0, 1, 3 and 5 wt%) alloys showed similar potential polarisation (Figure 2.18a) and excellent pitting corrosion resistance (Figure 2.18b). Thus, additions of Cu did not affect the corrosion resistance of the alloys (Ren et al., 2014). Zhang et al. (2016a) and Fowler et al. (2019b) also reported no significant difference in corrosion resistance of CP-Ti and Ti-*x*Cu alloys.

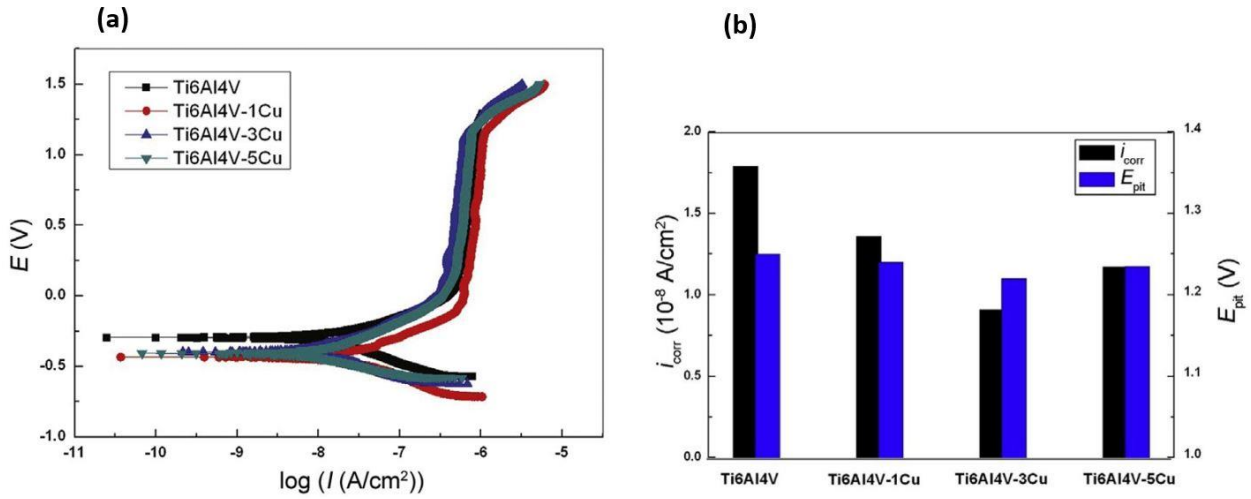


Figure 2.18: *Corrosion studies of Ti-6Al-4V-xCu: (a) Potential polarisation and (b) Electrochemical corrosion currents and pitting potentials (Ren et al., 2014).*

Since biocompatibility is also a primary requirement for implant materials (Long & Rack, 1998; Leyens & Peters, 2003), it is necessary to evaluate the cytocompatibility of implants (Ren et al., 2014; Ma et al., 2015). The as-cast Ti-6Al-4V-3Cu alloy was chosen for cytotoxicity evaluation (Ren et al., 2014) and showed no significant difference in cytocompatibility between the alloy and the Ti-6Al-4V for 2, 4 and 7 days. This also indicated that Ti-6Al-4V-3Cu had no cytotoxic effect on the L929 cells (from connective tissue of mouse species) tested (Ren et al., 2014). Ma et al. (2015) studied the cytocompatibility of the as-cast Ti-6Al-4V-5Cu alloy for 2, 4 and 7 days, and showed no toxicity effects. This confirmed a good cytocompatibility of the as-cast Ti-6Al-4V-5Cu alloy (Ma et al., 2015). Excess amounts of Cu could be toxic to human body (Bull et al., 1993), therefore 3 wt% Cu and 5 wt% Cu were recommended (Ren et al., 2014; Ma et al., 2015).

The biocompatibility of a Ti-10Cu (wt%) alloy was studied by Liu et al. (2014b) for 1 and 3 days. There was no difference in cell morphology between the Ti-10Cu and CP-Ti alloys, and both showed good cell growth and no cytotoxicity (Figure 2.19) (Liu et al., 2014b). Zhang et al. (2015) investigated the influence of Cu on the cell biocompatibility of the Ti-*x*Cu (x = 2, 5, 10 and 25 wt%) alloys. An increase in Cu content did not show any difference in the body's cell viability (Zhang et al., 2015). The results indicated that Ti-Cu alloys had excellent cell biocompatibility, however, 25 wt% Cu had no influence on the cell growth (Zhang et al., 2015).

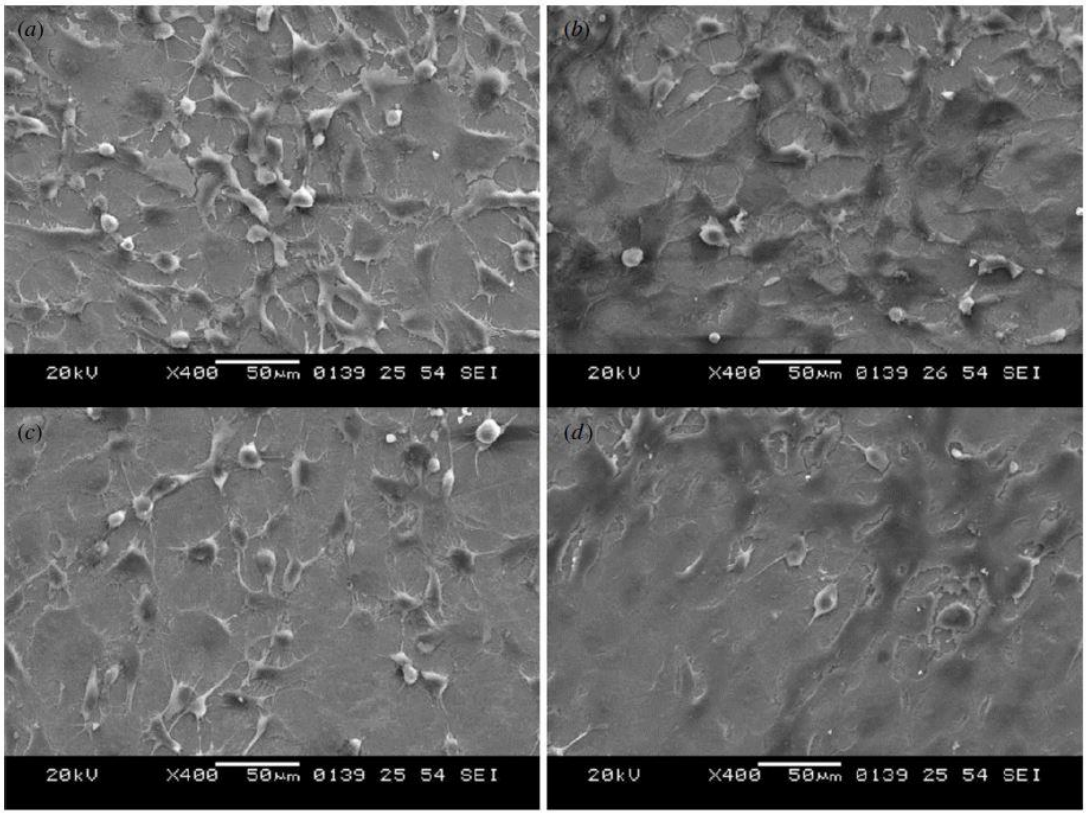


Figure 2.19: *Morphologies of MG63 cells cultured on Ti-10Cu and CP-Ti surfaces, showing similar cell growth: (a) Ti-10Cu for 1 day, (b) Ti-10Cu for 3 days, (c) CP-Ti for 1 day and (d) CP-Ti for 3 days (Liu et al., 2014b).*

2.10. Thermo-mechanical simulation using the Gleeble 3500® Thermomechanical Simulation Facility

Thermo-mechanical simulation studies using the Gleeble 3500® Thermomechanical Simulation Facility have been applied in metal processing industries including process optimisation, development of new alloys, quality/yield improvement and material characterisation (Kumar, 2015). The Gleeble 3500® is a thermo-mechanical simulation system that can be used for hot tensile, compression, ductility and fatigue testing (Kumar, 2015). Metallurgical processes such as continuous casting, hot rolling, strip annealing, forging, and welding can also be studied to

investigate the high strength, ductility, creep and high fatigue resistance (Kumar, 2015) required for the new Ti alloys.

Titanium alloys can be forged into desired shapes by deformation. However, the alloys are challenging to forge (Damkroger & Edwards, 1990; Kumar, 2015). Therefore, it is essential to control the forging temperature due to the phase transformations that may degrade the mechanical properties or cause embrittlement at 940-980°C (Altan et al., 1973; Jha & Kumar, 2010). Hot compression testing can be done to study hot deformation behaviour, by heat treating the specimen to the deformation temperature and compressing it (Jha & Kumar, 2010). Heat treatment by annealing for Ti alloys involves heating to a temperature of 700-1050°C, holding for 120-300 seconds and cooling to room temperatures (Jha & Kumar, 2010). This helps with good formability and improved microstructure, and good fracture toughness, ductility and creep resistance (Gilbert & Shannon, 1991; Jha & Kumar, 2010). Hot compression can also be used to study flow stress, stress-relaxation, hot workability, and flow softening behaviour due to recrystallisation and recovery (Jha & Kumar, 2010). Hot compression can be divided into two categories; (i) uniaxial flow stress compression and (ii) plane strain compression, depending upon the stress conditions. Uniaxial compression is closer to forging, whereas plane strain compression is experienced in hot rolling (Jha & Kumar, 2010).

For effective use of hot compression studies, it is important to consider the heating cycle and soaking temperatures. On-heating thermal cycles involve heating the test specimen to the deformation temperature and compressing, whereas on-cooling thermal cycles involve heating the specimen to high soaking temperature followed by cooling to a deformation temperature (Kumar, 2015). On-heating hot compression testing is easier to perform, and on-cooling hot compression requires good control over cooling rate, which is possible with a Gleeble 3500® system (Kumar, 2015). Both produce entirely different flow behaviours (Jha & Kumar, 2010). Selection of soaking temperature depends upon the alloying elements present and their solubility temperature. Higher soaking temperatures may result in higher flow stress values (Kumar, 2015).

Different types of specimens are used for different studies. A cylindrical specimen (10 mm diameter x 15 mm height) is used for uniaxial compression and rectangular specimens (10 x 15 x 20 mm) are used for plane strain compression (Kumar, 2015). However, Roebuck et al. (2006) and

Li et al. (2010) recommended specimens of 8 mm diameter x 12 mm height. The minimum thickness of the deformed specimen in plane strain compression cannot be less than 3 mm. In other words, 12 mm height specimen can be deformed to 75% only, whereas a 15 mm height specimen can be deformed to 80% (Kumar, 2015). In uniaxial compression, a 15 mm height sample can be deformed to 72% for a 10 mm standard diameter, and up to 80% if the diameter is reduced to 8.5 mm (Kumar, 2015).

Metal alloys exhibit different plastic deformation at different temperatures and strain rates (Pearson, 1934, Tiley, 2002). The hot working performance of Ti-6Al-4V alloy is sensitive to the process parameters and initial microstructure (Shell & Semiatin, 1999; Shaikh et al., 2015). The alloy is usually forged at 30-50°C below its β transus temperature so that a fine equiaxed grain structure and good mechanical properties are obtained (Wang et al., 2010; Arulselvan & Ganesan, 2014). To identify favourable hot working conditions of the Ti-6Al-4V alloy, Shaikh et al. (2015) studied the deformation behaviour in the 700-1000°C range and strain rate range of 0.1-100 s^{-1} using a Gleeble 3500®. The favourable conditions were found to be 0.1-1 s^{-1} for 950°C and 1000°C, and above 10 s^{-1} for 750°C and 850°C. The flow stress increased with increased strain rate, and decreased with increased deformation temperature (Shaikh et al., 2015).

True stress-true strain curves and processing maps are widely used to characterise the deformation behaviour of Ti alloys, to control their microstructures and optimise manufacturing processes (Wang et al., 2010). The stress-strain curves give the flow hardening, flow softening and steady state flow behaviour of the alloys (Shaikh et al., 2015). Figure 2.20 shows the tensile stress-strain curves for Ti-6Al-4V by Vanderhasten (2008). Higher flow stresses were observed at higher strain rates and lower temperatures (Figure 2.20). The results indicated grain boundary sliding and good ductility for slow deforming ($5x10^{-4}$ s^{-1}) at 800°C (Vanderhasten, 2008).

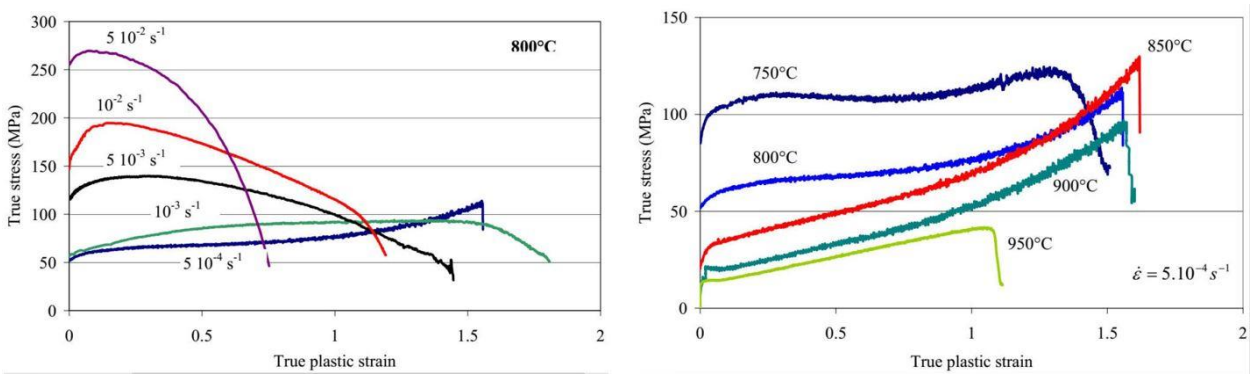


Figure 2.20: *Tensile stress-strain curves of Ti-6Al-4V at 5x10^{-2}-5x10^{-4} s^{-1} and 750-950°C from a Gleeble 3800® (Vanderhasten, 2008).*

Hot tensile studies of Ti-6Al-4V, at 600-950°C and 10^{-1} s^{-1}, 10^{-2} and 10^{-3} s^{-1} strain rate, by Dos Santos (2017) also showed a higher flow stress for a higher strain rate (10^{-1} s^{-1}). However, Figure 2.21 shows that the elongation increased with increased deformation temperature at lower strain rates (10^{-3} s^{-1}). Therefore, a slow strain rate at higher temperature improves the ductility of the material (Vanderhasten, 2008; Shaikh et al., 2015; Dos Santos, 2017).

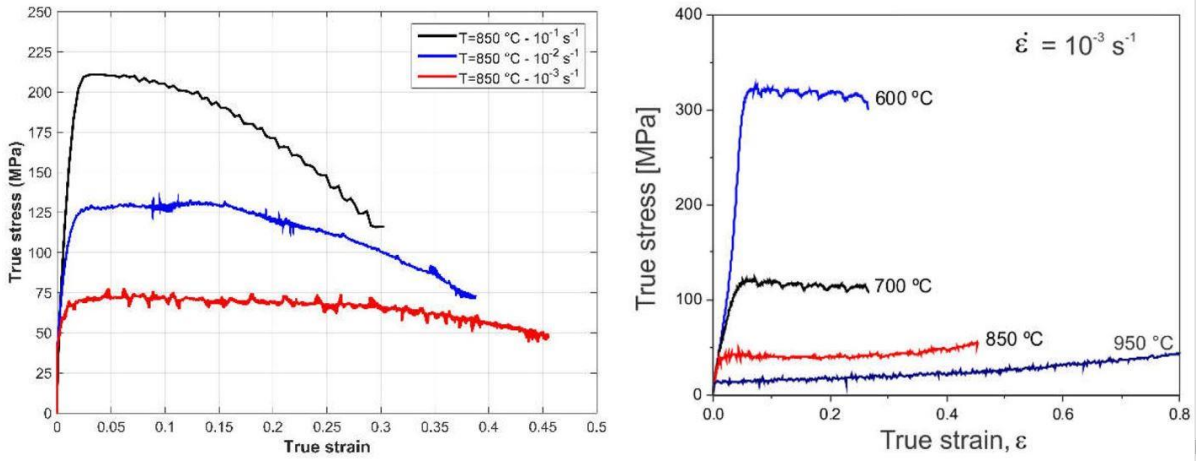


Figure 2.21: *Tensile stress-strain curves of Ti-6Al-4V at 600-950°C and 10^{-1}-10^{-3} s^{-1} strain rate from a Gleeble 3800® (Dos Santos, 2017).*

Figure 2.22 shows the starting microstructure of Ti-6Al-4V (Dos Santos, 2017). Microstructures with lamellae were observed after deformation at 700°C and 850°C (Figure 2.23) and 950°C (Figure 2.24) for 10^{-3} s^{-1} strain rate. Figure 2.24 shows the α and β phases (Dos Santos, 2017).

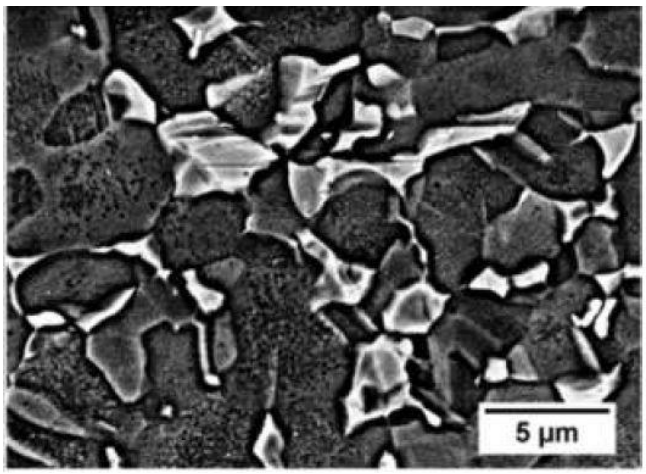


Figure 2.22: *Starting microstructure of Ti-6Al-4V (dark phase is α and light is β) (Dos Santos, 2017).*

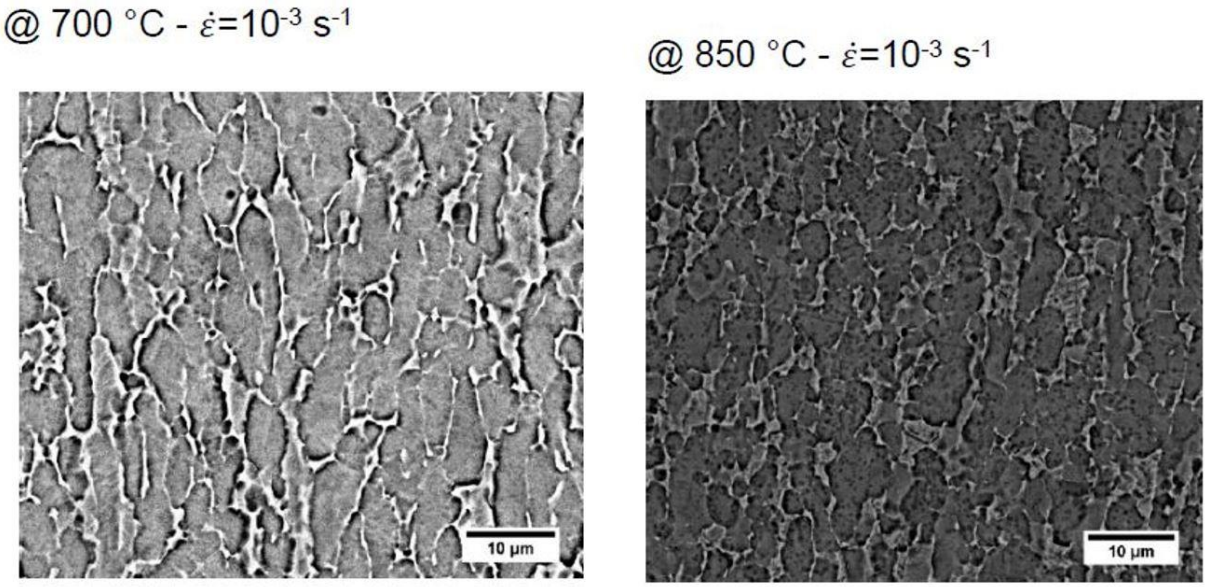


Figure 2.23: *Microstructures of deformed Ti-6Al-4V at 700°C and 850°C for 10^{-3} s^{-1} strain rate (dark phase is α and light is β) (Dos Santos, 2017).*

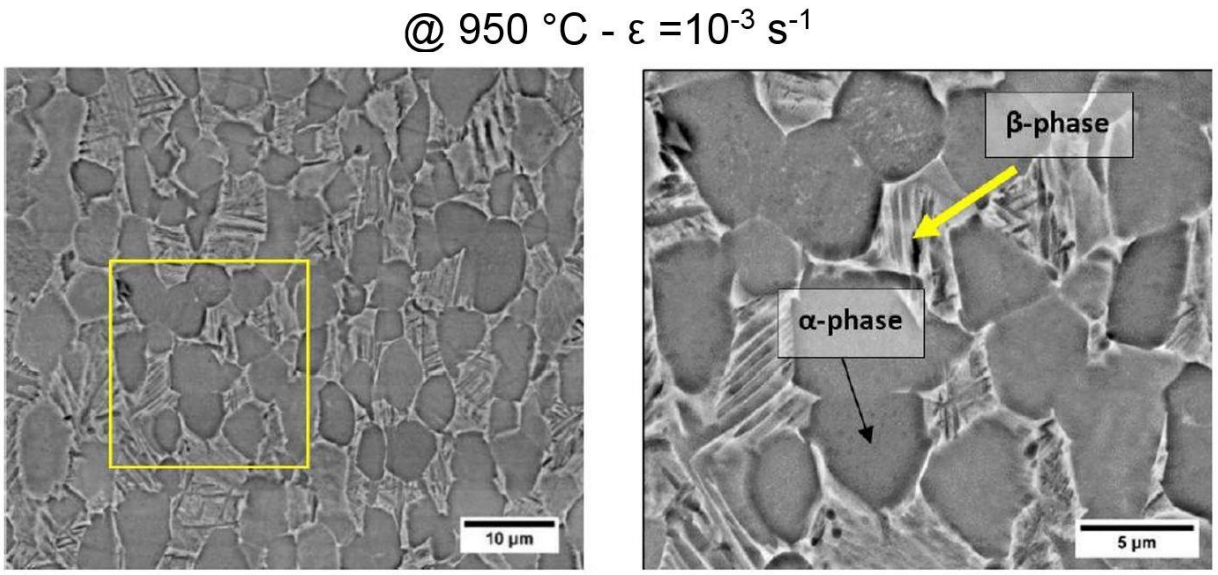


Figure 2.24: *Microstructures of deformed Ti-6Al-4V at 950°C for 10^{-3} s^{-1} strain rate (Dos Santos, 2017).*

Bodunrin et al. (2017) investigated hot deformation behaviour of Ti-6Al-*x*V-*y*Fe (*x* = 1, 2, 3 and 4 wt%, *y* = 0, 1, 2 and 3 wt%). The goal was to substitute V with Fe to reduce the cost of the alloys. They optimised the microstructure and mechanical properties of the alloys by heat treatments. This was done to reduce the possibility of forming Ti-Fe intermetallic phases, to maintain the α+β phases at lower temperatures. The Ti-Fe intermetallic phases have a deleterious effect on the ductility and toughness of the α+β Ti alloys (Fujii & Maeda, 2014; Bodunrin et al., 2017) because they are brittle. Small ingots were machined to produce plane strain compression samples (8 x 15 x 20 mm) for hot isothermal compression testing on a Gleeble 3500® simulator, at 900°C. Partial substitution of V with Fe (*y* = 1 and 2 wt%) decreased the flow stress and deformation resistance of the Ti-6Al-3V-1Fe and Ti-6Al-2V-2Fe alloys (Figure 2.25). The Ti-6Al-1V-3Fe alloy had a small increase in deformation resistance, indicating a balance between reduced cost and improved mechanical properties of the Ti alloys (Bodunrin et al., 2017).

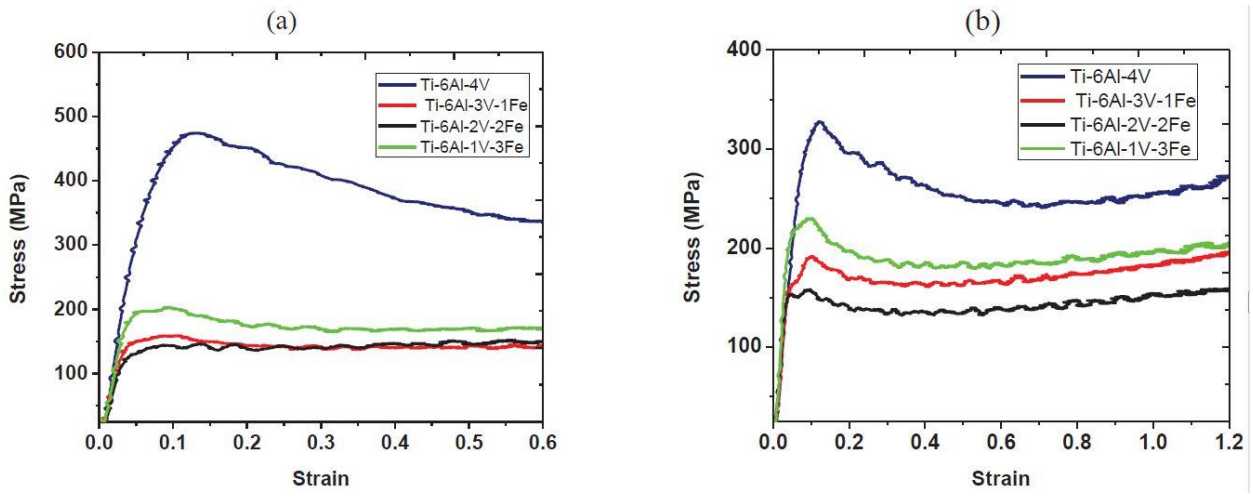


Figure 2.25: *Compressive engineering stress-strain curves of as-cast Ti-6Al-xV-yFe at a strain of (a) 0.6 and (b) 1.2, from a Gleeble 3500® (Bodunrin et al., 2017).*

2.11. Summary of the literature review and rationale of the research project

Commercially pure titanium (CP-Ti) and the Ti-6Al-4V (wt%) have been widely used in aerospace, power generation and biomedical applications due to their high mechanical strength, excellent corrosion resistance and good biocompatibility (Steinemann, 1998; Leyens & Peters, 2003). However, CP-titanium does not have sufficient strength for load bearing implant applications, whereas Ti-6Al-4V has raised concerns due to the toxic aluminium and vanadium (Eisenbarth et al., 2004; Akahori et al., 2005). Zirconium, tantalum, niobium and molybdenum have been proposed as the potential non-toxic, biocompatible, alloying elements to replace Al and V (Eisenbarth et al., 2004), because they are not released into the environment and they can minimise adverse tissue reactions (Kovacs & Davidson, 1993; Meng et al., 2014).

There have been attempts to develop new biomedical alloys with microstructures and mechanical properties similar to the α+β Ti-6Al-4V alloy (Long & Rack, 1998; Niinomi, 2003a), and to add copper for its good antibacterial properties (Ren et al., 2014; Fowler et al., 2019a).

By studying and understanding the relationship between the chemical compositions, thermo-mechanical treatment and microstructures, it should be possible to optimise the mechanical and antibacterial properties of Ti-Cu alloys for biomedical applications (Liu et al., 2014a). Based on

the literature, sufficient Cu can be added to give the Ti_2Cu phase and good antibacterial resistance without degrading the mechanical properties of Ti alloys. Therefore, new Ti alloys were investigated, to achieve similar α+β phase proportions to Ti-6Al-4V, and Ti-10.1Ta-1.7Nb-1.6Zr (Stenlund et al., 2015) (an analogue for Ti-6Al-4V), and also have the Ti_2Cu phase by adding Cu (Zhang et al., 2016a; Fowler et al., 2019a). The microstructures and microhardness of selected Ti compositions were studied, and the deformation behaviour of Ti-6Al-4V and Ti-10.1Ta-1.7Nb-1.6Zr was investigated.

Chapter 3: Experimental Procedure

This chapter provides information on the starting materials, consumables, facilities and experimental methods used in this study. A detailed description is given on the Thermo-Calc calculations, cost analysis, production of the experimental alloys, characterisation techniques, hardness testing and hot compression testing. Figure 3.1 shows the flow diagram of the experimental procedure, of the new alloys and the Gleeble studies of the commercial and reported alloys.

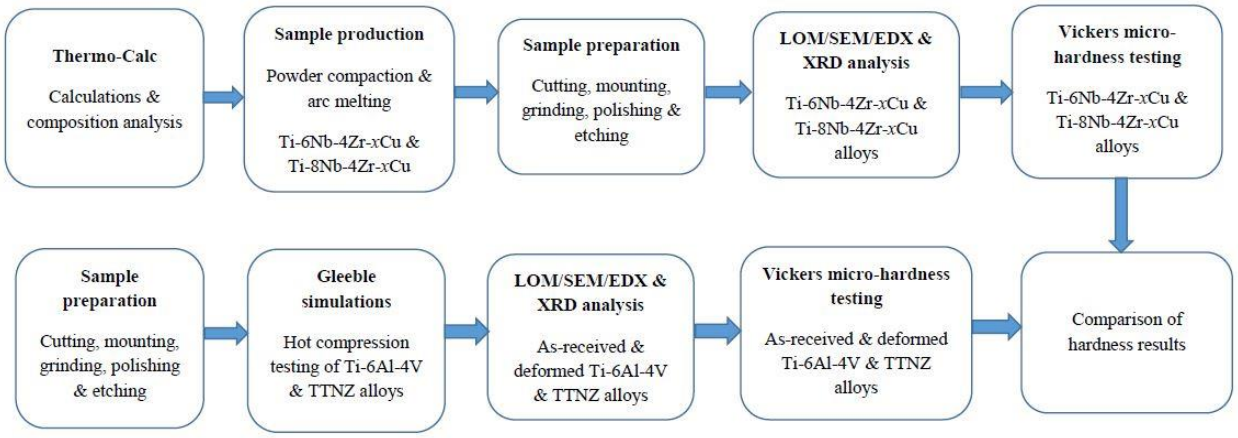


Figure 3.1: *Flow diagram showing the experimental procedure for the project.*

3.1. Thermo-Calc calculations

Thermo-Calc is a software used to perform thermodynamic and phase diagram calculations for multi-component systems (Andersson, 2002), and available at www.thermocalc.com, and is a quick way to easily calculate the phases and their proportions for different alloy compositions. The Thermo-Calc program with the TTTI3 (TT Ti-alloy) database was used to calculate new Ti compositions, without toxic Al and V as alloying elements. The elemental compositions were calculated in weight percent (wt%), at 400-2000°C temperature range, and under one atmospheric pressure (1 atm), with the TTTI3. Database. The Ti-6Al-4V (wt%) alloy and the Ti-10.1Ta-1.7Nb-1.6Zr (wt%) alloy developed by Stenlund et al. (2015) were used as the basis to determine the Ti compositions. The calculations were done to find alloys which mimiced the α+β phase proportions

found in Ti-6Al-4V and Ti-10.1Ta-1.7Nb-1.6Zr at lower temperatures, and to have some copper. Copper compostions (1, 3, 5 and 10 wt%) were varied for the calculated Ti compositions. Table 3.1 was used as a guide for α-β stabilising and alloying of titanium, and Table 3.2 gives the calculated Ti compositions.

Table 3.1: *The α-β stabilisers and alloying elements for titanium (Leyens & Peters, 2003).*

α-stabilisers	**Neutral**	**β-isomorphous stabilisers**	**β-eutectoid stabilisers**
Al, O, N, C, Ga	Sn, Zr	V, Mo, Ta, Nb	Fe, Mn, Co, Ni, Cu, Si, H, W, Cr

Table 3.2: *Compositions calculated with Thermo-Calc.*

Compositions calculated with Thermo-Calc				
Ti-6Nb-4Zr	Ti-6Nb-2Zr-1.7Ta	Ti-6Ta-2Zr-1.5Mo	Ti-10Ta-8Zr	Ti-8Ta-1.5Mo-1.5Zr
Ti-8Nb-4Zr	Ti-4Ta-1.8Zr-1.5Mo	Ti-8Zr-4Ta-2Mo	Ti-6Zr-4Nb	Ti-10.1Ta-1.7Nb-1.6Zr
Ti-6Zr-2Mo	Ti-3.5Ta-3Nb-3Zr	Ti-6Zr-4Ta-4Nb	Ti-4.5Nb-4Ta-1.5Zr	Ti-6Al-4V

3.2. Cost analysis

A cost analysis was done to identify the potential Ti alloys with reduced cost. Table 3.3 gives the costs for the powders for titanium and alloying elements proposed for this project, as at 8 October 2019. This was just for the material costs and not for any processing costs, which were assumed to be the same and so not considered.

Table 3.3: *Costs for the powders for Ti and alloying elements (https://www.sigmaaldrich.com) (8/10/2019).*

Element	**Price (R)/50 g**
Mo	626.00
Ti	1 463.00
Nb	1 832.00
Zr	2 629.00
Ta	4 178.00
V	8 035.00
Al	10 516.00
Cu	14 353.00

Titanium sample alloys of 20-30 g (total mass) are usually produced to study the mechanical properties (Aoki et al., 2004; Toss, 2009). Based on Table 3.3 and using Equation 3.1, titanium alloys of 10 g with reduced cost were calculated.

$$m_i = y_i \, x \, \mathbf{M} \qquad \ldots\ldots\ldots\ldots\ldots\ldots \quad \text{Equation 3.1.}$$

where:

i = element

m = mass of element i in the alloy (g)

y = mass % of element i

M = total mass of the alloy i.e. 10 g.

3.3. Materials and Methods

3.3.1. Production and Preparation of samples

Powders of pure titanium (99.999% Ti), niobium (99.999% Nb), zirconium (99.999% Zr) and copper (99.999% Cu) were used to produce new Ti alloys (Table 3.4) from the Thermo-Calc results. For each sample, the powders were weighed on an electronic balance in the proportions given in Table 3.4, to give a total mass of 10 g. The powders were then mixed and cold compacted in a 20 mm diameter die at 220 kPa, using a hydraulic press. The samples were melted and water-cooled in a copper-hearth button arc furnace to produce as-cast buttons. The samples were turned-over and re-melted four times, to attempt homogenisation. Before melting the samples, the furnace chamber was flushed three times with pure argon (99.999% Ar) at 6×10^{-3} bar to create a vacuum environment. A pure titanium sample was used as an oxygen-getter and melted for 5 minutes prior to melting, to reduce oxygen contamination. Titanium has high affinity to oxygen, and would form TiO_2 (Leyens & Peters, 2003) and contaminate the samples. Table 3.4 gives the samples produced (Samples 1-4) and as-received (Ti-6Al-4V and TTNZ) sample compositions for this study.

Table 3.4: *Compositions of the samples studied.*

Sample #	Alloy	Composition (wt%)						
		Ti	Al	Nb	Ta	V	Zr	Cu
1	Ti-6Nb-4Zr	90	---	6	---	---	4	0
2	Ti-6Nb-4Zr-5Cu	85	---	6	---	---	4	5
3	Ti-8Nb-4Zr	88	---	8	---	---	4	0
4	Ti-8Nb-4Zr-5Cu	83	---	8	---	---	4	5
5	As-received TTNZ	86.6	---	1.7	10.1	---	1.6	0
6	As-received Ti-6Al-4V	90	6	---	---	4	---	0

The samples were cut in half using a Struers Secotom-10 cutting machine with a diamond MOD13 blade. This was done at 3500 rpm speed and 0.015 mm/s feed rate. Water was used as the coolant throughout, to prevent the samples from heating up during cutting. A half of each sample was embedded in Polyfast resin (ATM, GMBH, Germany), and mounted in a (citoPress-10) ATM-Opal 410 hot mounting press for metallographic preparation. This was done at 200°C and a pressure of 6 bar for 6 minutes, with water as the coolant.

The metallographic preparation included grinding, polishing and etching for microstructural studies and micro-hardness testing. The preparation steps developed by Vander Voort (2006) and Struers (2016), and Kroll's etchant (2 ml HF : 6 ml HNO_3 : 92 ml distilled water, for 20 seconds using cotton swabbing) were employed (Table 3.5). Grinding was done manually on an Imptech grinding machine using an abrasive silicon carbide (SiC) paper of different grit sizes, while polishing was done on a Struers Tegramin-20® automatic polishing machine using MD-Chem polishing cloths (Table 3.5). After etching, the samples were cleaned with ethanol in an ultrasonic bath and dried with compressed air. Etching was done to enhance the microstructural features for SEM analysis, to aid focussing.

Table 3.5: *Metallographic preparation of the Ti alloys studied.*

Parameters	Steps				
	1	**2**	**3**	**4**	**Polishing**
Abrasive (Silicon carbide- P grit)	P800	P1000	P1200	P2400	MD Chem cloth
Coolant	Water	Water	Water	Water	Non-crystallising colloidal silica suspension + 30% hydrogen peroxide
Platen speed/direction	320 rpm	320 rpm	320 rpm	320 rpm	150 rpm/contra
Force	Hand	Hand	Hand	Hand	~15 N
Time	2 min	1 min	1 min	1 min	20 min

The standard safety precautions described by Koontz (2013) and the safety data sheet for HF and HNO_3 were considered when working with the chemicals. Personal protective equipment (PPE) such as goggles, gloves, closed shoes, long trousers and lab-coats were used.

3.3.2. Microstructural Studies

The microstructures were studied to obtain the information about the surface topography, the present phases and the composition of the alloys. The Light Optical Microscopy (LOM) and Scanning Electron Microscopy (SEM) were used to study the microstructural features (phases and precipitates), and possible defects/cracks on the surface. The Energy Dispersive X-ray Spectroscopy (EDX) was used for composition analysis of the alloys as well as their phases. Since the surface condition of the sample affects the light during reflection or transmission (Struers, 2016), careful sample preparation was done to achieve the required surface quality and contrast. The SEM was good for large area analysis, and was limited for small localised regions, thus difficult to analyse smaller precipitates below ~2μm, so care was taken to only analyse features larger than these.

The microstructures were studied using cross-polarized and a Leica DM 6000®-Light Optical Microscope (LOM), as well as Zeiss Sigma Field Emission-Scanning Electron Microscope (FEG-SEM) with both Energy Dispersive X-ray Spectroscope (EDX) system and a back-scattered detector

(BSD). The FEG-SEM was operated in back-scattered electron imaging (BSE) mode at 20 kV to distinguish the phases present. The EDX spot and area analyses were performed at 25 kV and 5.4 ± 1.4 mm working distance to verify homogeneity, and to determine the compositional variations in the alloys.

3.3.3. X-ray diffraction analysis

The identification of phases was done using X-ray diffraction (XRD), with limitations to samples with flat and smooth surfaces. Therefore, care was taken to have well-polished samples with a flat upper surface during sample preparation (Struers, 2016). The XRD is a technique for analysing the atomic or molecular structure of materials (Struers, 2016), which was useful for identifying the phases observed in the microstructures by LOM and SEM.

The XRD patterns were obtained using a Bruker D2 Phaser® diffractometer, with a cobalt Kα radiation source (Kα = 1.79026 Å), and analysed using PANalytical X'pert Highscore software (v3.0e). The measurements were taken within the range of 2θ = 10-120°. The machine was operated at 30 kV and 10 mA, at a temperature of 25°C.

3.3.4. Vickers micro-hardness testing

The Vickers micro-hardness testing was done to study the hardness of the alloys. Hardness is the resistance to scratching, cutting or abrasion. Therefore, hardness enables a quick evaluation of a material's strength, ductility and wear resistance and so helps to determine whether a material is suitable for the required purpose (Struers, 2016). Hardness testing is especially useful when comparing samples made in a similar way, and so can be used as a quick and initial test to choose between samples when checking mechanical properties. Although micro-hardness is more limited than conventional hardness (because a smaller area is tested), it can still be used in comparison. However, it is very important to undertake several measurements and take an average to ensure that the results are statistically representative, and this is even more important for micro-hardness measurements because the indentations are much smaller. For accurate results, factors such as surface preparation, surface vibrations, loading, indenter orientation and calibration were taken

into consideration. Micro-hardness testing required a clean and polished surface for a good interpretation of the indentation. Etching and rough surfaces would make it difficult to evaluate the corners of an indentation, and scratches may cause a misreading of the indentation size (Struers, 2016).

A FutureTech FM700® micro-hardness tester fitted with a diamond indenter was used to measure the Vickers hardness of the samples. A load of 300 g and a 15 seconds dwelling time was employed according to ASTM standard E92-17(ASTM E 92-17, 2017). Five measurements were taken at different positions on each sample, and the average $HV_{0.3}$ and standard deviation were calculated.

3.3.5. Hot compression testing

Hot compression testing was done to evaluate the hot deformation behaviour of the as-received Ti-6Al-4V and Ti-10.1Ta-1.7Nb-1.6Zr (TTNZ) alloys, using stress-strain curves obtained. This was done to understand the differences between the commercial (Ti6Al-4V) and the reported (TTNZ) alloys since for complicated dental parts, the alloys might be forged (if 3D printing was not available). The flow stresses were observed at different strain rates and temperatures. This also helped to evaluate the formability and ductility of the alloys. The recommended size and dimensions of the samples were considered for this study.

The as-received Ti-6Al-4V and Ti-10.1Ta-1.7Nb-1.6Zr (TTNZ) alloys, the latter by Stenlund et al. (2015), were subjected to isothermal compression testing using a Gleeble 3500® Thermo-mechanical Simulation Facility. Cylindrical samples of 8 mm diameter x 12 mm height (Figure 3.1a) were machined using electrical discharged machining. The dimensions were chosen according to recommendations by Roebuck et al. (2006) and Li et al. (2010). A chromel-alumel thermocouple was welded at the centre of the test samples using a spot welder, prior to compression testing, to measure the temperature. The samples were then placed on the Hydrawedge autoloader. Graphite foil and nickel paste were placed between the Iso-T tungsten carbide anvils and the sample to reduce the effect of friction during deformation. The samples were heated at 5°C/s to the deformation temperature, and held for 360 s for homogenisation (Figure 3.1b). The samples were deformed at the specified parameters in Table 3.6, followed by compressed air cooling. The test parameters (Table 3.6) were used in the Quicksim software using

the (.hds) program. The program was then converted to Gleeble Script Language (.gsl) before running each experiment.

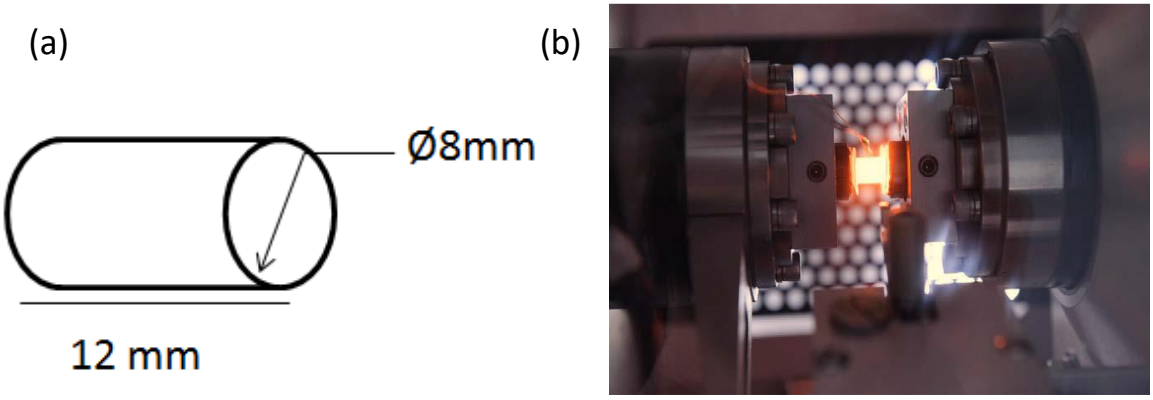


Figure 3.2: *Hot compression testing: (a) test sample and (b) testing in the Gleeble 3500® (Bodunrin, 2018).*

Table 3.6: *Hot compression testing parameters.*

Deformation parameters		**Temperature (°C)**	
Strain	Strain rate (s^{-1})		
0.6	0.1	850	950
0.6	10	850	950

Chapter 4: Thermo-Calc Results

This chapter summaries the results from the Thermo-Calc calculations, and the costs for the calculated Ti compositions. The compositions were calculated in weight percent (wt%) at 400-2000°C, using the TTTI3 (TT Ti-alloy) database. Table 4.1 shows the phases in the TTTI3 database.

Table 4.1: *Phases in the TTTI3 database*.

Phases	Liquid, BCC_A2, HCP_A3, Ti_2Cu, Ti_3Al, BETA_TIMN, ALPHA_TIMN, C15_FCC, LAVES, Ti_5SI_3, TIH2, TIM_B2, FCC_A1, Ti_2NI

4.1. Ti-6Al-4V-*x*Cu compositions

The phase proportion diagrams for Ti-6Al-4V-*x*Cu (*x* = 0, 1, 3, 5 and 10 wt%) are shown in Figures 4.1 - 4.5, and Table 4.2 gives the phase information. At 1698°C, the liquid phase solidified to BCC_A2 (Figure 4.1). The 0.97 fraction of the BCC_A2 phase transformed into HCP_A3 at 485-942°C (Figure 4.1). Thermo-Calc predicted the Ti_3Al phase at 485-654°C, resulting in a reduced HCP_A3 amount at 400°C (Figures 4.1 - 4.5). The Ti_2Cu phase formed at 624°C for 1 wt% Cu (Figure 4.2), and at 788°C for 10 wt% Cu added (Figure 4.5). The formation temperature and amount of Ti_2Cu increased with increased Cu compositions. The BCC_A2 amount remained the same at 400°C, whereas HCP_A3 was continually reduced by Cu additions (Figures 4.2 - 4.5).

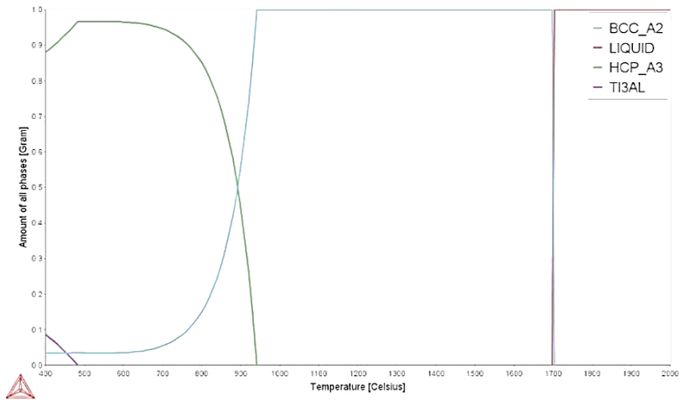


Figure 4.1: *Phase proportion diagram for Ti-6Al-4V (wt%).*

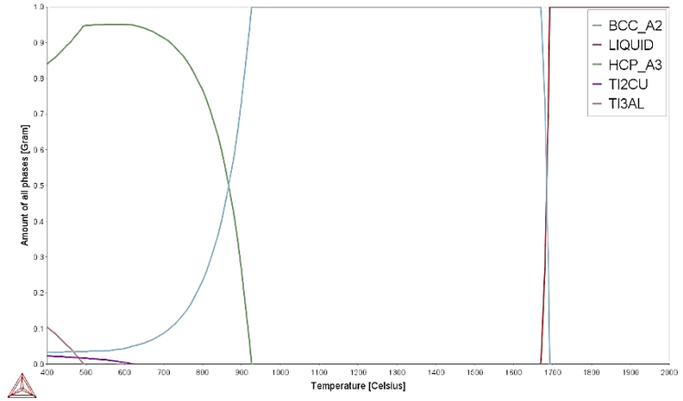


Figure 4.2: *Phase proportion diagram for Ti-6Al-4V-1Cu (wt%).*

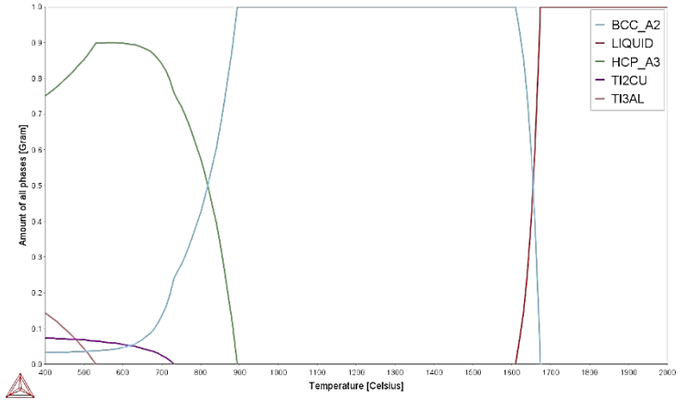


Figure 4.3: *Phase proportion diagram for Ti-6Al-4V-3Cu (wt%).*

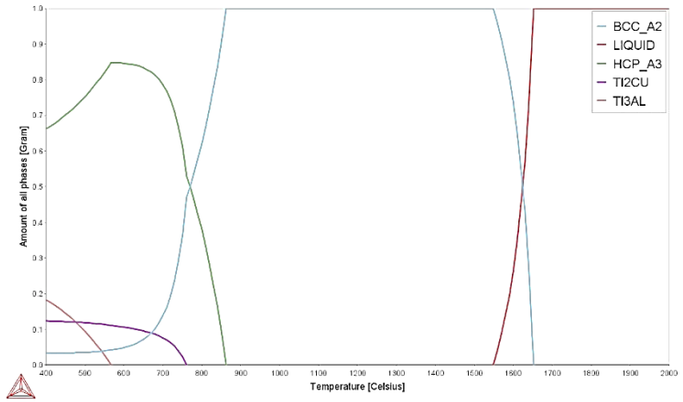


Figure 4.4: *Phase proportion diagram for Ti-6Al-4V-5Cu (wt%).*

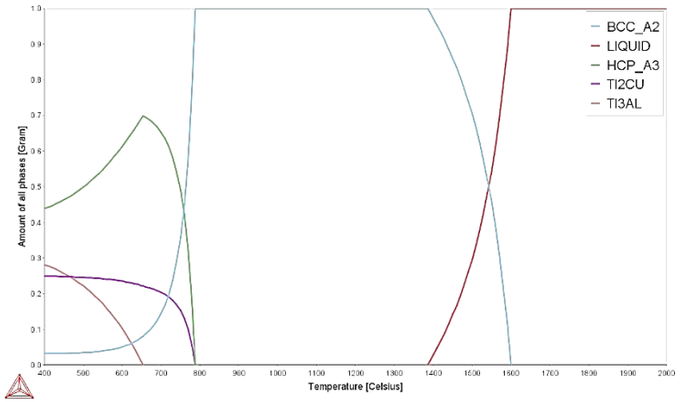


Figure 4.5: *Phase proportion diagram for Ti-6Al-4V-10Cu (wt%).*

Table 4.2: *Phase information for the Ti-6Al-4V-xCu compositions.*

Composition (wt%)	Phase formation temperature (°C)	Phase proportions				
		Liquid	BCC_A2	HCP_A3	Ti_2Cu	Ti_3Al
Ti-6Al-4V	1703	1	0	---	---	---
	1698	0	1	---	---	---
	942	---	1	0	---	---
	485	---	0.03	0.97	---	0
	400	---	0.03	0.88	---	0.09
Ti-6Al-4V-1Cu	1693	1	0	---	---	---
	1670	0	1	---	---	---
	925	---	1	0	---	---
	624	---	0.05	0.95	0	---
	494	---	0.04	0.94	0.02	0
	400	---	0.03	0.84	0.02	0.1
Ti-6Al-4V-3Cu	1673	1	0	---	---	---
	1610	0	1	---	---	---
	894	---	1	0	---	---
	730	---	0.24	0.76	0	---
	531	---	0.04	0.9	0.06	0
	400	---	0.03	0.75	0.07	0.15
Ti-6Al-4V-5Cu	1652	1	0	---	---	---
	1548	0	1	---	---	---
	863	---	1	0	---	---
	760	---	0.47	0.53	0	---
	567	---	0.04	0.85	0.11	0
	400	---	0.03	0.66	0.12	0.19
Ti-6Al-4V-10Cu	1600	1	0	---	---	---
	1386	0	1	---	---	---
	790	---	1	0	---	---
	788	---	0.99	0.01	0	---
	654	---	0.08	0.7	0.22	0
	400	---	0.03	0.44	0.25	0.28

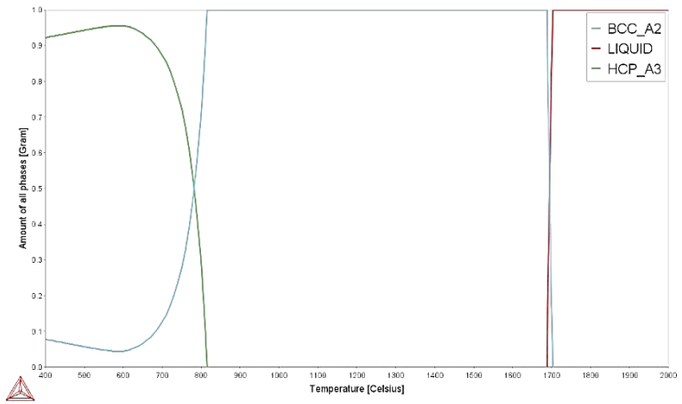
4.2. Ti-10.1Ta-1.7Nb-1.6Zr-*x*Cu compositions

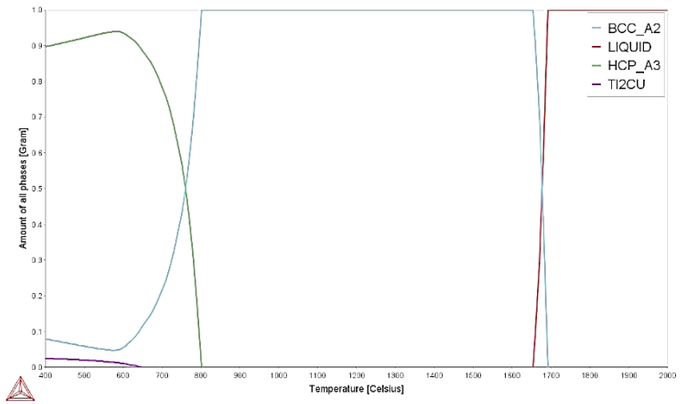
Figures 4.6 - 4.10 show the phase proportion diagrams for Ti-10.1Ta-1.7Nb-1.6Zr-*x*Cu (x = 0, 1, 3, 5 and 10 wt%). The liquid phase solidified to BCC_A2 at 1688°C (Figure 4.6). At 400-816°C, the 0.92 proportion of the BCC_A2 phase transformed into HCP_A3 (Figure 4.6 and Table 4.3). Additions of Cu resulted in the Ti_2Cu phase forming at 640-880°C, as shown in Figures 4.7 - 4.10. Increasing the Cu composition led to increased Ti_2Cu amounts and higher formation temperatures. The HCP_A3 proportion at 400°C was reduced by the 1-10 wt% Cu additions, compared to the

BCC_A2 proportions which were less affected (Figures 4.6 - 4.10). The phase information for Ti-10.1Ta-1.7Nb-1.6Zr-*x*Cu (x = 0, 1, 3, 5 and 10 wt%) is given in Table 4.3.

Table 4.3: *Phase information for Ti-10.1Ta-1.7Nb-1.6Zr-xCu compositions.*

Composition (wt%)	**Phase formation temperature (°C)**	**Phase proportions**			
		Liquid	BCC_A2	HCP_A3	Ti_2Cu
Ti-10.1Ta-1.7Nb-1.6Zr	1704	1	0	---	---
	1688	0	1	---	---
	816	---	1	0	---
	590	---	0.04	0.96	---
	400	---	0.08	0.92	---
Ti-10.1Ta-1.7Nb-1.6Zr-1Cu	1693	1	0	---	---
	1654	0	1	---	---
	801	---	1	0	---
	640	---	0.1	0.9	0
	400	---	0.08	0.9	0.02
Ti-10.1Ta-1.7Nb-1.6Zr-3Cu	1670	1	0	---	---
	1580	0	1	---	---
	773	---	1	0	---
	721	---	0.53	0.47	0
	400	---	0.08	0.84	0.08
Ti-10.1Ta-1.7Nb-1.6Zr-5Cu	1647	1	0	---	---
	1450	0	1	---	---
	745	---	1	0	---
	741	---	0.96	0.04	0
	400	---	0.08	0.79	0.13
Ti-10.1Ta-1.7Nb-1.6Zr-10Cu	1588	1	0	---	---
	1275	0	1	---	---
	880	---	1	---	0
	736	---	0.85	0	0.15
	400	---	0.09	0.66	0.25





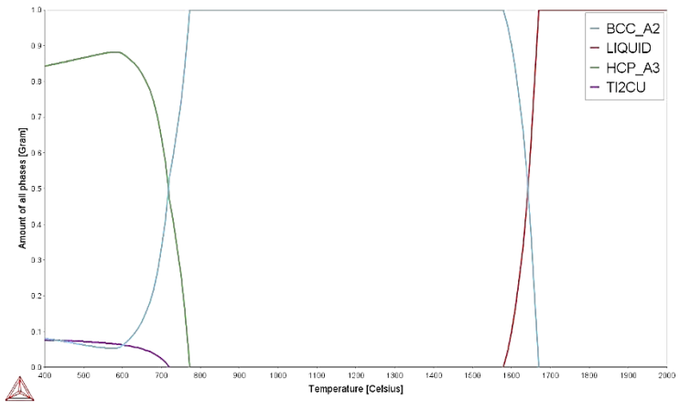
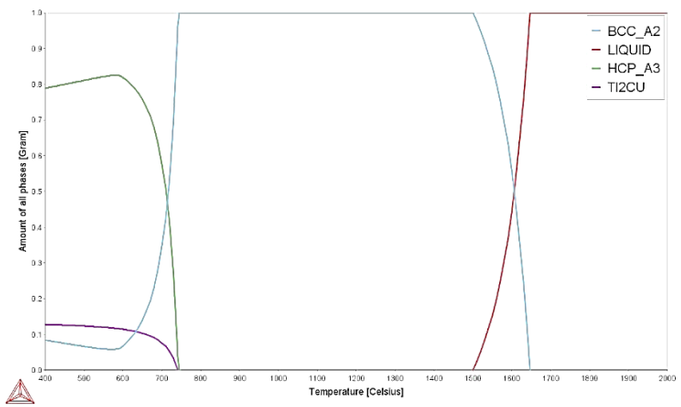
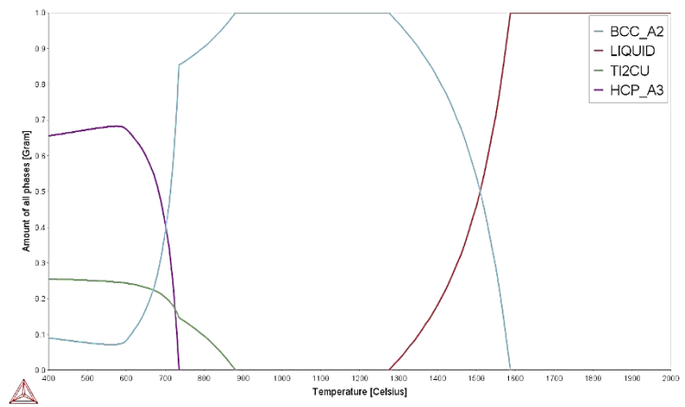


Figure 4.6: *Phase proportion diagram for Ti-10.1Ta-1.7Nb-1.6Zr.* ***Figure 4.7:*** *Phase proportion diagram for Ti-10.1Ta-1.7Nb-1.6Zr-1Cu.* ***Figure 4.8:*** *Phase proportion diagram for Ti-10.1Ta-1.7Nb-1.6Zr-3Cu.*





. ***Figure 4.9:*** *Phase proportion diagram for Ti-10.1Ta-1.7Nb-1.6Zr-5Cu.* ***Figure 4.10:*** *Phase proportion diagram for Ti-10.1Ta-1.7Nb-1.6Zr-10Cu.*

4.3. Ti-6Nb-4Zr-*x*Cu compositions

Figures 4.11 - 4.15 show the phase proportion diagrams for Ti-6Nb-4Zr-*x*Cu (*x* = 0, 1, 3, 5 and 10 wt%), and Table 4.4 gives the phase information. The liquid phase solidified to BCC_A2 phase at 1661°C (Figure 4.11). At 400-809°C, the 0.95 fraction of BCC_A2 transformed to the HCP_A3 phase, resulting in two phases at 400°C, shown in Figure 4.11. Figures 4.12 - 4.15 show that additions of Cu led to the formation of the Ti_2Cu phase at 663-901°C. The Ti_2Cu proportions and formation temperatures increased with increased Cu. Additions of 1-10 wt% Cu led to reduced HCP_A3 proportions at 400°C, whereas BCC_A2 remained the same (Figures 4.12 - 4.15).

Table 4.4: *Phase information for Ti-6Nb-4Zr-xCu compositions.*

Composition (wt%)	**Phase formation temperature (°C)**	**Phase proportions**			
		Liquid	BCC_A2	HCP_A3	Ti_2Cu
Ti-6Nb-4Zr	1665	1	0	---	---
	1661	0	1	---	---
	809	---	1	0	---
	518	---	0.04	0.96	---
	400	---	0.05	0.95	---
Ti-6Nb-4Zr-1Cu	1654	1	0	---	---
	1626	0	1	---	---
	795	---	1	0	---
	663	---	0.15	0.85	0
	400	---	0.05	0.92	0.03
Ti-6Nb-4Zr-3Cu	1632	1	0	---	---
	1551	0	1	---	---
	767	---	1	0	---
	727	---	0.62	0.38	0
	400	---	0.05	0.87	0.08
Ti-6Nb-4Zr-5Cu	1609	1	0	---	---
	1467	0	1	---	---
	756	---	1	---	0
	743	---	0.99	0	0.01
	400	---	0.05	0.82	0.13
Ti-6Nb-4Zr-10Cu	1552	1	0	---	---
	1223	0	1	---	---
	901	---	1	---	0
	738	---	0.84	0	0.16
	400	---	0.05	0.69	0.26

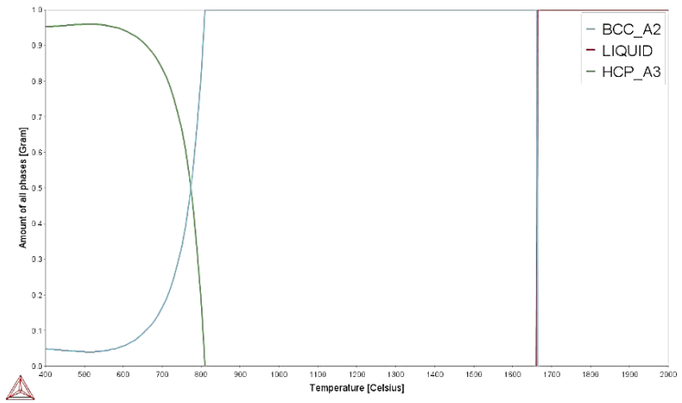


Figure 4.11: *Phase proportion diagram for Ti-6Nb-4Zr.*

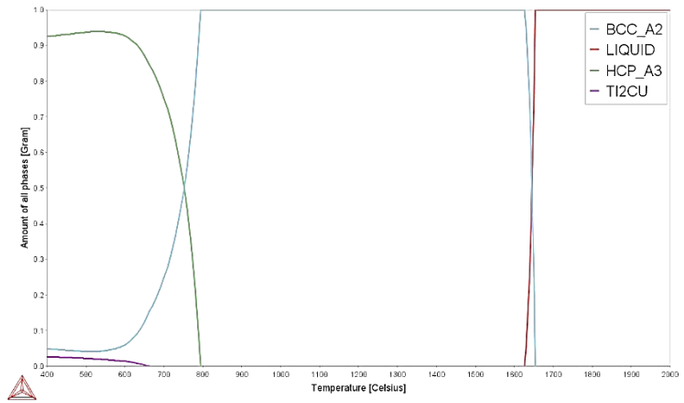


Figure 4.12: *Phase proportion diagram for Ti-6Nb-4Zr-1Cu.*

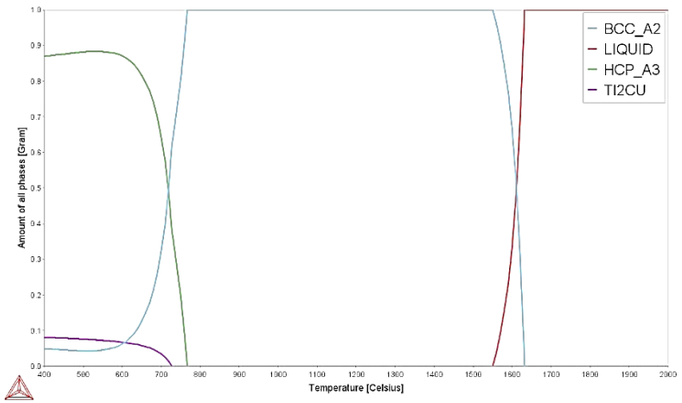


Figure 4.13: *Phase proportion diagram for Ti-6Nb-4Zr-3Cu.*

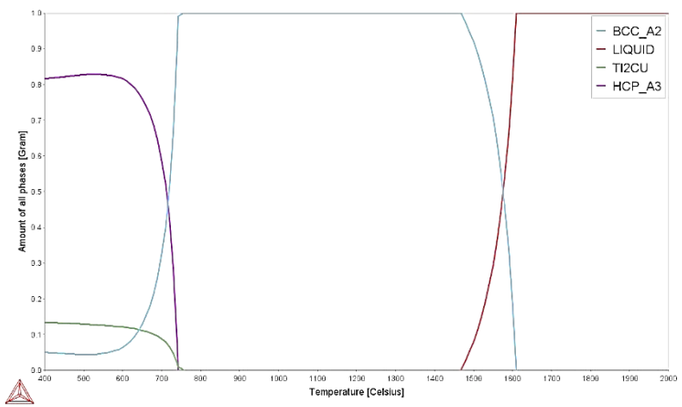


Figure 4.14: *Phase proportion diagram for Ti-6Nb-4Zr-5Cu.*

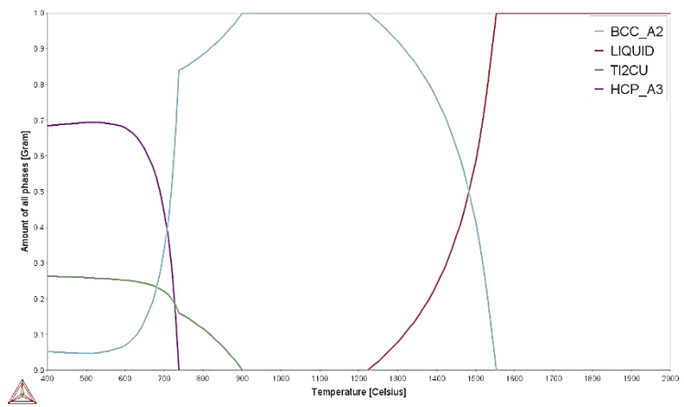


Figure 4.15: *Phase proportion diagram for Ti-6Nb-4Zr-10Cu.*

4.4. Ti-8Nb-4Zr-*x*Cu compositions

The phase proportion diagrams for Ti-8Nb-4Zr-*x*Cu (*x* = 0, 1, 3, 5 and 10 wt%) are shown in Figures 4.16 - 4.20, and the phase information is given in Table 4.5. The liquid phase solidified to BCC_A2 at 1664°C, and 0.93 proportion of BCC_A2 transformed to a HCP_A3 phase at 400-793°C (Figure 4.16). Additions of Cu led to formation of the Ti_2Cu phase at 669-899°C, as shown in Figures 4.17- 4.20. The formation temeperatures and proportions of Ti_2Cu increased with increased Cu. Adding 10 wt% Cu resulted in 0.68 fraction of HCP_A3 at 400°C (Table 4.5), compared to the initial 0.93 fraction, whereas BCC_A2 remained the same (Figures 4.17 - 4.20).

Table 4.5: *Phase information for Ti-8Nb-4Zr-xCu compositions.*

Composition (wt%)	**Phase formation temperature (°C)**	**Phase proportions**			
		Liquid	BCC_A2	HCP_A3	Ti_2Cu
Ti-8Nb-4Zr	1669	1	0	---	---
	1664	0	1	---	---
	793	---	1	0	---
	502	---	0.06	0.94	---
	400	---	0.07	0.93	---
Ti-8Nb-4Zr-1Cu	1658	1	0	---	---
	1631	0	1	---	---
	791	---	1	0	---
	659	---	0.18	0.82	0
	400	---	0.06	0.92	0.02
Ti-8Nb-4Zr-3Cu	1636	1	0	---	---
	1558	0	1	---	---
	763	---	1	0	---
	723	---	0.63	0.37	0
	400	---	0.06	0.86	0.08
Ti-8Nb-4Zr-5Cu	1613	1	0	---	---
	1468	0	1	---	---
	762	---	1	---	0
	731	---	0.98	0	0.02
	400	---	0.06	0.81	0.13
Ti-8Nb-4Zr-10Cu	1558	1	0	---	---
	1244	0	1	---	---
	899	---	1	---	0
	733	---	0.84	0	0.16
	400	---	0.06	0.68	0.26

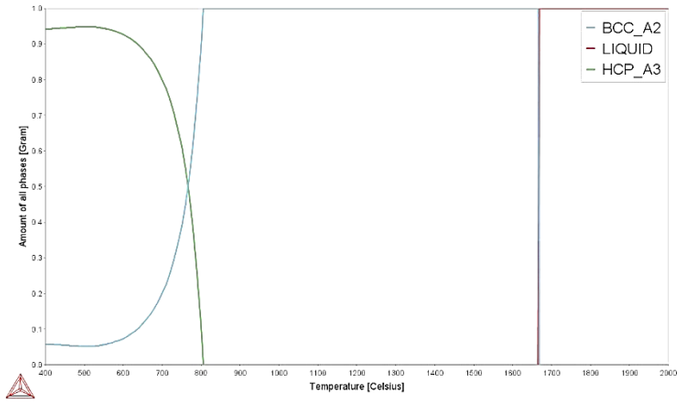


Figure 4.16: *Phase proportion diagram for Ti-8Nb-4Zr.*

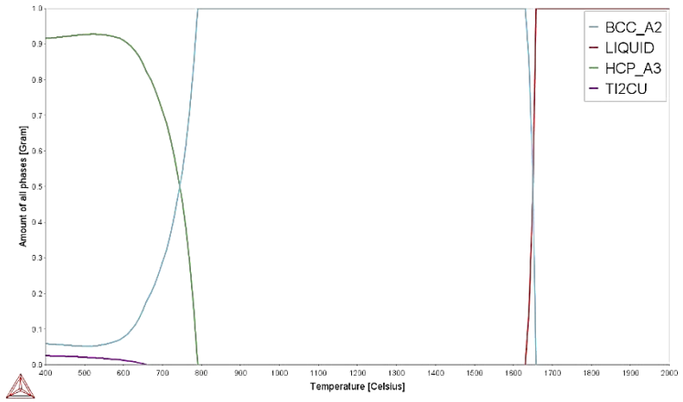


Figure 4.17: *Phase proportion diagram for Ti-8Nb-4Zr-1Cu.*

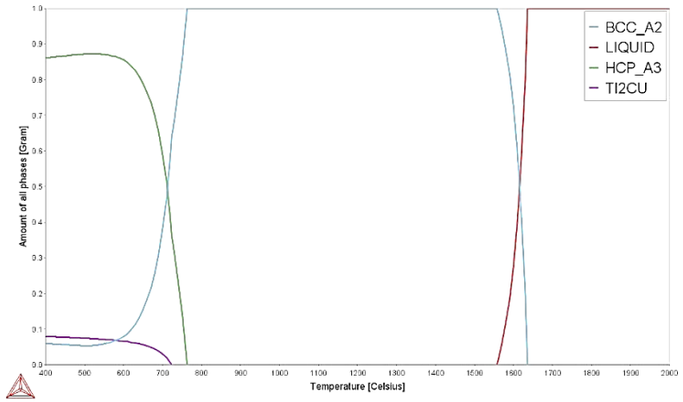


Figure 4.18: *Phase proportion diagram for Ti-8Nb-4Zr-3Cu.*

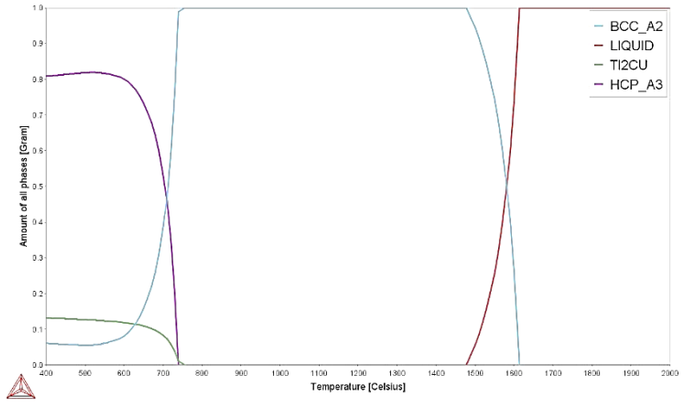


Figure 4.19: *Phase proportion diagram for Ti-8Nb-4Zr-5Cu.*

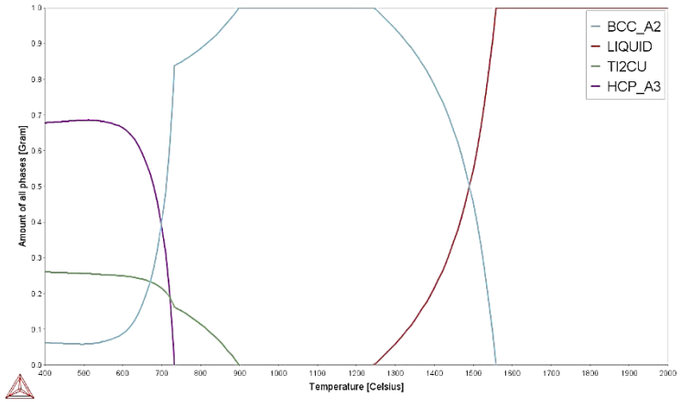


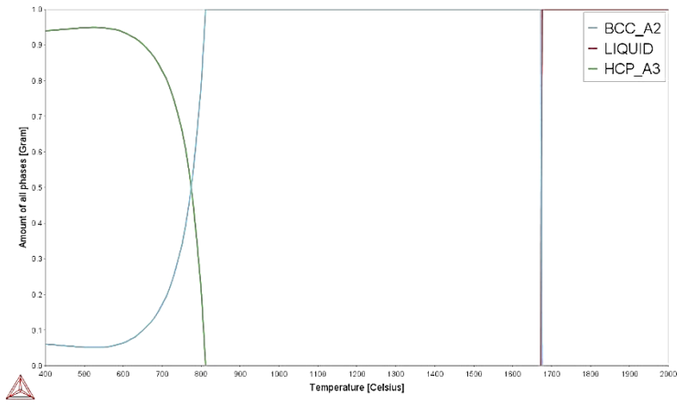
Figure 4.20: *Phase proportion diagram for Ti-8Nb-4Zr-10Cu.*

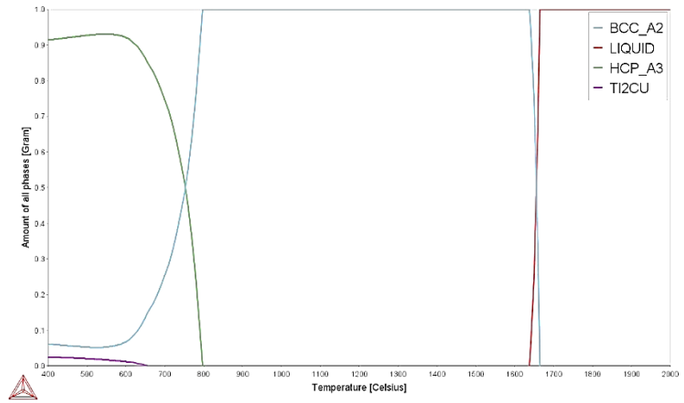
4.5. Ti-6Nb-2Zr-1.7Ta-*x*Cu compositions

The BCC_A2 to HCP_A3 transformation temperatures for Ti-6Nb-2Zr-1.7Ta-*x*Cu (Table 4.6) were very similar to Ti-6Nb-4Zr-*x*Cu (Table 4.4). Ti-6Nb-2Zr-1.7Ta-*x*Cu (Table 4.6) and Ti-8Nb-4Zr-*x*Cu (Table 4.5) had same BCC_A2, HCP_A3 and Ti_2Cu at 400°C. The phase proportion diagrams for Ti-6Nb-2Zr-1.7Ta-*x*Cu (*x* = 0, 1, 3, 5 and 10 wt%) are shown in Figures 4.21 - 4.25, and Table 4.6 gives the phase information. At 400°C, the Ti-6Nb-2Zr-1.7Ta-*x*Cu (Table 4.6) had higher BCC_A2 and HCP_A3 fractions than Ti-6Al-4V-*x*Cu (Table 4.2).

Table 4.6: *Phase information for the Ti-6Nb-2Zr-1.7Ta-xCu compositions.*

Composition (wt%)	**Phase formation temperature (°C)**	**Phase proportions**			
		Liquid	BCC_A2	HCP_A3	Ti_2Cu
Ti-6Nb-2Zr-1.7Ta	1676	1	0	---	---
	1671	0	1	---	---
	812	---	1	0	---
	530	---	0.05	0.95	---
	400	---	0.06	0.94	---
Ti-6Nb-2Zr-1.7Ta-1Cu	1665	1	0	---	---
	1638	0	1	---	---
	797	---	1	0	---
	656	---	0.15	0.85	0
	400	---	0.06	0.92	0.02
Ti-6Nb-2Zr-1.7Ta-3Cu	1643	1	0	---	---
	1566	0	1	---	---
	769	---	1	0	---
	724	---	0.59	0.41	0
	400	---	0.06	0.86	0.08
Ti-6Nb-2Zr-1.7Ta-5Cu	1621	1	0	---	---
	1488	0	1	---	---
	747	---	1	---	0
	742	---	0.99	0	0.01
	400	---	0.06	0.81	0.13
Ti-6Nb-2Zr-1.7Ta-10Cu	1565	1	0	---	---
	1266	0	1	---	---
	891	---	1	---	0
	736	---	0.85	0	0.15
	400	---	0.07	0.68	0.25





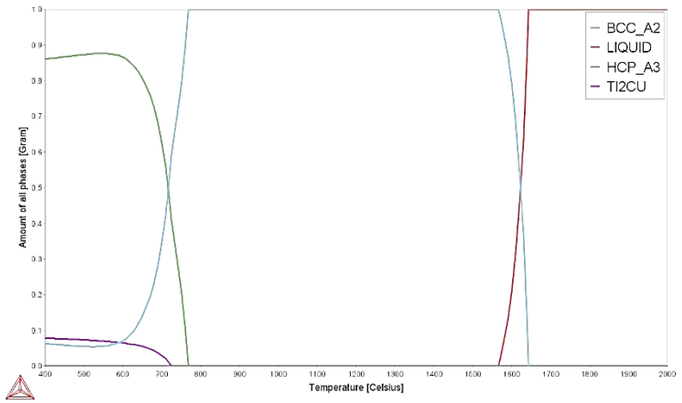
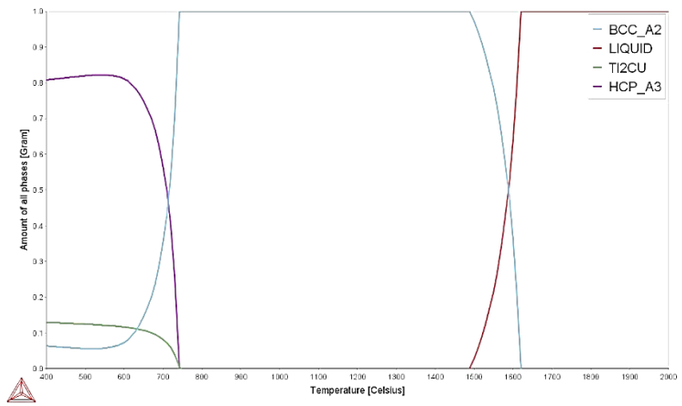


Figure 4.21: *Phase proportion diagram for Ti-6Nb-2Zr-1.7Ta.* ***Figure 4.22:*** *Phase proportion diagram for Ti-6Nb-2Zr-1.7Ta-1Cu.* ***Figure 4.23:*** *Phase proportion diagram for Ti-6Nb-2Zr-1.7Ta-3Cu.*



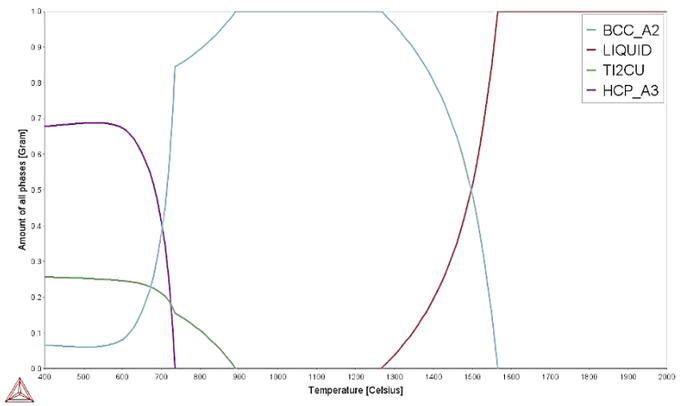


Figure 4.24: *Phase proportion diagram for Ti-6Nb-2Zr-1.7Ta-5Cu.* ***Figure 4.25:*** *Phase proportion diagram for Ti-6Nb-2Zr-1.7Ta-10Cu.*

4.6. Ti-6Zr-4Ta-4Nb-*x*Cu compositions

Figure 4.26 shows the solidification of liquid phase to BCC_A2 phase at 1663°C, which was similar to Ti-8Nb-4Zr (Figure 4.16). Table 4.7 gave similar BCC_A2, HCP_A3 and Ti_2Cu proportions, compared with Ti-8Nb-4Zr-*x*Cu (Table 4.5) at 400°C. Table 4.7 gives the phase information for Ti-6Zr-4Ta-4Nb-*x*Cu (*x* = 0, 1, 3, 5 and 10 wt%), and Figures 4.26 - 4.30 show the phase proportion diagrams.

Table 4.7: *Phase information for Ti-6Zr-4Ta-4Nb-xCu compositions.*

Composition (wt%)	**Phase formation temperature (°C)**	**Phase proportions**			
		Liquid	BCC_A2	HCP_A3	Ti_2Cu
Ti-6Zr-4Ta-4Nb	1673	1	0	---	---
	1663	0	1	---	---
	801	---	1	0	---
	530	---	0.04	0.96	---
	400	---	0.06	0.94	---
Ti-6Zr-4Ta-4Nb-1Cu	1662	1	0	---	---
	1624	0	1	---	---
	786	---	1	0	---
	660	---	0.17	0.83	0
	400	---	0.06	0.92	0.02
Ti-6Zr-4Ta-4Nb-3Cu	1639	1	0	---	---
	1542	0	1	---	---
	758	---	1	0	---
	723	---	0.66	0.34	0
	400	---	0.06	0.86	0.08
Ti-6Zr-4Ta-4Nb-5Cu	1616	1	0	---	---
	1450	0	1	---	---
	760	---	1	---	0
	738	---	0.98	0	0.02
	400	---	0.06	0.81	0.13
Ti-6Zr-4Ta-4Nb-10Cu	1556	1	0	---	---
	1178	0	1	---	---
	908	---	1	---	0
	732	---	0.83	0	0.17
	400	---	0.06	0.67	0.27

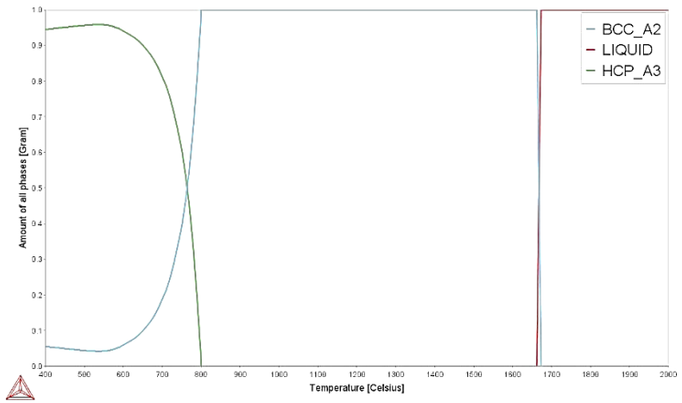


Figure 4.26: *Phase proportion diagram for Ti-6Zr-4Ta-4Nb.*

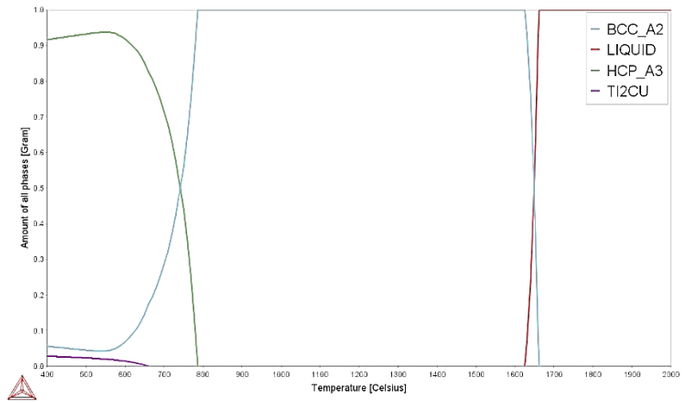


Figure 4.27: *Phase proportion diagram for Ti-6Zr-4Ta-4Nb-1Cu.*

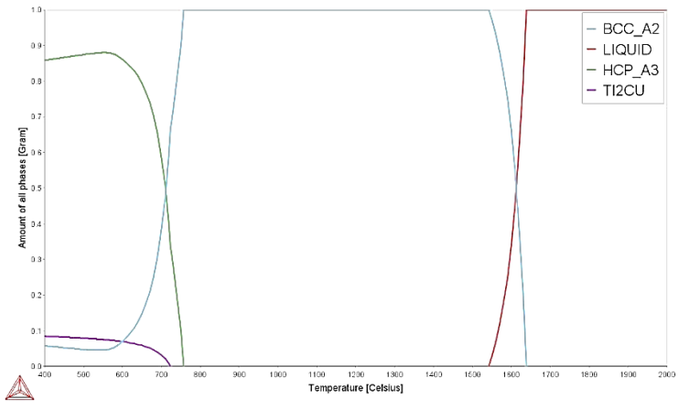


Figure 4.28: *Phase proportion diagram for Ti-6Zr-4Ta-4Nb-3Cu.*

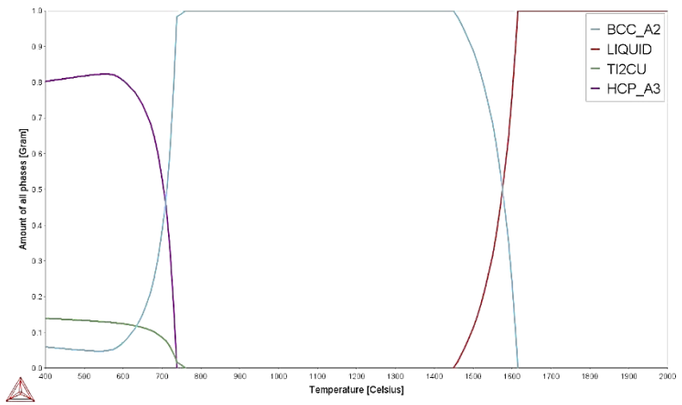


Figure 4.29: *Phase proportion diagram for Ti-6Zr-4Ta-4Nb-5Cu.*

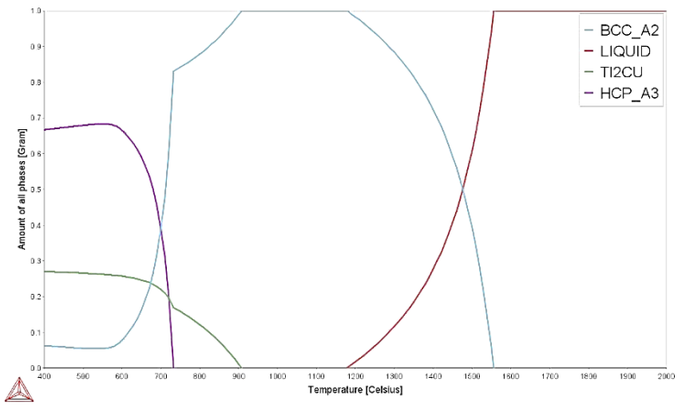


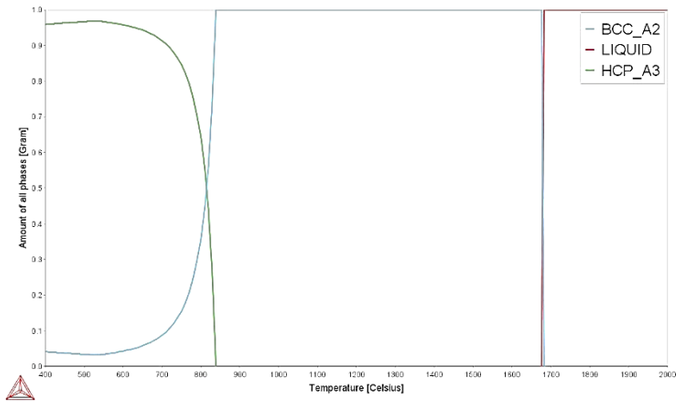
Figure 4.30: *Phase proportion diagram for Ti-6Zr-4Ta-4Nb-10Cu.*

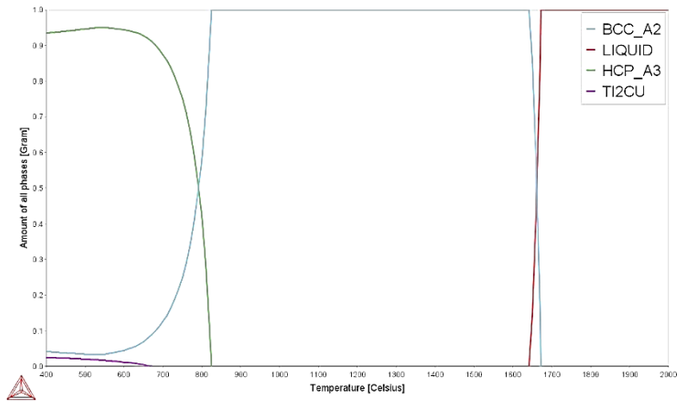
4.7. Ti-4Ta-1.8Zr-1.5Mo-*x*Cu compositions

The Ti-4Ta-1.8Zr-1.5Mo-*x*Cu (*x* = 0, 1, 3, 5 and 10 wt%) phase proportion diagrams are shown in Figures 4.31 - 4.35, and Table 4.8 gives the phase information. The Ti-4Ta-1.8Zr-1.5Mo-*x*Cu had a lower BCC_A2 proportion at 400°C compared to Ti-10.1Ta-1.7Nb-1.6Zr-*x*Cu (Table 4.3) and Ti-8Nb-4Zr-*x*Cu (Table 4.5). However, the Ti_2Cu fractions were similar at 400°C for The Ti-4Ta-1.8Zr-1.5Mo-*x*Cu (Table 4.8), Ti-10.1Ta-1.7Nb-1.6Zr-*x*Cu (Table 4.3) and Ti-8Nb-4Zr-*x*Cu (Table 4.5).

Table 4.8: *Phase information for Ti-4Ta-1.8Zr-1.5Mo-xCu compositions*

Composition (wt%)	**Phase formation temperature (°C)**	**Phase proportions**			
		Liquid	BCC_A2	HCP_A3	Ti_2Cu
Ti-4Ta-1.8Zr-1.5Mo	1683	1	0	---	---
	1675	0	1	---	---
	839	---	1	0	---
	530	---	0.03	0.97	---
	400	---	0.04	0.96	---
Ti-4Ta-1.8Zr-1.5Mo-1Cu	1673	1	0	---	---
	1641	0	1	---	---
	825	---	1	0	---
	670	---	0.09	0.91	0
	400	---	0.04	0.93	0.03
Ti-4Ta-1.8Zr-1.5Mo-3Cu	1649	1	0	---	---
	1567	0	1	---	---
	796	---	1	0	---
	745	---	0.49	0.51	0
	400	---	0.04	0.88	0.08
Ti-4Ta-1.8Zr-1.5Mo-5Cu	1629	1	0	---	---
	1485	0	1	---	---
	767	---	1	0	---
	759	---	0.92	0.08	0
	400	---	0.04	0.83	0.13
Ti-4Ta-1.8Zr-1.5Mo-10Cu	1571	1	0	---	---
	1250	0	1	---	---
	894	---	1	---	0
	758	---	0.86	0	0.14
	400	---	0.04	0.7	0.26





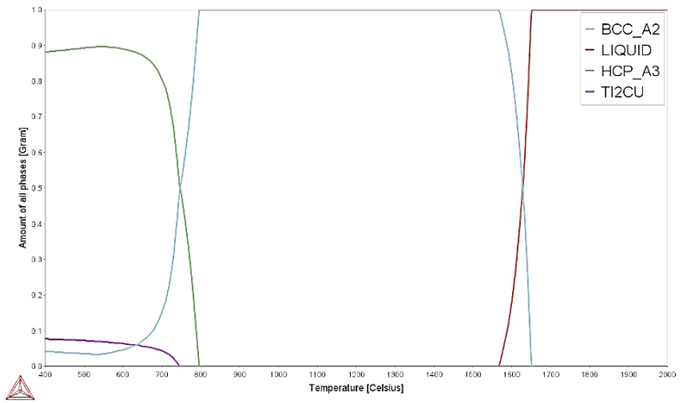
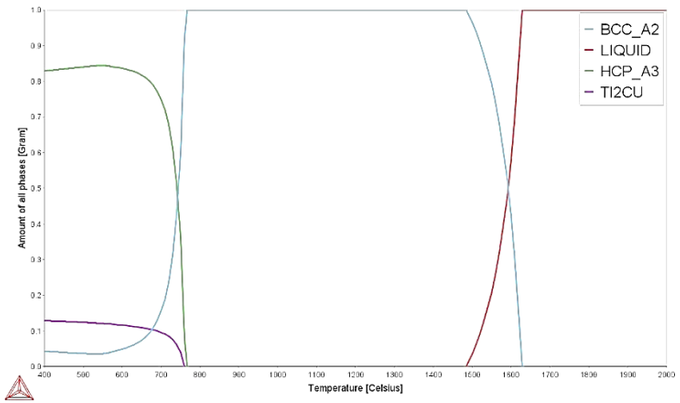


Figure 4.31: *Phase proportion diagram for Ti-4Ta-1.8Zr-1.5Mo.* ***Figure 4.32:*** *Phase proportion diagram for Ti-4Ta-1.8Zr-1.5Mo-1Cu.* ***Figure 4.33:*** *Phase proportion diagram for Ti-4Ta-1.8Zr-1.5Mo-3Cu.*



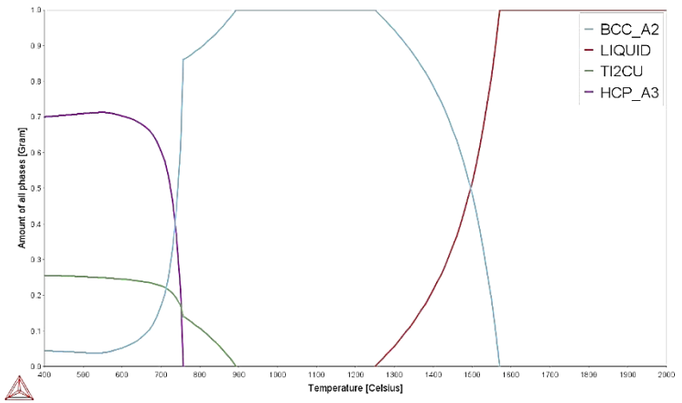


Figure 4.34: *Phase proportion diagram for Ti-4Ta-1.8Zr-1.5Mo-5Cu.* ***Figure 4.35:*** *Phase proportion diagram for Ti-4Ta-1.8Zr-1.5Mo-10Cu.*

4.8. Ti-6Ta-2Zr-1.5Mo-*x*Cu compositions

The results for Ti-6Ta-2Zr-1.5Mo-*x*Cu (*x* = 1, 3, 5 and 10 wt%) (Table 4.9) were similar to Ti-8Nb-4Zr-*x*Cu (*x* = 1, 3, 5 and 10 wt%) (Table 4.5) at 400°C. However, the BCC_A2 to HCP_A3 transformation temperatures were different, as given in Table 4.9 and Table 4.5. The phase proportion diagrams for Ti-6Ta-2Zr-1.5Mo-*x*Cu (*x* = 0, 1, 3, 5 and 10 wt%) are shown in Figures 4.36 - 4.40, and Table 4.9 gives the phase information.

Table 4.9: *Phase information for Ti-6Ta-2Zr-1.5Mo-xCu compositions.*

Composition (wt%)	**Phase formation temperature (°C)**	**Phase proportions**			
		Liquid	BCC_A2	HCP_A3	Ti_2Cu
Ti-6Ta-2Zr-1.5Mo	1691	1	0	---	---
	1679	0	1	---	---
	830	---	1	0	---
	555	---	0.04	0.96	---
	400	---	0.05	0.95	---
Ti-6Ta-2Zr-1.5Mo-1Cu	1679	1	0	---	---
	1645	0	1	---	---
	815	---	1	0	---
	666	---	0.12	0.88	0
	400	---	0.06	0.92	0.02
Ti-6Ta-2Zr-1.5Mo-3Cu	1658	1	0	---	---
	1569	0	1	---	---
	786	---	1	0	---
	737	---	0.53	0.47	0
	400	---	0.06	0.88	0.08
Ti-6Ta-2Zr-1.5Mo-5Cu	1635	1	0	---	---
	1485	0	1	---	---
	757	---	1	0	---
	754	---	0.96	0.04	0
	400	---	0.06	0.81	0.13
Ti-6Ta-2Zr-1.5Mo-10Cu	1578	1	0	---	---
	1245	0	1	---	---
	895	---	1	---	0
	751	---	0.85	0	0.15
	400	---	0.06	0.68	0.26

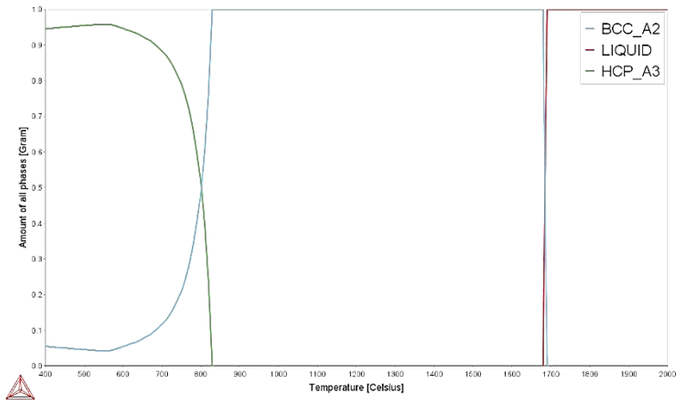


Figure 4.36: *Phase proportion diagram for Ti-6Ta-2Zr-1.5Mo.*

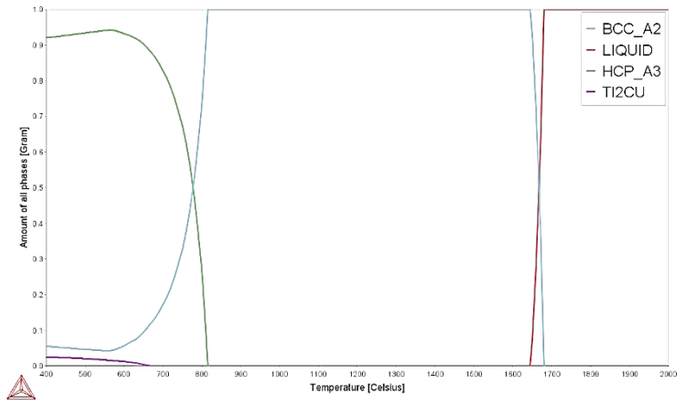


Figure 4.37: *Phase proportion diagram for Ti-6Ta-2Zr-1.5Mo-1Cu.*

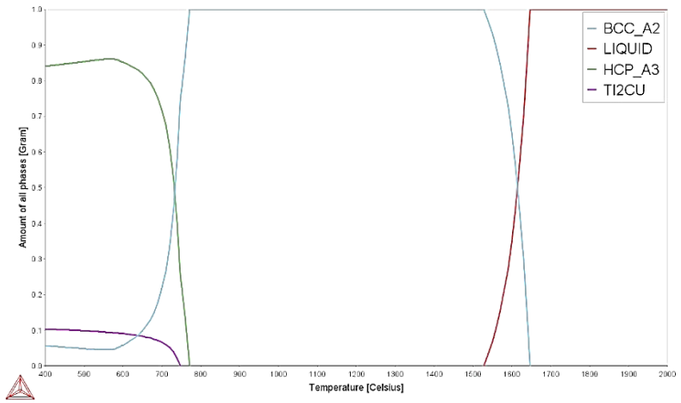


Figure 4.38: *Phase proportion diagram for Ti-6Ta-2Zr-1.5Mo-3Cu.*

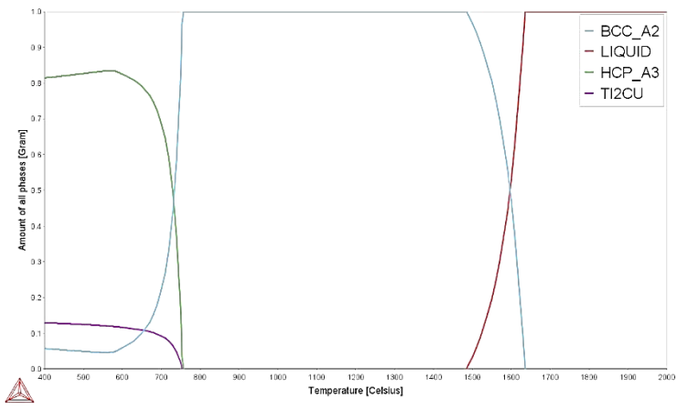


Figure 4.39: *Phase proportion diagram for Ti-6Ta-2Zr-1.5Mo-5Cu.*

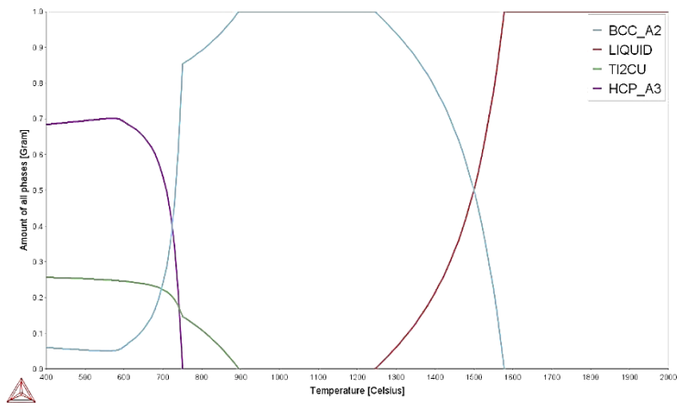


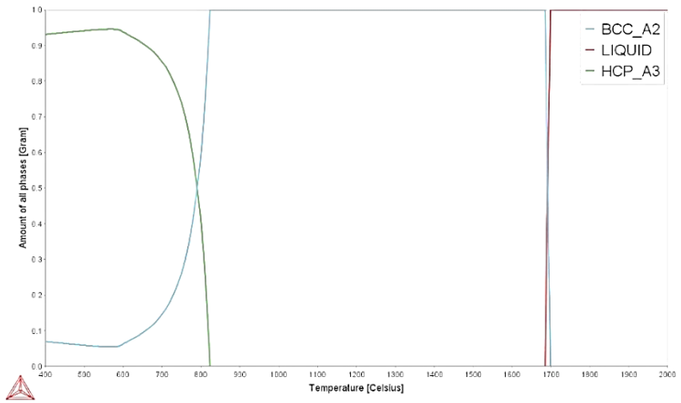
Figure 4.40: *Phase proportion diagram for Ti-6Ta-2Zr-1.5Mo-10Cu.*

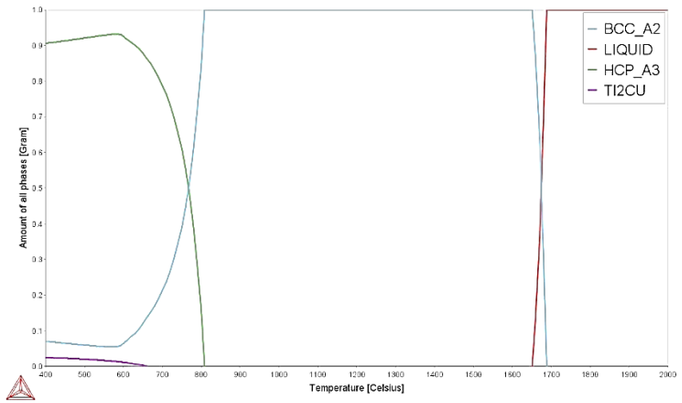
4.9. Ti-8Ta-1.5Mo-1.5Zr-*x*Cu compositions

Table 4.10 gives the phase information for Ti-8Ta-1.5Mo-1.5Zr-*x*Cu (*x* = 0, 1, 3, 5 and 10 wt%). Ti-8Ta-1.5Mo-1.5Zr-*x*Cu had higher BCC_A2, and lower HCP_A3 fractions than Ti-6Nb-4Zr-*x*Cu (Table 4.4) at 400°C. The same HCP_A3 fractions were found in Ti-8Ta-1.5Mo-1.5Zr (Table 4.10) and Ti-8Nb-4Zr (Table 4.5) at 400°C. Thermo-Calc predicted similar Ti_2Cu proportions in Ti-8Ta-1.5Mo-1.5Zr-*x*Cu (Table 4.10), Ti-6Nb-4Zr-*x*Cu (Table 4.4), Ti-8Nb-4Zr-*x*Cu (Table 4.5), Ti-6Al-4V-*x*Cu (Table 4.2) and Ti-10.1Ta-1.7Nb-1.6Zr-*x*Cu (Table 4.3) at 400°C. The phase proportion diagrams for Ti-8Ta-1.5Mo-1.5Zr-*x*Cu (*x* = 0, 1, 3, 5 and 10 wt%) are shown in Figures 4.41 - 4.45.

Table 4.10: *Phase information for Ti-8Ta-1.5Mo-1.5Zr-xCu compositions.*

Composition (wt%)	**Phase formation temperature (°C)**	**Phase proportions**			
		Liquid	BCC_A2	HCP_A3	Ti_2Cu
Ti-8Ta-1.5Mo-1.5Zr	1699	1	0	---	---
	1686	0	1	---	---
	824	---	1	0	---
	570	---	0.05	0.95	---
	400	---	0.07	0.93	---
Ti-8Ta-1.5Mo-1.5Zr-1Cu	1689	1	0	---	---
	1651	0	1	---	---
	809	---	1	0	---
	660	---	0.14	0.86	0
	400	---	0.07	0.91	0.02
Ti-8Ta-1.5Mo-1.5Zr-3Cu	1667	1	0	---	---
	1576	0	1	---	---
	779	---	1	0	---
	731	---	0.56	0.44	0
	400	---	0.07	0.85	0.08
Ti-8Ta-1.5Mo-1.5Zr-5Cu	1644	1	0	---	---
	1493	0	1	---	---
	750	---	1	0	---
	749	---	0.99	0.01	0
	400	---	0.07	0.8	0.13
Ti-8Ta-1.5Mo-1.5Zr-10Cu	1587	1	0	---	---
	1256	0	1	---	---
	893	---	1	---	0
	744	---	0.85	0	0.15
	400	---	0.07	0.67	0.26





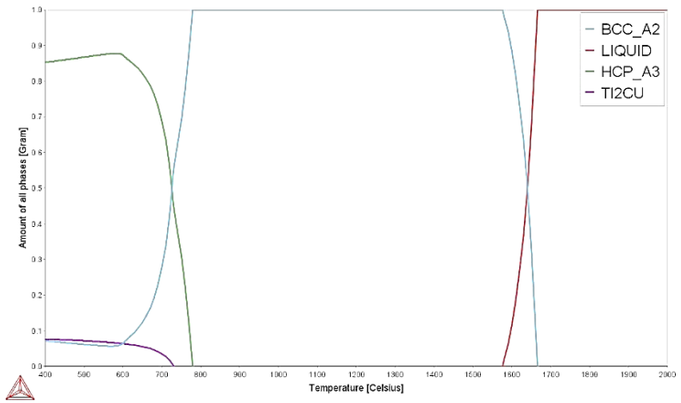
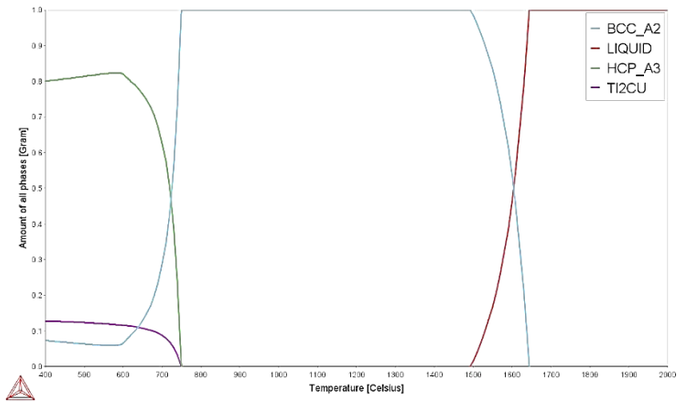


Figure 4.41: *Phase proportion diagram for Ti-8Ta-1.5Mo-1.5Zr.* ***Figure 4.42:*** *Phase proportion diagram for Ti-8Ta-1.5Mo-1.5Zr-1Cu.* ***Figure 4.43:*** *Phase proportion diagram for Ti-8Ta-1.5Mo-1.5Zr-3Cu.*



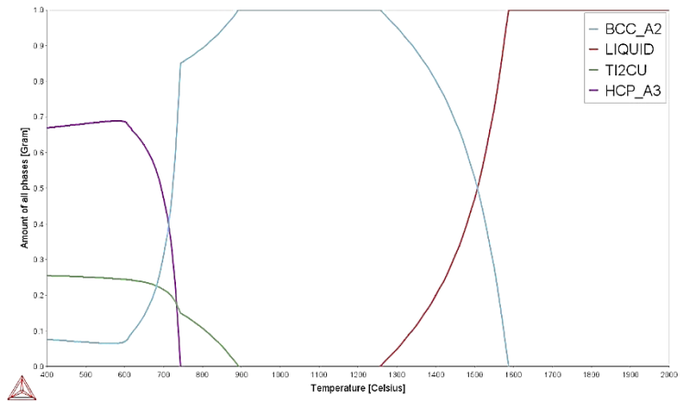


Figure 4.44: *Phase proportion diagram for Ti-8Ta-1.5Mo-1.5Zr-5Cu.* ***Figure 4.45:*** *Phase proportion diagram for Ti-8Ta-1.5Mo-1.5Zr-10Cu.*

4.10. Ti-8Zr-4Ta-2Mo-*x*Cu compositions

At 400°C, Ti-8Zr-4Ta-2Mo (Table 4.11) had less BCC_A2 and more HCP_A3 than Ti-10.1Ta-1.7Nb-1.6Zr (Table 4.3) and Ti-8Nb-4Zr (Table 4.5), whereas similar phase proportions were found in Ti-8Zr-4Ta-2Mo when compared to Ti-6Nb-4Zr (Table 4.4). Table 4.11 gives the phase information for Ti-8Zr-4Ta-2Mo-*x*Cu (*x* = 0, 1, 3, 5 and 10 wt%), and Figures 4.46 - 4.50 show the phase proportion diagrams.

Table 4.11: *Phase information for Ti-8Zr-4Ta-2Mo-xCu compositions.*

Composition (wt%)	**Phase formation temperature (°C)**	**Phase proportions**			
		Liquid	BCC_A2	HCP_A3	Ti_2Cu
Ti-8Zr-4Ta-2Mo	1671	1	0	---	---
	1658	0	1	---	---
	805	---	1	0	---
	490	---	0.05	0.95	---
	400	---	0.05	0.95	---
Ti-8Zr-4Ta-2Mo-1Cu	1659	1	0	---	---
	1616	0	1	---	---
	790	---	1	0	---
	677	---	0.22	0.78	0
	400	---	0.05	0.92	0.03
Ti-8Zr-4Ta-2Mo-3Cu	1637	1	0	---	---
	1523	0	1	---	---
	760	---	1	0	---
	734	---	0.73	0.27	0
	400	---	0.05	0.86	0.09
Ti-8Zr-4Ta-2Mo-5Cu	1614	1	0	---	---
	1415	0	1	---	---
	781	---	1	---	0
	744	---	0.97	0	0.03
	400	---	0.05	0.81	0.14
Ti-8Zr-4Ta-2Mo-10Cu	1555	1	0	---	---
	1087	0	1	---	---
	931	---	1	---	0
	741	---	0.82	0	0.18
	400	---	0.05	0.67	0.28

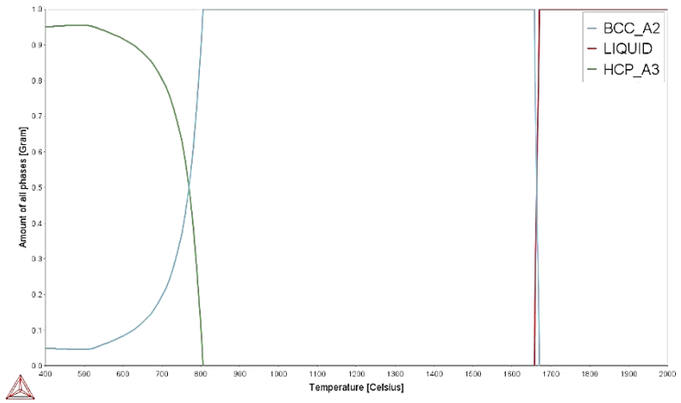


Figure 4.46: *Phase proportion diagram for Ti-8Zr-4Ta-2Mo.*

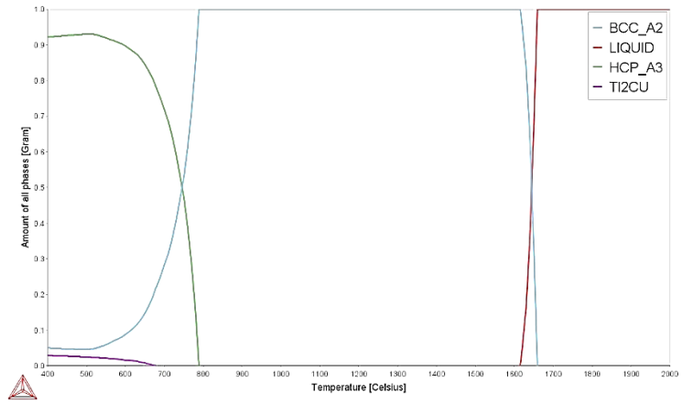


Figure 4.47: *Phase proportion diagram for Ti-8Zr-4Ta-2Mo-1Cu.*

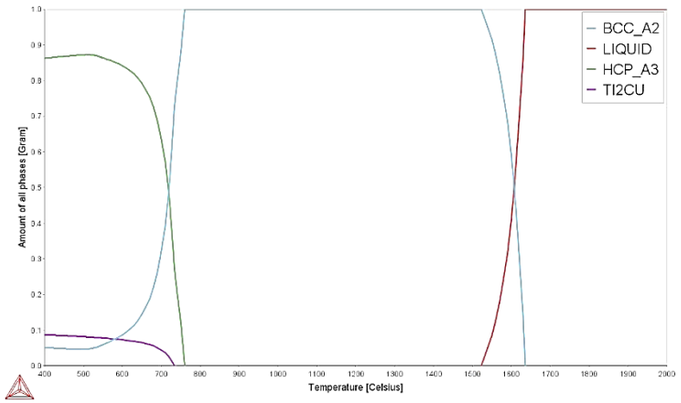


Figure 4.48: *Phase proportion diagram for Ti-8Zr-4Ta-2Mo-3Cu.*

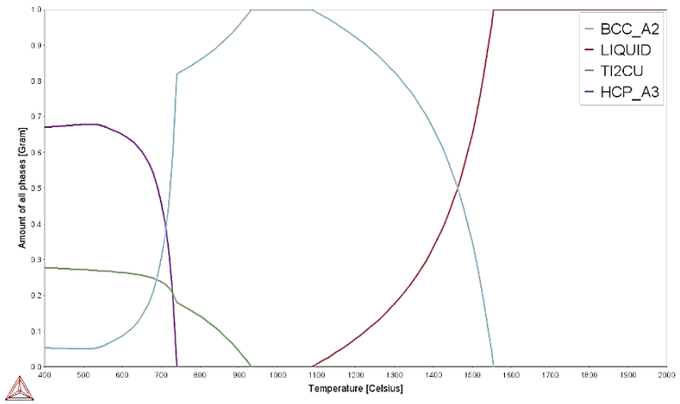


Figure 4.49: *Phase proportion diagram for Ti-8Zr-4Ta-2Mo-5Cu.*

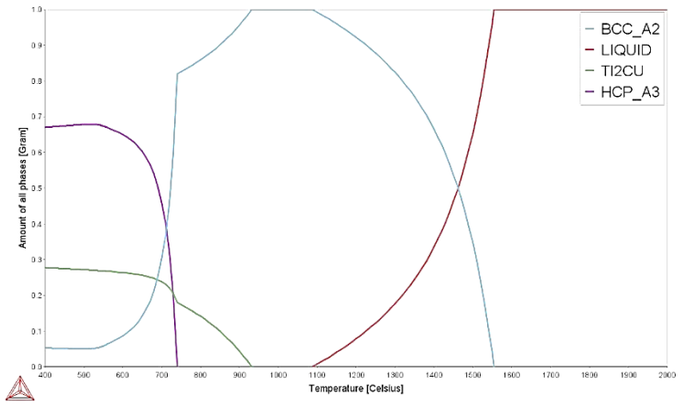


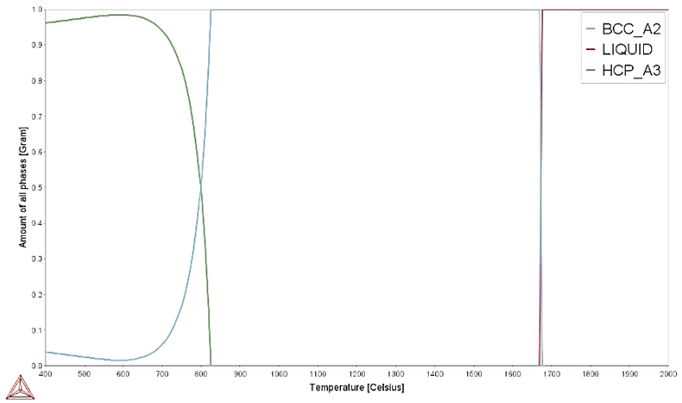
Figure 4.50: *Phase proportion diagram for Ti-8Zr-4Ta-2Mo-10Cu.*

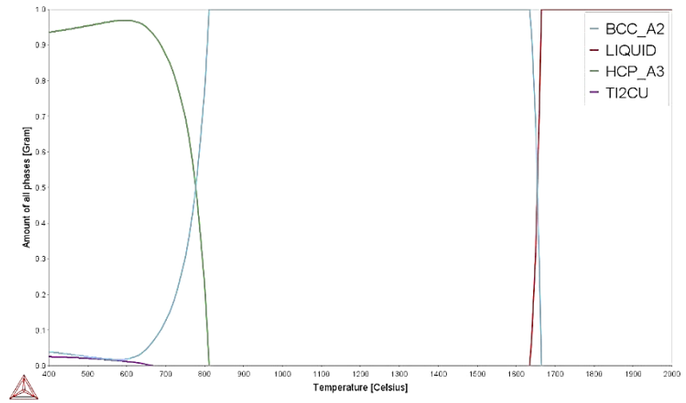
4.11. Ti-3.5Ta-3Nb-3Zr-*x*Cu compositions

Table 4.12 gives the phase information for Ti-3.5Ta-3Nb-3Zr-*x*Cu (*x* = 0, 1, 3, 5 and 10 wt%). The results were very similar to Ti-6Nb-4Zr-*x*Cu (Table 4.4). The BCC_A2 fractions at 400°C were slightly less, whereas HCP_A3 were more compared to Ti-8Nb-4Zr-*x*Cu (Table 4.5) and Ti-10.1Ta-1.7Nb-1.6Zr-*x*Cu (Table 4.3). The phase proportion diagrams for Ti-3.5Ta-3Nb-3Zr-*x*Cu (*x* = 0, 1, 3, 5 and 10 wt%) are shown in Figures 4.51 - 4.55.

Table 4.12: *Phase information for Ti-3.5Ta-3Nb-3Zr-xCu compositions.*

Composition (wt%)	**Phase formation temperature (°C)**	**Phase proportions**			
		Liquid	BCC_A2	HCP_A3	Ti_2Cu
Ti-3.5Ta-3Nb-3Zr	1677	1	0	---	---
	1669	0	1	---	---
	825	---	1	0	---
	590	---	0.02	0.98	---
	400	---	0.04	0.96	---
Ti-3.5Ta-3Nb-3Zr-1Cu	1665	1	0	---	---
	1635	0	1	---	---
	812	---	1	0	---
	666	---	0.07	0.93	0
	400	---	0.04	0.93	0.03
Ti-3.5Ta-3Nb-3Zr-3Cu	1643	1	0	---	---
	1560	0	1	---	---
	784	---	1	0	---
	735	---	0.5	0.5	0
	400	---	0.04	0.88	0.08
Ti-3.5Ta-3Nb-3Zr-5Cu	1620	1	0	---	---
	1479	0	1	---	---
	756	---	1	0	---
	751	---	0.94	0.06	0
	400	---	0.04	0.83	0.13
Ti-3.5Ta-3Nb-3Zr-10Cu	1562	1	0	---	---
	1246	0	1	---	---
	890	---	1	---	0
	749	---	0.86	0	0.14
	400	---	0.04	0.70	0.26





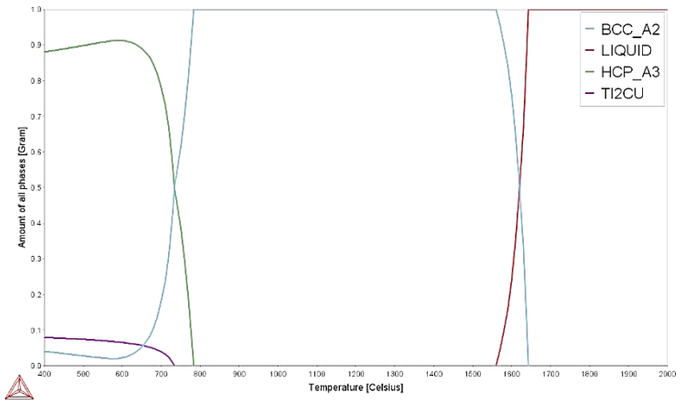
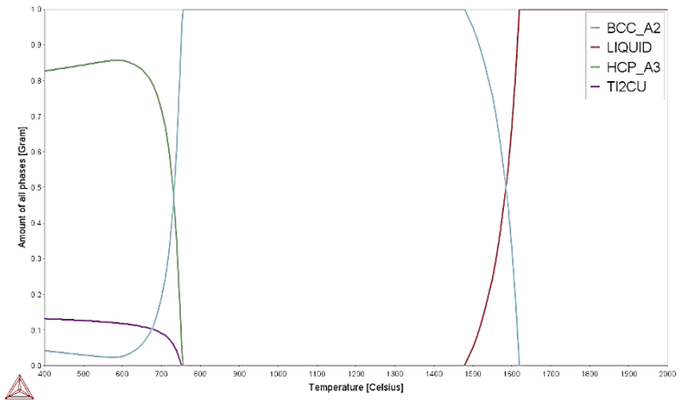


Figure 4.51: *Phase proportion diagram for Ti-3.5Ta-3Nb-3Zr.* ***Figure 4.52:*** *Phase proportion diagram for Ti-3.5Ta-3Nb-3Zr-1Cu.* ***Figure 4.53:*** *Phase proportion diagram for Ti-3.5Ta-3Nb-3Zr-3Cu.*



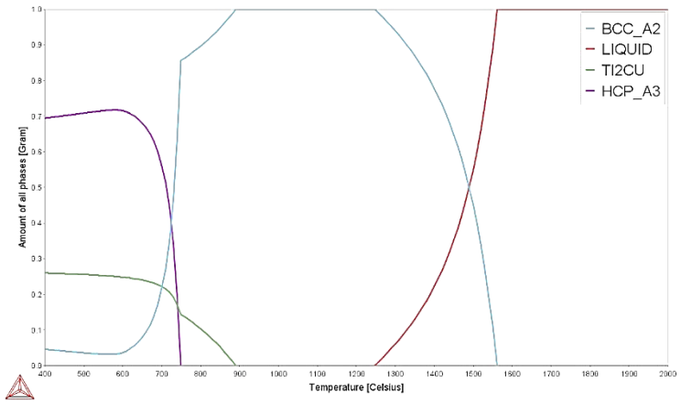


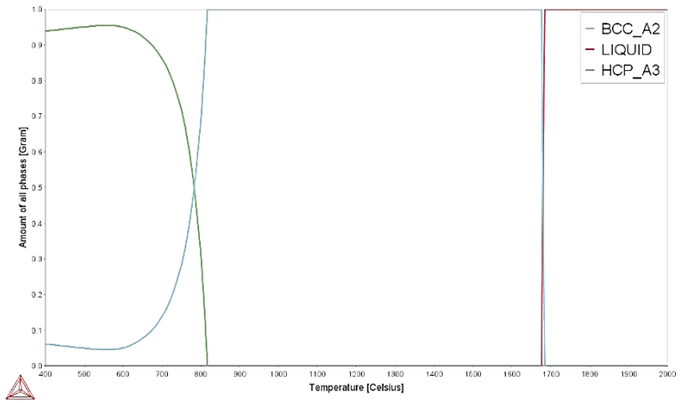
Figure 4.54: *Phase proportion diagram for Ti-3.5Ta-3Nb-3Zr-5Cu.* ***Figure 4.55:*** *Phase proportion diagram for Ti-3.5Ta-3Nb-3Zr-10Cu.*

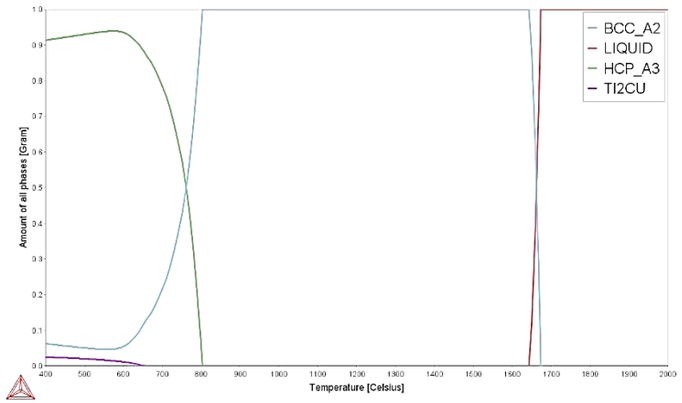
4.12. Ti-4.5Nb-4Ta-1.5Zr-*x*Cu compositions

The results for Ti-4.5Nb-4Ta-1.5Zr-*x*Cu (*x* = 0, 1, 3, 5 and 10 wt%) (Table 4.13) were similar to Ti-6Nb-4Zr-*x*Cu (Table 4.4) and Ti-8Nb-4Zr-*x*Cu (Table 4.5). Ti-4.5Nb-4Ta-1.5Zr-*x*Cu had less BCC_A2 and more HCP_A3 than Ti-10.1Ta-1.7Nb-1.6Zr-*x*Cu (Table 4.3) at 400°C. The BCC_A2 and HCP_A3 fractions were higher in Ti-4.5Nb-4Ta-1.5Zr-*x*Cu compared to Ti-6Al-4V-*x*Cu (Table 4.2). Table 4.13 gives the phase information for Ti-4.5Nb-4Ta-1.5Zr-*x*Cu (*x* = 0, 1, 3, 5 and 10 wt%), and Figures 4.56 - 4.60 show the phase proportion diagrams.

Table 4.13: *Phase information for the Ti-4.5Nb-4Ta-1.5Zr-xCu compositions.*

Composition (wt%)	**Phase formation temperature (°C)**	**Phase proportions**			
		Liquid	BCC_A2	HCP_A3	Ti_2Cu
Ti-4.5Nb-4Ta-1.5Zr	1684	1	0	---	---
	1677	0	1	---	---
	817	---	1	0	---
	560	---	0.05	0.95	---
	400	---	0.06	0.94	---
Ti-4.5Nb-4Ta-1.5Zr-1Cu	1673	1	0	---	---
	1643	0	1	---	---
	803	---	1	0	---
	654	---	0.12	0.88	0
	400	---	0.06	0.92	0.02
Ti-4.5Nb-4Ta-1.5Zr-3Cu	1651	1	0	---	---
	1572	0	1	---	---
	775	---	1	0	---
	725	---	0.54	0.46	0
	400	---	0.06	0.86	0.08
Ti-4.5Nb-4Ta-1.5Zr-5Cu	1629	1	0	---	---
	1495	0	1	---	---
	747	---	1	0	---
	744	---	0.98	0.02	0
	400	---	0.06	0.81	0.13
Ti-4.5Nb-4Ta-1.5Zr-10Cu	1572	1	0	---	---
	1277	0	1	---	---
	886	---	1	---	0
	739	---	0.85	0	0.15
	400	---	0.07	0.68	0.25





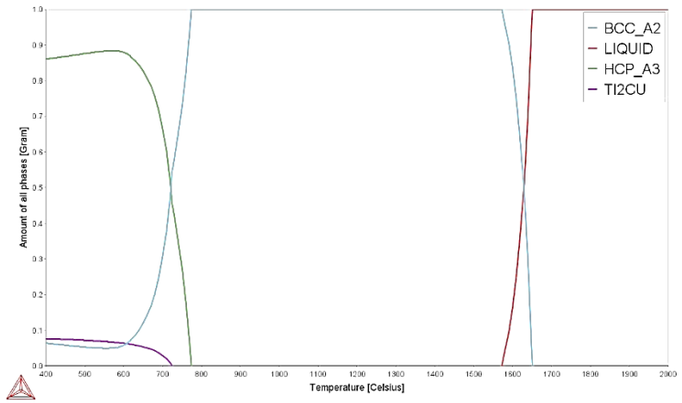


Figure 4.56: *Phase proportion diagram for Ti-4.5Nb-4Ta-1.5Zr.* ***Figure 4.57:*** *Phase proportion diagram for Ti-4.5Nb-4Ta-1.5Zr-1Cu.* ***Figure 4.58:*** *Phase proportion diagram for Ti-4.5Nb-4Ta-1.5Zr-3Cu.*

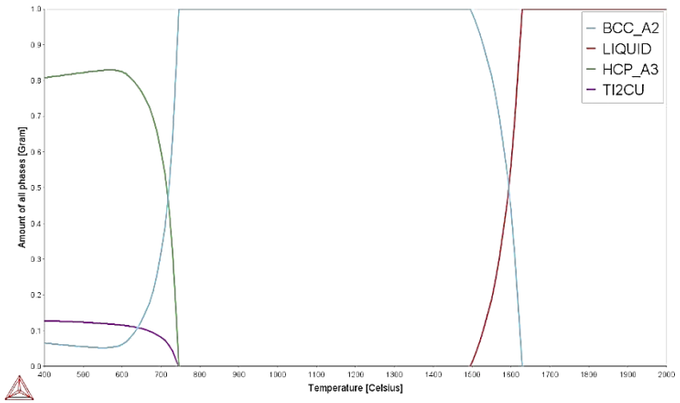


Figure 4.59: *Phase proportion diagram for Ti-4.5Nb-4Ta-1.5Zr-5Cu.*

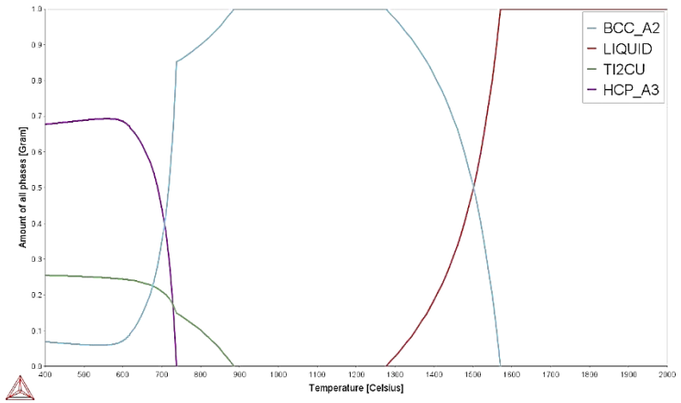


Figure 4.60: *Phase proportion diagram for Ti-4.5Nb-4Ta-1.5Zr-10Cu.*

4.13. Ti-6Zr-4Nb-*x*Cu compositions

Figures 4.61 - 4.65 show the phase proportion diagrams, and Table 4.14 gives the phase information for the Ti-6Zr-4Nb-*x*Cu (*x* = 0, 1, 3, 5 and 10 wt%). Ti-6Zr-4Nb-*x*Cu and Ti-6Al-4V-*x*Cu (Table 4.2) had same BCC_A2 proportions at 400°C, but lower HCP_A3 amounts in Ti-6Al-4V-*x*Cu due to the Ti_3Al phase being formed. Ti-6Zr-4Nb-*x*Cu (Table 4.14) had less BCC_A2, and more HCP_A3 than Ti-6Nb-4Zr-*x*Cu (Table 4.4), Ti-8Nb-4Zr-*x*Cu (Table 4.5) and Ti-10.1Ta-1.7Nb-1.6Zr-*x*Cu (Table 4.3) at 400°C.

Table 4.14: *Phase information for Ti-6Zr-4Nb-xCu compositions.*

Composition (wt%)	**Phase formation temperature (°C)**	**Phase proportions**			
		Liquid	BCC_A2	HCP_A3	Ti_2Cu
Ti-6Zr-4Nb	1657	1	0	---	---
	1653	0	1	---	---
	818	---	1	0	---
	550	---	0.02	0.98	---
	400	---	0.03	0.97	---
Ti-6Zr-4Nb-1Cu	1646	1	0	---	---
	1616	0	1	---	---
	804	---	1	0	---
	676	---	0.09	0.91	0
	400	---	0.03	0.94	0.03
Ti-6Zr-4Nb-3Cu	1623	1	0	---	---
	1535	0	1	---	---
	776	---	1	0	---
	737	---	0.57	0.43	0
	400	---	0.03	0.89	0.08
Ti-6Zr-4Nb-5Cu	1601	1	0	---	---
	1446	0	1	---	---
	758	---	1	---	0
	751	---	0.99	0	0.01
	400	---	0.03	0.83	0.14
Ti-6Zr-4Nb-10Cu	1541	1	0	---	---
	1181	0	1	---	---
	906	---	1	---	0
	748	---	0.84	0	0.16
	400	---	0.03	0.7	0.27

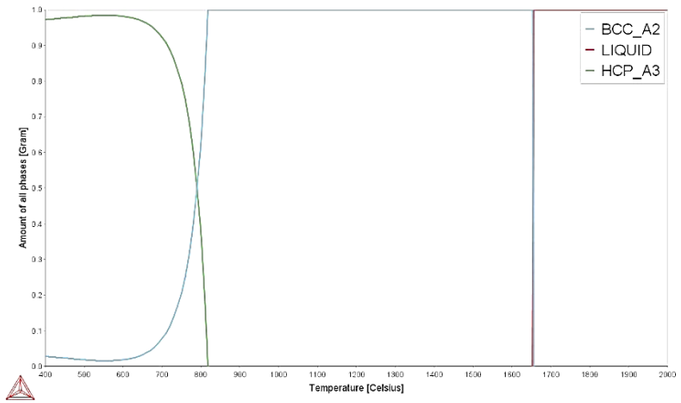


Figure 4.61: *Phase proportion diagram for Ti-6Zr-4Nb.*

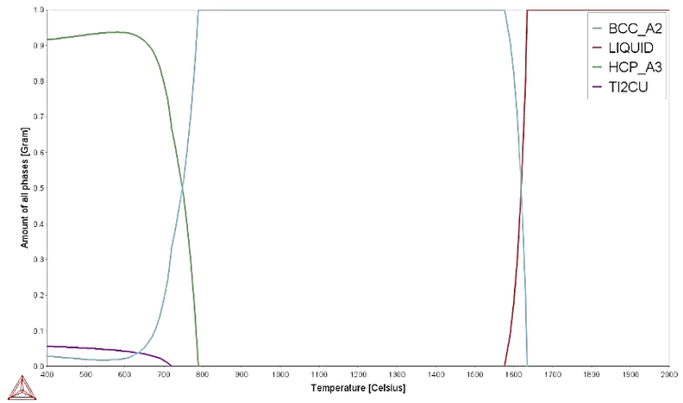


Figure 4.62: *Phase proportion diagram for Ti-6Zr-4Nb-1Cu.*

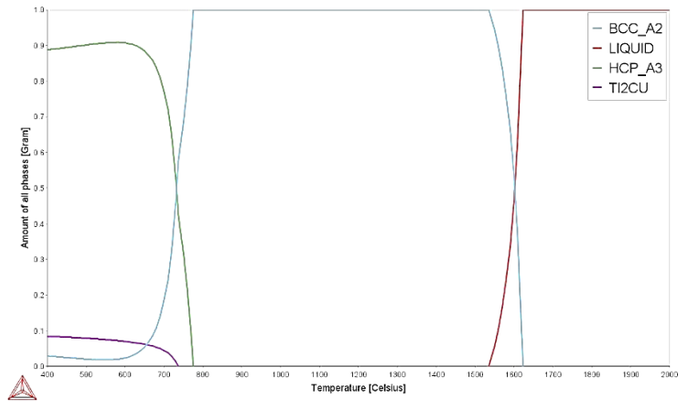


Figure 4.63: *Phase proportion diagram for Ti-6Zr-4Nb-3Cu.*

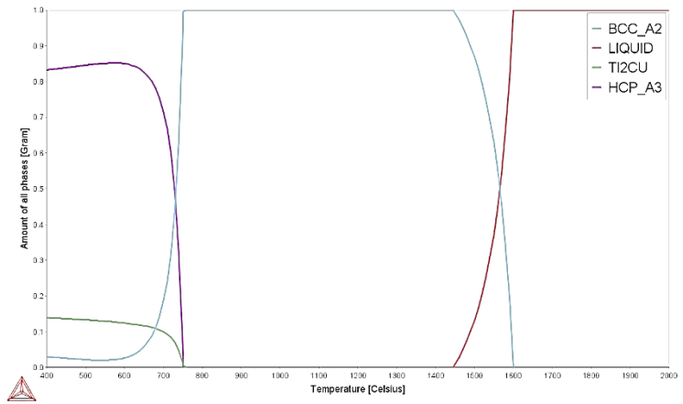


Figure 4.64: *Phase proportion diagram for Ti-6Zr-4Nb-5Cu.*

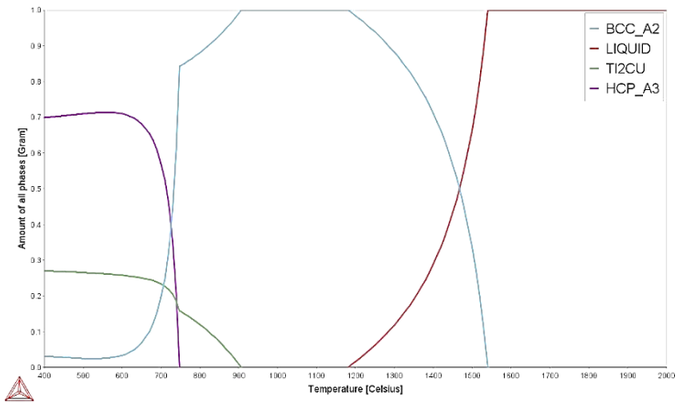


Figure 4.65: *Phase proportion diagram for Ti-6Zr-4Nb-10Cu.*

4.14. Ti-6Zr-2Mo-*x*Cu compositions

The BCC_A2 proportions at 400°C for Ti-6Zr-2Mo-*x*Cu (*x* = 0, 1, 3, 5 and 10 wt%) (Table 4.15) were very similar to Ti-6Al-4V-*x*Cu (Table 4.2). Table 4.15 shows less BCC_A2 and more HCP_A3 compared to Ti-6Nb-4Zr-*x*Cu (Table 4.4), Ti-8Nb-4Zr-*x*Cu (Table 4.5) and Ti-10.1Ta-1.7Nb-1.6Zr-*x*Cu (Table 4.3) at 400°C. Table 4.15 gives the phase information for Ti-6Zr-2Mo-*x*Cu (*x* = 0, 1, 3, 5 and 10 wt%), and Figures 4.66 - 4.70 show the phase proportion diagrams.

Table 4.15: *Phase information for Ti-6Zr-2Mo-xCu compositions.*

Composition (wt%)	**Phase formation temperature (°C)**	**Phase proportions**			
		Liquid	BCC_A2	HCP_A3	Ti_2Cu
Ti-6Zr-2Mo	1661	1	0	---	---
	1655	0	1	---	---
	832	---	1	0	---
	530	---	0.04	0.96	---
	400	---	0.03	0.97	---
Ti-6Zr-2Mo-1Cu	1649	1	0	---	---
	1617	0	1	---	---
	817	---	1	0	---
	688	---	0.12	0.88	0
	400	---	0.03	0.94	0.03
Ti-6Zr-2Mo-3Cu	1627	1	0	---	---
	1532	0	1	---	---
	788	---	1	0	---
	750	---	0.58	0.42	0
	400	---	0.03	0.89	0.08
Ti-6Zr-2Mo-5Cu	1604	1	0	---	---
	1435	0	1	---	---
	770	---	1	---	0
	762	---	0.99	0	0.01
	400	---	0.03	0.83	0.14
Ti-6Zr-2Mo-10Cu	1547	1	0	---	---
	1146	0	1	---	---
	919	---	1	---	0
	761	---	0.84	0	0.16
	400	---	0.03	0.7	0.27

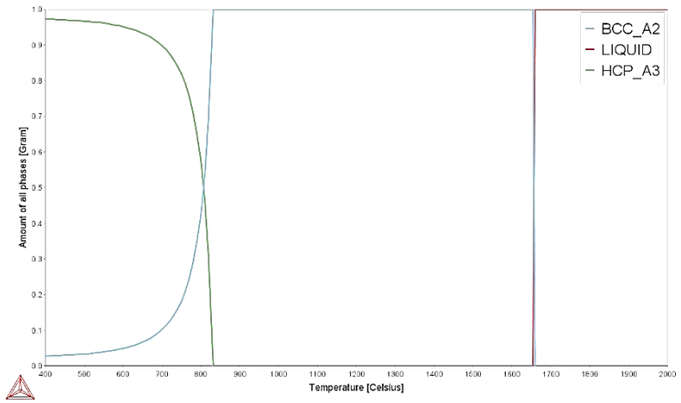


Figure 4.66: *Phase proportion diagram for Ti-6Zr-2Mo.*

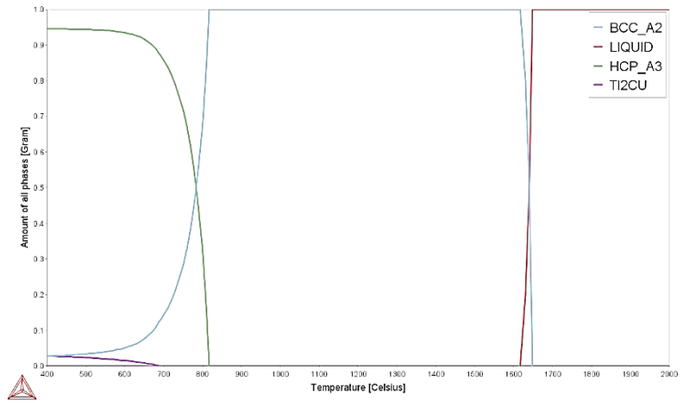


Figure 4.67: *Phase proportion diagram for Ti-6Zr-2Mo-1Cu.*

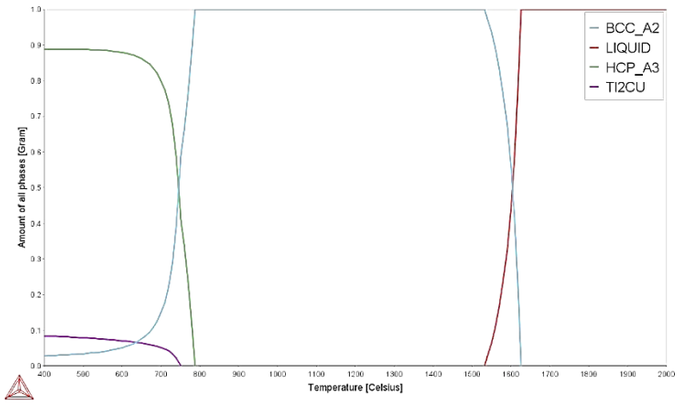


Figure 4.68: *Phase proportion diagram for Ti-6Zr-2Mo-3Cu.*

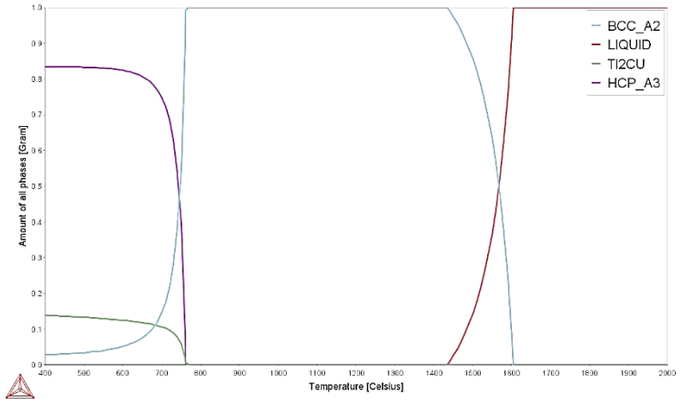


Figure 4.69: *Phase proportion diagram for Ti-6Zr-2Mo-5Cu.*

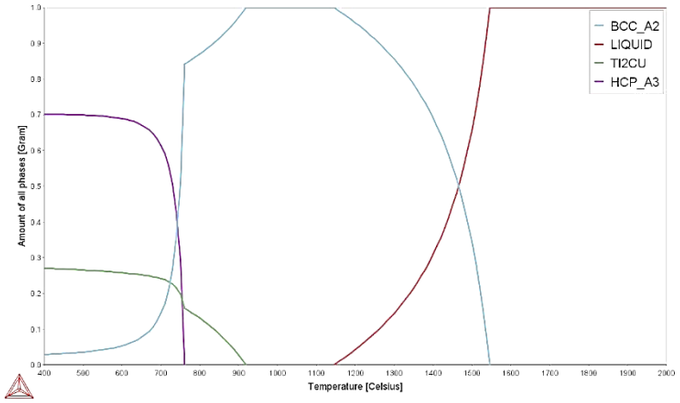


Figure 4.70: *Phase proportion diagram for Ti-6Zr-2Mo-10Cu.*

4.15. Ti-10Ta-8Zr-*x*Cu compositions

Ti-10Ta-8Zr-*x*Cu (Table 4.16) and Ti-8Nb-4Zr-*x*Cu (*x* = 1, 3, 5 and 10 wt%) (Table 4.5) had the same BCC_A2 proportions at 400°C. Lower BCC_A2 proportions and higher HCP_A3 proportions were found in Ti-10Ta-8Zr-*x*Cu (Table 4.16) at 400°C compared to Ti-10.1Ta-1.7Nb-1.6Zr-*x*Cu (Table 4.3). The phase proportion diagrams for Ti-10Ta-8Zr-*x*Cu (*x* = 0, 1, 3, 5 and 10 wt%) are shown in Figures 4.71-4.75, and Table 4.16 gives the phase information.

Table 4.16: *Phase information for Ti-10Ta-8Zr-xCu compositions.*

Composition (wt%)	**Phase formation temperature (°C)**	**Phase proportions**			
		Liquid	BCC_A2	HCP_A3	Ti_2Cu
Ti-10Ta-8Zr	1687	1	0	---	---
	1667	0	1	---	---
	802	---	1	0	---
	590	---	0.02	0.98	---
	400	---	0.06	0.94	---
Ti-10Ta-8Zr-1Cu	1675	1	0	---	---
	1625	0	1	---	---
	788	---	1	0	---
	664	---	0.13	0.87	0
	400	---	0.06	0.91	0.03
Ti-10Ta-8Zr-3Cu	1651	1	0	---	---
	1534	0	1	---	---
	761	---	1	0	---
	725	---	0.63	0.37	0
	400	---	0.06	0.85	0.09
Ti-10Ta-8Zr-5Cu	1627	1	0	---	---
	1432	0	1	---	---
	759	---	1	---	0
	739	---	0.99	0	0.01
	400	---	0.06	0.8	0.14
Ti-10Ta-8Zr-10Cu	1563	1	0	---	---
	1135	0	1	---	---
	909	---	1	---	0
	735	---	0.83	0	0.17
	400	---	0.06	0.66	0.28

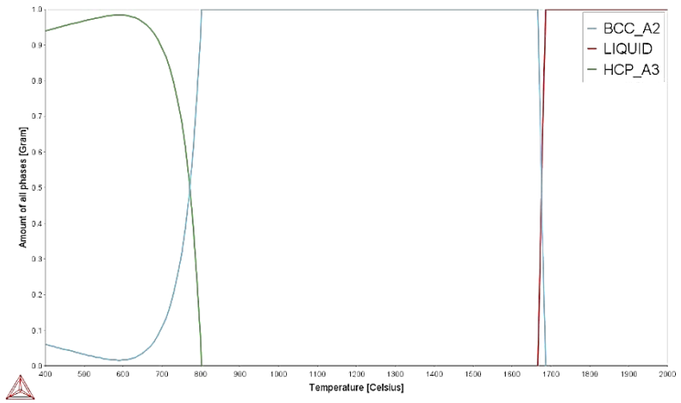


Figure 4.71: *Phase proportion diagram for Ti-10Ta-8Zr.*

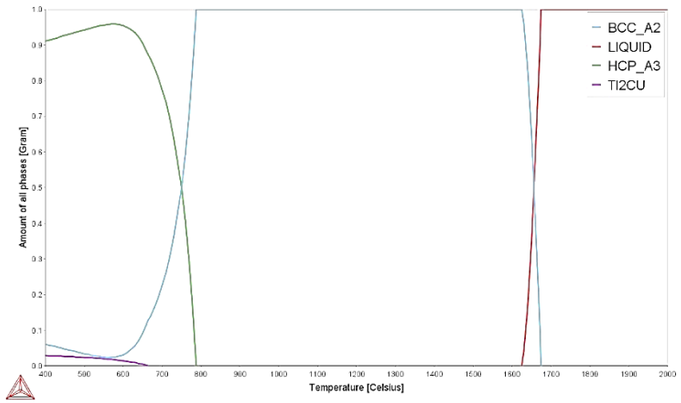


Figure 4.72: *Phase proportion diagram for Ti-10Ta-8Zr-1Cu.*

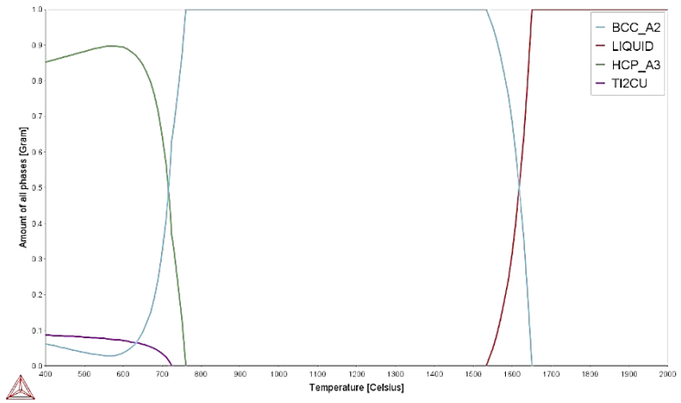


Figure 4.73: *Phase proportion diagram for Ti-10Ta-8Zr-3Cu.*

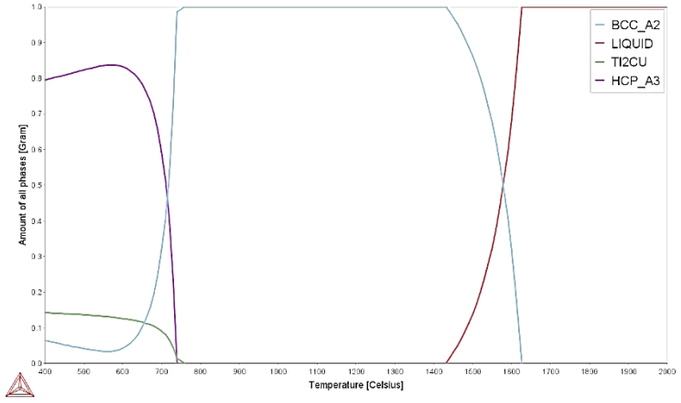


Figure 4.74: *Phase proportion diagram for Ti-10Ta-8Zr-5Cu.*

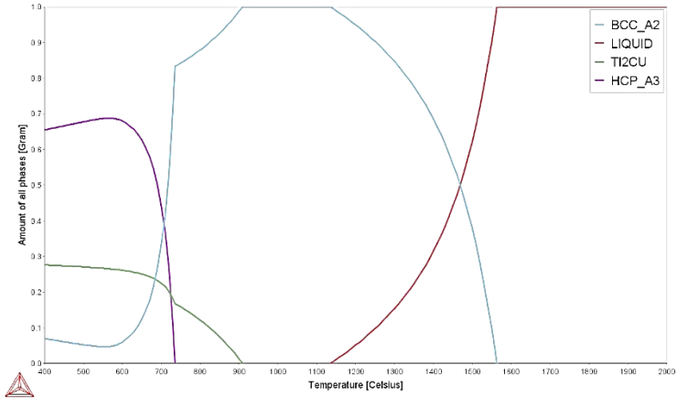


Figure 4.75: *Phase proportion diagram for Ti-10Ta-8Zr-10Cu.*

4.16. Discussion of Thermo-Calc results

Titanium compositions were calculated to mimic the α+β phase proportions found in Ti-6Al-4V and Ti-10.1Ta-1.7Nb-1.6Zr (Stenlund et al., 2015) at 400°C, and to have some copper for its antibacterial properties (Ren et al., 2014). A two-phase (α+β) Ti alloy has high Young's modulus, high strength and good formability, which are some of the desired mechanical properties for biomedical applications (Ren et al., 2014; Zhang et al., 2016b). New Ti compositions were identified (Tables 4.4 - 4.16), and zirconium, tantalum, niobium and molybdenum were used as non-toxic alloying elements (Leyens & Peters, 2003) to replace the toxic Al and V (Leyens & Peters, 2003; Stenlund et al., 2015). Different copper compositions (Cu = 1, 3, 5 and 10 wt%) were added to form the Ti_2Cu phase, which gives good mechanical and antibacterial properties (Ren et al., 2014; Zhang et al., 2016b).

The following compositions had the α+β phases at 400°C: Ti-10.1Ta-1.7Nb-1.6Zr (Figure 4.6), Ti-6Nb-4Zr (Figure 4.11), Ti-8Nb-4Zr (Figure 4.16), Ti-6Nb-2Zr-1.7Ta (Figure 4.21), Ti-6Zr-4Ta-4Nb (Figure 4.26), Ti-4Ta-1.8Zr-1.5Mo (Figure 4.31), Ti-6Ta-2Zr-1.5Mo (Figure 4.36), Ti-8Ta-1.5Mo-1.5Zr (Figure 4.41), Ti-8Zr-4Ta-2Mo (Figure 4.46), Ti-3.5Ta-3Nb-3Zr (Figure 4.51), Ti-4.5Nb-4Ta-1.5Zr (Figure 4.56), Ti-6Zr-4Nb (Figure 4.61), Ti-6Zr-2Mo (Figure 4.66) and Ti-10Ta-8Zr (Figure 4.71). Thermo-Calc predicted a Ti_3Al phase in Ti-6Al-4V (Figure 4.1) below 485°C. The Ti_3Al phase was not found by Stenlund et al. (2015), who used the COST507 database, whereas the calculations in this work used a different database, TTTI3. The formation temperatures and proportions of Ti_2Cu increased with increased Cu additions in all compositions calculated (Tables 4.2 - 4.16). Adding Cu (1, 3, 5 and 10 wt%) decreased the HCP_A3 proportions at 400°C, whereas BCC_A2 was less affected (Tables 4.2 - 4.16). The BCC_A2 and HCP_A3 formation temperatures decreased when the Cu content was increased, in all calculated Ti compositions.

Kikuchi et al. (2003) and Zhang et al. (2016b) reported that as-cast Ti-5Cu (wt%) had a good balance between strength and ductility for biomedical applications. The as-cast Ti-6Al-4V-5Cu (wt%) alloy by Ren et al. (2014) and Ma et al. (2015) gave good antibacterial properties. Based on the findings of Kikuchi et al. (2003), Ren et al. (2014), Ma et al. (2015) and Zhang et al. (2016b) and the Thermo-Calc results (Sections 4.1-4.15) which showed Ti_2Cu could be produced, 5 wt% Cu addition was considered for this project because it gave good antimicrobial results. Table 4.17 gives the liquidus (T_L) and solidus (T_S), and Ti_2Cu formation temperatures of the calculated Ti compositions. Adding 5 wt% Cu decreased the liquidus and solidus temperatures, Table 4.17. Figure 4.76 shows the Ti_2Cu formation temperatures of the different titanium compositions for 5 wt% Cu additions. Figure 4.77 shows the effect of β stabilisers (Cu, Ta, Mo, V and Nb) on the beta (β) phase proportions at 400°C (Figure 4.77a) and Ti_2Cu formation temperatures (Figure 4.77b). On a broad band, as the amount of β stabiliser increased, the amount of β also increased at 400°C (Figure 4.77a). It is on a very broad band, because some β stabilisers were more effective. Figure 4.77b shows that on average, as the proportion of β stabiliser increased, the formation temperature of Ti_2Cu decreased. This agreed with Leyens & Peters (2003) and Akahori et al. (2005) for more stable β.

Table 4.17: *Liquidus (T_L) and solidus (T_S), and Ti_2Cu formation temperatures of the different titanium compositions.*

Composition (wt%)	T_L (ºC)	T_S (ºC)	Ti_2Cu form. (ºC)
Ti-6Zr-4Nb	1657	1653	---
Ti-6Zr-4Nb-5Cu	1601	1446	758
Ti-6Zr-2Mo	1661	1655	---
Ti-6Zr-2Mo-5Cu	1604	1435	770
Ti-6Zr-4Ta-4Nb	1673	1663	---
Ti-6Zr-4Ta-4Nb-5Cu	1616	1450	760
Ti-8Zr-4Ta-2Mo	1671	1658	---
Ti-8Zr-4Ta-2Mo-5Cu	1614	1415	781
Ti-4.5Nb-4Ta-1.5Zr	1684	1677	---
Ti-4.5Nb-4Ta-1.5Zr-5Cu	1629	1495	744
Ti-6Nb-4Zr	1665	1661	---
Ti-6Nb-4Zr-5Cu	1609	1467	756
Ti-8Nb-4Zr	1669	1664	---
Ti-8Nb-4Zr-5Cu	1613	1468	762
Ti-6Nb-2Zr-1.7Ta	1676	1671	---
Ti-6Nb-2Zr-1.7Ta-5Cu	1621	1488	747
Ti-3.5Ta-3Nb-3Zr	1677	1669	---
Ti-3.5Ta-3Nb-3Zr-5Cu	1620	1479	751
Ti-4Ta-1.8Zr-1.5Mo	1683	1675	---
Ti-4Ta-1.8Zr-1.5Mo-5Cu	1629	1485	759
Ti-6Ta-2Zr-1.5Mo	1691	1679	---
Ti-6Ta-2Zr-1.5Mo-5Cu	1635	1485	754
Ti-8Ta-1.5Mo-1.5Zr	1699	1686	---
Ti-8Ta-1.5Mo-1.5Zr-5Cu	1644	1493	749
Ti-10Ta-8Zr	1687	1667	---
Ti-10Ta-8Zr-5Cu	1627	1432	759
Ti-10.1Ta-1.7Nb-1.6Zr	1704	1688	---
Ti-10.1Ta-1.7Nb-1.6Zr-5Cu	1647	1450	741
Ti-6Al-4V	1703	1698	---
Ti-6Al-4V-5Cu	1652	1548	760

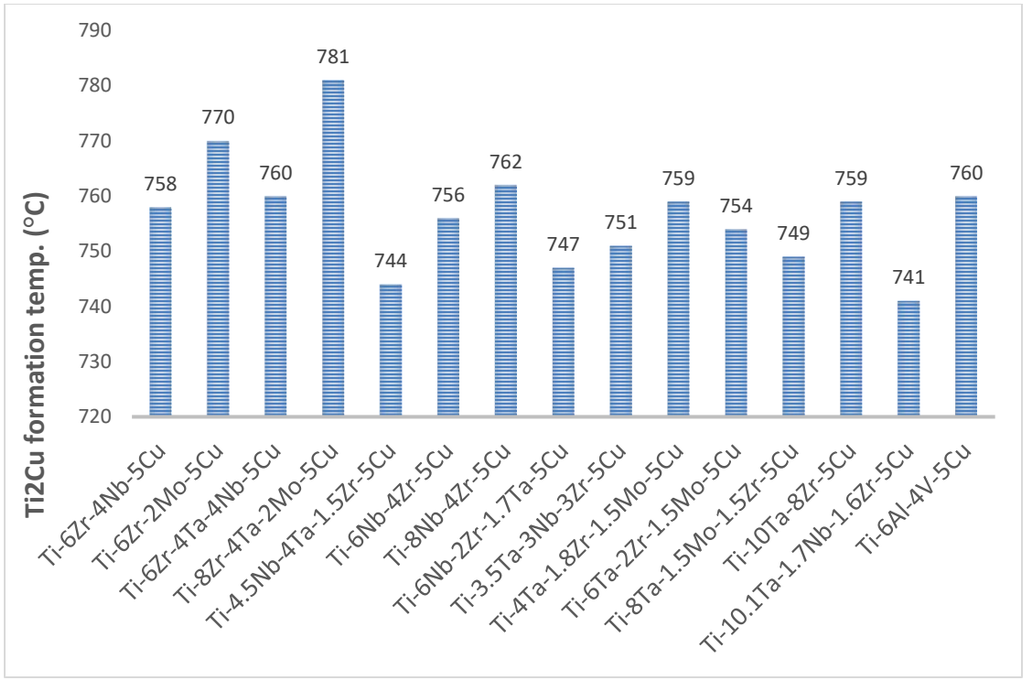


Figure 4.76: *Ti_2Cu formation temperatures of the different titanium compositions.*

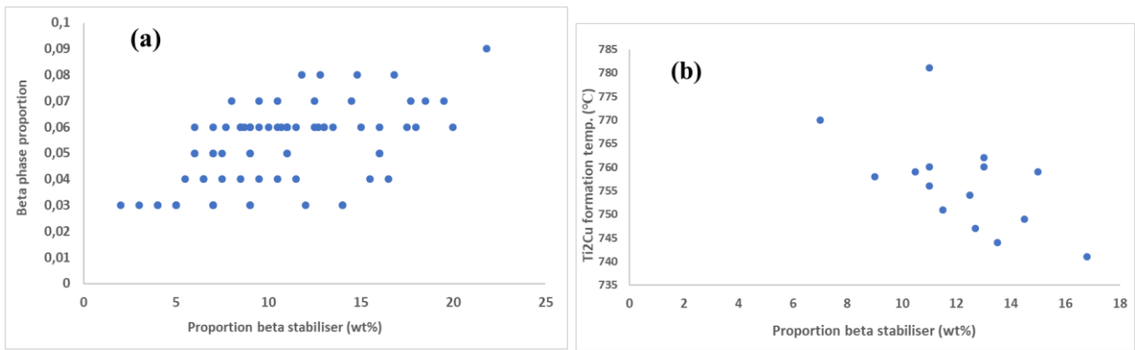


Figure 4.77: *Effect of beta-stabilisers on: (a) beta phase proportions at 400°C and (b) Ti_2Cu formation temperatures.*

4.17. Cost analysis

The costs and availability of alloying elements to make the alloys were considered. Table 4.18 gives the materials costs for the calculated Ti compositions, and Appendix A gives the actual calculations. This does not consider the processing costs, which were assumed to be the same for the different alloys, and so could be ignored in comparing different potential alloys. The Ti-6Al-4V alloy was considered expensive (Table 4.18) due to expensive Al and V (Table 3.2), and CP-Ti was the cheapest. The Ti-6Zr-2Mo-*x*Cu (*x* = 0 and 5 wt%) were the cheapest amongst the newly identified Ti compositions, followed by Ti-6Nb-4Zr-*x*Cu and Ti-8Nb-4Zr-*x*Cu (*x* = 0 and 5 wt%) (Table 4.18). The cost of Ti-10.1Ta-1.7Nb-1.6Zr (TTNZ) was neither cheap nor expensive (Table 4.18).

Table 4.18: *Costs for the different Ti compositions.*

Composition (wt%)	Cost (R)/10 g	Composition (wt%)	Cost (R)/10 g
Ti-6Zr-2Mo	303.24	Ti-6Ta-2Zr-1.5Mo	327.33
Ti-6Zr-2Mo-5Cu	446.77	Ti-6Ta-2Zr-1.5Mo-5Cu	470.86
Ti-6Nb-4Zr	306.36	Ti-8Zr-4Ta-2Mo	329.63
Ti-6Nb-4Zr-5Cu	449.89	Ti-8Zr-4Ta-2Mo-5Cu	473.16
Ti-8Nb-4Zr	307.83	Ti-6Zr-4Ta-4Nb	331.26
Ti-8Nb-4Zr-5Cu	451.36	Ti-6Zr-4Ta-4Nb-5Cu	474.79
Ti-6Zr-4Nb	309.54	Ti-8Ta-1.5Mo-1.5Zr	337.03
Ti-6Zr-4Nb-5Cu	453.07	Ti-8Ta-1.5Mo-1.5Zr-5Cu	480.56
Ti-6Nb-2Zr-1.7Ta	310.92	Ti-10Ta-8Zr	365.56
Ti-6Nb-2Zr-1.7Ta-5Cu	454.45	Ti-10Ta-8Zr-5Cu	509.09
Ti-4Ta-1.8Zr-1.5Mo	316.01	Ti-10.1Ta-1.7Nb-1.6Zr	352.43
Ti-4Ta-1.8Zr-1.5Mo-5Cu	459.54	Ti-10.1Ta-1.7Nb-1.6Zr-5Cu	481.33
Ti-3.5Ta-3Nb-3Zr	320.82	Ti-6Al-4V	453.81
Ti-3.5Ta-3Nb-3Zr-5Cu	464.35	Ti-6Al-4V-5Cu	582.71
Ti-4.5Nb-4Ta-1.5Zr	321.14	CP-Ti	292.60
Ti-4.5Nb-4Ta-1.5Zr-5Cu	464.67	CP-Ti-5Cu	421.50

Based on the costs (Table 4.18) and similar α+β phase proportions (Tables 4.4 - 4.16) to Ti-6Al-4V (Table 4.2) and Ti-10.1Ta-1.7Nb-1.6Zr (TTNZ) (Table 4.3), the Ti-6Nb-4Zr-*x*Cu and Ti-8Nb-4Zr-*x*Cu (*x* = 0 and 5 wt%) were the proposed Ti compositions for this project (Table 3.4), and these were manufactured for subsequent testing.

Chapter 5: Experimental Results

This chapter presents the experimental results to address the aims/objectives of the project. The summary of the experimental findings on the study of the microstructures, hardness and the thermo-mechanical testing of Ti alloys is given.

5.1. Optical and SEM microstructural analysis

The microstructures of as-cast Ti-6Nb-4Zr-*x*Cu and Ti-8Nb-4Zr-*x*Cu (*x* = 0 and 5 wt%) were studied, and compared with the as-received Ti-6Al-4V and Ti-10.1Ta-1.7Nb-1.6Zr (Stenlund et al., 2015) alloys. The microstructures were classified as lamellar, equiaxed and/or bimodal, depending on the morphology of the αTi and βTi phases (Lütjering, 1998; Leyens & Peters, 2003). The XRD analysis were done to identify the existing phases, and EDX for composition analysis.

5.1.1. As-received Ti-6Al-4V alloy

The optical micrographs and SEM-BSE images of the as-received Ti-6Al-4V alloy are shown in Figure 5.1, and Table 5.1 gives the EDX results. The microstructure consisted of αTi lamellae within the prior βTi grains (Figure 5.1a), which were also shown in the SEM-BSE image (Figure 5.1b). Figure 5.2 shows the XRD patterns of the as-received Ti-6Al-4V alloy. The XRD analysis showed broad αTi and βTi peaks, which were mostly matched and shifted from pure Ti values because of the Al and V additions (Figure 5.2). The Ti_3Al phase predicted by Thermo-Calc (Table 4.2) was identified by XRD but was not identified in the microstructures either optically or using SEM. However, TEM could be a possible method, although it might have also been missed because of its small proportion.

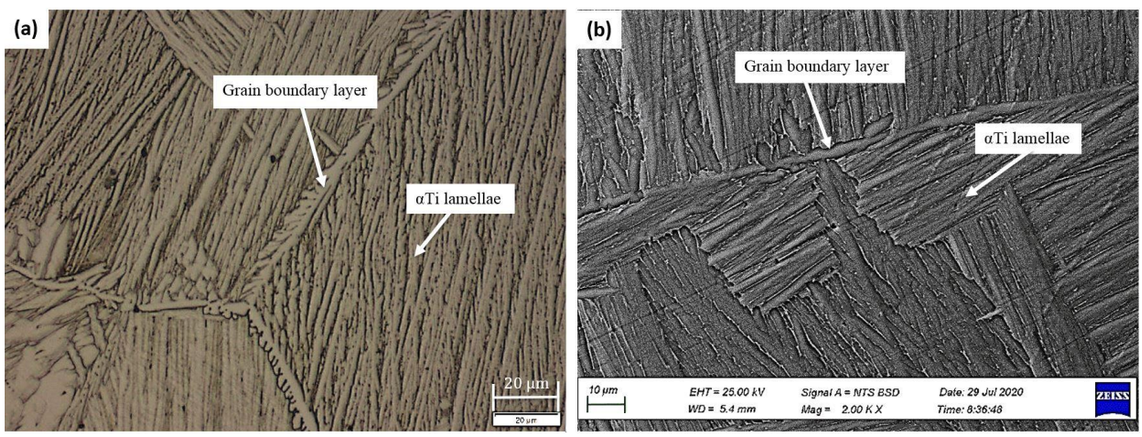


Figure 5.1: *As-received Ti-6Al-4V (wt%): (a) Optical micrograph and (b) SEM-BSE image.*

Table 5.1: *EDX analyses of the as-received Ti-6Al-4V (wt%) alloy.*

Alloy	Phase description	Ti	Al	V	Phase
As-received Ti-6Al-4V	Overall	89.9 ± 0.5	6.1 ± 0.5	4.0 ± 0.2	---
	Grain boundary layer	89.6 ± 1.1	6.2 ± 0.4	4.2 ± 1.3	αTi
	Lamellae/basketweave	89.8 ± 1.0	6.5 ± 0.4	3.7 ± 1.0	αTi

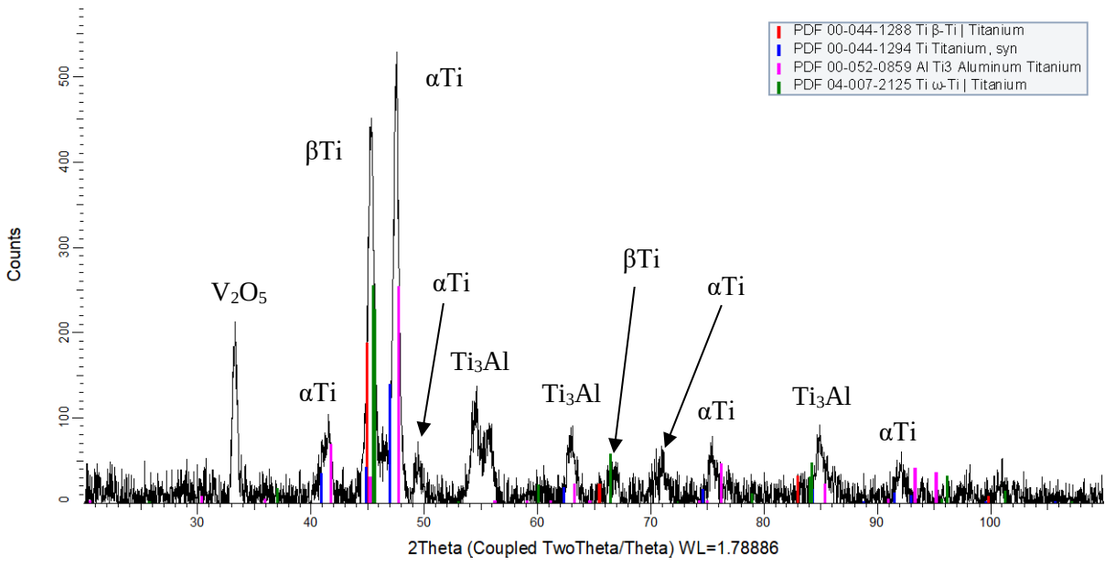


Figure 5.2: *XRD analysis of the wrought Ti-6Al-4V (wt%) alloy (Bodunrin, 2018), showing αTi and βTi peaks shifted due to alloying.*

5.1.2. As-received Ti-10.1Ta-1.7Nb-1.6Zr (TTNZ) alloy

Figure 5.3 shows the optical micrograph and SEM-BSE images of the as-received Ti-10.1Ta-1.7Nb-1.6Zr alloy, which was in bar form, and the EDX results are given in Table 5.2. The optical micrograph (Figures 5.3a) shows an equiaxed microstructure, which consisted of globular αTi grains within the transformed βTi matrix, and was confirmed by the SEM-BSE image (Figure 5.3b). The EDX analyses (Table 5.2) indicated a higher Ta content in the βTi matrix compared to the αTi phase. The overall compositions were outside the range of the αTi and βTi phase, suggesting inhomogeneity in the Ti-10.1Ta-1.7Nb-1.6Zr alloy (Table 5.2). The XRD analysis showed mainly shifted αTi peaks due to the alloying (Figure 5.4).

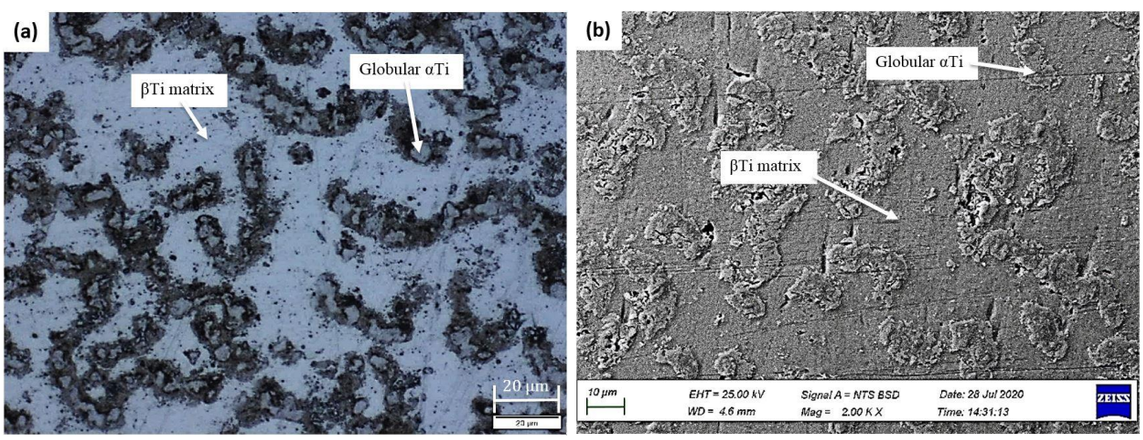


Figure 5.3: *As-received Ti-10.1Ta-1.7Nb-1.6Zr (wt%): (a) Optical micrograph and (b) SEM-BSE image.*

Table 5.2: *EDX analyses of the as-received Ti-10.1Ta-1.7Nb-1.6Zr (wt%) (TTNZ) alloy.*

Alloy	Phase description	Ti	Ta	Nb	Zr	Phase
As-received TTNZ	Overall	87.4 ± 1.5	10.6 ± 1.5	0.6 ± 0.4	1.4 ± 1.1	---
	Matrix	86.9 ± 1.1	10.8 ± 0.9	0.2 ± 0.4	2.2. ± 0.4	βTi
	Globules	87.3 ± 0.7	10.2 ± 1.1	0.3 ± 0.5	2.2. ± 0.6	αTi

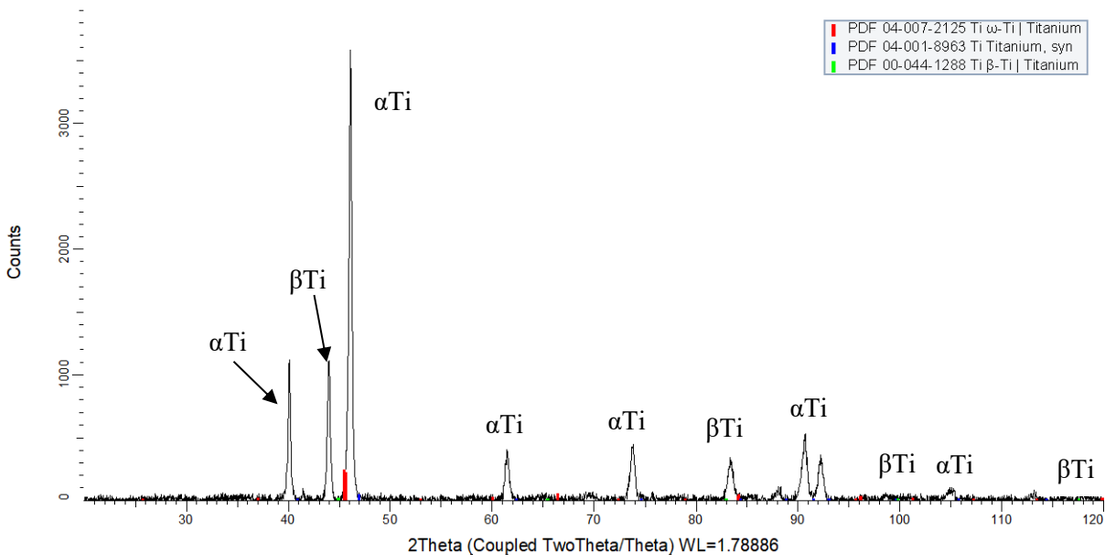


Figure 5.4: *XRD analysis of the as-received Ti-10.1Ta-1.7Nb-1.6Zr (wt%) (TTNZ) alloy, showing mainly shifted αTi peaks due to the alloying.*

5.1.3. As-cast Ti-6Nb-4Zr-*x*Cu alloy

The optical micrograph and SEM-BSE images of the as-cast Ti-6Nb-4Zr-*x*Cu (*x* = 0 and 5 wt%) alloys are shown in Figures 5.5 and 5.6. The Ti-6Nb-4Zr alloy comprised fine αTi laths growing in different directions and forming clusters within the βTi matrix (Figure 5.5a). Figure 5.5a showed αTi laths, and also visible in the SEM-BSE image shown in Figure 5.5b. The dark precipitates in the optical micrograph (Figure 5.6a) were thought to be the Ti_2Cu phase, and formed within the grains and grain boundaries of the Ti-6Nb-4Zr-5Cu alloy (Figure 5.6a), but were not as clearly visible in the SEM-BSE image of Ti-6Nb-4Zr-5Cu (Figure 5.6b). Table 5.3 gives the EDX results of the Ti-6Nb-4Zr-*x*Cu (*x* = 0 and 5 wt%) alloys. The EDX analyses for Ti-6Nb-4Zr-5Cu indicated a higher Cu content in the βTi phase compared to the αTi phase (Table 5.3). The EDX results also confirmed the dark phases in Ti-6Nb-4Zr-5Cu (Figure 5.6a) as the Ti_2Cu precipitates, and indicated inhomogeneity in Ti-6Nb-4Zr and Ti-6Nb-4Zr-5Cu due to the overall Zr composition lying outside the range of the αTi and βTi phase (Table 5.3). The XRD results of the Ti-6Nb-4Zr alloy (Figure 5.7) showed mainly shifted αTi (hcp) peaks due to alloying, and some Ti_2Cu for 5 wt% Cu added (Ti-6Nb-4Zr-5Cu) (Figure 5.8).

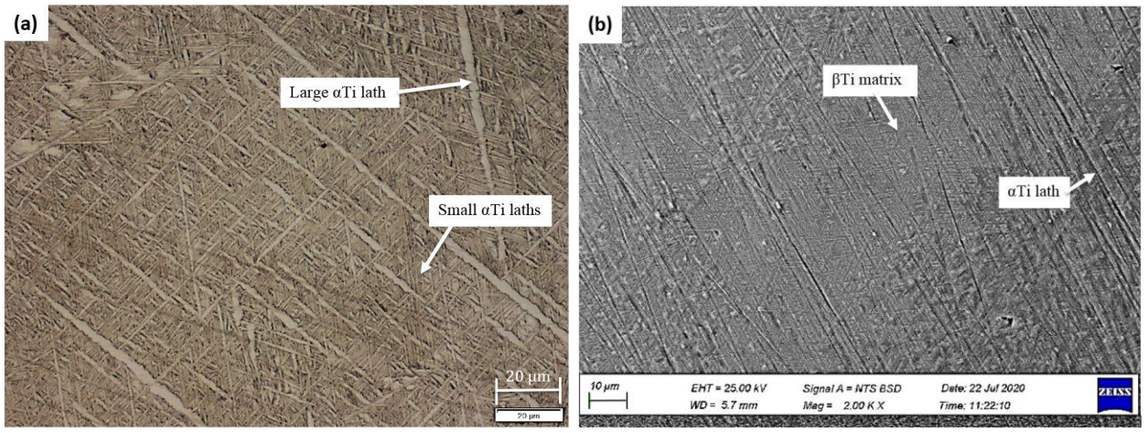


Figure 5.5: *As-cast Ti-6Nb-4Zr (wt%): (a) Optical micrograph and (b) SEM-BSE image.*

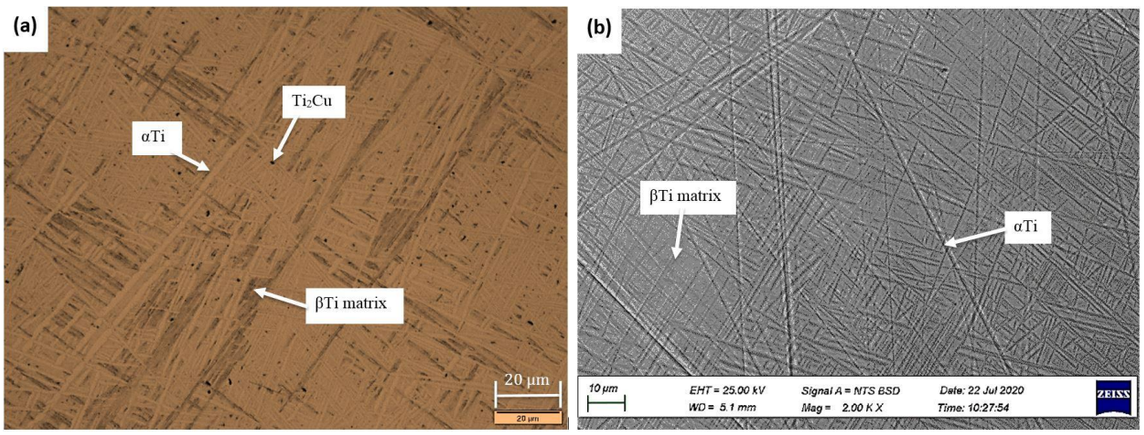


Figure 5.6: *As-cast Ti-6Nb-4Zr-5Cu (wt%): (a) Optical micrograph and (b) SEM-BSE image.*

Table 5.3: *EDX analyses of the as-cast Ti-6Nb-4Zr-xCu (wt%) alloys.*

Alloy	Phase description	Ti	Nb	Zr	Cu	Phase
Ti-6Nb-4Zr	Overall	87.9 ± 2.1	8.1 ± 1.2	4.0 ± 1.2	---	---
	Matrix (light)	88.6 ± 1.2	8.5 ± 0.9	2.9 ± 0.5	---	βTi
	Laths (dark)	88.6 ± 1.0	8.2 ± 0.6	3.2 ± 0.6	---	αTi
Ti-6Nb-4Zr-5Cu	Overall	85.6 ± 1.8	6.3 ± 0.9	3.4 ± 0.4	4.7 ± 0.9	---
	Matrix (light)	84.7 ± 1.9	7.1 ± 1.0	3.0 ± 0.8	5.2 ± 1.3	βTi
	Fine laths (dark)	88.6 ± 1.6	5.7 ± 0.4	3.2 ± 0.7	2.5 ± 1.1	αTi

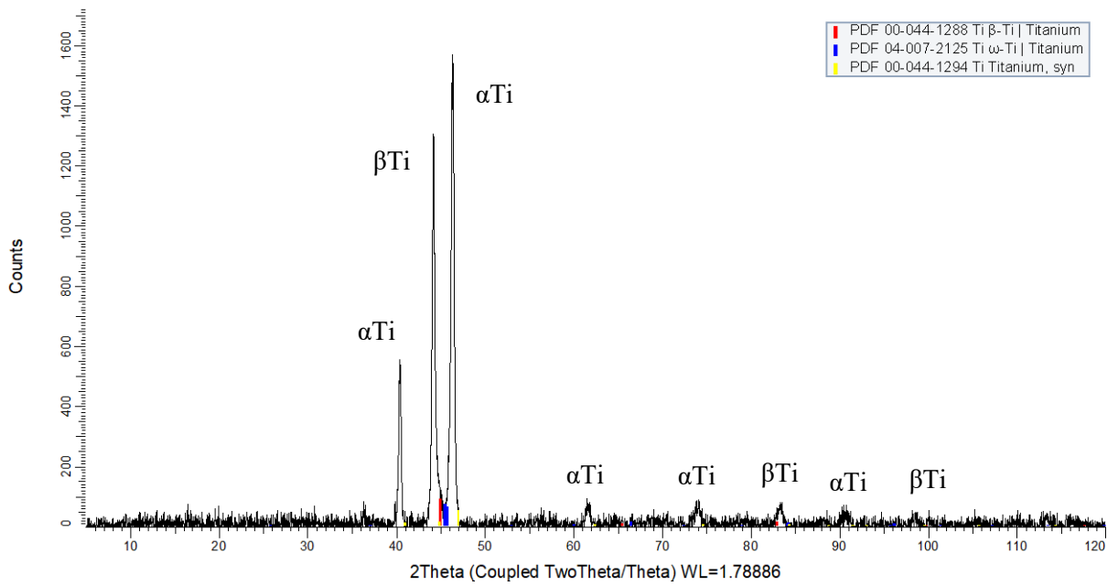


Figure 5.7: *XRD analysis of the as-cast Ti-6Nb-4Zr (wt%) alloy, showing mainly shifted αTi peaks due to alloying.*

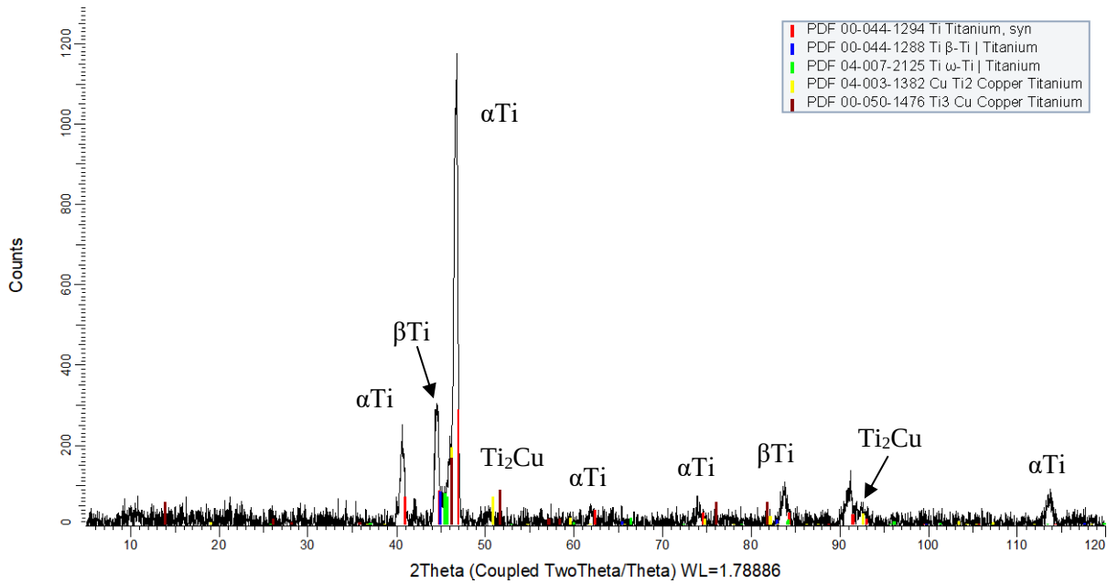


Figure 5.8: *XRD analysis of the as-cast Ti-6Nb-4Zr-5Cu (wt%) alloy, showing mainly shifted αTi peaks, with some Ti_2Cu.*

5.1.4. As-cast Ti-8Nb-4Zr-*x*Cu alloy

Figures 5.9 and 5.10 show the optical micrographs and SEM-BSE image of the as-cast Ti-8Nb-4Zr-*x*Cu (*x* = 0 and 5 wt%) alloys. The bimodal microstructure of Ti-8Nb-4Zr (Figures 5.9a) consisted of clusters of αTi laths within the prior βTi grains. The SEM-BSE image (Figure 5.9b) also showed the αTi laths, and retained βTi. The dark precipitates were thought to be the Ti_2Cu phase (Figure 5.10a), which formed when 5 wt% Cu was added (Ti-8Nb-4Zr-5Cu). Table 5.4 gives the EDX results of the Ti-8Nb-4Zr-*x*Cu (*x* = 0 and 5 wt%) alloys, which indicated a higher Cu content in the βTi phase than the αTi phase for 5 wt% Cu. The EDX analyses had large errors and also suggested inhomogeneity in the Ti-8Nb-4Zr-*x*Cu (*x* = 0 and 5 wt%) alloys because the overall

composition was outside the range of the αTi and βTi phase (Table 5.4). The XRD patterns are shown in Figures 5.11 and 5.12. The XRD patterns showed the presence of the αTi (hcp) and small peaks for βTi (bcc) in the Ti-8Nb-4Zr alloy (Figure 5.11), and the Ti_2Cu phase in the Ti-8Nb-4Zr-5Cu alloy (Figure 5.12).

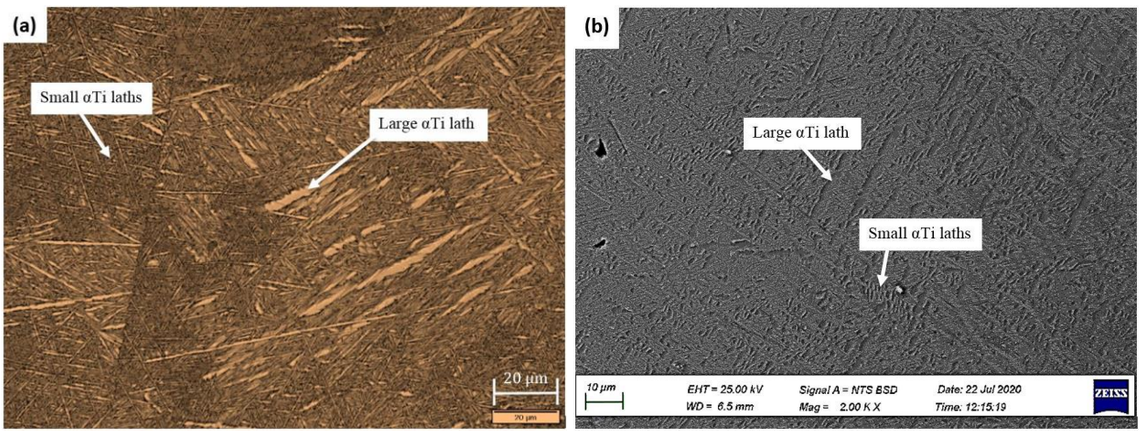


Figure 5.9: *As-cast Ti-8Nb-4Zr (wt%): (a) Optical micrograph and (b) SEM-BSE image.*

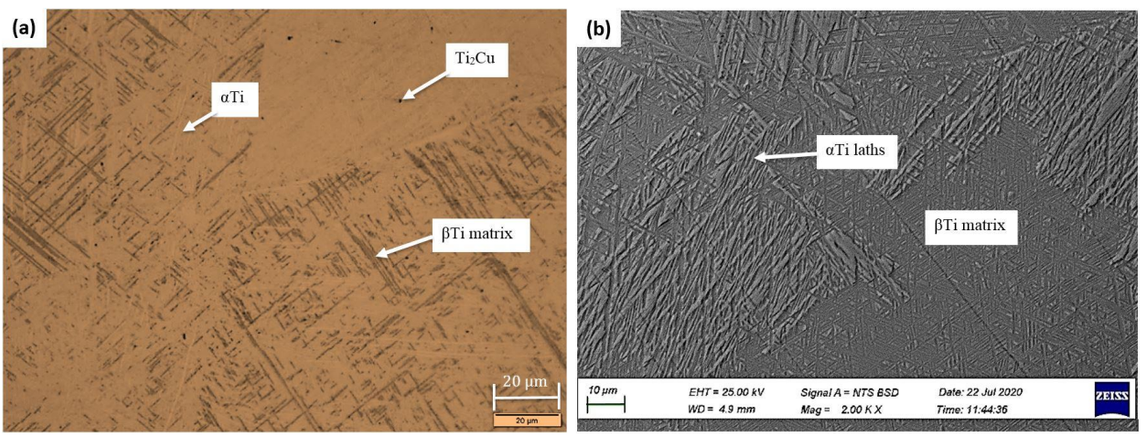


Figure 5.10: *As-cast Ti-8Nb-4Zr-5Cu (wt%): (α) Optical micrograph and (b) SEM-BSE image.*

Table 5.4: *EDX analyses of the as-cast Ti-8Nb-4Zr-xCu (wt%) alloys.*

Alloy	Phase description	Ti	Nb	Zr	Cu	Phase
Ti-8Nb-4Zr	Overall	87.9 ± 1.1	8.2 ± 0.5	4.0 ± 0.2	---	---
	Large laths	88.5 ± 1.3	8.5 ± 0.8	3.0 ± 0.6	---	αTi
	Small laths	89.0 ± 1.5	8.1 ± 0.9	2.9 ± 0.6	---	αTi
Ti-8Nb-4Zr-5Cu	Overall	82.6 ± 2.9	7.5 ± 1.9	4.7 ± 1.2	5.3 ± 2.1	---
	Matrix	83.4 ± 3.1	8.3 ± 2.2	2.5 ± 1.8	5.8 ± 2.5	βTi
	Dark	85.2 ± 2.9	8.9 ± 1.8	1.6 ± 1.6	4.3 ± 2.5	αTi

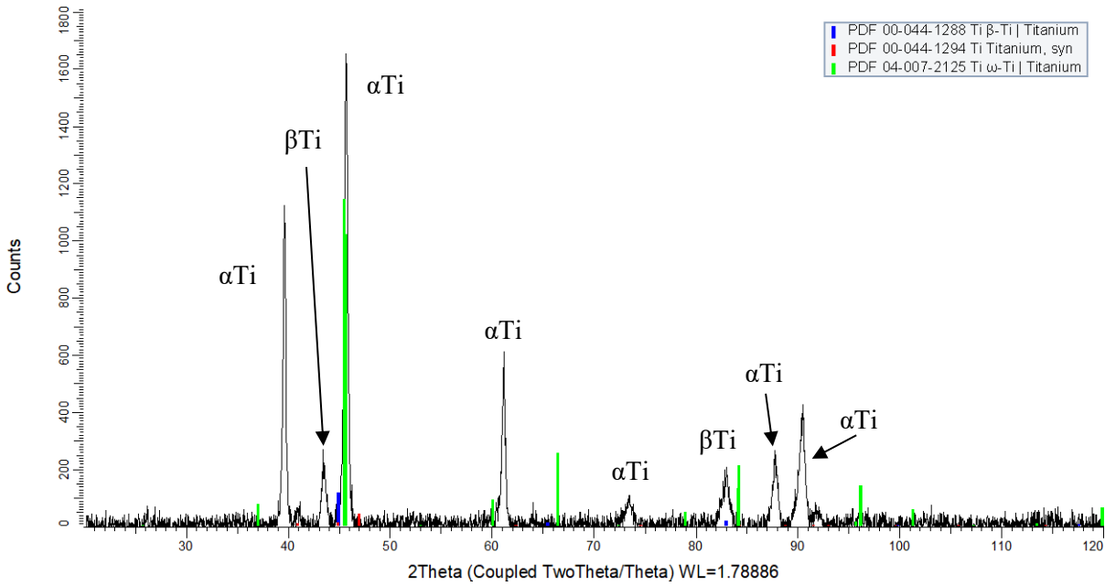


Figure 5.11: *XRD analysis of the as-cast Ti-8Nb-4Zr (wt%) alloy, showing peaks for αTi, and small peaks for βTi shifted by alloying.*

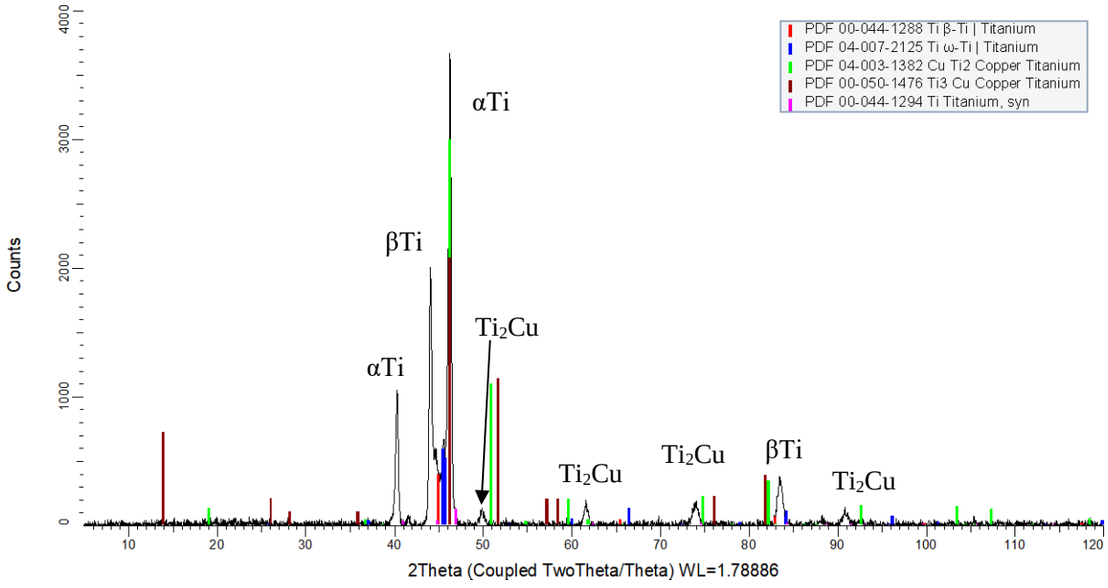


Figure 5.12: *XRD analysis of the as-cast Ti-8Nb-4Zr-5Cu (wt%) alloy, showing αTi, and small βTi peaks shifted by alloying and Ti_2Cu.*

5.2. Vickers micro-hardness testing

The Vickers micro-hardness testing was done to study the mechanical properties. The micro-hardness measurements of the as-cast Ti-6Nb-4Zr-*x*Cu and Ti-8Nb-4Zr-*x*Cu (*x* = 0 and 5 wt%) alloys, and the average hardness values are shown in Figure 5.13. The hardness of the as-received Ti-6Al-4V (335 ± 9 HV) and Ti-10.1Ta-1.7Nb-1.6Zr (TTNZ) (136 ± 6 HV) alloys were also measured for comparison. The hardnesses of Ti-6Nb-4Zr (280 ± 13 HV) and Ti-8Nb-4Zr (285 ± 7 HV) were lower than the Ti-6Al-4V, and higher than TTNZ (Figure 5.13). Figure 5.13 shows that adding 5 wt% Cu increased the hardness of Ti-6Nb-4Zr (334 ± 11 HV) and Ti-8Nb-4Zr (358 ± 7 HV), thus giving ~16% increase in hardness for Ti-6Nb-4Zr, and ~20% for Ti-8Nb-4Zr. The

hardness results (Figure 5.13) indicated Ti-8Nb-4Zr-5Cu as the hardest alloy, although the overlapping error bars showed that the hardnesses of Ti-8Nb-4Zr-5Cu, Ti-6Nb-4Zr-5Cu and Ti-6Al-4V were statistically the same, and the Ti-10.1Ta-1.7Nb-1.6Zr (TTNZ) as the less hard alloy. The error bars of Ti-8Nb-4Zr and Ti-6Nb-4Zr also overlapped considerably, showing that they were nearly the same statistically.

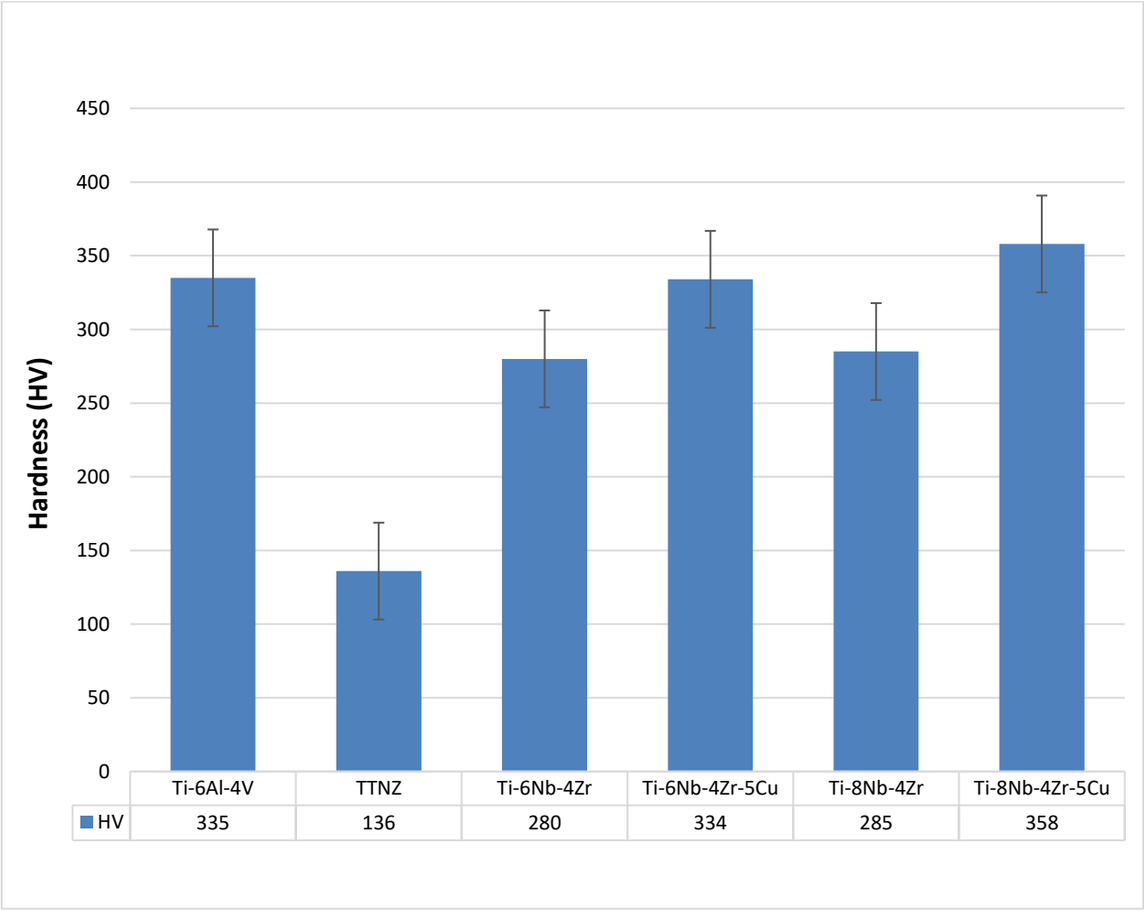


Figure 5.13: *Mean Vickers hardness of the investigated alloys.*

5.3. Hot compression testing

Hot deformation behaviour of the as-received Ti-6Al-4V and Ti-10.1Ta-1.7Nb-1.6Zr (TTNZ) alloys was evaluated using stress-strain curves. The microstructures as a function of deformation temperature and strain rates were also investigated. Figure 5.30 shows the stress-strain curves obtained from uniaxial compression testing of the Ti-6Al-4V and Ti-10.1Ta-1.7Nb-1.6Zr alloys, at 850°C and 950°C, and 0.1 s^{-1} and 10 s^{-1} strain rates.

5.3.1. Microstructures of the deformed Ti-6Al-4V alloy

The microstructure of Ti-6Al-4V, deformed at 850°C and 0.1 s^{-1} strain rate (Figure 5.14a), consisted of αTi laths and transformed βTi phases, whereas at 950°C and 0.1 s^{-1} (Figure 5.14b) the microstructure comprised globular αTi in the transformed βTi matrix. The SEM-BSE images showed αTi globules within the transformed βTi matrix (Figure 5.15b). This indicated that

increasing the deformation temperature led to globularisation and growth of the alpha phase. Table 5.5 gives the EDX analyses and suggested inhomogeneity because the overall composition was outside of range of the αTi and βTi phases. The XRD results (Figures 5.16 and 5.17) showed αTi and βTi peaks shifted by alloying, and the low peaks of the Ti_3Al phase.

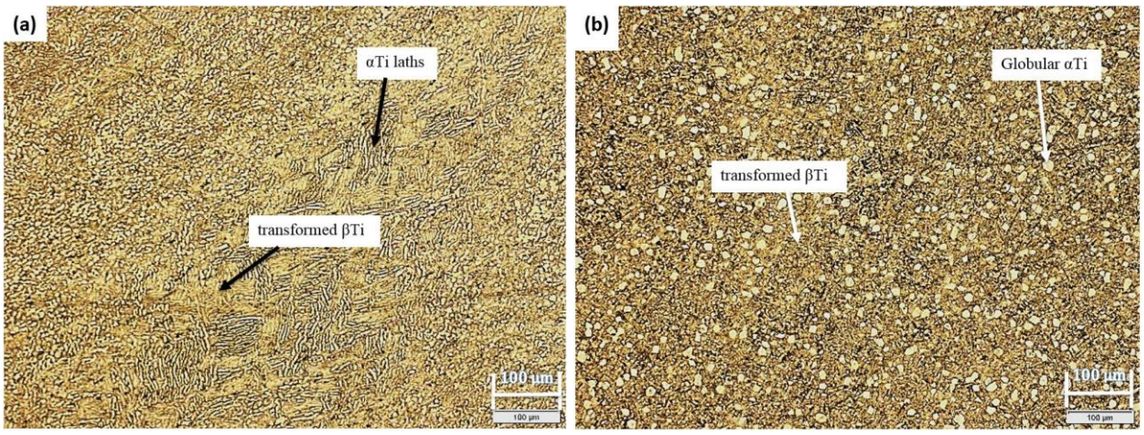


Figure 5.14: *Optical micrographs of as-received Ti-6Al-4V (wt%) deformed at 0.1 s^{-1} strain rate: (a) 850°C and (b) 950°C.*

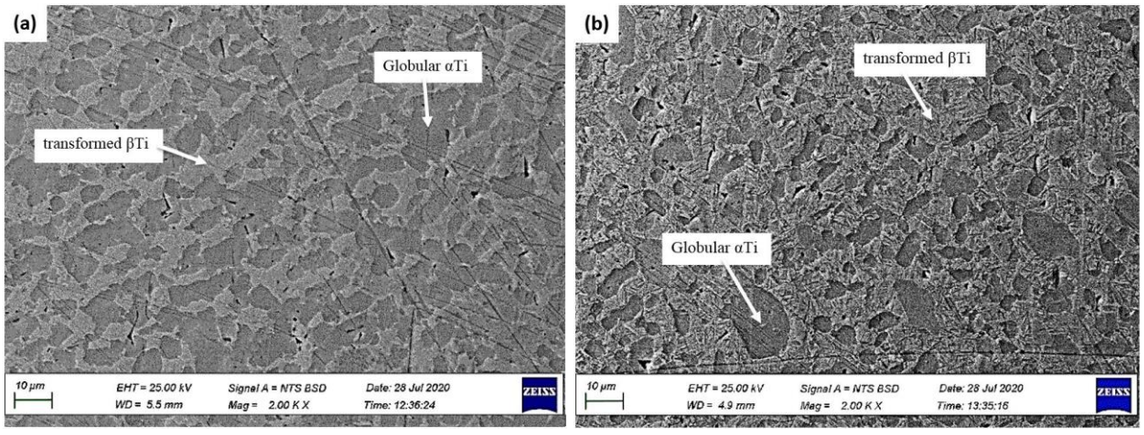


Figure 5.15: *SEM-BSE images of as-received Ti-6Al-4V (wt%) deformed at 0.1 s^{-1} strain rate: (a) 850°C and (b) 950°C.*

Table 5.5: *EDX analyses of the as-received Ti-6Al-4V (wt%) alloy deformed 850°C and 950°C for 0.1 s^{-1} strain rate.*

Alloy	Phase description	Ti	Al	V	Phase
Ti-6Al-4V (850°C and 0.1 s^{-1})	Overall	90.4 ± 1.5	5.4 ± 1.1	4.2 ± 1.2	---
	Matrix	90.6 ± 1.1	5.9 ± 0.8	3.5 ± 0.8	βTi
	Globules	90.9 ± 1.3	5.9 ± 0.6	3.2 ± 1.1	αTi
Ti-6Al-4V (950°C and 0.1 s^{-1})	Overall	90.2 ± 2.0	5.9 ± 0.5	3.9 ± 1.8	---
	Matrix	91.1 ± 1.5	5.8 ± 0.6	3.1 ± 1.1	βTi
	Globules	90.8 ± 0.6	6.6 ± 0.3	2.6 ± 0.5	αTi

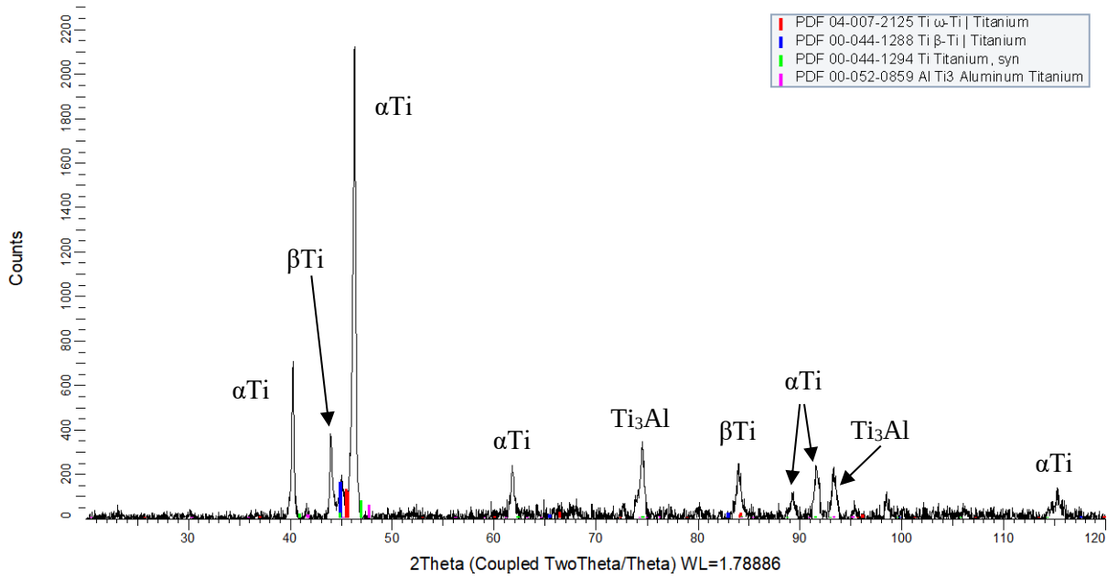


Figure 5.16: *XRD analysis of the as-received Ti-6Al-4V deformed at 850°C and 0.1 s^{-1} strain rate, showing αTi and βTi peaks shifted by alloying.*

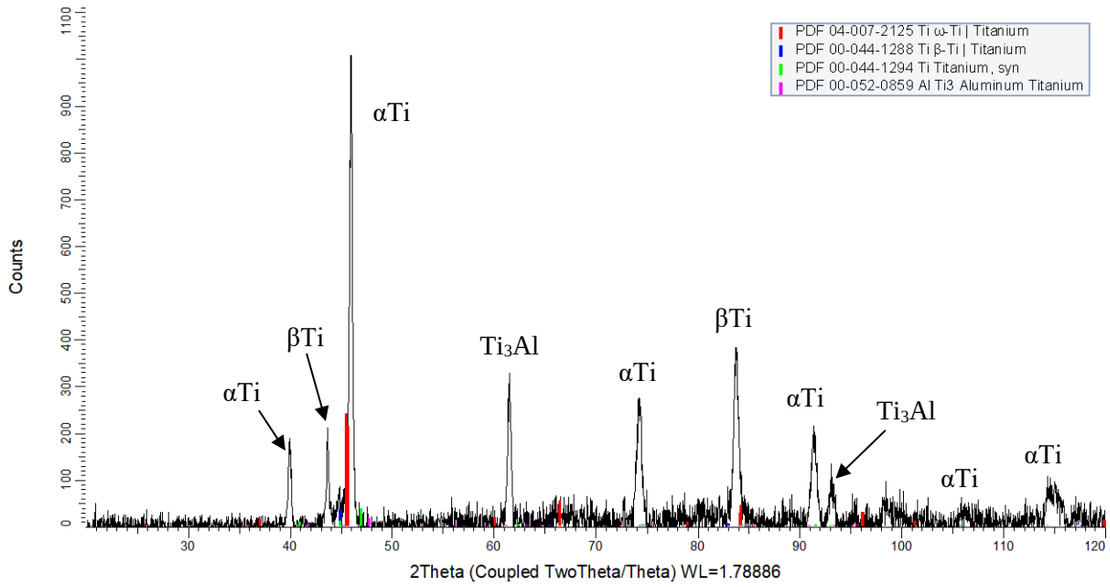


Figure 5.17: *XRD analysis of the as-received Ti-6Al-4V deformed at 950°C and 0.1 s^{-1} strain rate, showing αTi and βTi peaks shifted by alloying.*

Figure 5.18 shows the optical micrographs, and Figure 5.19 shows the SEM-BSE images of as-received Ti-6Al-4V deformed at 10 s^{-1} strain rate, and 850°C and 950°C. The coarser αTi globules were observed at 850°C (Figure 5.18a), whereas finer αTi globules were observed at 950°C (Figure 5.18b). The SEM-BSE images also showed finer αTi globules at 950°C (Figure 5.19b), and grain coarsening at 850°C (Figure 5.19a). The EDX analyses are given in Table 5.6. The overall V composition was outside the range of the αTi and βTi phase, suggesting inhomogeneity in the deformed Ti-6Al-4V alloy (950°C and 10 s^{-1}) (Table 5.6), although the EDX technique is limited for bulk analyses because of the small area analysed. The XRD results (Figures 5.20 and 5.21) showed shifted peaks of αTi and βTi due to alloying, and low peaks of the Ti_3Al phase.

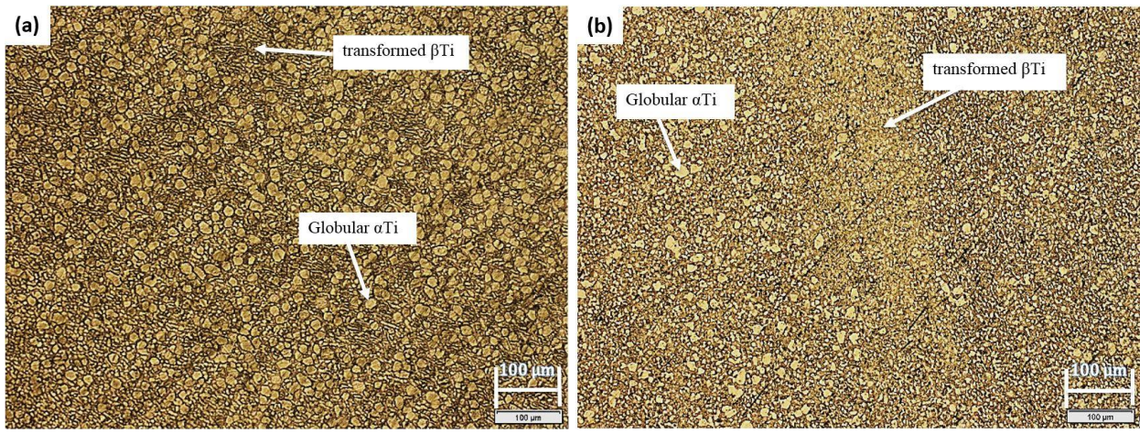


Figure 5.18: *Optical micrographs of as-received Ti-6Al-4V deformed at 10 s^{-1}strain rate: (a) 850°C and (b) 950°C.*

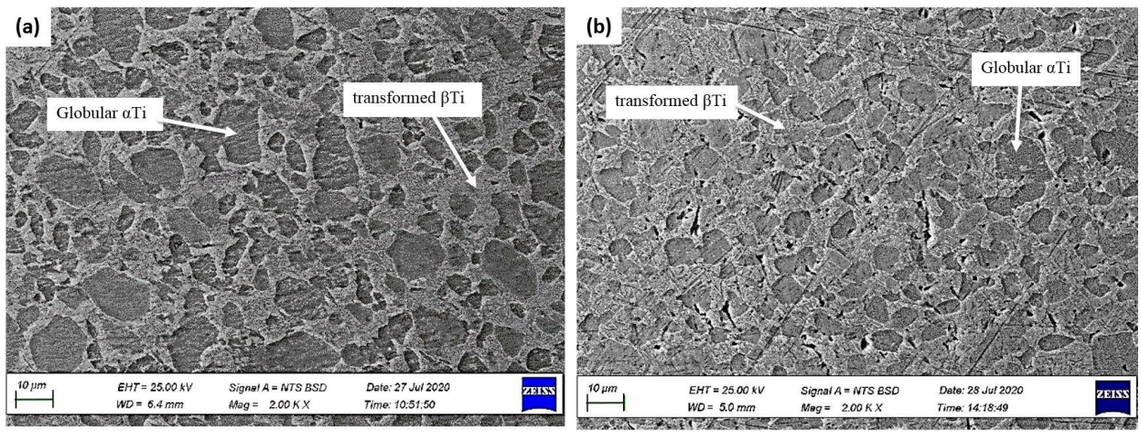


Figure 5.19: *SEM-BSE images of as-received Ti-6Al-4V deformed at 10 s^{-1}strain rate: (a) 850°C and (b) 950°C.*

Table 5.6: *EDX analyses of the as-received Ti-6Al-4V (wt%) alloy deformed 850°C and 950°C for 10 s^{-1} strain rate.*

Alloy	Phase description	Ti	Al	V	Phase
Ti-6Al-4V (850°C and 10 s^{-1})	Overall	89.3 ± 0.7	6.1 ± 0.4	4.5 ± 0.6	---
	Matrix	87.2 ± 0.7	4.3 ± 0.3	8.5 ± 0.6	βTi
	Globules	92.4 ± 1.3	6.6 ± 0.3	1.0 ± 0.7	αTi
Ti-6Al-4V (950°C and 10 s^{-1})	Overall	89.0 ± 0.7	6.1 ± 0.3	4.9 ± 0.7	---
	Matrix	89.8 ± 0.9	5.9 ± 0.4	4.3 ± 0.8	βTi
	Globules	90.1 ± 1.2	6.5 ± 0.5	3.4 ± 1.4	αTi

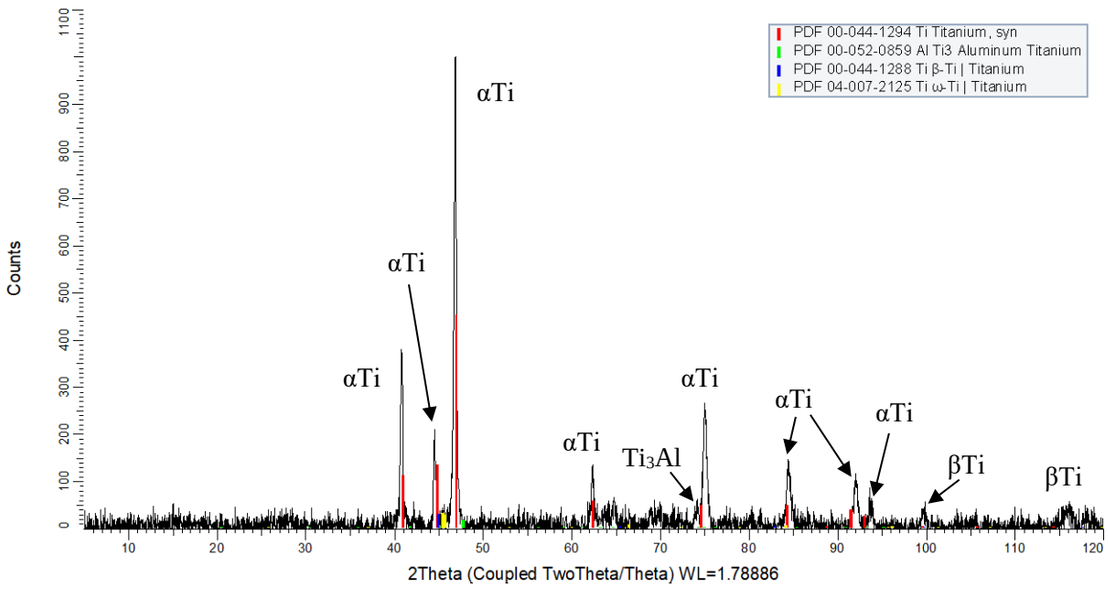


Figure 5.20: *XRD analysis of the as-received Ti-6Al-4V deformed at 850°C and 10 s^{-1} strain rate, showing αTi and βTi peaks shifted by alloying.*

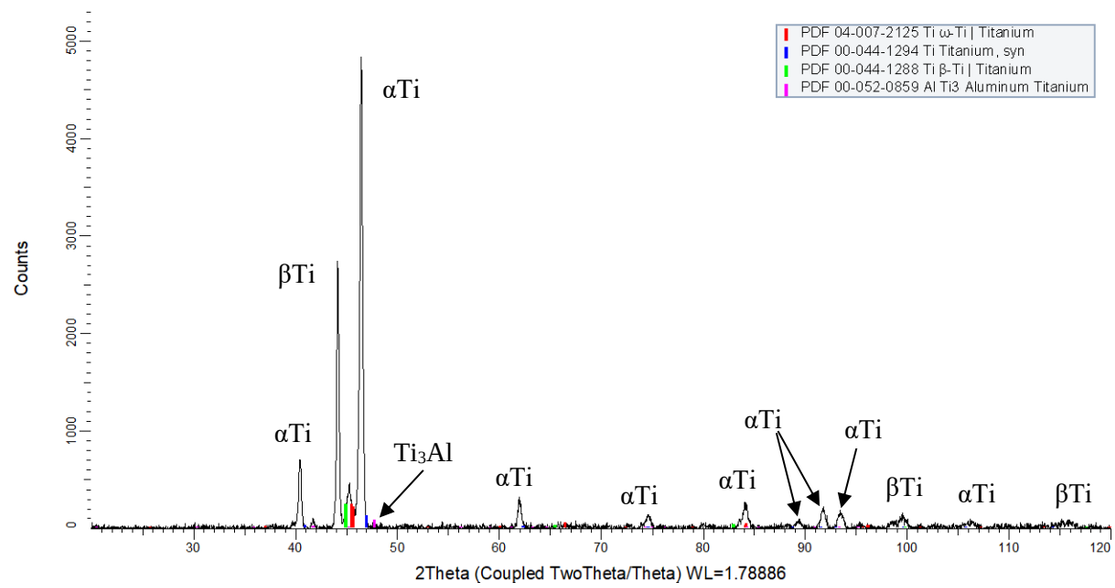


Figure 5.21: *XRD analysis of the as-received Ti-6Al-4V deformed at 950°C and 10 s^{-1} strain rate, showing αTi and βTi peaks shifted by alloying.*

5.3.2. Microstructures of the deformed Ti-10.1Ta-1.7Nb-1.6Zr alloy

The optical micrographs of the as-received Ti-10.1Ta-1.7Nb-1.6Zr alloy deformed at 850°C and 950°C, and 0.1 s^{-1} strain rate, are shown in Figure 5.22. Figure 5.23 shows the SEM-BSE images. At 850°C (Figure 5.22a), the microstructure consisted of coarser αTi grains, whereas finer αTi grains were observed at 950°C (Figure 5.22b). This was consistent with the SEM-BSE images shown in Figures 5.23a and 5.23b. The EDX results (Table 5.7) gave the matrix as βTi and the globular phases as αTi. The alloys were thought to be inhomogeneous due to the overall composition lying outside the range of the αTi and βTi phase (Table 5.7), which also demonstrated again that EDX is not suitable for bulk analysis (because of the small area analysed). The XRD analysis confirmed the

existence of αTi and βTi phases (Figures 5.24 and 5.25). However, the βTi phase was not clearly visible in Figure 5.24.

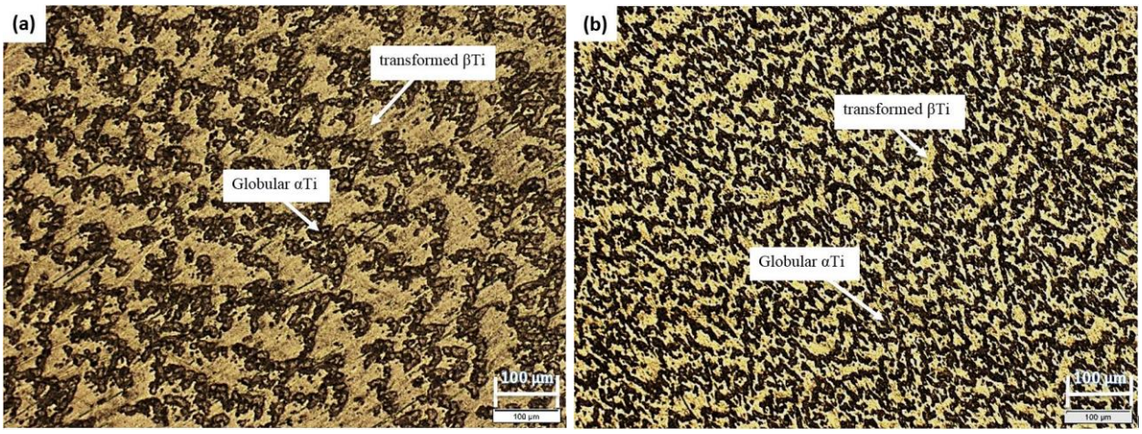


Figure 5.22: *Optical micrographs of as-received Ti-10.1Ta-1.7Nb-1.6Zr deformed at 0.1 s^{-1} strain rate: (a) 850°C and (b) 950°C.*

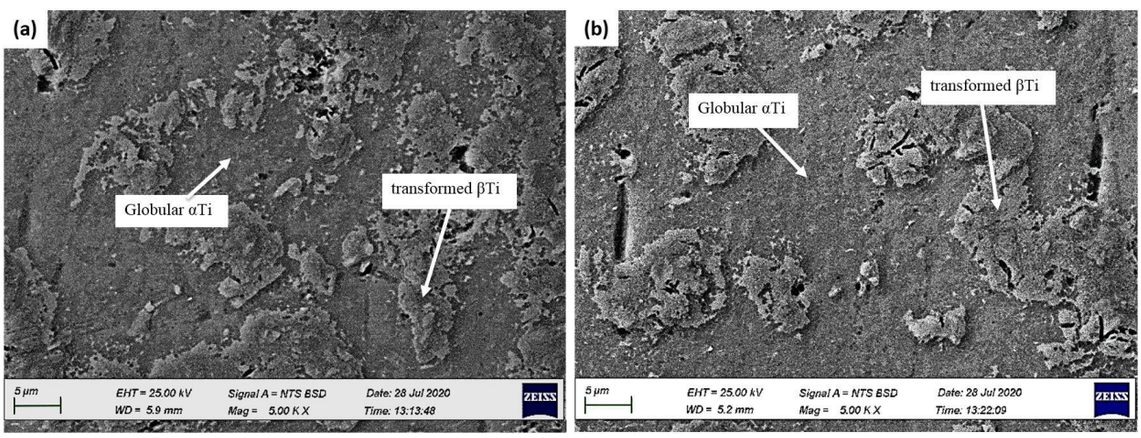


Figure 5.23: *SEM-BSE images of as-received Ti-10.1Ta-1.7Nb-1.6Zr deformed at 0.1 s^{-1}strain rate: (a) 850°C and (b) 950°C.*

Table 5.7: *EDX analyses of the as-received Ti-10.1Ta-1.7Nb-1.6Zr (wt%) alloy deformed 850°C and 950°C for 0.1 s^{-1} strain rate.*

Alloy	Phase description	Ti	Ta	Nb	Zr	Phase
Ti-10.1Ta-1.7Nb-1.6Zr (850°C and 0.1 s^{-1})	Overall	87.0 ± 1.2	9.9 ± 1.3	0.8 ± 0.6	2.3 ± 1.1	---
	Matrix	87.3 ± 1.1	10.5 ± 0.1	0.4 ± 0.5	1.9 ± 0.4	βTi
	Globules	87.3 ± 0.4	10.3 ± 0.8	0.3 ± 0.2	2.1 ± 0.5	αTi
Ti-10.1Ta-1.7Nb-1.6Zr (950°C and 0.1 s^{-1})	Overall	87.4 ± 1.6	10.2 ± 1.5	0.6 ± 0.4	1.8 ± 1.1	---
	Matrix	86.9 ± 1.1	10.7 ± 0.8	0.3 ± 0.4	2.1 ± 0.4	βTi
	Globules	88.2 ± 0.8	9.3 ± 1.0	0.4 ± 0.3	2.1 ± 0.4	αTi

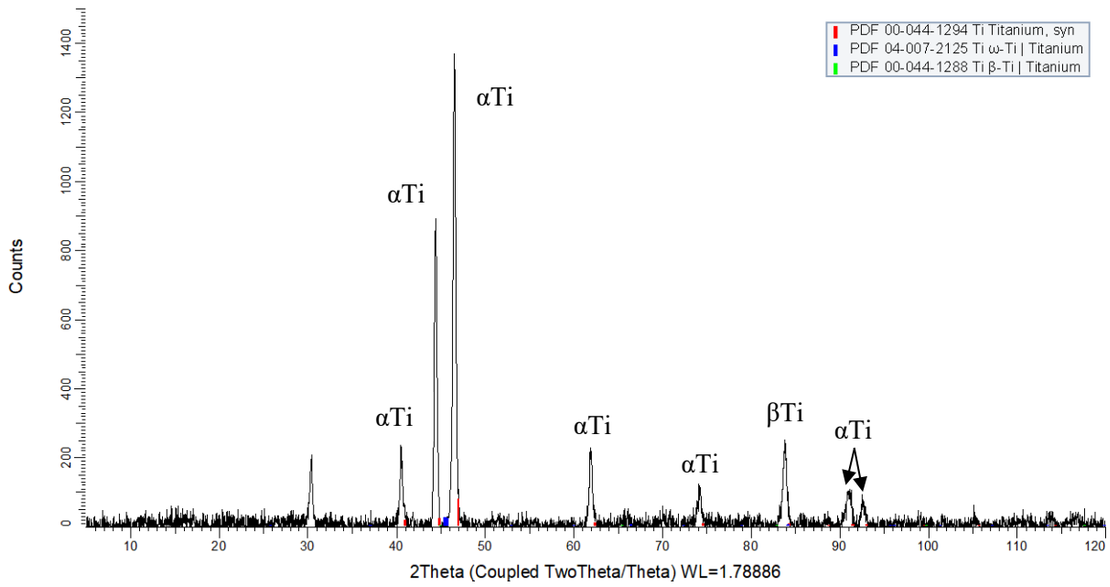


Figure 5.24: *XRD analysis of the as-received Ti-10.1Ta-1.7Nb-1.6Zr deformed at 850°C and 0.1 s^{-1} strain rate, showing mainly αTi with βTi peaks, shifted by alloying.*

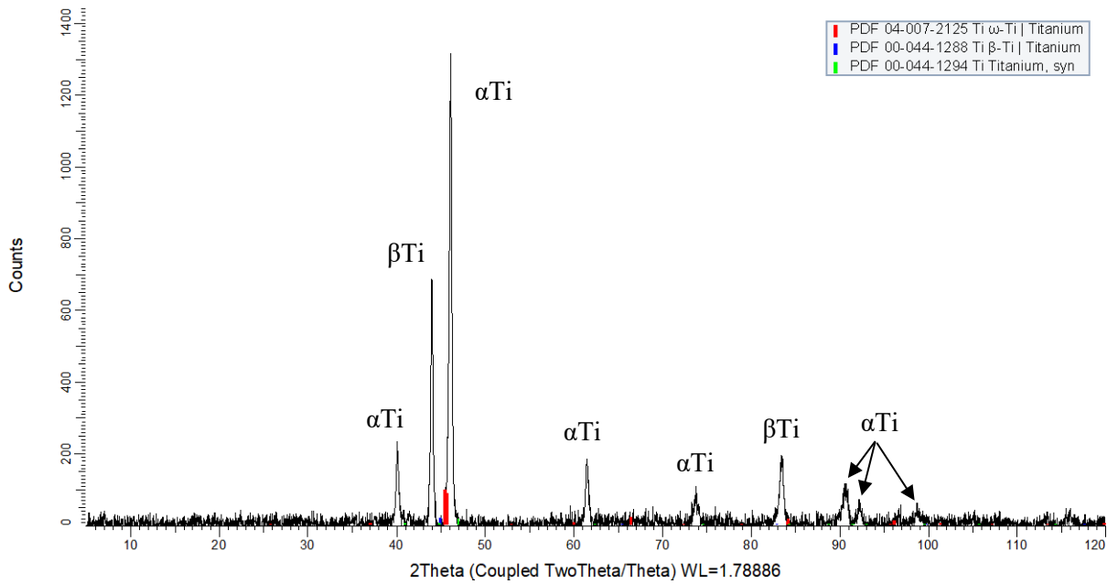


Figure 5.25: *XRD analysis of the as-received Ti-10.1Ta-1.7Nb-1.6Zr deformed at 950°C and 0.1 s^{-1} strain rate, showing mainly αTi with βTi peaks, shifted by alloying.*

Figure 5.26 shows the optical micrographs of the as-received Ti-10.1Ta-1.7Nb-1.6Zr alloy deformed at 850°C and 950°C, and 10 s^{-1} strain rate. The optical micrographs show globular αTi grains, and the transformed βTi matrix (Figure 5.26). The αTi globules appeared to be coarser at 950°C (Figure 5.26b), than at 850°C (Figure 5.26a). The SEM-BSE images (Figure 5.27) confirmed the globular αTi grains within the transformed βTi matrix. The EDX analyses (Table 5.8) show higher compositions of Ta and Nb in the βTi phase compared to the αTi phase. The EDX results also suggested inhomogeneity in the deformed Ti-10.1Ta-1.7Nb-1.6Zr alloy (850°C and 10 s^{-1}) due to the overall Nb composition lying outside the range of the αTi and βTi phase (Table 5.8). The XRD results showed shifted peaks of αTi and βTi due to alloying (Figures 5.28 and 5.29).

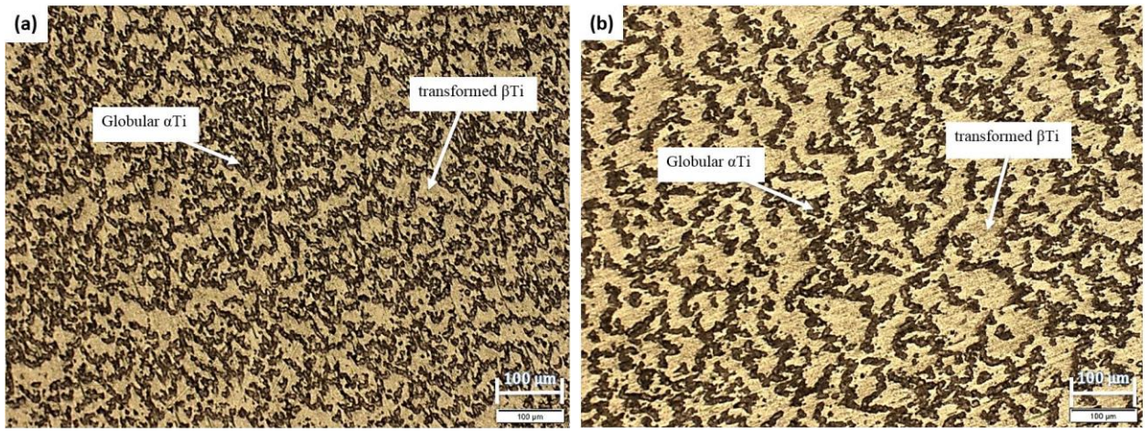


Figure 5.26: *Optical micrographs of as-received Ti-10.1Ta-1.7Nb-1.6Zr deformed at 10 s^{-1}strain rate: (a) 850°C and (b) 950°C.*

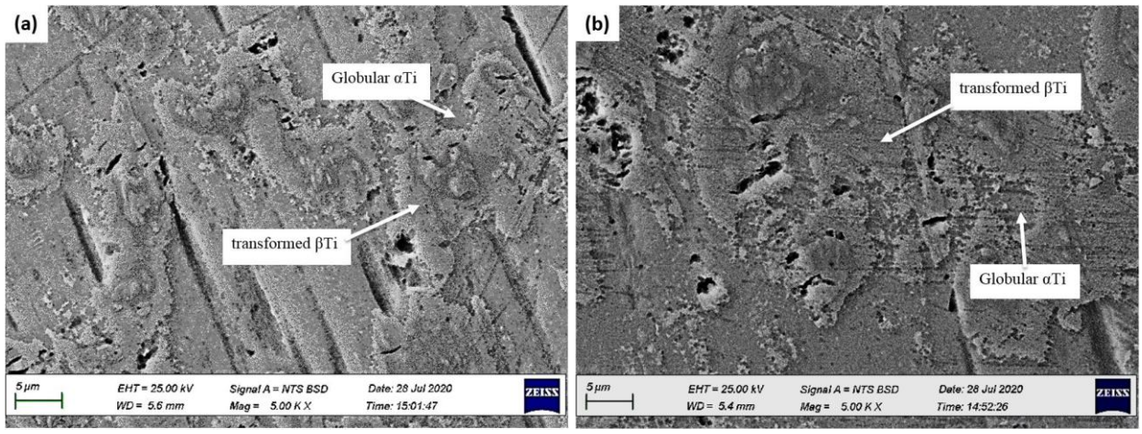


Figure 5.27: *SEM-BSE images of as-received Ti-10.1Ta-1.7Nb-1.6Zr deformed at 10 s^{-1}strain rate: (a) 850°C and (b) 950°C.*

Table 5.8: *EDX analyses of the as-received Ti-10.1Ta-1.7Nb-1.6Zr (wt%) alloy deformed 850°C and 950°C for 10 s^{-1} strain rate.*

Alloy	Phase description	Ti	Ta	Nb	Zr	Phase
Ti-10.1Ta-1.7Nb-1.6Zr (850°C and 10 s^{-1})	Overall	86.7 ± 1.3	10.2 ± 0.8	0.8 ± 0.4	2.3 ± 1.1	---
	Matrix	86.6 ± 0.6	10.9 ± 0.8	0.1 ± 0.2	2.5. ± 0.4	βTi
	Globules	88.0 ± 1.5	9.9 ± 1.1	0.5 ± 0.5	1.7 ± 0.6	αTi
Ti-10.1Ta-1.7Nb-1.6Zr (950°C and 10 s^{-1})	Overall	86.1 ± 0.9	10.3 ± 0.8	1.3 ± 0.7	2.3 ± 0.6	---
	Matrix	85.2 ± 1.4	10.6 ± 1.4	0.9 ± 0.6	3.3 ± 0.3	βTi
	Globules	86.4 ± 2.4	11.2 ± 0.8	0.5 ± 0.6	1.9 ± 1.3	αTi

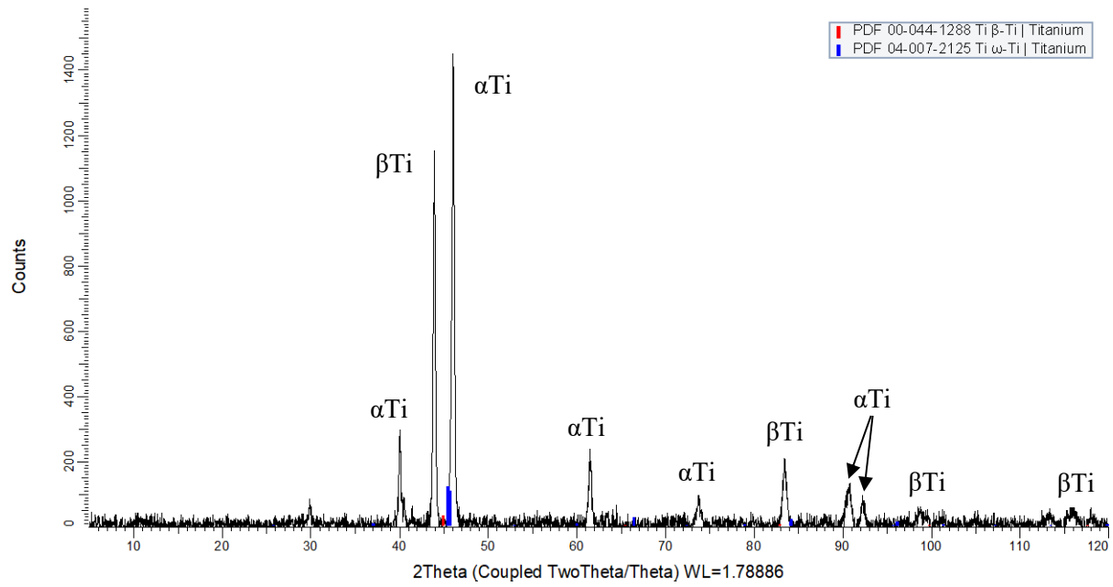


Figure 5.28: *XRD analysis of the as-received Ti-10.1Ta-1.7Nb-1.6Zr deformed at 850°C and 10 s^{-1} strain rate, showing mainly αTi with βTi peaks, shifted by alloying.*

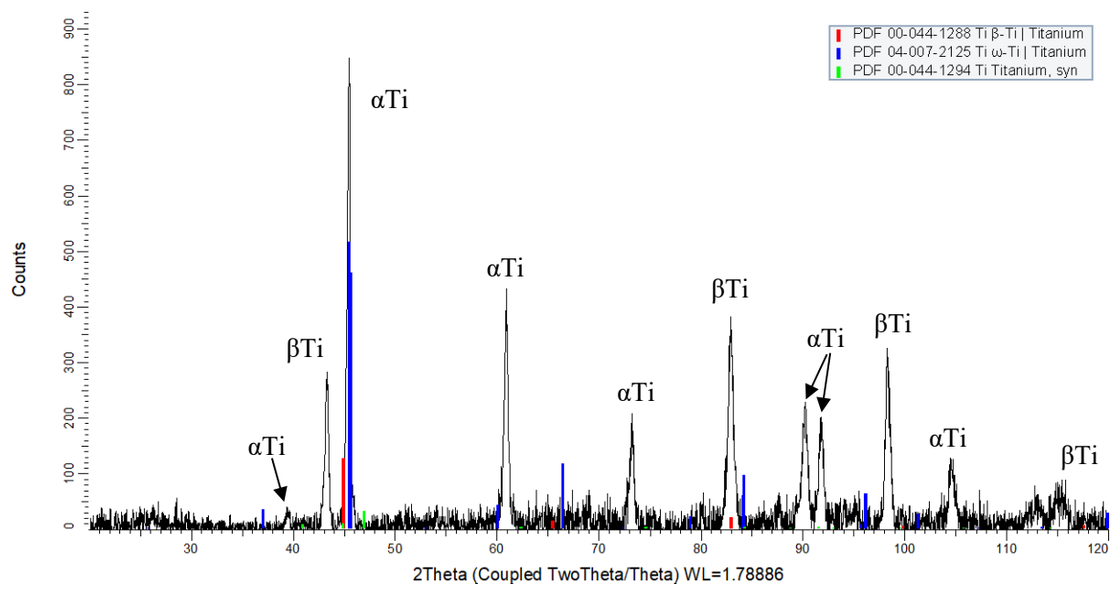


Figure 5.29: *XRD analysis of the as-received Ti-10.1Ta-1.7Nb-1.6Zr deformed at 950°C and 10 s^{-1} strain rate, showing mainly αTi with βTi peaks, shifted by alloying.*

5.3.3. Deformation behaviour of the as-received Ti-6Al-4V and Ti-10.1Ta-1.7Nb-1.6Zr alloys

Figure 5.30 shows the stress-strain curves of the as-received Ti-6Al-4V and Ti-10.1Ta-1.7Nb-1.6Zr alloys deformed at 850°C and 950°C, and 0.1 s^{-1} and 10 s^{-1} strain rates. At 850°C, the Ti-6Al-4V and Ti-10.1Ta-1.7Nb-1.6Zr alloys had higher flow stresses for both 0.1 s^{-1} and 10 s^{-1} strain rates than at 950°C (Figures 5.30). Figure 5.30 shows that at 850°C, the Ti-6Al-4V alloy had a higher flow stress (270 MPa) at 10 s^{-1} than at 0.1 s^{-1} (170 MPa), whereas Ti-10.1Ta-1.7Nb-1.6Zr had 75 MPa at 10 s^{-1} and 35 MPa at 0.1 s^{-1}. This indicated that higher flow stresses were observed at higher strain rate (10 s^{-1}) and lower temperature (850°C) (Figure 5.30).

Figure 5.30 shows that the strain of Ti-6Al-4V was not affected by an increase in strain rate. However, the strain was higher (0.53) at 850°C than at 950°C (0.51 strain) for both 0.1 s^{-1} and 10 s^{-1} strain rates, indicating that deformation at lower temperature improved the ductility of the Ti-6Al-4V alloy (Figure 5.30). At 850°C, the Ti-10.1Ta-1.7Nb-1.6Zr alloy had a higher strain (0.53) at 10 s^{-1} than at 0.1 s^{-1} strain rate (0.45 strain), whereas at 950°C, a higher strain (0.48) was obtained at 0.1 s^{-1} than 0.40 at 10 s^{-1} strain rate (Figure 5.30). The results for Ti-10.1Ta-1.7Nb-1.6Zr indicated that the ductility improved at higher temperature (950°C) and reduced strain rate (0.1 s^{-1}), and at lower temperature (850°C) and increased strain rate (10 s^{-1}) (Figure 5.30). The Ti-6Al-4V had a strain above 0.5 at 850°C and 950°C for both 0.1 s^{-1} and 10 s^{-1} (Figure 5.30), whereas 0.5 strain for Ti-10.1Ta-1.7Nb-1.6Zr was obtained only at 850°C and 10 s^{-1} (Figure 5.30b). Therefore, the Ti-6Al-4V alloy showed better ductility than the Ti-10.1Ta-1.7Nb-1.6Zr alloy (Figure 5.30). The alloys lost their initial shapes, but neither fractured.

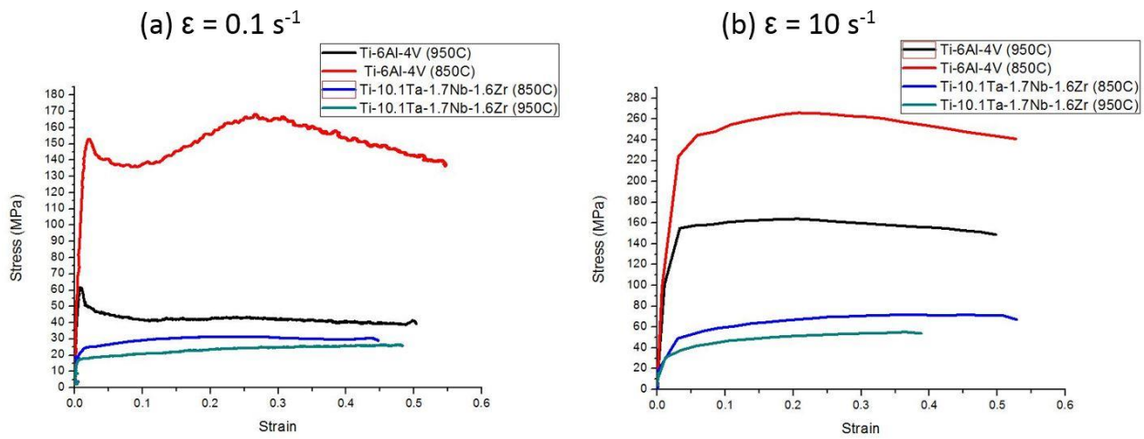


Figure 5.30: *Stress-strain curves of the as-received Ti-6Al-4V and Ti-10.1Ta-1.7Nb-1.6Zr (wt%) alloys deformed at 850°C and 950°C, and (a) 0.1 s^{-1} and (b) 10 s^{-1} strain rates.*

Figure 5.31 shows the average hardness values of the as-received and deformed Ti-6Al-4V and Ti-10.1Ta-1.7Nb-1.6Zr (TTNZ). At 950°C, Ti-6Al-4V had similar hardness for both 0.1 s^{-1} (316 ± 5 HV) and 10 s^{-1} (315 ± 7 HV) strain rates (Figure 5.31). However, the hardness of Ti-6Al-4V increased at 850°C and 0.1 s^{-1} (324 ± 9 HV) as shown in Figure 5.31. The as-received Ti-6Al-4V (335 ± 9 HV) had a higher hardness than all deformed Ti-6Al-4V and Ti-10.1Ta-1.7Nb-1.6Zr (TTNZ) alloys (Figure 5.31).

The as-received Ti-10.1Ta-1.7Nb-1.6Zr (TTNZ) (136 ± 6 HV) had a similar hardness to TTNZ (136 ± 10 HV) deformed at 950°C and 10 s^{-1} (Figure 5.31). The TTNZ deformed at 850°C and 10 s^{-1} (149 ± 6 HV) had a higher hardness than all other deformed TTNZ alloys, as shown in Figure 5.31. However, given that the error bars of the samples with higher hardnesses all overlapped, these hardnesses were statistically the same, as were all the samples with lower hardnesses.

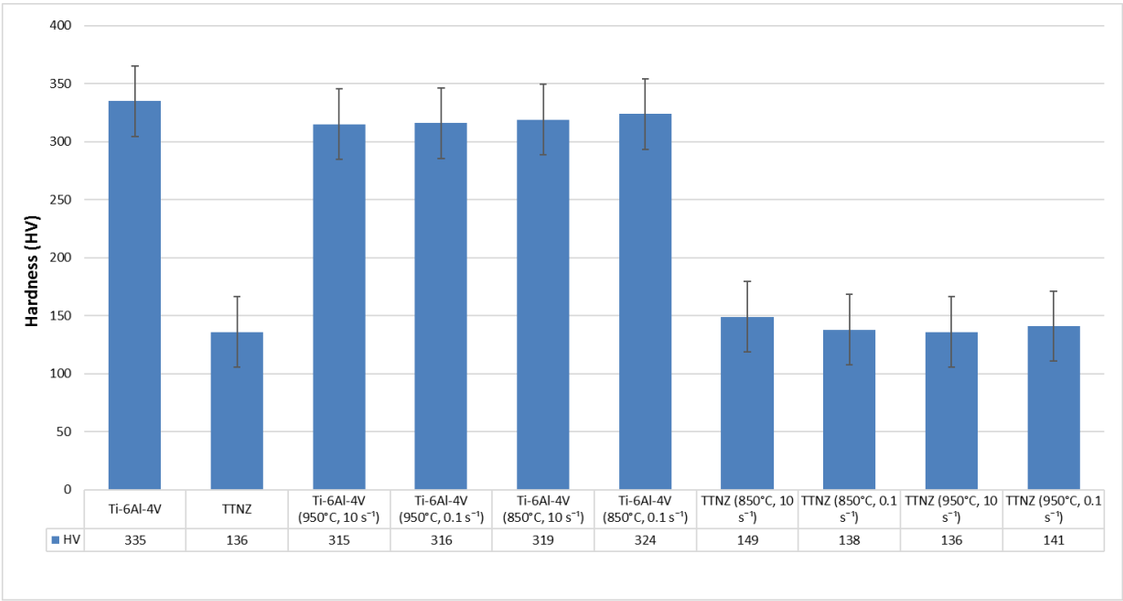


Figure 5.31: *Mean Vickers hardness of the as-received and deformed Ti-6Al-4V and Ti-10.1Ta-1.7Nb-1.6Zr alloys.*

Chapter 6: Discussion

This chapter discusses and compares the experimental results.

6.1. XRD analyses and phase identification

The XRD analyses of the as-cast Ti-6Nb-4Zr-*x*Cu (Figures 5.7 and 5.8) and Ti-8Nb-4Zr-*x*Cu (*x* = 0 and 5 wt%) (Figures 5.11 and 5.12) alloys were done to identify the phases found, compared with the as-received Ti-6Al-4V (Figure 5.2) and Ti-10.1Ta-1.7Nb-1.6Zr (Figure 5.4) alloys. Peaks of αTi (hcp) and βTi (bcc) were identified in the as-received Ti-6Al-4V, Ti-10.1Ta-1.7Nb-1.6Zr, and the as-cast Ti-6Nb-4Zr-*x*Cu and Ti-8Nb-4Zr-*x*Cu (*x* = 0 and 5 wt%) alloys. The peaks were shifted due to alloying. The Ti_3Al phase, predicated by the Thermo-Calc, was only identified in the as-received Ti-6Al-4V alloy (Figure 5.2). The Ti_2Cu phase was identified in both Ti-6Nb-4Zr-5Cu (Figure 5.8) and Ti-8Nb-4Zr-5Cu alloys (Figure 5.12), due to the 5 wt% Cu added. According to the phase proportion diagrams (Figures 4.1, 4.6, 4.11, 4.14, 4.16 and 4.19), the solidification sequences are given in Table 6.1. The βTi formed at higher temperature for Ti-6Nb-4Zr and Ti-8Nb-4Zr compared with 5 wt% Cu added (Table 6.1). The Ti_2Cu formation temperature was lower in Ti-6Nb-4Zr-5Cu than Ti-8Nb-4Zr-5Cu (Table 6.1).

Table 6.1: *Solidification sequences of the different titanium alloy compositions.*

Alloy	Solidification sequence	Solidification temperature, from Thermo-Calc (°C)
Ti-6Nb-4Zr	L → βTi	1661
	βTi → αTi	809
Ti-6Nb-4Zr-5Cu	L → βTi	1467
	βTi → Ti_2Cu	756
	βTi → Ti_2Cu + αTi	743
Ti-8Nb-4Zr	L → βTi	1664
	βTi → αTi	793
Ti-8Nb-4Zr-5Cu	L → βTi	1468
	βTi → Ti_2Cu	762
	βTi → Ti_2Cu + αTi	731
Ti-6Al-4V	L → βTi	1698
	βTi → αTi	942
	αTi → Ti_3Al	485
Ti-10.1Ta-1.7Nb-1.6Zr	L → βTi	1688
	βTi → αTi	816

6.2. Microstructures

Lütjering (1998) and Leyens & Peters (2003) reported that titanium alloys consist of lamellar, equiaxed or bimodal microstructures, depending on the αTi and βTi morphologies. The microstructures of the as-received Ti-6Al-4V (Figure 5.1) and Ti-10.1Ta-1.7Nb-1.6Zr (Figure 5.3),

and as-cast Ti-6Nb-4Zr (Figure 5.5) and Ti-8Nb-4Zr (Figure 5.9) consisted of the αTi and βTi phases. However, different microstructures due to different αTi and βTi morphologies were observed. The Ti-6Nb-4Zr (Figure 5.5a) and Ti-8Nb-4Zr (Figure 5.9a) alloys had bimodal microstructures consisting of αTi laths within the βTi matrix, whereas the as-received Ti-6Al-4V alloy had a fully lamellar microstructure (Figure 5.1), and the as-received Ti-10.1Ta-1.7Nb-1.6Zr had an equiaxed microstructure of globular αTi grains in the transformed βTi matrix (Figure 5.3). The Ti_3Al phase, predicated by the Thermo-Calc and identified by XRD, was not found in the microstructures of as-received Ti-6Al-4V alloy, because it was missed in the sampling and study of a small area in the SEM.

The microstructures of as-cast Ti-6Nb-4Zr-5Cu (Figure 5.6) and Ti-8Nb-4Zr-5Cu (Figure 5.10) were also studied, and consisted of bimodal structures of αTi and βTi phases, and Ti_2Cu precipitates within the αTi grains and the βTi matrix. The microstructures Ti-6Nb-4Zr-5Cu and Ti-8Nb-4Zr-5Cu had similar αTi, βTi and Ti_2Cu morphologies. Fowler et al. (2019d) also found that the Ti_2Cu phase formed at the interfaces, including grain boundaries between the αTi and βTi phases. The EDX analyses indicated high Cu contents in the βTi phase regions than the αTi phase regions in both Ti-6Nb-4Zr-5Cu (Table 5.3) and Ti-8Nb-4Zr-5Cu (Table 5.4). The solid solubility of Cu in βTi was 5.2 ± 1.3 wt% for Ti-6Nb-4Zr-5Cu (Table 5.3), and 5.8 ± 2.5 wt% for Ti-8Nb-4Zr-5Cu (Table 5.4). The EDX results were consistent with Leyens & Peters (2003) regarding Cu as a β-stabiliser.

6.3. Vickers micro-hardness

The microstructure and alloying elements can significantly affect the mechanical properties of metal alloys (Kikuchi et al., 2003; Zhang et al., 2016b). Addition of 5 wt% Cu increased the hardness of the as-cast Ti-6Nb-4Zr and Ti-8Nb-4Zr alloys (Figure 5.13), due to the Ti_2Cu phase identified by the XRD results (Figures 5.8 and 5.12). This was consistent with the results by Kikuchi et al. (2003) and Zhang et al. (2016b) for Ti-5Cu (wt%) alloys. The solid solubility of Cu in βTi gave solid solution strengthening, and the Ti_2Cu precipitates could give precipitation strengthening (Kikuchi et al., 2003; Zhang et al., 2016b), hence the improved hardness for the as-cast Ti-6Nb-4Zr and Ti-8Nb-4Zr alloys (Figure 5.13).

The Ti-6Nb-4Zr alloy had a slightly lower hardness than the Ti-8Nb-4Zr alloy, shown in Figure 5.13. The Ti-10.1Ta-1.7Nb-1.6Zr (TTNZ) alloy had the lowest hardness of the Ti-6Al-4V, Ti-6Nb-4Zr and Ti-8Nb-4Zr alloys (Figure 5.13). This low hardness was attributed to the high Ta content, which stabilises the softer βTi phase (Collings, 1984; Leyens & Peters, 2003). This was consistent with the SEM results, which showed that Ti-10.1Ta-1.7Nb-1.6Zr (TTNZ) (Figure 5.3) had more βTi phase retained than Ti-6Al-4V (Figure 5.1), Ti-6Nb-4Zr (Figure 5.5) and Ti-8Nb-4Zr (Figure 5.9). The hcp αTi and Ti_3Al in Ti-6Al-4V (Figure 5.2) may have contributed more to its hardness than the βTi (bcc) phases. Hence, the higher hardness in Ti-6Al-4V than the Ti-6Nb-4Zr and Ti-8Nb-4Zr alloys (Figure 5.13). This agreed with Collings (1984) and Leyens & Peters (2003) who reported that the hardness of Ti alloys increased with increased αTi phase proportions.

The as-cast Ti-8Nb-4Zr-*x*Cu (*x* = 0 and 5 wt%) alloys were considered the best compared to the as-cast Ti-6Nb-4Zr-*x*Cu alloys due to their better hardness with lower standard deviations, although the alloys had similar α+β phase proportions and microstructures.

6.4. Hot deformation behaviour of the as-received Ti-6Al-4V and Ti-10.1Ta-1.7Nb-1.6Zr alloys

The stress-strain curves (Figure 5.30) were used to evaluate the hot deformation behaviour of the as-received Ti-6Al-4V and Ti-10.1Ta-1.7Nb-1.6Zr (TTNZ) alloys, and their microstructures were compared. The alloys were hot compressed at 850°C and 950°C, and 0.1 s^{-1} and 10 s^{-1} strain rates.

The as-received Ti-6Al-4V alloy deformed at 850°C and 0.1 s^{-1} showed αTi laths (Figure 5.14a), which grew into globular αTi grains at 850°C and 10 s^{-1} (Figure 5.18a), and 950°C and 10 s^{-1} (Figure 5.18b). This agreed with Bodunrin (2018) who reported that the elongated αTi laths (Figure 5.14a) were due to flow softening by dislocation glide and climb, whereas globular αTi grains (Figures 5.18a and 5.18b) formed by dynamic globularisation. The results also suggested that the globularisation of αTi was influenced by the higher strain rate and an increased deformation temperature. The coarser αTi grains (Figure 5.18a) and the finer αTi grains (Figure 5.18b) suggested that a higher deformation temperature and strain rate resulted in a finer Ti-6Al-4V microstructure. The deformed Ti-6Al-4V microstructures (Figures 5.14 and 5.18) were different from the initial microstructure, which was a fully αTi lamellar microstructure (Figure 5.1). The SEM-BSE images (Figures 5.15 and 5.19) agreed with Dos Santos (2017) who showed αTi globules within the transformed βTi matrix (Figure 2.24).

The microstructures of the as-received Ti-10.1Ta-1.7Nb-1.6Zr (Figure 5.3a) and the deformed Ti-10.1Ta-1.7Nb-1.6Zr (Figures 5.22 and 5.26) alloys showed similar morphology of globular αTi grains. The deformed Ti-10.1Ta-1.7Nb-1.6Zr (Figures 5.22b and 5.26a) had finer αTi globules, and similar to the initial Ti-10.1Ta-1.7Nb-1.6Zr microstructure (Figure 5.3a), whereas Figures 5.22a and 5.26b showed coarser αTi globules. This suggested that a combination of lower temperature and higher strain rate, and/or a higher temperature and lower strain rate, gave a finer Ti-10.1Ta-1.7Nb-1.6Zr microstructure. Therefore, the effect of temperature and strain rate on the microstructures of the Ti-10.1Ta-1.7Nb-1.6Zr alloys was different to the Ti-6Al-4V alloys. The SEM-BSE images of deformed Ti-10.1Ta-1.7Nb-1.6Zr (Figures 5.23 and 5.27) showed αTi globules and transformed βTi, and consistent with Dos Santos (2017).

It was expected that the finer microstructures would give a higher hardness compared to the coarser microstructures (Lütjering, 1998; Leyens & Peters, 2003). This was confirmed (Figure 5.31) for finer TTNZ at 850°C and 10 s^{-1} (149 ± 6 HV), and 950°C and 0.1 s^{-1} (141 ± 4 HV) had a higher hardness compared to the coarser TTNZ at 850°C and 0.1 s^{-1} (138 ± 5 HV), and 950°C and 10 s^{-1} (136 ± 10 HV). These results (Figure 5.31) showed that the αTi laths in Ti-6Al-4V (Figure 5.14a) deformed at 850°C and 0.1 s^{-1} (324 ± 9 HV) had a higher hardness than both globular Ti-6Al-4V (Figures 5.18a and 5.18b) at 850°C and 10 s^{-1} (319 ± 5 HV), and 950°C and 10 s^{-1} (315 ± 7 HV). However, the hardness results were within each other's experimental error region for all deformed

Ti6Al4V alloys, and for all deformed TTNZ alloys (Figure 5.31). All deformed Ti6Al4V alloys were significantly harder than all deformed TTNZ alloys (Figure 5.31).

Bodunrin et al. (2017) reported that the αTi to βTi phase transformation contributes to flow softening at high temperatures. Figure 5.30 suggested the ductility of Ti-10.1Ta-1.7Nb-1.6Zr improved at higher temperature (950°C) and lower strain rate (0.1 s^{-1}), and at lower temperature (850°C) and higher strain rate (10 s^{-1}). The ductility of Ti-6Al-4V improved at lower deformation temperature (Figure 5.30), and was consistent with the results by Vanderhasten (2008), Bodunrin et al. (2017) and Dos Santos (2017).

Vanderhasten (2008) and Bodunrin (2018) reported that higher flow stresses were observed at higher strain rates and lower temperatures. This agreed with the results of the deformed Ti-6Al-4V and Ti-10.1Ta-1.7Nb-1.6Zr alloys (Figure 5.30). However, the Ti-6Al-4V alloy had higher flow stresses than Ti-10.1Ta-1.7Nb-1.6Zr, at 850°C (Figure 5.30). This showed that Ti-6Al-4V had higher compressive strength than Ti-10.1Ta-1.7Nb-1.6Zr, thus indicating that Ti-10.1Ta-1.7Nb-1.6Zr had better formability than Ti-6Al-4V. The Ti-10.1Ta-1.7Nb-1.6Zr alloy with more βTi stabilisers than Ti-6Al-4V would be easy to form into shape. This agreed with Leyens & Peters (2003) who reported βTi (bcc) as a softer phase than the αTi (hcp) phase.

The Ti-10.1Ta-1.7Nb-1.6Zr alloy was considered the better alloy due to its less flow stress, thus better formability than Ti-6Al-4V, whereas the Ti-8Nb-4Zr-*x*Cu (*x* = 0 and 5 wt%) alloys were considered to be better than the Ti-6Nb-4Zr-*x*Cu alloys due to their higher hardness. Comparing the hardnesses of all the alloys (Figures 5.13 and 5.31) showed that the new alloys in this work were similar to Ti-6Al-4V and all were higher than TTNZ. This suggests that they might be suitable for similar applications as Ti-6Al-4V, although more thorough testing needs to be done (tensile, fatigue).

Chapter 7: Conclusions

The following compositions had the α+β phases at 400°C: Ti-10.1Ta-1.7Nb-1.6Zr, Ti-6Nb-4Zr, Ti-8Nb-4Zr, Ti-6Nb-2Zr-1.7Ta, Ti-6Zr-4Ta-4Nb, Ti-4Ta-1.8Zr-1.5Mo, Ti-6Ta-2Zr-1.5Mo, Ti-8Ta-1.5Mo-1.5Zr, Ti-8Zr-4Ta-2Mo, Ti-3.5Ta-3Nb-3Zr, Ti-4.5Nb-4Ta-1.5Zr, Ti-6Zr-4Nb, Ti-6Zr-2Mo and Ti-10Ta-8Zr. The formation temperatures and proportions of Ti_2Cu increased with increased Cu additions (Cu = 1, 3, 5 and 10 wt%) in all compositions calculated by the Thermo-Calc program.

The bimodal microstructures of the as-cast Ti-6Nb-4Zr and Ti-8Nb-4Zr alloys comprised αTi laths within the βTi matrix. The Ti-6Nb-4Zr-5Cu and Ti-8Nb-4Zr-5Cu alloys showed similar αTi and βTi morphologies, and Ti_2Cu within the αTi grains and the βTi matrix. The EDX results indicated inhomogeneity in the Ti-6Nb-4Zr-*x*Cu and Ti-8Nb-4Zr-*x*Cu (*x* = 0 and 5 wt%) alloys. The XRD analyses of the as-cast Ti-6Nb-4Zr and Ti-8Nb-4Zr alloys showed peaks for αTi, and small peaks for βTi, and some Ti_2Cu for 5 wt% Cu added.

The as-cast Ti-6Nb-4Zr and Ti-8Nb-4Zr had a lower hardness compared to the as-received Ti-6Al-4V, but higher than the as-received Ti-10.1Ta-1.7Nb-1.6Zr (TTNZ). However, the Ti-6Nb-4Zr alloy had a slightly lower hardness compared to the Ti-8Nb-4Zr alloy. Adding 5 wt% Cu increased the hardness of the Ti-6Nb-4Zr and Ti-8Nb-4Zr alloys, due to the Ti_2Cu phase formed. The Ti-8Nb-4Zr-5Cu alloy had similar hardness to Ti-6Nb-4Zr-5Cu, but with a lower standard deviation, and was considered the better alloy. Generally, the new alloys produced had similar hardnesses to Ti-6Al-4V, and were higher than for TTNZ.

An increased deformation temperature and strain rate led to finer globular αTi, thus a finer Ti-6Al-4V microstructure. A combination of lower temperature and higher strain rate, and/or a higher temperature and lower strain rate, gave a finer Ti-10.1Ta-1.7Nb-1.6Zr microstructure. The XRD analyses of all deformed Ti-6Al-4V and Ti-10.1Ta-1.7Nb-1.6Zr alloys showed αTi and βTi peaks.

The hardness and the ductility of the Ti-6Al-4V and Ti-10.1Ta-1.7Nb-1.6Zr (TTNZ) alloys increased at lower deformation temperature (850°C). The as-received Ti-6Al-4V had a higher hardness than all deformed Ti-6Al-4V and Ti-10.1Ta-1.7Nb-1.6Zr (TTNZ) alloys.

The Ti-6Al-4V alloy had higher flow stress than the Ti-10.1Ta-1.7Nb-1.6Zr (TTNZ) alloy. Therefore, the Ti-10.1Ta-1.7Nb-1.6Zr alloy was considered the better alloy due to its lower flow stress, which indicated better formability.

Chapter 8: Recommendations

For future studies of the potential Ti-6Nb-4Zr-*x*Cu and Ti-8Nb-4Zr-*x*Cu (*x* = 0 and 5 wt%) alloys, the following recommendations were made:

- Study the corrosion and antibacterial properties of the Ti-6Nb-4Zr-5Cu and Ti-8Nb-4Zr-5Cu alloys.
- Anneal the Ti-6Nb-4Zr-*x*Cu and Ti-8Nb-4Zr-*x*Cu (*x* = 0 and 5 wt%) alloys to promote homogeneity, then check EDX and XRD.
- Study the thermo-mechanical properties of Ti-6Nb-4Zr and Ti-8Nb-4Zr, and compare with the Ti-6Al-4V and Ti-10.1Ta-1.7Nb-1.6Zr (TTNZ) alloys.
- Undertake more thorough mechanical tests on the new alloys, e.g. tensile and fatiguge testing.

References

Ahmed T.A., Long M., Silverstri J., Ruiz C. & Rack H.J.: A new low modulus, biocompatible titanium alloy, Titanium 95'. The Institute of Materials, London. *Science and Technology* 2 (1996) 1760-1767.

Akahori T., Niinomi M., Fukui H. & Suzuki A.: Fatigue and Corrosion Characteristics of New Beta Type Titanium Alloy Conducted with Various Thermo-Mechanical Treatments. Special Issue on Recent Research and Developments in Titanium and Its Alloys. The Japan Institute of Metals. *Materials Transactions* 45 (2004) 1540-1548.

Akahori T., Niinomi M., Fukui H., Ogawa M. & Toda H.: Improvement in fatigue characteristics of newly developed beta type titanium alloy for biomedical applications by thermo-mechanical treatments. *Materials Science and Engineering* C 25 (2005) 248-254.

Alani A., Kelleher M. & Bishop K.: Peri-implantitis. Part 1: Scope of the problem. *British Dental Journal* 217 (2014) 281-287.

Albrektsson T.: Hard tissue implant interface. *Australian Dental Journal* 53 (2008) 34-38.

Albrektsson T., Brånemark P.I. & Zarb G.A.: Bone Tissue Response. *Tissue-integrated prostheses,* Quintessenz Verlag, Berlin. ISBN 978-0-86715-129-9 C 6 (2015) 120-129.

Altan T., Boulger F.W., Becker J.R., Akgerman N. & Henning H.J.: "Forging equipment, materials and practices", Columbus, Ohio: *Metals and Ceramics Information Centre,* MCIC-HB-03 (1973) 406-429.

Andersson J.O., Helander T., Höglund L., Shi P.F. & Sundman B.: Thermo-Calc and DICTRA, Computational tools for materials science. *Calphad* 26 (2002) 273-312.

Ansara I., Dinsdale A.T, Rand M.H, editors: Thermochemical database for light metal alloys, EUR18499, Final report: EU-COST507. vol. 2 (1998). As quoted by Stenlund P., Omar O., Brohede U., Norgren S., Norlindh B., Johansson A., Lausmaa J., Thomsen P. & Palmquist A.: Bone response to a novel Ti-Ta-Nb-Zr alloy. *Acta Biomaterialia* 20 (2015) 165-175.

Ansara I., Ivanchenko V., Cornish L., Ukabhai K. & Nape K.: Cu-Ti Binary Phase Diagram Evaluation, in *MSI Eureka*, Watson, A. (Ed.), MSI, Materials Science International Services GmbH, Stuttgart (2021), Document ID: 20.11457.2.4.

Aoki T., Okafor I.C.I., Watanabe I., Hattori M., Oda Y. & Okabe T.: Mechanical properties of cast Ti-6Al-4V-*xCu* alloys. *Journal of Oral Rehabilitation* 31 (2004) 1109-1114.

Appel F. & Oehring M.: γ-titanium aluminide alloys: Alloy design and properties. *In Titanium and Titanium Alloys,* 1st edition. Leyens C. & Peters M., editors: Wiley-VCH Verlag GmbH & Co. KGaA: Weinheim, Germany (2003) 89-152.

Arciola C.R., Campoccia D., Speziale P., Montanaro L. & Costerton J.W.: Biofilm formation in Staphylococcus implant infections. A review of molecular mechanisms and implications for biofilm-resistant materials. *Biomaterials* 33 (2012) 5967-5982.

Arulselvan M. & Ganesan G.: Hot Deformation Behaviour of Ti-6Al-4V in Different Strain Rates. *International Journal of Innovative Research in Advanced Engineering* 1 (2014) 207-212.

ASM International, Material Properties Handbook: *Titanium Alloys*. ASM International (1994) 483-636.

Atieh M.A., Alsabeeha N.H.M., Faggion C.M. & Duncan W.J.: The frequency of peri-implant diseases: a systematic review and meta-analysis. *Journal of Periodontology* 84 (2013) 1586-1598.

Banerjee R., Nag S. & Fraser H.L.: A novel combinatorial approach to the development of beta titanium alloys for orthopaedic implants. *Materials Science and Engineering* C 25 (2005) 282-289.

Bania P.J.: Beta Titanium Alloys and Their Role in the Titanium Industry In: Eylon D., Boyer R.R., Koss D.A., editors. *Titanium Alloys in the 1990's*. Warrendale: The Mineral, Metals & Materials Society (1993) 3-14. As quoted by Long & Rack (1998).

Bania P.J.: Beta Titanium Alloys and Their Role in the Titanium Industry. *Journal of Materials* 46 (1994) 16-19.

Bodunrin M.O., Prozesky D.J. & Chown L.H.: Hot-deformation Behaviour of α+β Ti-Al-V-Fe Experimental Alloys. *Proceedings of the 20th International ESAFORM Conference on Material Forming AIP Conference Proc. 1896*. Published by AIP Publishing. 978-0-7354-1580-5/$30.00, (2017) 160019-1-160019-6.

Bodunrin M.O.: *Hot deformation and corrosion behaviour of low-cost α+β titanium alloys with aluminium, vanadium and iron additions,* School of Chemical and Metallurgical Engineering, University of the Witwatersrand, Johannesburg. PhD Thesis (2018) 1-293.

Bothe R.T., Beaton L.E. & Davenport H.A.: Reaction of Bone to Multiple Metallic Implants. *Surgery, Gynecology and Obstetrics* 71 (1940) 98-602.

Boyer R.R. & Hall J.A.: Microstructure-property relationships in titanium alloys (critical review). In: Froes F.H., Caplan I., editors. *Titanium 92'. Science and Technology,* Warrendale, PA, USA. The Mineral, Metals and Materials Society (1993) 77-88. As quoted by Long & Rack (1998).

Brånemark P.I., Breine U., Adell R., Hansson B.O., Lindström J. & Ohlsson Å.: Intra-Osseous Anchorage of Dental Prostheses: *International Experimental Studies, Scandinavian Journal of Plastic Reconstructive Surgery* 3 (1969) 81-100.

Brånemark P.I., Hansson B.O., Adell R., Breine U., Lindstrom J. & Hallen O.: Osseointegrated implants in the treatment of the edentulous jaw. Experience from a 10-year period. *Scandinavian Journal of Plastic and Reconstructive Surgery* 16 (1977) 1-132.

Bull P.C., Thomas G.R., Rommens J.M., Forbes J.R. & Cox D.W.: The Wilson disease gene is a putative copper transporting P-type ATPase similar to the Menkes gene. *Nature Genetics* 5 (1993) 327-337.

Canale P. & Servant C.: Thermodynamic Assessment of the Cu-Ti System Taking into Account the New Stable Phase $CuTi_3$. *Zeitschrift für Metallkunde* 93 (2002) 273-276.

Cao Y., Su B., Chinnaraj S., Jana S., Bowen L., Charlton S., Duan P., Jakubovics N.S. & Chen J.: Nanostructured titanium surfaces exhibit recalcitrance towards *Staphylococcus epidermidis* biofilm formation. *Science Report* 8 (2018).

Chandrasekaran M. & Zhang S.X.: Effect of alloying time and composition on the mechanical properties of Ti alloy. *Materials Science and Engineering* A 394 (2005) 220-228.

Collings E.W.: *The Physical Metallurgy of Titanium Alloys*, ASM Series in Metal Processing. Gegel H.L., editor. Cleveland, Metals Park, OH: American Society for Metals (1984) 1-261. As quoted by Long & Rack (1998).

Damkroger B.K. & Edwards G.R.: *Continuous cooling transformation kinetics in alpha-beta titanium alloys. Simulation and Theory of Evolving Microstructures*. Metals and Materials Society (1990) 129-150.

Derks J. & Tomasi C.: Peri-implant health and disease. A systematic review of current epidemiology. *Journal of Clinical Periodontology 42 Supplementary* 16 (2015) 158-171.

Ding R. & Guo Z.X.: Microstructural evolution of a Ti-6Al-4V alloy during β-phase processing: experimental and simulative investigations. *Materials Science and Engineering* A 365 (2004) 172-179.

Donachie M.J.: *Titanium: A Technical Guide, 2nd Edition*. ASM International, Materials Park, OH (2000) 512-513.

Dos Santos M.W.B.: Investigation of the mechanical behaviour and microstructural evolution of titanium alloys under superplastic and hot forming conditions. *Materials*. Ecole des Mines d'Albi-Carmaux; Escola politécnica, São Paulo (2017) 1-135.

Eisenbarth E., Velten D., Müller M., Thull R. & Breme J.: Biocompatibility of β-stabilizing elements of titanium alloys. *Biomaterials* 25 (2004) 5705-13.

Fan Z.: On the Young's Moduli of Ti-6Al-4V Alloys. *Scripta Metallurgica et Materiala* 29 (1993) 1427-1432.

Filip R., Kubiak K., Ziaja W. & Sieniawski J.: The effect of microstructure on the mechanical properties of two-phase titanium alloys. *Journal of Materials Processing Technology*, 7th International Scientific Conference: Achievements in Mechanical & Materials Engineering 133 (2003) 84-89.

Fowler L., Janson O., Engqvist H., Norgren S. & Öhman-Mägi C.: Antibacterial investigation of titanium-copper alloys using luminescent *Staphylococcus epidermidis* in a direct contact test. *Materials Science and Engineering* C 97 (2019a) 707-714.

Fowler L., Masia N., Cornish L.A., Chown L.H., Engqvist H., Norgren S. & Öhman-Mägi C.: Development of antibacterial Ti-*x*Cu alloys for dental applications: Effects of Ageing for alloys with up to 10 wt% Cu. *Materials-Biomaterials* 12 (2019b) 4017, 1-13.

Fowler L., Engqvist H. & Öhman-Mägi C.: Effect of Cu ion concentration on bacteria and cells. *Materials* 12, 3798 (2019c) 1-13.

Fowler L., Van Vuuren A.J., Goosen W., Engqvist H., Öhman- Mägi C. & Norgren S.: Investigation of copper alloying in a TNTZ-Cu*x* alloy. *Materials 12* (2019d) 3691, 1-13.

Fransson C., Lekholm U., Jemt T. & Berglundh T.: Prevalence of subjects with progressive bone loss at implants. *Clinical and Oral Implants Resources* 16 (2005) 440-446.

Fransson C., Wennström J., Tomasi C. & Berglundh T.: Extent of peri-implantitis- associated bone loss. *Journal of Clinical Periodontology* 36 (2009) 357-363.

Fujii H. & Maeda T.: Titanium Alloys Developed by Nippon Steel & Sumitomo Metal Corporation. *Technical Report* 106 (2014) 16-21.

Gepreel M.A.H. & Niinomi M.: Biocompatibility of Ti-alloys for long-term implantation. *Journal of the Mechanical Behaviour of Biomedical Materials* 20 (2013) 407-415.

Gilbert R. & Shannon C. R.: *Heat treating of titanium alloys*. ASM handbook volume 4*:* Heat treating (1991) 913-923.

Gill S.R., Fouts D.E., Archer G.L., Mongodin E.F., Deboy R.T., Ravel J., Paulsen I.T., Kolonay J.F., Brinkac L., Beanan M., Dodson R.J., Daugherty S.C., Madupu R., Angiuoli S.V., Durkin A.S., Haft D.H., Vamathevan J., Khouri H., Utterback T., Lee C., Dimitrov G., Jiang L., Qin H., Weidman J., Tran K., Kang K., Hance I.R., Nelson K.E. & Fraser C.M.: Insights on evolution of virulence and resistance from the complete genome analysis of an early methicillin-resistant *Staphylococcus aureus* strain and a biofilm-producing methicillin-resistant *Staphylococcus epidermidis* strain. *Journal of Bacteriology* 187 (2005) 2426-2438.

Guillemot F., Prima F., Bareille R., Gordin D., Gloriant T., Porte-Durrieu M.C., Ansel D. & Baquey C.: Design of new titanium alloys for orthopaedic applications. *Medical & Biological Engineering & Computing* 42 (2004) 137-141.

Guillermet A.F.: Thermodynamic analysis of the stable phases in the Zr-Nb system and calculation of the phase-diagram. *Zeitschrift für Metallkunde* 82 (1991) 478-487.

Gurappa I.: Characterization of different materials for corrosion resistance under simulated body fluid conditions. *Materials Characterization* 49 (2002) 73-79.

Han C., Johansson C., Wennerberg A. & Albrektsson T.: Quantitative and qualitative investigations of surface enlarged titanium and titanium alloy implants. *Clinical Oral Implants Research* 9 (1998) 1-10.

Hanawa T.: Research and development of metals for medical devices based on clinical needs. *Science and Technology of Advanced Materials* 13 (2012) 1-15.

Hanssen A.D. & Rand J.A.: Evaluation and treatment of infection at the site of a total hip or knee arthroplasty. *Journal of Bone and Joint Surgery* A 80 (1998) 910-922.

Hao Y.L., Yang R., Niinomi M., Kuroda D., Zhou Y.L., Fukunaga K. & Suzuki A.: Young's modulus and mechanical properties of Ti-29Nb-13Ta-4.6Zr in relation to α'' martensite. *Metallurgical and Materials Transactions* A 33 (2002) 3137-3144.

Hao Y.L., Li S.J., Sun S.Y. & Yang R.: Effect of Zr and Sn on Young's modulus and superelasticity of Ti-Nb-based alloys. *Materials Science and Engineering* A 441 (2006) 112-118.

Hawkey P.M.: The growing burden of antimicrobial resistance. *Journal of Antimicrobial Chemother.* 62 (2008) 1-9.

Ho W.F., Ju C.P. & Chern Lin J.H.: Structure and properties of cast binary Ti-Mo alloys. *Biomaterial* 20 (1999) 2115-2122.

Huiskes H.W.J., Weinans H. & van Rietbergen B.: The relationship between stress shielding and bone resorption around total hip stems and the effects of flexible materials. *Clinics and Orthopaedics* 274 (1992) 124-134.

Hultin M., Gustafson A., Hallström H., Johansson L.A., Ekfeldt A. & Klinge B.: Microbiological findings and host response in patients with peri-implantitis. *Clinical and Oral Implants Resources* 13 (2002) 349-358.

Jablokov V.R., Nutt M.J., Richelsoph M.E. & Fraser H.L.: Influence of Oxygen Content on the Mechanical Properties of Titanium-35Niobium-7Zirconium-5Tantalum Beta Titanium Alloy. *Journal of ASTM International* 2 (2005) 1-12.

Jäger E., Schmidt J., Pfuch A., Spange S., Beier O., Jäger N., Jantschner O., Daniel R. & Mitterer C.: Antibacterial silicon oxide thin films doped with zinc and copper grown by atmospheric pressure plasma chemical vapor deposition. *Nanomaterials* 9 (2019) 1-255.

Jha B.K. & Kumar V.: Role of Thermo-mechanical Simulation in the Development of Special Steel Products. *Published in the Proceedings of National Conference and 2nd Gleeble User Workshop, RDCIS,* Ranchi (2010) 18-19.

Jha S.K. & Ravichandran K.S.: High-Cycle Fatigue Resistance in Beta-Titanium Alloys. *The Journal of the Minerals, Metals & Materials Society (TMS)* 52 (2000) 30-35.

Jin X., Gao L., Liu E., Yu F., Shu X. & Wang H.: Microstructure, corrosion and tribological and antibacterial properties of Ti-Cu coated stainless steel. *Journal of Mechanical Behaviour of Biomedical Materials* 50 (2015) 23-32.

Johansson C., Lausmaa J., Ask M., Hansson H.A. & Albrektsson T.: Ultrastructural differences of the interface zone between bone and Ti-6Al-4V or commercially pure titanium. *Journal of Biomedical Engineering* 11 (1989) 3-8.

Jung C., Straumann L., Kessler A., Pieles U. & de Wild M.: Antibacterial copper deposited onto and into the oxide layer of titanium implants. *Bio and Nano Materials* 15 (2014) 1-180.

Jung T.K., Semboshi S., Masahashi N. & Hanada S.: Mechanical properties and microstructures of β Ti-25Nb-11Sn ternary alloy for biomedical applications. *Materials Science and Engineering* C 33 (2013) 1629-1635.

Ke Z., Yi C., Zhang L., He Z., Tan J. & Jiang Y.: Characterization of a new Ti-13Nb-13Zr-10Cu alloy with enhanced antibacterial activity for biomedical applications. *Materials Letters* 253 (2019) 335-338.

Khan S.T., Khan M., Ahmad J., Wahab R., Abd-Elkader O.H., Musarrat J., Alkhathlan H.Z. & Al-Kedhairy A.A.: Thymol and carvacrol induce autolysis, stress, growth inhibition and reduce the biofilm formation by *Streptococcus mutans*. *AMB Express* 7 (2017).

Kikuchi M., Takada Y., Kiyosue S., Yoda M., Woldu M., Cai Z., Okuno O. & Okabe T.: Mechanical properties and microstructures of cast Ti-Cu alloys. *Dental Materials* 19 (2003) 174-181.

Kokuoz B.K, Kosaka Y. & Rack H.J.: High-Cycle Fatigue Crack Initiation and Growth in TIMETAL LCB. *Journal of Materials Engineering and Performance* 14 (2005) 773-777.

Kolli R.P. & Devaraj A.: A Review of Metastable Beta Titanium Alloys. *Metals* 8 (2018) 1-41.

Koontz P.: *Guidelines for the Safe Use of Hydrofluoric Acid*. Department of Chemistry and Chemical Biology. Harvard University (2013) 1-8.

Kovacs P. & Davidson J.A.: The electrochemical behaviour of a new titanium alloy with superior biocompatibility. *In: Titanium 92':* Science and Technology, Warrendale. The Minerals, Metals and Materials Society (1993) 2705-2712. As quoted by Long & Rack (1998).

Kumar K.C.H., Ansara I., Wollants P. & Delaey L.: Thermodynamic optimisation of the Cu-Ti system. *Zeitschrift für Metallkunde* 87 (1996) 666-672.

Kumar V.: Thermo-Mechanical Simulation Using Gleeble System-Advantages & Limitations. *National Conference on Thermo-mechanical processing of Steels & 5th Gleeble User Workshop,* India (2015) 146-156.

Kuroda D., Niinomi M., Morinaga M., Kato Y. & Yashiro T.: Design and mechanical properties of new β type titanium alloys for implant materials, A Structure and Material Properties, Microstructural Process. *Materials Science and Engineering* A 243 (1998) 244-249.

Laheurte P., Prima F., Eberhardt A., Gloriant T., Wary M. & Patoor E.: Mechanical properties of low modulus β titanium alloys designed from the electronic approach. *Journal of the Mechanical Behaviour of Biomedical Materials* 3 (2010) 565-573.

Lee Y.T. & Welsch G.: Young's Modulus and Damping of Ti-6AI-4V Alloy as a Function of Heat Treatment and Oxygen Concentration. *Materials Science and Engineering* A 128 (1990) 77-89.

Leventhal G.S. & Bone Jt J.: Titanium, a Metal for Surgery. *The Journal of Bone and Joint Surgery* 33 (1951) 473-474.

Leyens C. & Peters M.: *Titanium and Titanium Alloys*. Wiley-VCH, ISBN 3-527-30534-3 (2003) 1-58.

Li Y., Onodera E. & Chiba A.: Friction coefficient in hot compression of cylindrical sample. *Materials Transactions* 51 (2010) 1210-1215.

Lin J.H.C., Moser J.B., Taira M. & Greener E.H.: Cu-Ti, Co-Ti and Ni-Ti systems: corrosion and micro-hardness. *Journal of Oral Rehabilitation* 17 (1990) 383-393.

Liu C. & Zhang E.: Biocorrosion properties of antibacterial Ti-10Cu sintered alloy in several simulated biological solutions. *Journal of Materials Science, Materials and Medical* 26 (2015) 1-142.

Liu J., Li F., Liu C., Wang H., Ren B., Yang K. & Zhang E.: Effect of Cu content on the antibacterial activity of titanium–copper sintered alloys. *Materials Science and Engineering* C 35 (2014a) 392-400.

Liu J., Zhang X., Wang H., Li F., Li M., Yang K. & Zhang E.: The antibacterial properties and biocompatibility of a Ti-Cu sintered alloy for biomedical application. *Biomedical and Materials* 9 (2014b) 1-11.

Liu X., Chu P.K. & Ding C.: Surface modification of titanium, titanium alloys, and related materials for biomedical applications. *Materials Science and Engineering* R 47 (2004) 49–121.

Long M. & Rack H.J.: Titanium alloys in total joint replacement-A materials science perspective. *Biomaterials* 19 (1998) 1621-1639.

Long Y., Wang T., Zhang H.Y. & Huang X.L.: Enhanced ductility in a bimodal ultrafine-grained Ti-6Al-4V alloy fabricated by high energy ball milling and spark plasma sintering. *Materials Science and Engineering* A 608 (2014) 82-89.

Lütjering G.: Influence of processing on microstructure and mechanical properties of (α+β) titanium alloys. *Materials Science and Engineering* A 243 (1998) 32-45.

Lütjering G. & Williams J.C.: *Titanium*. Engineering Materials and Processes. Springer Verlag: Berlin, Heidelberg, New York (2003) 247-281.

Ma Z., Ren L., Liu R., Yang K., Zhang Y., Liao Z., Liu W., Qi M. & Misra R.D.K.: Effect of heat treatment on Cu distribution, antibacterial performance and cytotoxicity of Ti-6Al-4V-5Cu alloy. *Journal of Material Science and Technology* 31 (2015) 723-732.

Manivasagam G., Mundali U.K., Asokamani R. & Raj B.: Corrosion and microstructural aspects of titanium and its alloys as orthopaedic devices. *Corrosion Reviews* 21 (2003) 2-3.

Massalski T.B.: *Binary Alloys Phase Diagrams*, 7th Edition. ASM International. Metals Park OH 1 (3) (1990). ISBN: 0-87170-405-6.

Mathews S., Hans M., Mücklich F. & Solioz M.: Contact killing of bacteria on copper is suppressed if bacterial-metal contact is prevented and is induced on iron by copper ions. *Applied and Environmental Microbiology* 79 (2013) 2605-2611.

Matlakhova L.A., Matlakhova A.N., Monteiro S.N., Fedotov S.G. & Goncharenko B.A.: Properties and structural characteristics of Ti-Nb-Al alloys. *Materials Science and Engineering* A 393 (2005) 320-326.

Mazel A., Belkacemi S., Tavitian P., Stéphan G., Tardivo D., Catherine J.H., Aboudharam G.: Peri-implantitis risk factors: A prospective evaluation. *Journal of Investigations, Clinical and Dental* 10 (2019) 12398-41.

Meng Q., Guo S., Liu Q., Hu L. & Zhao X.: A β-type TiNbZr alloy with low modulus and high strength for biomedical applications. *Progress in Natural Science: Materials International* 24 (2014) 157-162.

Michels H.T., Noyce J.O. & Keevil C.W.: Effects of temperature and humidity on the efficacy of methicillin-resistant *Staphylococcus aureus* challenged antimicrobial materials containing silver and copper. *Letters in Applied Microbiology*. 49 (2009) 191-195.

Mishra A.K., Davidson J.A., Kovacs P. & Poggie R.A.: Ti-13Nb-13Zr: a new low modulus, high strength, corrosion resistant near-beta alloy for orthopaedic implants. In: *Beta Titanium in the 1990s*. Warrendale. The Minerals, Metals and Materials Society (1993) 61-72. As quoted by Long & Rack (1998).

Moreira J.M.R., Ponmozhi J., Campos J.B.L.M., Miranda J.M. & Mergulhão F.J.: Micro-and macro-flow systems to study *Escherichia coli* adhesion to biomedical materials. *Chemical Engineering Sciences* 126 (2015) 440-445.

Murray J.L.: The Cu-Ti (copper-titanium) system. *Bulletin of Alloy Phase Diagrams* 4 (1983) 81-95.

Nag S., Banerjee R., Stechschulte J. & Fraser H.L.: Comparison of microstructural evolution in Ti-Mo-Zr-Fe and Ti-15Mo biocompatible alloys. *Journal of Material Science: Materials in Medicine* 16 (2005) 679-685.

Nag S., Banerjee R. & Fraser H.L.: A novel combinatorial approach for understanding microstructural evolution and its relationship to mechanical properties in metallic biomaterials. *Acta Biomaterialia* 3 (2007) 369-376.

Niinomi M.: Mechanical properties of biomedical titanium alloys. *Materials Science and Engineering* A 243 (1998) 231-236.

Niinomi M.: Recent research and development in titanium alloys for biomedical applications and healthcare goods. *Science and Technology of Advanced Materials* 4 (2003a) 445-454.

Niinomi M.: Fatigue performance and cyto-toxicity of low rigidity titanium alloy, Ti-29Nb-13Ta-4.6Zr. *Biomaterials* 24 (2003b) 2673-2683.

Niinomi M. & Nakai M.: Titanium-based biomaterials for preventing stress shielding between implant devices and bone. *International Journal of Biomaterials* (2011) 1-10.

Niinomi M., Liu Y., Nakai M., Liu H. & Li H.: Biomedical titanium alloys with Young's moduli close to that of cortical bone. *Regeneration of Biomaterials* 3 (2016) 173-185.

Nutt M.J., Jablokov V.R., Richelsoph M.E. & Freese H.H.: The Application of Ti-15Mo Beta Titanium Alloy in High Strength Structural Orthopaedic Applications. *Journal of ASTM International* 2 (2005) 1-18.

Okazaki Y., Gotoh E., Manabe T. & Kobayashi K.: Comparison of metal concentrations in rat tibia tissues with various metallic implants. *Biomaterials* 25 (2004) 5913-5920.

Okazaki Y. & Gotoh E.: Comparison of metal release from various metallic biomaterials *in vitro*. *Biomaterials* 26 (2005) 11-21.

Olsson N.: *Mechanical Properties, Phases and Structures of Titanium Alloys.* Master of Science Thesis Stockholm: Royal Institute of Technology, KTH, Sweden. Thesis (2008) 1-62.

Pearson C.: The viscous properties of extruded eutectic alloys of lead-tin and bismuth-tin. *Journal of the Institute of Metals* 54 (1934) 111-124.

Pederson R.: *Microstructure and Phase Transformation of Ti-6Al-4V*. Department of Applied Physics and Mechanical Engineering. Division of Engineering Materials. Thesis (2002) 1-62. ISSN: 1402-1757. ISRN: LUT-LIC-02/30-SE.

Peters J.O. & Lütjering G.: Comparison of the Fatigue and Fracture of α+β and β Titanium Alloys. *Metallurgical and Materials Transactions* A 32 (2001) 1-66.

Polmear J.J.: *Titanium alloys*. In: Light alloys. London, UK, Edward Arnold Publications (1981) 299-365.

Rack H.J. & Qazi J.I.: Titanium alloys for biomedical applications. *Materials Science and Engineering* C 26 (2006) 1269-1277.

Rayant G.A.: *Peri-Implantitis,* Gum Disease Can Cause Dental Implant Failure. *Dear Doctor, Inc. 2016 (https://www.deardoctor.com%2Farticles%2Fperi-implantitis-can-cause-implant-failure).*

Ren L., Zheng M., Li M., Zhang Y., Liu W., Liao Z. & Yang K.: Antibacterial Properties of Ti-6Al-4V-*x*Cu Alloys. *Journal of Material Science and Technology* 30 (2014) 699-705.

Roebuck B., Lord J.D., Brooks M., Loveday M.S., Sellars C.M. & Evans R.W.: Measurement of flow stress in hot axisymmetric compression tests. *Materials at High Temperature* 23 (2006) 59-83.

Roos-Jansaker A-M., Renvert S. & Egelberg J.: Treatment of peri-implant infections: a literature review. *Journal of Clinical Periodontology* 30 (2003) 467-485.

Russel A.D. & Hugo W.B.: Antimicrobial activity and action of silver. *Progress in Medicals and Chemistry* 31 (1994) 351-370.

Schutz R.W.: An overview of beta titanium alloy environmental behaviour. In: Eylon D., Boyer R.R., Koss D.A., editors. *Beta Titanium Alloys in the 1990s*. Warrendale, PA. The Mineral, Metals and Materials Society (1993) 75-91. As quoted by Long & Rack (1998).

Shaikh A.A., Kashyap B.P. & Chauthai A.: Identification of Favorable Hot Working Condition for Ti-6Al-4V Alloy. *National Conference on Thermo-mechanical processing of Steels & 5th Gleeble User Workshop,* India (2015) 78-91.

Shell E.B. & Semiatin S.L.: Effect of Initial Microstructure on Plastic Flow and Dynamic Globularization during Hot Working of Ti-6Al-4V. *Metallurgical and Materials Transactions A* A 30 (1999) 3219-3229.

Shirai T., Tsuchiya H., Shimizu T., Ohtani K., Zen Y. & Tomita K.: Prevention of pin tract infection with titanium–copper alloys. Biomedical Applications. *Journal of Biomedical Materials Resources, Biomaterials* B 91 (2009) 373-380.

Smith W.F.: *Structure and Properties of Engineering Alloys.* New York, USA, McGraw-Hill Publishing (1981) 433-484.

Song D.H., Uhm S.H., Kim S.E., Kwon J.S., Han J.G. & Kim K.N.: Synthesis of titanium oxide thin films containing antibacterial silver nanoparticles by a reactive magnetron co-sputtering system for application in biomedical implants. *Materials Resources Bulletin* 47 (2012) 2994-2998.

Song Y., Xu D.S., Yang R., Li D., Wu W.T. & Guo Z.X.: Theoretical study of the effects of alloying elements on the strength and modulus of β-type bio-titanium alloys. A Structure and Material Properties, Microstructural Process. *Materials Science and Engineering* A 260 (1999a) 269-274.

Song Y., Yang R., Li D., Hu Z. & Guo Z.: Calculation of bulk modulus of titanium alloys by first principles electronic structure theory. *Journal of Computer-Aided Materials Design* 6 (1999b) 355-362.

Steinemann S.G.: Titanium-the material of choice? *Peridontology 2000* 17 (1998) 7-21.

Stenlund P., Omar O., Brohede U., Norgren S., Norlindh B., Johansson A., Lausmaa J., Thomsen P. & Palmquist A.: Bone response to a novel Ti-Ta-Nb-Zr alloy. *Acta Biomaterialia* 20 (2015) 165-175.

Stewart P.S.: Mechanisms of antibiotic resistance in bacterial biofilms. *International Journal of Medical and Microbiology* 292 (2002) 107-113.

Stranak V., Wulf H., Rebl H., Zietz C., Arndt K., Bogdanowicz R., Nebe B., Bader R., Podbielski A. & Hubicka Z.: Deposition of thin titanium-copper films with antimicrobial effect by advanced magnetron sputtering methods. *Materials Science and Engineering* C 31 (2011) 1512-1519.

Struers: Metallographic preparation of titanium (2016). As quoted by Bodunrin (2018).

Sumner D.R., Turner T.M., Igloria R., Urban R.M. & Galante J.O.: Functional adaptation and ingrowth of bone vary as a function of hip implant stiffness. *Journal of Biomechanical* 31 (1998) 909-917.

Takada Y., Nakajima H., Okuno O. & Okabe T.: Microstructure and corrosion behaviour of binary titanium alloys. *Journal of Dental Materials* 20 (2001) 34-52.

Takahashi M., Kikuchi M., Takada Y. & Okuno O.: Mechanical Properties and Microstructures of Dental Cast Ti-Ag and Ti-Cu Alloys. *Journal of Dental Materials* 21 (2002) 270-280.

Tiley J.S.: *Modeling of Microstructure Property Relationships in Ti-6Al-4V*. The Ohio State University, Ohio. Doctoral Thesis (2002) 1-208.

Toss H.C.A.: *Titanium Alloys for Load Bearing Bone Implant Purposes.* Master of Science Thesis in the Master Degree Programme, MPBME Biomedical Engineering. Department of Signals and Systems Chalmers University of Technology Göteborg, Sweden. Thesis (2009) 1-32.

Unosson E., Morgenstern M., Engqvist H. & Welch K.: In vitro antibacterial properties and UV induced response from *Staphylococcus epidermidis* on Ag/Ti oxide thin films. *Journal of Materials Science, Materials and Medicals* 27 (2016) 1-49.

Vander Voort G.F.: Materials characterization & testing: microstructure of titanium and its alloys. *Industrial Heating.* Research & Technology, Buehler Ltd., Lake Bluff, Illinois (2006) 77–84.

Vanderhasten M.: Ti-6Al-4V: *Deformation map and modelisation of tensile behaviour.* Katholieke Universiteit Leuven. Doctoral Thesis (2008) 1-150.

Vasudevan S., Joseph H.A., Swamy S.S. & Solomon A.P.: *Antibiotic Resistance in Biofilms*; ACS Symposium Series. Rathinam N.K. & Sani R.K., editors. American Chemical Society: Washington, DC, USA (2019) 205-224.

Velasco C.S., Cavaleiro A. & Carvalho S.: Functional properties of ceramic-Ag nanocomposite coatings produced by magnetron sputtering. *Progress in Materials Science* 84 (2016) 158-191.

Wang K.: The use of titanium for medical applications in the USA. *Materials Science and Engineering* A 213 (1996) 134-137.

Wang K.K., Gustavson L.J. & Dumbleton J.H.: The characterization of Ti-12Mo-6Zr-2Fe. A new biocompatible titanium alloy developed for surgical implants, *Beta Titanium in the 1990's*. Warrendale, Pennsylvania. The Mineral, Metals and Materials Society (1993) 49-60. As quoted by Long & Rack (1998).

Wang K.L., Lu S.Q., Fu M.W., Li X., Dong X.J.: Identification of the optimal (α+β) forging process parameters of Ti-6.5Al-3.5Mo-1.5Zr-0.3Si based on processing-maps. *Materials Science and Engineering* A 527 (2010) 7279-7285.

Welsch G., Boyer R. & Collings E.W.: *Materials Properties Handbook: Titanium Alloys*. ASM International. Materials Park, Ohio (1993) 1-3.

Wood E.: *Thermal Processing and Mechanical Properties of Beta Phase Titanium Alloys for Biomedical Applications*. Department of Metallurgical and Materials Engineering, Montana Tech of the University of Montana, Butte. Thesis (2015) 1-69: *Graduate Theses & Non-Theses.* 26. http://digitalcommons.mtech.edu/grad_rsch/26

Yanovska A.A., Stanislavov A.S., Sukhodub L.B., Kuznetsov V.N., Yu V., Illiashenko I., Danilchenko S.N. & Sukhodub L.F.: Silver-doped hydroxyapatite coatings formed on Ti-6Al-4V substrates and their characterization. *Materials Science and Engineering* C 36 (2014) 215-220.

Yoda I., Koseki H., Tomita M., Shida T., Horiuchi H., Sakoda H. & Osaki M.: Effect of surface roughness of biomaterials on *Staphylococcus epidermidis* adhesion. *BMC Microbiology* 14 (2014) 1-234.

Zhang D.C., Yang S., Wei M., Mao Y.F., Tan C.G. & Lin J.G.: Effect of Sn addition on the microstructure and superelasticity in Ti-Nb-Mo-Sn alloys. *Journal of the Mechanical Behaviour of Biomedical Materials* 13 (2012) 156-165.

Zhang E., Zheng L., Liu J., Ba B. & Liu C.: Influence of Cu content on the cell biocompatibility of Ti-Cu sintered alloys. *Materials Science and Engineering* C 46 (2015) 148-157.

Zhang E., Ren J., Li S., Yang L. & Qin G.: Optimization of mechanical properties, biocorrosion properties and antibacterial properties of as-cast Ti-Cu alloys. *Biomedical and Materials* 11 (2016a) 065001-5.

Zhang E., Wang X., Chen M. & Hou B.: Effect of the existing form of Cu element on the mechanical, bi-corrosion and antibacterial properties of Ti-Cu alloys for biomedical application. *Materials Science and Engineering* C 69 (2016b) 1210-1221.

Zhang Y.Q., Ren S.X., Li H.L., Wang Y.X., Fu G., Yang J., Qin Z.Q., Miao Y.G., Wang W.Y. & Chen R.S.: Genome-based analysis of virulence genes in a non-biofilm-forming *Staphylococcus epidermidis* strain (ATCC 12228). *Molecular Microbiology* 49 (2003) 1577-1593.

Zhou Y.L., Niinomi M. & Akahori T.: Effects of Ta content on Young's modulus and tensile properties of binary Ti-Ta alloys for biomedical applications. *Materials Science and Engineering* A 371 (2004) 283-290.

Appendix A: Cost calculations

The actual calculations for the costs for different Ti compositions were:

Let: Ti-6Nb-4Zr (wt%) = 10 g (total mass)

Then: mass $_{(Ti)}$ = $90\% \; x \; 10 \; g = 9.0 \; g \; Ti$

mass $_{(Nb)}$ = $6\% \; x \; 10 \; g = 0.6 \; g \; Nb$

mass $_{(Zr)}$ = $4\% \; x \; 10 \; g = 0.4 \; g \; Zr$

Based on Table 3.2, therefore:

$$50 \; g \; Ti = R \; 1\,463.00$$

$$9.0 \; g \; Ti = R \; X.00 \text{ (let X be unknown)}$$

$$\therefore \text{X} = \frac{R \; 1\,463.00 \; x \; 9.0 \; g \; Ti}{50 \; g \; Ti} = \textbf{R 263.34} \text{ (i.e. 9.0 g Ti would cost R 263.34)}$$

The same calculation procedure was done for Zr and Nb, and gave:

$$\text{X} = \frac{R \; 2\,629.00 \; x \; 0.4 \; g \; Zr}{50 \; g \; Zr} = \textbf{R 21.04} \text{ (i.e. 0.4 g Zr would cost R 21.04)}$$

$$\text{X} = \frac{R \; 1\,832.00 \; x \; 0.6 \; g \; Nb}{50 \; g \; Nb} = \textbf{R 21.98} \text{ (i.e. 0.6 g Nb would cost R 21.98)}$$

Therefore, 10 g Ti-6Nb-4Zr (wt%) would cost:

$$Total \; (R) = R \; 263.34 + R \; 21.04 + \; R \; 21.98$$

$$= \boldsymbol{R \; 306.36}$$

For each 10 g sample alloy with 5 wt% Cu added, 0.5 g (5% x 10 g) would be copper. Therefore, the cost of Cu to make 10 g Ti alloy (with 5 wt% Cu) would be:

$$\text{X} = \frac{R \; 14\,353 \; x \; 0.5 \; g \; Cu}{50 \; g \; Cu} = \textbf{R 143.53} \text{ (i.e. 0.5 g Cu would cost R 143.53)}$$

The same calculation procedure was done for the cost analysis of all identified Ti compositions for this project, and Table 4.18 gives the results.

Appendix B: Published and submitted work from this research

N.G. Hashe, L. Fowler, S. Norgren, W.E. Goosen, C. Öhman Mägi, N.D. Masia, L.A. Cornish, J. Westraadt, L.H. Chown, S. Magadla, **K.T. Nape**, M. Mavundla and L. Spotose, A microstructural analysis of A Ti-Ta-Cu-Nb-Zr alloy, 56th Annual Microscopy Society of Southern Africa Conference, Volume 48, p. 30, Mykonos Resort, Langebaan, Western Cape, 1st – 5th December 2019. ISBN 978-0-6398435-0-6

K. Dyal Ukabhai, L. Fowler, **K.T. Nape**, M. Mavundla, L. Spotose, S. Magadla, N.D. Masia, D.E.P. Klenam, N.G. Hashe, C. Öhman Mägi, S. Norgren, L.H. Chown and L.A. Cornish, Effect of Different Copper Additions to Ti–10.1Ta–1.7Nb–1.6Zr (MASS%), 56th Annual Microscopy Society of Southern Africa Conference, Volume 48, p. 37, Mykonos Resort, Langebaan, Western Cape, 1st – 5th December 2019. ISBN 978-0-6398435-0-6

K. Dyal Ukabhai, **K.T. Nape**, L. Spotose, M. Mavundla, I.A. Mwamba, M.O. Bodunrin, L.H. Chown and L.A. Cornish, Thermo-mechanical processing and phase analysis of titanium alloys with copper additions, SA Journal of Science and Technology, Conference of the South African Advanced Materials Initiative (CoSAAMI) 2021, 84-90. doi.org/10.36303/SATNT.2021cosaami.17

Ansara I., Ivanchenko V., Cornish L., Ukabhai K. & **Nape K**.: Cu-Ti Binary Phase Diagram Evaluation, in *MSI Eureka*, Watson, A. (Ed.), MSI, Materials Science International Services GmbH, Stuttgart (2021), Document ID: 20.11457.2.4. (Copy not available).

A MICROSTRUCTURAL ANALYSIS OF A Ti-Ta-Cu-Nb-Zr ALLOY

N.G. Hashe[1], L. Fowler[2], W.E. Goosen[3], S. Norgren[2], N.D. Masia[4], L.A. Cornish[4], C. Öhman-Mägi[2], L.H. Chown[4], S. Magadla[1], K.T. Nape[4], M. Mavundla[4] and L. Spotose[4]

[1]Department of Physics, Nelson Mandela University, Port Elizabeth, [2]Department of Engineering Science, Uppsala University, Uppsala, Sweden, [3]CHRTEM, Nelson Mandela University, Port Elizabeth, [4]School of Chemical and Metallurgical Engineering, and DST-NRF Centre of Excellence in Strong Materials, hosted by the University of the Witwatersrand, Johannesburg

Titanium and its alloys are used in the medical industry as implants because of their biocompatibilities and excellent mechanical and physical properties[1]. The Ti-6Al-4V alloy is used as an implant material due to its high corrosion resistance and excellent biocompatibility[1]. However, there are concerns about the toxicity of aluminium and vanadium[2]. The other concern is the formation of the adherent biofilms around the surface area of the implants[3]. Therefore, the current research is aimed at replacing V and Al with Ta, Nb and Zr to produce a biocompatible alloy with antibacterial[4] and osseointegrative properties that has a similar microstructure to that of an alpha-beta Ti-6Al-4V alloy.

The Ti-10.1Ta-1.7Nb-1.6Zr (wt%) alloy produced by Stenlund *et al.*[5] was studied further. Titanium and Zr sponges were mixed with Ta and Nb wires and compressed into a 7 kg lump, which was melted four times in vacuum in an Electron Beam furnace for homogeneity. The Ti-10.1Ta-1.7Nb-1.6Zr alloy was mixed with 3 mass% Cu and the mixture was melted five times in a custom built arc-furnace. Annealing was done in a sealed quartz-ampoule at 1.333 mbar (after flushing) in a conventional furnace. Heat treatment was done at 980 °C for 10 hours, followed by 798 °C for 6 hours, with a final rapid salt-brine water quench. The annealing temperatures were chosen to obtain the alpha Ti (hcp) and beta Ti (bcc)[5]. After heat treatment, the samples were prepared metallographically and analysed by scanning electron microscopy (SEM) and X-ray diffraction (XRD).

Backscattered SEM imaging (Fig. 1) shows that the microstructure of the Ti-Ta-Cu-Nb-Zr alloy was lamellar, which are reported to have a high fatigue crack propagation resistance and high fracture toughness[6]. There were small, irregular regions of a much darker phases (indicated by a white arrow) , within the dark phase (indicated by a white star). Energy dispersive spectroscopy (EDX) showed the light contrast phase (indicated by a black arrow) had more Ta and Cu, with less Nb than the dark phase. However, the Nb content was less than 1 mass%, so the results were too near the detection limit to be reliable. The dark phase was identified as alpha Ti since it had more Ti. The small regions of the darkest phase were too small to analyse accurately with EDX.

The XRD patterns only showed alpha-Ti (Fig, 2). The pattern for the heat treated samples also showed apparent preferred orientation, which was surprising considering that the pattern from the as-cast sample was more random. Further work is required to identify the darkest phase, and XRD needs to be repeated with a more suitable X-ray source in order to quantify the phases present in the material.

References:
1. Geetha, M. *et al.* (2009) Prog. Mat. Sci. 54, 397.
2. Niinomi M. and Nakai M. (2011) Int. J. Biomater. 2011, 1.
3. Lorenzetti, M. *et al.* (2015) Appl. Mater. Interfaces 7, 1644.
4. Magadla, S. *et al.* (2019) Euromat 2019 Abstracts, 2288.
5. Stenlund, P. *et al.* (2015) Acta Biomat. 20, 165.
6. Filip, R. *et al.* (2003) J. Mat. Proc. Techn. 133, 84.

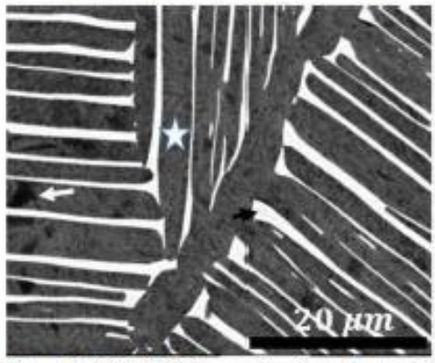


Figure 1. SEM-BSE image showing the typical microstructure of Ti-Ta-Nb-Zr-Cu alloy with three phases.

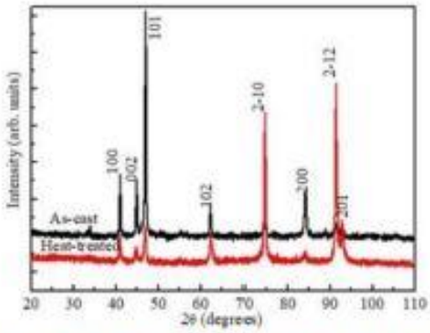


Figure 2. XRD patterns of the as-cast and heat treated Ti-Ta-Cu-Nb-Zr alloy, showing only alpha-Ti.

Corresponding author: nobom.hashe@mandela.ac.za

EFFECT OF DIFFERENT COPPER ADDITIONS TO Ti–10.1Ta–1.7Nb–1.6Zr

K. Dyal Ukabhai[1], L. Fowler[2], K.T. Nape[1], M. Mavundla[1], L. Spotose[1], S. Magadla[3], N.D. Masia[1,4], D.E.P. Klenam[1], N.G. Hashe[3], C. Öhman Mägi[2], S. Norgren[5], L.H. Chown[1] and L.A. Cornish[1]

[1]Sch. Chem. & Met. Eng. and DST-NRF CoE Strong Materials, hosted by U.Witwatersrand, [2]Dept of Eng. Sciences, Ångström Lab. Uppsala University, Sweden, [3]Dept Physics, Nelson Mandela University, Port Elizabeth, [4]Advanced Materials Division, Mintek, Randburg, [5]Sandvik Coromant R&D, Stockholm, Sweden

Commercially pure titanium is popular for bone-anchored dental devices, while the stronger Ti-6Al-4V alloy is preferred for higher load applications. However, Al and V are potentially toxic, giving reason to develop new (α+β) alloys without these elements, but with similar proportions of the two phases: (αTi) (brackets denote the solid solution based on Ti with that structure) and (βTi), for similar mechanical properties to Ti-6Al-4V. Stenlund *et al.*[1] undertook computer calculations to derive "TTNZ", an (α+β) alloy with similar phase proportions to Ti-6Al-4V, but without Al or V: Ti-10.1Ta-1.7Nb-1.6Zr (in wt%). The alloy was manufactured from Ti and Zr sponge, and Ta and Nb wire, which were mixed, compressed, then melted in vacuum in an electron beam furnace to generate a homogeneous alloy.

Around 7% of patients with dental implants suffer from peri-implantitis within 10 years due to infection[2]. Copper is known to have antimicrobial properties[3]. Liu *et al.*[4] studied sintered Ti–xCu alloys (x = 2, 5, 10 and 25 wt%) using XRD and SEM, and the antibacterial activity was assessed. The Ti_2Cu phase was found in all alloys. A Cu-rich phase formed in alloys with >5wt% Cu, which were also the best alloys for antibacterial activity.

This study used TTNZ samples made in the same way as Stenlund *et al.*[1] with nominal 1, 3, 5 and 10 wt% Cu added. The samples were prepared metallograpically, and studied using XRD and SEM-EDX after Vickers hardness tests ($HV_{0.1}$). XRD showed only (αTi) and (βTi) in the 0 and 1 wt% Cu TTNZ-Cu alloys, but the 3, 5 and 10 wt% Cu alloys had increasing amounts of Ti_3Cu[5], instead of the more commonly-reported Ti_2Cu[4]. SEM-EDX gave the copper content of Ti_2Cu as 28.1±0.3 to 29.7±1.1 at.% Cu. Increased Cu changed the microstructures from mainly (βTi) with small amounts of precipitated (αTi) for 0 and 1 wt% Cu (Fig. 1) to more equal amounts of the two phases with 3 wt% Cu (Fig. 2). Further increase in Cu increased the Ti_3Cu proportions. The 10 wt% Cu alloy had a totally different microstructure (Fig. 3), with fewer and shorter (αTi) laths, and Ti_3Cu precipitated on the prior (βTi) grain boundaries. Hardness increased with copper addition up to 5 wt% Cu, but 10 wt% Cu had lower hardness due to its different microstructure. The hardnesses were: 145±8, 182±6, 200±10, 201±8 and 178±8 $HV_{0.1}$ for 0, 1, 3, 5 and 10 wt% Cu respectively. Although most of the hardness indentations were square, Fig. 2 shows there was less plastic deformation of the harder Ti_3Cu phase. The lower hardness of the 10 wt% Cu alloy indicated too much copper had been added.

References:
1. Stenlund, P. *et al.* (2015) Acta Biomat. 20, 165.
2. Derks, J. *et al.* (2015) J. Dent. Res. 94(3), 44S.
3. Grass, G., Rensing, C. and Solioz, M. (2011) Appl. Environ. Microbiol. 77, 1541.
4. Liu, J. *et al.* (2014) Mat. Sci. & Eng. C35, 392.
5. Canale, P. and Servant, C. (2002) Z.Metallkd. 93(4), 273.

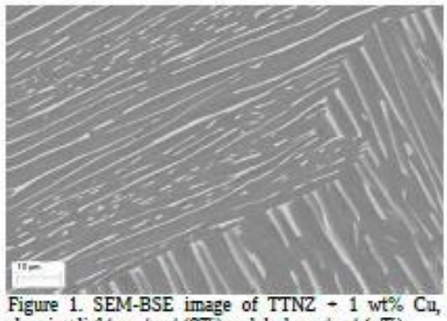


Figure 1. SEM-BSE image of TTNZ + 1 wt% Cu, showing light contrast (βTi) and dark contrast (αTi).

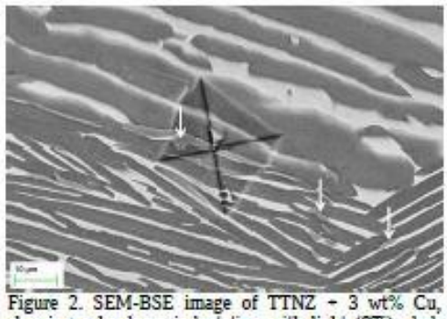


Figure 2. SEM-BSE image of TTNZ + 3 wt% Cu, showing a hardness indentation with light (βTi), dark (αTi) and medium contrast Ti_3Cu (shown by arrows).

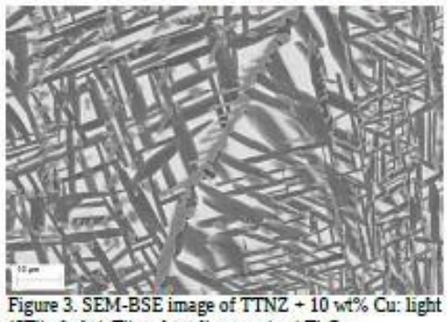


Figure 3. SEM-BSE image of TTNZ + 10 wt% Cu: light (βTi), dark (αTi) and medium contrast Ti_3Cu.

Corresponding author: lesley.cornish@wits.ac.za

Thermo-mechanical processing and phase analysis of titanium alloys with copper additions

KD Ukabhai[a,b,*], KT Nape[a,b], L Spotose[a,b], M Mavundla[a,b], IA Mwamba[b,c], MO Bodunrin[a,b,d], LH Chown[a,b], LA Cornish[a,b]

[a] School of Chemical and Metallurgical Engineering, University of the Witwatersrand, Private Bag 3, WITS, 2050, South Africa
[b] DSI-NRF Centre of Excellence in Strong Materials, hosted by the University of the Witwatersrand, Johannesburg, Private Bag 3, WITS, 2050, South Africa
[c] Advanced Materials Division, Mintek, Private Bag X3015, Randburg, 2125, South Africa
[d] African Academy of Sciences, P.O. Box 24916-00502, Nairobi, Kenya
Email: *669011@students.wits.ac.za, 573762@students.wits.ac.za, 2187508@students.wits.ac.za, 1597090@students.wits.ac.za, alainm@mintek.co.za, michael.bodunrin@wits.ac.za, lesleyhchown@gmail.com, Lesley.cornish@wits.ac.za

Abstract

In dentistry and orthopaedics, to replace and mend broken bones, any replacement material needs to have: low density, high strength, good biocompatibility and must be able to integrate closely with the bone. Titanium-based alloys have these properties, although currently used alloys contain toxic elements, and commercially pure Ti does not have sufficient strength. Within ten years, 7% of dental implants have complete failure, mainly from bacterial infection. Therefore α + β type Ti-alloys were developed by adding b stabilisers, with similar phase proportions to Ti-6Al-4V without the toxic elements, with Cu additions for antibacterial properties and Ru for corrosion resistance. Deformation behaviour of Ti-6Al-4V and Ti-Ta-Nb-Zr alloys were also studied using a Gleeble thermomechanical simulator. The compositions of the new alloys were derived using Thermo-Calc. Ti-8Nb-4Zr alloys had bimodal microstructures and the addition of Cu formed the Ti_2Cu phase. The Ti-6Ta-1.5Zr and Ti-6Ta-1.5Zr-0.2Ru alloys with no Cu had coarse α lamellae, whereas the alloys with Cu had parallel α plates. The Gleeble results showed that higher flow stresses were obtained at higher strain rates and lower temperatures, agreeing with literature. At 850 °C, the Ti-6Al-4V alloy had higher flow stresses than Ti-10.1Ta-1.7Nb-1.6Zr. The Ti-6Al-4V and Ti-10.1Ta-1.7Nb-1.6Zr alloys had steady-state flow stresses at 950 °C, and continuous flow softening at 850 °C for both strain rates.

1. Introduction

Biomedical materials are used daily to improve the lives of many people. These materials are used in various parts of the human body as intravascular stents, heart valves, replacement implants in knees, hips, elbows, shoulders, ears and dentistry (Geetha et al., 2009; Zhang et al., 2011). With ageing populations, there is increased demand for biomedical materials with long life spans that do not require revision surgery once implanted. One of the main causes for failure of dental implants is peri-implantitis, which is a site-specific infectious disease that causes inflammation in soft tissues, and bone loss around an osseointegrated implant (Persson and Renvert, 2014).

Biomedical materials have been studied since the 1980s, and typically include 316L stainless steel, Co-Cr based alloys and Ti alloys (Navarro et al., 2008; Khan et al., 2006). However, there are issues with these materials. For example, stainless steel is prone to sudden failure (Bundy et al., 1983), whereas Co-Cr based alloys and Ti alloys such as Ti-6Al-4V can release unfavourable toxic metals into the body (Okazaki and Gotoh, 2005).

Biomedical materials need to have high corrosion and wear resistance, be highly biocompatible and have a comparable modulus to the bone. For these reasons Ti-alloys have been used in recent years, due to their high specific strength, excellent corrosion resistance, low elastic modulus, and superior biocompatibility (Calin et al., 2007; Zhang et al., 2007). Titanium alloys have been designed not only for medical use, but also for jewellery, aerospace, military, automobiles and mobile phones (Calin et al., 2007; Zhang et al., 2007). Compared to 316L stainless steel and Co-Cr, Ti-alloys have significantly lower densities, and their elastic modulus is much closer to those of the bone (Mitragotri and Lahann, 2009).

There are five types of Ti-alloys: α-type and near α type, α + β type, β-type and shape memory (Zhang et al., 2011). The α-type alloys have not been used due to low mechanical and fatigue strength in load bearing applications (Mitragotri and Lahann, 2009). The α + β type alloys have good corrosion resistance and excellent capability of osseointegration (integration of materials into bone) (Stenlund et al., 2015; Sidambe, 2014), although the elastic moduli are higher than of the bone (Lindahl and Lindgren, 1967; Burnstein et al., 1976). The β-type alloys are currently being developed the most, due to their low elastic moduli, and high strength for load bearing uses (Zhang et al., 2011). However, β-type alloys are expensive since their alloying elements are expensive, and not many thorough investigations have been done to determine their reliability in the human body during long term service (Zhang et al., 2011). However, currently used Ti-6Al-4V contains toxic vanadium (V) (Choubey et al., 2004; Tamilselvi et al., 2006). Ti-6Al-7Nb and Ti-5Al-2.5Fe were developed to replace Ti-6Al-4V (Choubey et al., 2004; Tamilselvi et al., 2006), but these alloys contain aluminium (Al), which can lead to diseases such as Alzheimer's (Li et al., 2014).

Thus, it would be advantageous to develop a Ti alloy with neither V nor Al, so α + β type alloys for dental screws were derived by adding α and β stabilisers to Ti, to mimic the beneficial α + β phase proportions of Ti-6Al-4V, which was used as a reference material. Zirconium, tantalum, niobium and molybdenum were proposed as potential non-toxic alloying elements, since they are β stabilizers (Eisenbarth et al., 2004). They are considered as biocompatible (Kuroda et al., 1998; Eisenbarth et al., 2004), because they minimize adverse tissue reactions originating from the release of metal ions from the implant (Meng et al., 2014). Other additions to the alloys considered were copper (Cu) and ruthenium (Ru). Copper is one of the most promising alloying elements for clinical applications because of its low toxicity and high cytocompatibility (Jin et al., 2015), and Ru is a noble element which improves corrosion resistance in Ti-alloys, even in extremely small amounts (Schutz, 1996). The alloy must mimic the phase proportions of Ti-6Al-4V, which is done by varying the alloy component proportions to achieve the targeted phase proportions, as Stenlund et al. (2015) did. The alloys should be fairly low cost, easy to manufacture, have good mechanical properties and be biocompatible with the human body. The moduli of the alloys must be comparable to that of the bone (10-40 GPa) (Nang et al., 2005).

The Ti-10.1Ta-1.7Nb-1.6Zr (TTNZ) alloy was developed as an implant material (Stenlund et al., 2015) to improve mechanical strength and osseointegration, and mimic the phases of Ti-6Al-4V. However, no studies were done on thermo-mechanical processing of the alloy, which could provide information for shaping it. Hot compression testing is a thermo-mechanical test, which can be used to study flow stress, stress-relaxation, hot workability, and flow softening behaviour due to recrystallisation and recovery (Jha and Kumar, 2010). Therefore, hot compression testing was done on Ti-10.1Ta-1.7Nb-1.6Zr and Ti-6Al-4V alloys using the Gleeble3500® to compare their behaviour. Thermo-mechanical studies done on Ti-6Al-4V showed that low strain rate at higher temperature improved the ductility, and higher flow stresses were observed at higher strain rate and lower deformation temperatures (Vanderhasten, 2008; Shaikh et al., 2015; Dos Santos, 2017; Bodunrin, 2018).

2. Experimental procedure

2.1 α + β alloys

The compositions of different alloys were determined using Thermo-Calc, with the TTTI3 database, and composition which gave similar α (hcp) and β (bcc) proportions to Ti-6Al-4V and Ti-10.1Ta-1.7Nb-1.6Zr were selected (Table 1). The compositions were then made up as arc melted buttons, by mixing 99.9% pure elemental powders. The weighed out mixed powders were cold compacted with a hydraulic press and then melted in a button arc furnace, which was purged with argon gas and used a titanium oxygen-getter, as commonly used. The buttons were then cut and prepared metallographically for analysis.

Table 1: Compositions of alloys determined from Thermo-Calc

Alloy	Composition (wt%)	
1	Ti-8Nb-4Zr	Ti-8Nb-4Zr-5Cu
2	Ti-6Ta-1.5Zr	Ti-6Ta-1.5Zr-5Cu
3	Ti-6Ta-1.5Zr-0.2Ru	Ti-6Ta-1.5Zr-0.2Ru-5Cu
4	Ti-2Ta-8Mo-8Sn	Ti-2Ta-8Mo-8Sn-5Cu

The buttons were cut using a Struers Secotm-10 cutting machine, with a diamond MOD13 blade. The pieces were mounted in polyfast using an ATM-Opal 410 hot mounting press, then ground (P400, P800, P1200 and P2400 papers) and polished (MD-Chem cloth) by hand on a Struers Tegramin-20® machine.

The samples were then etched using Kroll's reagent and examined on a cross-polarized and Leica DM 6000®-Light Optical Microscope (LOM) and a Sigma Zeiss scanning electron microscope (SEM) in backscattered (BSE) and secondary electron (SE) modes, and representative images are shown here. The phases of the samples were analysed by energy dispersive X-ray spectroscopy (EDS) in the SEM.

2.2 Thermo-mechanical testing

The as-received Ti-6Al-4V and Ti-10.1Ta-1.7Nb-1.6Zr (TTNZ) (Stenlund et al., 2015) alloys were subjected to isothermal compression testing using a Gleeble 3500® Thermomechanical Simulation Facility. Cylindrical samples of 8 mm diameter x 12 mm height were machined using electric discharge machining. Prior to compression testing, a chromel-alumel thermocouple was welded to the centre of the test samples using a spot welder, to measure the temperature. The samples were then placed on the Hydrawedge autoloader. Graphite foil and nickel paste were placed between the Iso-T tungsten carbide anvils and the sample to reduce the effect of friction during deformation.

The samples were heated at 5 °C/s to the deformation temperature, and held for 360 s for homogenisation, then deformed at the parameters specified in Table 2, followed by compressed air cooling. The test parameters were used in the Quicksim software using the (.hds) program, which was then converted to Gleeble Script Language (.gsl) before running each experiment.

Table 2: Hot compression testing parameters

Deformation parameters		Temperature (°C)	
Strain	Strain rate (s^{-1})		
0.6	0.1	850	950
0.6	10	850	950

3. Results

3.1 α + β alloys

Results from Thermo-Calc were used only as guidelines for the compositions as the database used did not have all the reported phases in the alloys. The b stabiliser amounts added (Ta, Zr and Nb) were varied until the phase proportion mimicked those of Figure 1a. The amount of Ru and Cu that was added was based on Jin et al. (2015) and Schutz (1996). Figures 1 and 2 show the phase proportion diagrams for the as-received alloys and the experimental

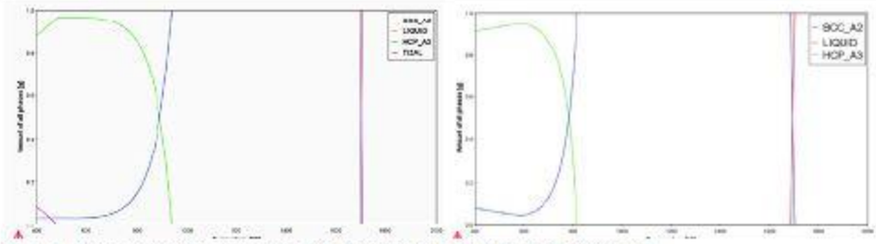


Figure 1. Phase proportion diagrams for: (a) Ti-6Al-4V (wt%) and (b) Ti-10.1Ta-1.7Nb-1.6Zr (wt%).

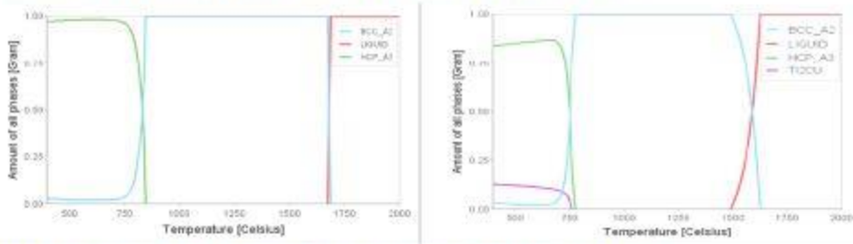


Figure 2: Phase proportion diagrams for: (a) Ti-6Ta-1.5Zr-0.2Ru (wt%) and (b) Ti-6Ta-1.5Zr-0.2Ru-5Cu (wt%)

alloys. Figures 1a and 1b show the phase proportions for Ti-6Al-4V are 0.88 αTi, 0.03 βTi and 0.09 Ti_2Cu, and for TTNZ are 0.92 αTi and 0.08 βTi at 400 °C (at lower temperatures the results are less reliable). From Figure 2a the phase proportions were 0.97 αTi and 0.03 βTi for Ti-6Ta-1.5Zr-0.2Ru and Ti-6Ta-1.5Zr-0.2Ru-5Cu had 0.84 αTi, 0.03 βTi and 0.13 Ti_2Cu at 400 °C as shown in Figure 2b. The phase proportions were quite similar, and when Cu was added the Ti_2Cu phase formed (Figure 2b).

Figure 3 shows the optical micrographs of the as-cast Ti-8Nb-4Zr-xCu (x = 0, 5 wt%) alloys. The bimodal microstructure of Alloy 1 (Figure 3a) consisted of clusters of α-laths within the transformed β matrix. The black precipitates were thought to be the Ti_2Cu phase (Figure 3b), which formed when 5 wt% Cu was added. The EDX results of the Ti-8Nb-4Zr-xCu (x = 0, 5 wt%) alloys indicated a higher Cu content in the light contrast βTi phase compared to the dark contrast αTi phase. The EDX analysis showed that the black precipitates (Figures 3b) were Ti_2Cu. The microstructures of Ti-8Nb-4Zr-xCu (x = 0.5 wt%) showed similar αTi, βTi and Ti_2Cu morphologies. The EDX analyses indicated higher Cu content in βTi phases than αTi in Ti-8Nb-4Zr-5Cu. The solid solubility of Cu in βTi was 4.5 ± 0.4 wt% for Ti-8Nb-4Zr-5Cu.

The SEM images are shown in Figures 4 and 5. Figures 4a and 5a show the Ti-6Ta-1.5Zr and Ti-6Ta-1.5Zr-0.2Ru alloy microstructures, and Figures 4b and 5b shows the same alloys with Cu additions. The microstructures comprised mostly αTi layers. The alloys in Figures 4 and 5 all had αTi laths which precipitated at the prior βTi grain boundaries. The Cu-containing alloys (Figures 4b and 5b) had less plate-like αTi phase and acicular αTi .

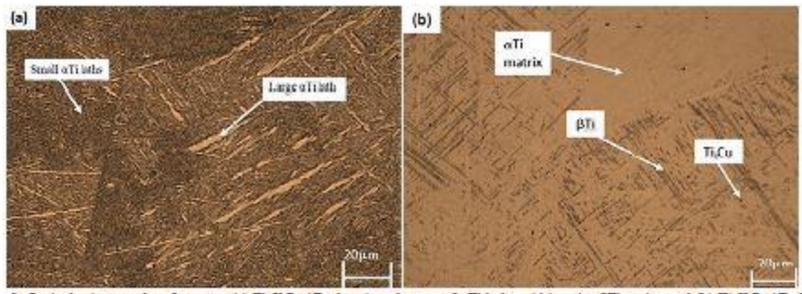


Figure 3: Optical micrographs of as-cast: (a) Ti-8Nb-4Zr showing clusters of αTi laths within prior βTi grains and (b) Ti-8Nb-4Zr-5Cu (wt%) showing βTi, αTi and Ti_2Cu phases

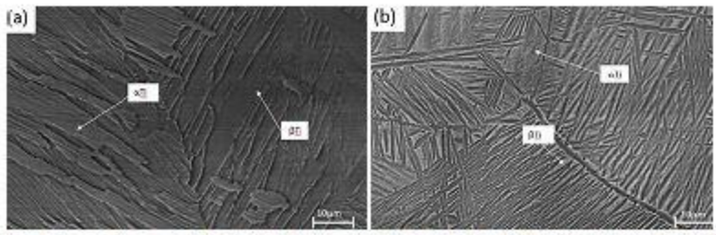


Figure 4: SEM-BSE images of as-cast: (a) Ti-6Ta-1.5Zr (wt%) and (b) Ti-6Ta-1.5Zr-5Cu showing thick and thin (αTi) lamellae, growing from prior βTi grain boundaries

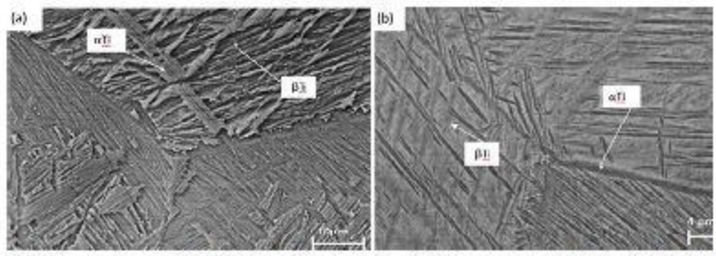


Figure 5: SEM-BSE images of as-cast: (a) Ti-6Ta-1.5Zr-0.2Ru (wt%) showing light contrast plate-like αTi, and (b) Ti-6Ta-1.5Zr-0.2Ru-5Cu showing parallel αTi laths growing from prior βTi grain boundaries

The αTi lamellae growing from the βTi grain boundaries into the matrix were present mostly in the alloys without Cu (Figures 4a and 5a). With Cu additions the microstructures (Figures 4b and 5b) exhibited needle-like and parallel αTi plates, grown from the prior βTi and into the matrix. Higher magnification had to be used to see the αTi plates in Ti-6Ta-1.5Zr-0.2Ru-5Cu (Alloy 3) compared to other alloys. The EDX analyses showed that the alloys without Cu had coarser αTi lamellae with more Ta, whereas the alloys with Cu had parallel αTi plates with more Ta and Cu than the nominal composition.

Figure 6 shows Alloy 4 (Ti-2Ta-8Mo-8Sn) with and without Cu. The microstructure was apparently single-phase cored dendritic, and any second phase was in a small proportion, and could not be analysed accurately by EDX.

3.2 Thermo-mechanical testing

Hot deformation behaviour of the as-received Ti-6Al-4V reference material and Ti-10.1Ta-1.7Nb-1.6Zr alloys was evaluated and Figure 7 shows the stress-strain curves obtained from uniaxial compression testing. The microstructures as a function of deformation temperature and strain rates are shown in Figures 8-11. The strain rates for Ti-6Al-4V were higher at both temperatures compared to Ti-10.1Ta-1.7Nb-1.6Zr. For 10 s^{-1} strain rate the Ti-6Al-4V at 950 °C was higher than 0.1 s^{-1} strain rate.

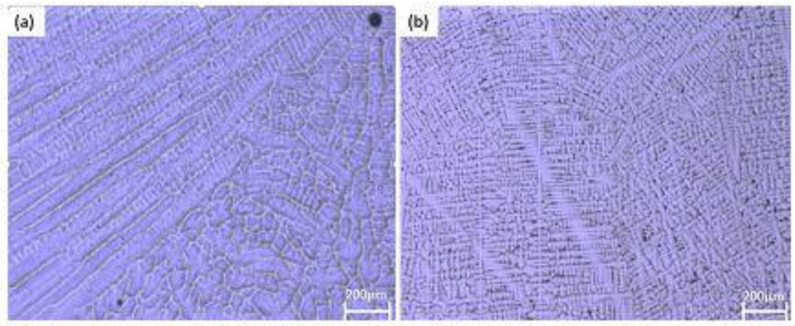


Figure 6: Optical micrographs of as-cast: (a) Ti-2Ta-8Mo-8Sn and (b) Ti-2Ta-8Mo-8Sn-5Cu (wt%) showing mainly a cored dendritic structure, with small proportions (Ti_2Cu)

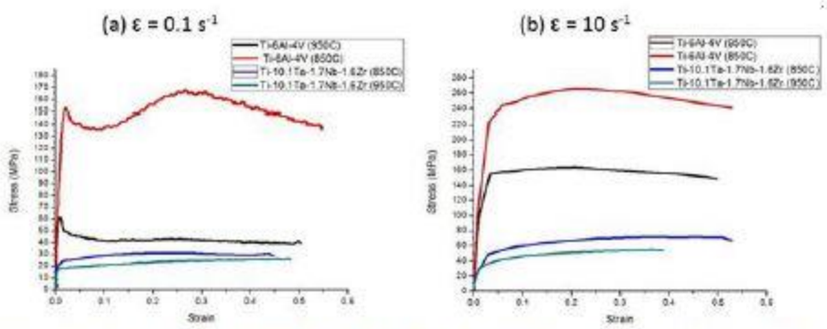


Figure 7: Stress-strain curves of the as-received Ti-6Al-4V and Ti-10.1Ta-1.7Nb-1.6Zr (wt%) alloys deformed at 850 °C and 950 °C, at: (a) 0.1 s^{-1} and (b) 10 s^{-1} strain rates

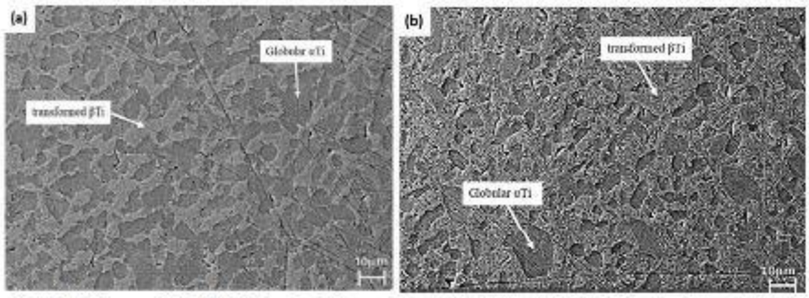


Figure 8: SEM-BSE images of Ti-6Al-4V deformed at 0.1 s^{-1} strain rate at: (a) 850 °C and (b) 950 °C, showing βTi matrix (light contrast) and αTi globules (dark contrast)

The SEM-BSE images (Figure 8) show αTi globules within the transformed βTi matrix. At 950 °C, the αTi globules decreased in size. There were coarser αTi globules and grain coarsening at 850 °C (Figure 9a), and finer αTi globules at 950 °C (Figure 9b).

At 850 °C, TTNZ comprised coarse αTi particles (Figure 10a), whereas at 950 °C there were fine αTi particles (Figure 10b). Figure 11 shows microstructures of globular αTi grains, and the βTi matrix. The αTi globules appeared to be coarser at 950 °C (Figure 11b), than at 850 °C (Figure 11a).

4. Discussion

4.1 α + β alloys

As the phase proportions for Ti-6Al-4V (Figure 1) and Ti-6Ta-1.5Zr-0.2Ru (Figure 2a) were similar, it is expected that Ti-6Ta-1.5Zr-0.2Ru could replace Ti-6Al-4V and have similar properties.

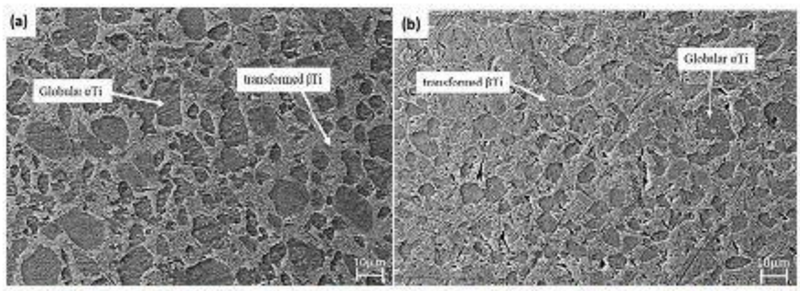


Figure 9: SEM-BSE images of Ti-6Al-4V (wt%) deformed at 10 s^{-1} strain rate at: (a) 850 °C and (b) 950 °C, showing βTi-matrix (light contrast) and αTi globules (dark contrast)

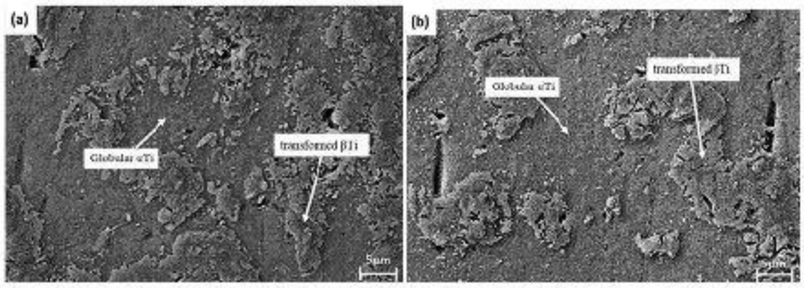


Figure 10: SEM-BSE images of Ti-10.1Ta-1.7Nb-1.6Zr (wt%) deformed at 0.1 s^{-1}strain rate at: (a) 850 °C and (b) 950 °C, showing αTi particles in βTi matrix

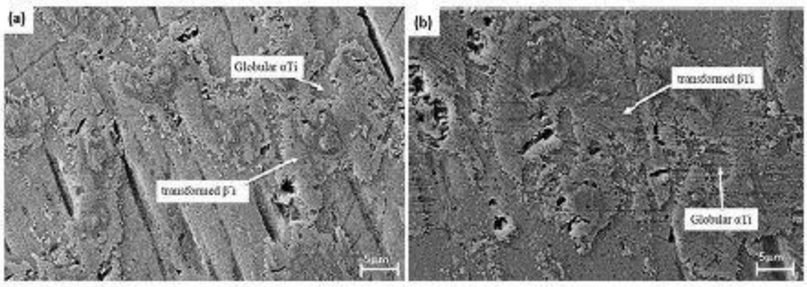


Figure 11: SEM-BSE images of Ti-10.1Ta-1.7Nb-1.6Zr (wt%) deformed at 10 s^{-1}strain rate at: (a) 850 °C and (b) 950 °C, showing αTi particles and βTi matrix

The phase proportion diagram in Figure 2b shows that the αTi phase proportions decreased slightly and Ti_2Cu formed when Cu was added to the alloy. The βTi phase proportion was not affected by the addition of Cu.

Alloys 1-3 (Table 1) had similar morphologies, although Alloy 4 had a dendritic microstructure. Due to Alloy 4 not being clearly two-phase (there could have been a small amount of a second phase, but insufficient for the microstructure targeted), no further analysis was done on that alloy. Possibly, the alloy solidified as apparently single-phase because of the high cooling rate from arc-melting, which was not at equilibrium, whereas Thermo-Calc shows equilibrium phases and compositions. However, this shows that Alloy 4 was more cooling-rate dependent than the other alloys. Alloys 1-3 with Cu additions formed the Ti_2Cu phase, which would improve the antibacterial properties of the alloys (Jin et al. 2005) and make them suitable candidates to replace the existing Ti alloys.

4.2 Thermo-mechanical testing

The thermo-mechanical results for Ti-10.1Ta-1.7Nb-1.6Zr showed that ductility improved at higher temperature (950 °C) and lower strain rate (0.1 s^{-1}), and at lower temperature (850 °C) and higher strain rate (10 s^{-1}). The ductility of Ti-6Al-4V improved at lower deformation temperature, consistent with Prozesky et al. (2017) and Dos Santos et al. (2017). An increased strain rate (10 s^{-1}) led to increased flow stress, compared to 0.1 s^{-1}, and increasing the temperature (950 °C) gave reduced flow stress for both Ti-6Al-4V and Ti-10.1Ta-1.7Nb-1.6Zr alloys. The Ti-6Al-4V alloy had higher flow stress (170 MPa at 0.1 s^{-1} and 270 MPa at 10 s^{-1}) than Ti-10.1Ta-1.7Nb-1.6Zr (35 MPa 0.1 s^{-1} and 75 MPa at10 s^{-1}) at 850 °C. The Ti-6Al-4V and Ti-10.1Ta-1.7Nb-1.6Zr alloys had steady-state flow stress at 950 °C, and continuous flow softening at 850 °C for both 0.1 s^{-1} and 10 s^{-1} strain rates.

The Ti-6Al-4V alloy deformed at 850 °C and 0.1 s^{-1} had elongated αTi laths (Figure 6a), which grew into globular α grains at 950 °C and 10 s^{-1} (Figure 7b). This suggested that globularisation of αTi occurred from the higher strain rate and increased deformation temperature. Thus, a higher deformation temperature and strain rate gave a finer Ti-6Al-4V microstructure. The deformed Ti-6Al-4V microstructures were different from the initial microstructure, which were fully αTi lamellar microstructures.

The microstructures of the TTNZ alloy before and after deformation (Figures 8 and 9) were similar, with globular αTi grains. At 850 °C and 10 s^{-1} (Figure 9a), and at 950 °C and 0.1 s^{-1} (Figure 8b), there were finer αTi globules, similar to the initial microstructure. The coarser αTi globules at 850 °C and 0.1 s^{-1} (Figure 8a) and 950 °C and 10 s^{-1} (Figure 9b) suggested that a combination of lower temperature and higher strain rate, and/or a higher temperature and lower strain rate, would produce finer microstructures.

5. Conclusions

The Ti-8Nb-4Zr alloys studied had bimodal microstructures comprising αTi laths in a transformed β matrix. Alloys without Cu (Alloys 2 and 3) had coarser αTi lamellae with more Ta, whereas the alloys with Cu had parallel αTi plates with higher Ta and Cu contents. All the alloys with Cu formed sufficient Ti_2Cu, except for Alloy 4 which had only small amounts. Alloy 4 was the only unsuccessful alloy, as it did not have a sufficientyly high proportion of the second phase as the other alloys.

Higher flow stresses were obtained at higher strain rates (10 s^{-1}) and lower temperature (850 °C). At 850 °C, the Ti-6Al-4V alloy had higher flow stresses (170 MPa at 0.1 s^{-1} and 270 MPa at10 s^{-1}) than Ti-10.1Ta-1.7Nb-1.6Zr (35 MPa 0.1 s^{-1} and 75 MPa at10 s^{-1}). The Ti-6Al-4V and Ti-10.1Ta-1.7Nb-1.6Zr alloys had steady-state flow stresses at 950 °C, and continuous flow softening at 850 °C for both 0.1 s^{-1} and 10 s^{-1} strain rates.

Acknowledgements

This work was supported by the National Research Foundation [Grant numbers 41292, STNT170905261815].

Contribution of each author

K Dyal Ukabhai undertook calculations, experiments and wrote the paper; K T Nape, L Spotose and M Mavundla undertook calculations and experiments; I A Mwamba gave advice on some aspects and was the Mintek co-supervisor; M O Bodunrin gave advice on calculations and thermomechanical simulations; L H Chown co-supervised all the students, hosted the postdoctoral fellow and helped with the interpretation; and L A Cornish conceived the overall project, co-supervised the students, helped with interpretation and checked the writing of the paper.

References

1. Bodunrin M.O. 2018. Hot deformation and corrosion behaviour of low-cost α+β titanium alloys with aluminium, vanadium and iron additions, School of Chemical and Metallurgical Engineering, University of the Witwatersrand, Johannesburg. PhD Thesis, *1-293*.
2. Bundy K J, Marek M and Hochman R F. 1983. In vivo and in vitro studies of the stress-corrosion cracking behaviour of surgical implant alloys. Journal of Biomedical Materials Research *17, 467-87*.
3. Burnstein A, Reilly D and Martens M. 1976. Aging of bone tissue: mechanical properties. Journal of Bone and Joint Surgery *58 (1), 82-86*.
4. Calin M, Zhang L C and Eckert J. 2007. Tailoring of microstructure and mechanical properties of a Ti-based bulk metallic glass-forming alloy. Scripta Materialia *57 (12), 1101-1104*.
5. Choubey A, Balasubramaniam R and Basu B. 2004. Effect of replacement of V by Nb and Fe on the electrochemical and corrosion behaviour of Ti–6Al–4V in simulated physiological environment. Journal of Alloys and Compounds *381 (1), 288-294*.
6. Dos Santos M W B. 2017. Investigation of the mechanical behaviour and microstructural evolution of titanium alloys under superplastic and hot forming conditions. Ecole des Mines d'Albi-Carmaux Polytechnic School of Engineering of the University of Sao Paulo (EPUSP).
7. Eisenbarth E, Velten D, Müller M, Thull R and Breme J. 2004. Biocompatibility of β-stabilizing elements of titanium alloys. Biomaterials *25, 5705-13*.
8. Geetha M, Singh A K, Asokamani R and Gogia A K. 2009. Ti based biomaterials, the ultimate choice for orthopaedic implants – A review. Progress in Materials Science *54 (3), 397-425*.
9. Jha B K and Kumar V. 2010. Role of thermo-mechanical simulation in the development of special steel products. Proceedings of National Conference and 2nd Gleeble User Workshop RDCIS Ranchi 1-10.
10. Jin L G X, Liu E, Yu F, Shu X and Wang H. 2015. Microstructure, corrosion and tribological and antibacterial properties of Ti-Cu coated stainless steel. Journal of the Mechanical Behaviour of Biomedical Materials *50, 23–32*.
11. Khan W, Marew T and Kumar N. 2006 Immobilization of drugs and biomolecules on in situ copolymerized active ester polypyrrole coatings for biomedical applications. Biomedical Materials *1 (4), 235-241*.
12. Kuroda D, Niinomi M, Morinaga M, Kato Y and Yashiro T. 1998. Design and mechanical properties of new β type titanium alloys for implant materials, A Structure and Material Properties, Microstructural Process. Materials Science and Engineering A *243, 244-249*.
13. Li Y, Yang C, Zhao H, Qu S, Li X and Li Y. 2014. New developments of Ti-based alloys for biomedical applications. Journal of Materials *7 (3), 1709-1800*.
14. Lindahl O and Lindgren A G H. 1967. Cortical bone in man: II. Variation in tensile strength with age and sex. Acta Orthopaedica Scandinavica *38, 141-147*.
15. Meng Q, Guo S, Lin Q, Hu L and Zhao X. 2014. A β-type TiNbZr alloy with low modulus and high strength for biomedical applications. Progress in Natural Science: Materials International *24, 157-162*.
16. Mitragotri S and Lahann J. 2009. Physical approaches to biomaterial design. Nature Materials *8, 15-23*.
17. Navarro M, Michiardi A, Castaño O and Planell J A. 2008. Biomaterials in orthopaedics. Journal of the Royal Society Interface *5 (27), 1137-1158*.
18. Okazaki Y and Gotoh E. 2005. Comparison of metal release from various metallic biomaterials in vitro. Biomaterials *26 (1), 11-21*.
19. Persson G R and Renvert S. 2014. Cluster of bacteria associated with peri-implantitis. Clinical Implant Dentistry and Related Research *16 (6), 783-793*.
20. Prozesky D J, Bodunrin M O and Chown L H. 2017. Hot-deformation behaviour of α+β Ti-Al-V-Fe experimental alloys. AIP Conference Proceedings 1896 1160019-1-6 https://doi.org/10.1063/1.5008194.
21. Schutz R. W. 1996. Ruthenium enhanced titanium alloys. Platinum Metals Review *40 (2), 54-61*.
22. Shaikh A A, Kashyap B P and Chauthai A. 2015. Identification of Favorable Hot Working Condition for Ti-6Al-4V Alloy. National Conference on Thermo-mechanical processing of Steels & 5th Gleeble User Workshop, India, *78-91*.
23. Sidambe A T. 2014. Biocompatibility of advanced manufactured titanium implants—a review. Materials *7 (12), 8168-8188*.
24. Stenlund P, Omar O, Brohede U, Norgren S, Norlindh B, Johansson A, Lausmaa J, Thomsen P and Palmquist A. 2015. Bone response to a novel Ti-Ta-Nb-Zr alloy. Acta Biomaterialia *20, 165-175*.
25. Nang S, Banerjee R, Stechschulte J and Fraser H L. 2005. Comparison of microstructural evolution in Ti-Mo-Zr-Fe and Ti-15Mo biocompatible alloys. Journal of Materials Science: Materials in Medicine *16 (7), 679-685*.
26. Tamilselvi S, Raman V and Rajendran N. 2006. Corrosion behaviour of Ti–6Al–7Nb and Ti–6Al–4V ELI alloys in the simulated body fluid solution by electrochemical impedance spectroscopy. Electrochimica Acta *52 (3), 839-846*.
27. Vanderhasten M. 2008. Ti-6Al-4V: Deformation map and modelisation of tensile behavior.
28. Katholieke Universitsit Leuven. Doctoral Thesis, *1-150*.
29. Zhang L C, Kim K B, Yu P, Zhang W Y, Kuma U and Eckert J. 2007. Amorphization in mechanically alloyed (Ti, Zr, Nb)– (Cu, Ni)–Al equiatomic alloys. Journal of Alloys and Compounds *428, 157-163*.
30. Zhang L C, Klemm D, Eckert J, Hao Y L and Sercombe T B. 2011. Manufacture by selective laser melting and mechanical behaviour of a biomedical Ti–24Nb–4Zr–8Sn alloy. Scripta Materialia *65 (1), 21-24*.